



**UNIVERSIDAD
DE ANTIOQUIA**

**DYNAMICS OF NEAR-SURFACE ATMOSPHERIC STABILITY
WITH IMPLICATIONS FOR LAND-ATMOSPHERE
INTERACTIONS IN COMPLEX TERRAIN AND
HETEROGENEOUS LANDSCAPES**

Juan José Henao Castañeda

Universidad de Antioquia

Facultad de Ingeniería, Escuela Ambiental

Medellín, Colombia

2020



Dynamics of near-surface atmospheric stability with implications for land-atmosphere interactions in complex terrain and heterogeneous landscapes

Juan José Henao Castañeda

Tesis de investigación presentada como requisito parcial para optar al título de:

Doctor en Ingeniería Ambiental

Asesores:

Ph.D. Angela María Rendón Pérez

Ph.D. Juan Camilo Villegas Palacio

Grupo de Investigación:

Grupo de Investigación en Ingeniería y Gestión Ambiental – GIGA

Universidad de Antioquia

Facultad de Ingeniería, Escuela Ambiental.

Medellín, Colombia

2020

Dynamics of near-surface atmospheric stability with implications for land-atmosphere interactions in complex terrain and heterogeneous landscapes

**Case studies: an idealized urban valley, the Aburrá Valley,
and the Amazon forest**

A dissertation submitted to the University of Antioquia in
partial fulfillment of the requirements of the degree of

Doctor of Engineering
(Doctor en Ingeniería Ambiental)

by

Juan José Henao Castañeda

Advisors:

Angela M. Rendón P.

Juan C. Villegas P.

Grupo de Ingeniería y Gestión Ambiental
Facultad de Ingeniería
Universidad de Antioquia

2020

*A mi familia:
Ignacio, Stella,
Isa, Ana, Nico
y Lina*

Acknowledgments

I would like to thank my advisors for their encouragement and guidance during these years. Their input and discussions were an invaluable source of learning. I am specially grateful to Juan Fernando Salazar for his support since day one at UdeA.

I thank John F. Mejía and the Desert Research Institute for the financial help and dedication during a six-month research visit at the Reno, Nevada campus. Important advances of this dissertation occurred during the visit. I am grateful to John for his contagious passion for science and always finding time for advice.

I would also like to thank my friends from the GIGA research group for making these years full of joy.

The main financial support for this dissertation was provided by the Colombian Administrative Department of Science, Technology and Innovation (COLCIENCIAS, now MINCIENCIAS), under the National Doctoral Grant Convocatoria 727 de 2015.

I sincerely thank Dr. R. Y. Ynoue, Dr. M. W. Rotach and Dr. C. D. Hoyos for their valuable comments and discussion in the evaluation of this thesis.

Finally, I would like to thank my family and Lina for their endless love and support.

Abstract

In this work three case studies are used to investigate the influence of atmospheric stability and land cover heterogeneity or transformation on land-atmosphere interactions in two different environments: urban valleys and a tropical forest. The work on urban valleys mainly focuses on the mechanisms of air pollution transport, which are studied using high-resolution numerical simulations. In the forest case, observed data is analyzed to study the dynamics of thermal stratification in a forest site and its contrast with a nearby cropland site.

The first study (Chapter 2) evaluates how urban heat island (UHI) mitigation affects air quality in an idealized urban valley by means of large-eddy simulations. A passive tracer represents air pollution transport in three UHI mitigation scenarios and under two initial stability conditions. Contrary to the common premise, results demonstrate that UHI mitigation can worsen air quality in urban valleys, via the alteration of the mechanisms of air pollution transport. Results also show the theoretical possibility of finding moderate UHI mitigation strategies in which UHI is reduced while limiting the impacts on air quality. A fundamental implication is that these strategies should be explored through case-specific realistic simulations for guiding decision-making in real systems. Large and often expensive urban transformations should not be accomplished under the generalized assumption that UHI mitigation improves environmental quality. This study contributes to building a more general understanding of the potential impacts of UHI mitigation, as well as of the mechanisms behind, which is a continuing challenge with important implications for urban management and planning.

The second study (Chapter 3) examines the dispersion of traffic emissions in the Aburrá valley (located in the Colombian Andes) during an episode of severe air pollution, using the WRF-Chem and a Lagrangian model at sub-kilometer resolution. The study focuses on the identification of areas with relatively large carbon monoxide (CO) concentrations, and analyze the role of local and regional airflows in the distribution of pollutants inside the valley. The meteorological model performance, considering different planetary boundary layer parameterizations and grid sizes, is evaluated using available observations. Overall, the meteorological model performance is within recommended benchmarks for complex terrain. Model performance improves with increasing grid resolution for surface temperature and wind direction, but not for wind speed. Both dispersion models reproduce important features of the spatial and diurnal variability of CO in the valley, but underestimate CO concentrations throughout the simulation period. The south and southeast areas of the valley present relatively large CO concentrations, associated to a prevalent northerly

transport along the valley axis and reduced transport on the eastern slope. The representation of CO improves when the model adequately reproduces observed rainfall, due to its effects on boundary layer height and stability, which condition ventilation. This study contributes to the research on atmospheric modelling of transport processes in complex terrain, which is crucial for informing decisions on air quality management in critical areas such as urban valleys.

The third study (Chapter 4) investigates the diurnal and seasonal dynamics of vertical temperature profiles in a dense Amazon forest, as well as a comparison of these dynamics between forested and non-forested landscapes. This is achieved through a comparative analysis using two meteorological towers, one located in a primary forest and the other in a neighboring agricultural site. Results show that thermal stratification within the forest canopy can be divided in three profile types. During the daytime, the forest is characterized by a below-canopy temperature inversion (stably stratified) and neutral or unstable conditions above-canopy. At night, the situation is reversed with near neutral conditions in the lower layers and a stable atmosphere starting either within canopy or above the canopy top. This diurnal oscillation occurs almost simultaneously and with opposite behaviors below- and above-canopy, with temperature gradients switching signs around 06 and 18 local time. The dry season results in stronger and more persistent daytime below-canopy inversions, and a nighttime inversion with larger gradients and starting within canopy (instead of above). The thermal stratification near the forest surface is mostly unaffected from the turbulence above the canopy top. In contrast to forest, the cropland site is characterized by mostly unstable conditions during the day and a temperature inversion during the night. These results provide new insights on the dynamics of thermal stratification within forest canopies and could be useful for model-based studies on land-atmosphere interactions and forest loss impacts.

Overall, this dissertation provides new evidence about how land heterogeneity, including pronounced elevation gradients in valleys and contrast between urban and rural land or forest and cropland landscapes, affect land-atmosphere interactions through effects on near-ground atmospheric stability. This has important implications for the transport of air pollutants in urban valleys as well as for land-atmosphere exchanges in forest landscapes.

Contents

List of Figures	vii
List of Tables	xiii
1 Introduction	1
1.1 References	5
2 Trade-off between urban heat island mitigation and air quality in urban valleys	12
2.1 Abstract	12
2.2 Introduction	12
2.3 Model and experiment design	15
2.3.1 Numerical model	15
2.3.2 Topography and model domain	16
2.3.3 Initial and boundary conditions	16
2.3.4 UHI mitigation scenarios	17
2.3.5 Air pollution: passive tracer	18
2.3.6 Averaging procedure	19
2.3.7 Turbulent kinetic energy	19
2.4 Results	19
2.4.1 Trade-off: impacts of UHI mitigation on air quality	19
2.4.2 Air pollution transport mechanisms	24
2.4.2.1 Transport through the slopes	24
2.4.2.2 Transport through the valley center and cross-valley circulation	28
2.4.2.3 Atmospheric stability	30
2.5 Discussion	32
2.6 Conclusions	35
2.7 References	35
3 Sub-kilometer dispersion simulation of a CO tracer for an inter-Andean urban valley	45
3.1 Abstract	45
3.2 Introduction	46
3.3 Data and Methods	49
3.3.1 Modeling framework	49

3.3.1.1	WRF-Chem model setup	51
3.3.1.2	Lagrangian model	52
3.3.1.3	Emission disaggregation	53
3.3.2	Observations	56
3.3.3	Model performance evaluation	57
3.4	Results	58
3.4.1	Model Evaluation	58
3.4.1.1	Surface wind and temperature	58
3.4.1.2	PBL height	61
3.4.1.3	Upper-air wind and temperature	63
3.4.2	Carbon monoxide tracer	66
3.4.3	Spatial Distribution of the Tracer	71
3.5	Discussion	77
3.6	Conclusions	79
3.7	References	80
4	Diurnal and seasonal dynamics of near-ground thermal stratification across neighboring Amazon forest and cropland sites	92
4.1	Abstract	92
4.2	Introduction	93
4.3	Data and Methods	95
4.4	Results	98
4.4.1	Comparison between forest and cropland sites	98
4.4.2	Forest	103
4.5	Discussion	108
4.6	Conclusions	111
4.7	References	112
5	Conclusions and Outlook	120
Appendix		123
A	Supplementary figures for chapter 2	123
B	Supplementary figures for chapter 3	131
C	Supplementary figures for chapter 4	141

List of Figures

2.1	Cross-section of the idealized urban valley topography (i.e. the $x - z$ plane). Terrain is uniform in the y -direction (along-valley). An urban area covers the entire valley floor (surface area below C1). The named volumes are used for the analysis.	17
2.2	Daytime evolution of normalized tracer mixing ratio from morning (top) to afternoon (bottom), with low stability ($\partial\theta/\partial z = 1 \text{ K km}^{-1}$ at initial condition). UHI mitigation varies from no- (left) to moderate- (center) and full-mitigation (right) scenarios. Isentropes are shown every 1 K. The gray hatched box indicates the location of the urban area. See supplementary Fig. A1 for results of the other scenarios . . .	21
2.3	As in Fig. 2.2 but for high stability ($\partial\theta/\partial z = 3 \text{ K km}^{-1}$ at initial condition). See supplementary Fig. A2 for results of the other scenarios	22
2.4	Daytime evolution of normalized tracer mixing ratio depending on the UHI mitigation scenario and initial stability: low (left and middle-left) or high (middle-right and right). Each panel shows average values for the volumes in Fig. 2.1. Each line represents a UHI mitigation scenario, as indicated by the corresponding Q_u value in panel a. The results of symmetric volumes (SL1, SL2, PL1, and PL2; not shown) are not presented.	23
2.5	Daytime evolution of the wind field (vectors) starting with low stability. Colors show the w wind component. See supplementary Fig. A3 for results of the other scenarios	25
2.6	As in Fig. 2.5 but starting with high stability. See supplementary Fig. A4 for results of the other scenarios	26
2.7	Daytime evolution of total TKE starting with low stability. Contours show isentropes every 1 K. See supplementary Fig. A6 for results of the other scenarios.	27
2.8	As in Fig. 2.7 but starting with high stability. See supplementary Fig. A7 for results of the other scenarios.	28
2.9	Time-height distribution of normalized tracer mixing ratio for the UHI mitigation scenarios, and for the low (top) and high (bottom) stability levels. Values represent spatial averages over the valley floor. The bold line shows the approximate height of the CBL. See supplementary Fig. A8 for results of the other scenarios.	31

3.1	Top panels: (a) Domain configuration for the WRF simulations. (b) Enlarged version of D5 with the model topography shaded, the location/code of CO stations (black triangles), the studied transects and AMVA limits in black, with the main municipality (Medellin) in cyan. Panel (c) shows location/code of surface meteorological stations (red and black triangles), a microwave radiometer (green triangle, MWR) and a radar wind profiler (blue triangle, RWP). Colorbar in (c) represents terrain height in m for (b) and (c). Panel (d) shows a zoom of the road network (green lines with line-width representing road category), and the spatial distribution of adimensional CO emissions for each grid cell (colorbar): the emission at each grid cell is divided by the maximum emission.	50
3.2	Model performance of 2-m temperature or T2 (top), 10-m wind speed or WS (middle), and 10-m wind direction or WD (bottom) for the three PBL schemes implemented and domains D5, D4 and D3. Recommended benchmarks are represented as dashed (dot-dash) lines for flat (complex) terrain.	60
3.3	Diurnal cycles of (a) T2, and (b) WS. Time series of 24-hour moving-averages for (c) T2, and (d) WS. All values are network-averaged, see supplementary Fig. B5 for results of the best and worst performing stations. Wind speed analysis (panels b and d) do not consider stations that exceeded recommendations for all model configurations (i.e., stations 202, 68, 38 are not included; Fig. 3.2b). Results from D4 and D3 are averaged for the 3 PBLs to facilitate visualization (dashed and dot-dash lines, respectively).	62
3.4	Diurnal cycles of observed and modeled PBL height. Shaded area indicates ± 0.5 standard deviation of the observations. Analysis for the entire simulation period, except for the observations during dry days, orange dots, averaged over March 11, 16, 18 and 19 when no rainfall occurred: see Fig. 3.9d.	63
3.5	Time series of potential temperature at 50 m (a) and 800 m (b) above terrain, from the microwave radiometer –MWR– (black) and the corresponding (closest) pixel in the WRF-Chem model configuration (red) and ERA5 (blue).	65
3.6	As Fig. 3.5 but for zonal (a) and meridional (b) wind components at 1.3 km (a, b) and 200 m (c, d) above terrain. Black lines represent the Radar Wind Profiler (RWP).	66

3.7	Diurnal cycles of simulated CO concentration at the first full model level and observed CO concentration at the available air quality stations. Left (right) panels show actual (standardized, i.e. centered and scaled) concentrations.	68
3.8	Standardized 24-hour moving averages of CO for the simulation period. A similar figure with hourly time series is presented in supplementary figure B8.	69
3.9	Time series of standardized CO (a), PBL height (b), potential temperature difference between 50 and 800 m above terrain (c), and hourly rainfall (d). Dashed line in panel b represents the mean valley depth.	70
3.10	Horizontal distribution of CO tracer concentrations (a, b) and simulated concentrations to emissions (C/E) ratio (c, d), both averaged over the entire simulation period. Blue line: Aburrá River. Black lines: 2,500 m terrain height contour. Cyan lines: main municipality limits.	72
3.11	Horizontal distribution of the simulated CO tracer shaded, averaged for the first three full model levels, and the horizontal 10-m wind vectors U,V at 06, 12, 18 and 00 LST, from the simulation-averaged diurnal cycle; wind vectors are shown at every tenth grid point in the horizontal directions. Blue line: Aburrá River. Black lines: 2,500 m terrain height contour. Cyan lines: main municipality limits.	74
3.12	Vertical cross sections for the transects shown in Fig. 1b with the CO tracer shaded. Left (right) panels present morning (afternoon) situations. Along-valley oriented transect A include wind vectors with V, W (a, b); across-valley transects B, C, D include wind vectors with U,W (c-h). Wind vectors are shown at every second grid point in x direction. Isentropes are presented as grey contours every 1 K. PBL height is indicated with a blue dashed line.	75
3.13	Percent probability of source grid cells for particles reaching the polygons shown in black dashed lines, within the first 3 vertical levels. Values considering the entire simulation period with the Lagrangian model. Solid black lines: 2,500 m terrain height contour.	76
4.1	Location of K67 and K77 flux tower sites with topography (bottom panel) and LANDSAT-5 satellite image for 2004-08-31 (top and right panels).	96

4.2	Daily evolution of the mean vertical temperature profile at a) K67 forest and b) K77 cropland sites. Mean profiles are standardized by subtracting at all levels the value of the lowest level. Values plotted represent temperature at the top/bottom of the profile for the wet/dry season in °C. The gray background in a) represents the continuous canopy between 18-40 m.	99
4.3	Categorized temperature profiles for the K67 forest site (top panels) and K77 cropland site (bottom panels). To facilitate visualization and comparison, all profiles have its origin point at zero, achieved by subtracting the value of the first level (T_0) to the values of all levels.	100
4.4	Diurnal cycle of occurrence of each temperature profile category in the forest (top, K67) and cropland (bottom, K77) sites during the dry (left) and wet (right) seasons. Values in legends are total number profiles for each category and season.	101
4.5	Mean daytime (07–17 local time) vertical profiles of temperature (a, d), mixing ratio (b, e) and vapor pressure deficit (c, f).	103
4.6	Maximum duration of below-canopy temperature inversion at forest for each season. Maximum duration refers to consecutive hourly profiles in a day categorized as surface-based inversion.	104
4.7	Diurnal cycles of temperature gradients above- and below-canopy, at the K67 forest site. Below-canopy: from 0.6m to 18m; Above-canopy: from 40m to 50m	105
4.8	Temperature profiles during the day and night, for strong wind speeds (top, WS > 3.3 m/s) and weak wind speeds (bottom, WS < 2 m/s). Values in blue (gray) represent the upper (lower) quartile for either the strong (top) or weak (bottom) wind speed regimes. The boxplots in the right show the distribution of wind speed regimes in m/s.	106
4.9	Temperature difference above the canopy (a; 40–50 m), in the canopy (b; 18–40 m) and below the canopy (c; 0.6–18 m) as a function of friction velocity. Values for daytime (07–17 local time).	107
4.10	Diurnal oscillation of the undercanopy inversion layer occurring in both the dry (a) and wet (b) seasons. The inversion layer (red areas) oscillates between the below-canopy layer at daytime and the in-canopy or above canopy layers at nighttime. Gradients are computed between consecutive levels of measurement and represent average values for the whole study period.	109

A1	Daytime evolution of normalized tracer mixing ratio from morning (top) to afternoon (bottom), with low stability ($\partial\theta/\partial z = 1 \text{ K km}^{-1}$ at initial condition). UHI contrasts varies from 300 W m^{-2} (left) to 150 W m^{-2} (center) and no contrast, i.e., full-mitigation scenario (right). Isentropes are shown every 1 K.	123
A2	As in Fig. A1 but for high stability ($\partial\theta/\partial z = 3 \text{ K km}^{-1}$ at initial condition).	124
A3	Daytime evolution of the wind field (vectors) starting with low stability. Colors show the w wind component.	125
A4	As in Fig. A3 but starting with high stability.	126
A5	Cross-valley wind (U) in the morning for all UHI scenarios and high stability ($\partial\theta/\partial z = 3 \text{ K km}^{-1}$ at initial condition)	127
A6	Daytime evolution of total TKE starting with low stability. Contours show isentropes every 1 K.	128
A7	As in Fig. A6 but starting with high stability.	129
A8	Time-height distribution of normalized tracer mixing ratio for the UHI mitigation scenarios, and for the low (top) and high (bottom) stability levels. Values represent spatial averages over the valley floor. The bold line shows the approximate height of the CBL.	130
B1	Urban category represented in land use databases: Modis 15 arc-second (light grey) and USGS 24-category database (dark grey).	131
B2	Normalized vehicle count for every weekday, derived from closed-circuit television cameras operated by the local mobility authority.	132
B3	Wind speed mean bias error and root-mean-square error for the five best/worst stations. The largest differences across horizontal resolutions (between domains) occur for stations where the model performance is worse.	133
B4	Diurnal cycle of T2 at station 41 for days with (blue) and without (red) rainfall.	134
B5	2-m air temperature for the best (top, station 83) and worst (middle top, station 73) performing stations. 10-m wind speed for the best (middle bottom, station 82) and worst (bottom, station 202) performing stations. Time series constructed with hourly information.	135
B6	Time series of hourly PBL height. Observed PBL height is estimated with the bulk Richardson number, see methods for further details and data source.	135

B7	Diurnal cycles of wind direction at stations 68, 12, and at the radar wind profiler (RWP) at 200 m above terrain, exhibiting the predominant northerly flow. The 200 m height RWP observations are included for comparison with surface winds, as it is away from the built environment but within the PBL. Red triangles: MYNN PBL; blue squares: Shin-Hong PBL; green circles: MYJ PBL.	136
B8	Hourly time series of standardized CO for the entire simulation period.	137
B9	Model topography as represented in domains D2-D5, with grid sizes of: a) 300 m, b) 900 m, c) 2.7 km, and d) 8.4 km.	138
B10	Vertical profiles of potential temperature during the morning (mean value for 7-5 AM) and afternoon (mean value for 3-5 PM), for the three PBL schemes used and observations with a microwave radiometer. Asterisks in the afternoon profiles show the estimated height of the convective boundary layer.	139
B11	Difference in terrain elevation between the model (pixel) and real elevation. Some stations used in the study are not included because terrain elevation is not available. Model values correspond to closest model pixel.	139
B12	Observed index values. Calculated using the observed concentration but using the rest of the needed information from the model. <i>Note: this figure is not included in the published paper as it was created after for the thesis.</i>	140
C1	Forest cover loss from 2000 to 2012 in the Amazon basin (blue line in the left panel). Map produced with the Global Forest Watch map builder with data from Hansen et al. 2013 (full reference in section 4.7). Zoom into the study sites, overlaid with LANDSAT-5 satellite image (right panel).	141
C2	Mean diurnal cycles of carbon dioxide concentration (top) and water vapor mixing ratio (bottom). Mixing ratio (r), derived from water vapor concentration, and CO_2 concentrations were measured at 8 vertical levels from 0.91–62.24 m.	142

List of Tables

3.1	Additional details and physical parameterizations employed in the experiments.	52
3.2	Model performance of 2-m temperature (T2), 10-m wind speed (WS) and 10-m wind direction (WD). Values for each domain are averaged over all available stations and the three PBLs, and values for each PBL are averaged over all available stations and the three domains.	59
3.3	Upper-air mean absolute error (MAE) and correlation coefficient (r) for potential temperature (θ) and the zonal and meridional (U,V) wind components using observations from a radar wind profiler (RWP) and a microwave radiometer (MWR). The analysis is performed on 24-h moving averages of results from domain D5 (0.3 km resolution) using the closest grid point to the instruments. See supplementary table B1 for results with hourly data.	64
4.1	Site and data descriptions. Further information can be found in Fitzjarrald and Sakai, 2010; Hutyra et al., 2008a; Hutyra et al., 2008b.	97
B1	Upper-air mean absolute error (MAE) and correlation coefficient (r) for potential temperature (θ) and the zonal and meridional (U,V) wind components using observations from a radar wind profiler (RWP) and a microwave radiometer (MWR). The analysis is performed with hourly results from domain D5 (0.3 km resolution) using the closest grid point to the instruments.	131

Common Acronyms & Abbreviations

AMVA	Metropolitan Area of the Aburrá Valley
CBL	Convective boundary layer
CO	Carbon Monoxide
EI	Emission Inventory
LES	Large eddy simulation
LST	Local standard time
MWR	Microwave radiometer
MYJ	Mellor–Yamada–Janjić PBL scheme
MYNN	Mellor–Yamada–Nakanishi–Niino PBL scheme
PBL	Planetary boundary layer
RWP	Radar wind profiler
ShinHong	Shin & Hong scale aware PBL scheme
T2	2-m temperature
TKE	Turbulence kinetic energy
UHI	Urban heat island effect
WD	10-m wind direction
WS	10-m wind speed

Chapter 1

Introduction

The exchange of heat, mass and momentum between the Earth's surface and the atmosphere plays a crucial role in the dynamics of weather and climate. Land-atmosphere interactions influence atmospheric variables such as temperature, humidity, wind, and pollutant concentrations near the surface, which are relevant for applications in a variety of disciplines, including the earth system sciences, agriculture and forestry, urban planning, air quality, among other (De Wekker et al., 2018). These exchange processes occur through the atmospheric boundary layer (ABL), where the flow is generally turbulent. Thus, turbulent transport plays a prominent role and determines to a large extent the efficiency of the exchange (Rotach et al., 2015). Due to the influence of atmospheric stability on vertical motions, and therefore on turbulent transport, the vertical structure of ABL stability affects the exchange efficiency, which is generally enhanced (reduced) due to the presence of unstable (stable) layers. Stability in the ABL follows the diurnal cycle of solar radiation, with radiative cooling of the ground surface being the most common source of stable layer formation (Mahrt, 2014). Land-atmosphere interactions are also affected by land use/cover changes, with urbanization and agriculture being among the most important anthropogenic influences on climate (Kalnay and Cai, 2003).

In this dissertation, the general science questions to be explored are: How does the dynamics of stability in the ABL affect land-atmosphere exchanges and atmospheric transport mechanisms? and how these dynamics and related impacts are influenced by land cover heterogeneity or transformation? Hence, the main research topics that are discussed throughout the dissertation are: atmospheric transport mechanisms, dynamics of atmospheric stability within the ABL, and land cover impacts. The core of the dissertation is composed of three chapters (Chapters 2 through 4) that deal with the general questions and research topics from different but interrelated perspectives.

The general research questions are investigated through a combination of case studies and approaches. Two different environments are considered: urban valleys

(Chapters 2 and 3) and a forest landscape (Chapter 4). Both cases represent complex landscapes in which the dynamics of atmospheric stability are known to play a significant role in land-atmosphere exchanges (e.g. Leukauf et al., 2016; Dupont and Patton, 2012). In urban valleys (Chapters 2 and 3), the focus is given to air quality, through the study of the physical mechanisms of air pollution transport. In the forest case (Chapter 4), the focus is given to the dynamics of thermal stratification below the forest canopy. Three methodological approaches are used: Chapters 2 and 3 are based on idealized and realistic numerical modelling, respectively, whereas Chapter 4 is based on observed data analysis. Land cover impacts are studied through simulation of scenarios (urban land modification, Chapter 2) and comparison of contrasting landscapes (forest versus cropland, Chapter 4). Further, Chapter 3 considers the heterogeneity of land cover in an urban valley through high-resolution realistic modelling. Multiple time scales are considered. In all cases, the diurnal cycle is regarded as a fundamental scale of analysis due to the marked variability of atmospheric stability and related processes at this temporal scale. However, in some cases the day-to-day (Chapter 3) and seasonal (Chapter 4) variability are also studied.

More specifically, the main goal of Chapter 2 is to investigate the potential impact of urban land transformation on air quality. This chapter is motivated by the general view that urban cooling strategies are considered as measures for improving the quality and sustainability of urban environments (Gago et al., 2013; Santamouris, 2014; Aleksandrowicz et al., 2017; Francis and Jensen, 2017; Saaroni et al., 2018). In this regard, surface temperature reduction is often considered as an indicator of environmental quality improvement (Santamouris, 2014; Tan et al., 2016; Ma et al., 2017; Morini et al., 2018). However, the dynamics of air pollution can be altered by urban modifications as these affect the surface energy balance (Makar et al., 2006; Rendón et al., 2014). Such modifications can be highly relevant in urban areas located in complex terrain, which are prone to pollution episodes (see, e.g., Malek et al., 2006; Whiteman et al., 2014; Wang et al., 2016; Largeron and Staquet, 2016; Toro A et al., 2019). The effects of urban cooling (a land cover change) on the daytime dispersion of pollutants in an idealized urban valley are analyzed by means of large-eddy simulations (LES) with the Weather Research and Forecasting model (Skamarock et al., 2019). LES is a numerical technique for integrating the filtered equations of motion in order to describe turbulent flow, where the largest and more energetic eddies (responsible for most of the turbulent transport) are resolved, while the smaller and unresolved eddies are parameterized. Different levels of atmospheric stability are

considered, as it is a relevant factor for transport processes in valleys (Rendón et al., 2014; De Wekker and Kossmann, 2015; Leukauf et al., 2016; Serafin et al., 2018). In all cases, the valley surface is divided into homogeneous areas of urban and rural land cover, which can differ only in their surface sensible heat flux. UHI mitigation scenarios are defined through different contrasts in sensible heat flux, based on observations and previous modeling studies (Christen and Vogt, 2004; Offerle et al., 2006; Wang, 2009; Zhang et al., 2014; Fan et al., 2017). The results challenge the common premise that urban heat island mitigation (i.e. “urban cooling”) generally improves environmental quality, including air quality.

The main goal of Chapter 3 is to investigate the mechanisms of air pollution transport in the Aburrá Valley, a densely populated inter-Andean urban valley in Colombia. The chapter presents a series of high-resolution numerical simulations of pollutant dispersion in the valley during a period of severe air pollution, using two different chemical transport models (CTM), WRF-Chem (Grell et al., 2005; Fast et al., 2006) and a stochastic Lagrangian dispersion model (Mejia et al., 2019). CTM are valuable tools for the understanding and management of air quality (Baklanov et al., 2014; Colette et al., 2013). The ability of such models to produce skillful forecasts depends on several critical factors, including a good representation of PBL processes (Hess et al., 2004; McKeen et al., 2007; Cuchiara et al., 2014), a fine grid resolution, especially for urbanized complex terrain (Fay and Neunh userer, 2006; Shrestha et al., 2009), and the emission inventories (EI), which should consider total emissions, as well as their spatial and temporal distribution (Saide et al., 2009; Kuik et al., 2016). The sensitivity of modelled meteorology on horizontal resolution and the selection of planetary boundary layer parameterization is evaluated using surface observations. A “top-down” approach (Loibl et al., 1993; Tuia et al., 2007; Eicker et al., 2008) using traffic information was employed to distribute the local emission inventory in space and time. Mobile emissions are represented by a passive tracer emulating carbon monoxide (CO), which in the region is mostly produced by mobile sources (AMVA, 2015). The analysis is aimed at the identification of areas with relatively larger concentrations, and the role of atmospheric stability and the local and regional airflows on pollutant distribution.

In Chapter 4 observed data is used to study the diurnal and seasonal dynamics of temperature inversions under the canopy of a dense tropical forest in the Amazon, and how these dynamics compare with a non-forested landscape. A characteristic feature of the near-ground atmosphere in forests is the formation of temperature

inversion layers during daytime (e.g. Shuttleworth, 1985; Fitzjarrald et al., 1990; Culf et al., 1997). Within these layers, air temperature increases in the upward direction, i.e. it is higher in the canopy than at the surface, due to the absorption of incident solar radiation in the upper canopy layers (Motzer, 2005; Goulden et al., 2006; Hardwick et al., 2015). The formation of these stable layers can influence land-atmosphere exchanges of scalars (Albertson et al., 2001; Staebler and Fitzjarrald, 2005; Miller et al., 2007; Pypker et al., 2007; Dupont and Patton, 2012; Freire et al., 2017; Santos et al., 2019), but a detailed enough representation of in-canopy stability and turbulence is rarely included in meteorological and chemical transport models (Theobald et al., 2015). Data comes from two eddy covariance towers in the Brazilian Amazon, which are approximately 20 km apart: one is located in a national forest reserve and the other in a cropland field. The analysis allows the discussion of potential effects of temperature inversion dynamics on the transport of scalars, as well as potential implications of forest loss.

Collectively, this dissertation provides new insights on the understanding of the dynamics of atmospheric stability in the ABL over complex landscapes (either urban valleys or contrasting vegetated landscapes), as well as how these dynamics affect land-atmosphere exchanges and can be altered by land cover transformation. Chapters 2, 3 and 4 are designed as separate manuscripts to submit for publication, whereas Chapter 5 concludes with a summary of the main findings and provides a perspective of the dissertation. This structure allows the reader to read Chapters 2 through 4 independently.

The work presented in Chapter 2 has been published in *Urban Climate* as “Trade-off between urban heat island mitigation and air quality in urban valleys” by Henao et al., 2020b. Chapter 3 has been published in *Atmospheric Pollution Research* as “Sub-kilometer dispersion simulation of a CO tracer for an inter-Andean urban valley” by Henao et al., 2020a. A preliminary version of the work in Chapter 2 was presented as a poster in the mountain meteorology session of EGU General Assembly 2019, in Vienna. Parts of the work presented in chapter 3 were presented as posters in the Urban and Regional Air Quality session of AGU Fall Meeting 2018, in Washington, and in the 2018 WRF/MPAS Users’ Workshop at NCAR in Boulder, Colorado.

1.1 References

- Albertson, J. D., G. G. Katul, and P. Wiberg (2001). “Relative importance of local and regional controls on coupled water, carbon, and energy fluxes”. *Advances in Water Resources* 24.9-10, 1103–1118. DOI: [10.1016/S0309-1708\(01\)00042-2](https://doi.org/10.1016/S0309-1708(01)00042-2).
- Aleksandrowicz, O., M. Vuckovic, K. Kiesel, and A. Mahdavi (2017). “Current trends in urban heat island mitigation research: Observations based on a comprehensive research repository”. *Urban Climate* 21, 1–26. DOI: [10.1016/J.UCLIM.2017.04.002](https://doi.org/10.1016/J.UCLIM.2017.04.002).
- AMVA - Área Metropolitana del Valle de Aburrá (2015). *Inventario de Emisiones Atmosféricas del Valle de Aburrá, año base 2013. In Spanish. Prepared by Universidad Pontificia Bolivariana - Grupo de Investigaciones Ambientales*. Convenio de Asociación No. CA 315 de 2014. Medellín: Área Metropolitana del Valle de Aburrá.
- Baklanov, A., K. Schlünzen, P. Suppan, J. Baldasano, D. Brunner, S. Aksoyoglu, G. Carmichael, J. Douros, J. Flemming, R. Forkel, S. Galmarini, M. Gauss, G. Grell, M. Hirtl, S. Joffre, O. Jorba, E. Kaas, M. Kaasik, G. Kallos, X. Kong, U. Korsholm, A. Kurganskiy, J. Kushta, U. Lohmann, A. Mahura, A. Manders-Groot, A. Maurizi, N. Moussiopoulos, S. T. Rao, N. Savage, C. Seigneur, R. S. Sokhi, E. Solazzo, S. Solomos, B. Sørensen, G. Tsegas, E. Vignati, B. Vogel, and Y. Zhang (2014). “Online coupled regional meteorology chemistry models in Europe: current status and prospects”. *Atmospheric Chemistry and Physics* 14.1, 317–398. DOI: [10.5194/acp-14-317-2014](https://doi.org/10.5194/acp-14-317-2014).
- Christen, A. and R. Vogt (2004). “Energy and radiation balance of a central European city”. *International Journal of Climatology* 24.11, 1395–1421. DOI: [10.1002/joc.1074](https://doi.org/10.1002/joc.1074).
- Colette, A., B. Bessagnet, R. Vautard, S. Szopa, S. Rao, S. Schucht, Z. Klimont, L. Menut, G. Clain, F. Meleux, G. Curci, and L. Rouil (2013). “European atmosphere in 2050, a regional air quality and climate perspective under CMIP5 scenarios”. *Atmospheric Chemistry and Physics* 13.15, 7451–7471. DOI: [10.5194/acp-13-7451-2013](https://doi.org/10.5194/acp-13-7451-2013).
- Cuchiara, G. C., X. Li, J. Carvalho, and B. Rappenglück (2014). “Intercomparison of planetary boundary layer parameterization and its impacts on surface ozone concentration in the WRF/Chem model for a case study in houston/texas”. *Atmospheric Environment* 96, 175–185. DOI: [10.1016/j.atmosenv.2014.07.013](https://doi.org/10.1016/j.atmosenv.2014.07.013).

- Culf, A., G. Fisch, Y. Malhi, and C. Nobre (1997). “The influence of the atmospheric boundary layer on carbon dioxide concentrations over a tropical forest”. *Agricultural and Forest Meteorology* 85.3-4, 149–158. DOI: [10.1016/S0168-1923\(96\)02412-4](https://doi.org/10.1016/S0168-1923(96)02412-4).
- De Wekker, S. F. J. and M. Kossmann (2015). “Convective Boundary Layer Heights Over Mountainous Terrain? A Review of Concepts”. *Frontiers in Earth Science* 3, 77. DOI: [10.3389/feart.2015.00077](https://doi.org/10.3389/feart.2015.00077).
- De Wekker, S. F. J., M. Kossmann, J. Knievel, L. Giovannini, E. Gutmann, and D. Zardi (2018). “Meteorological Applications Benefiting from an Improved Understanding of Atmospheric Exchange Processes over Mountains”. *Atmosphere* 9.10, 371. DOI: [10.3390/atmos9100371](https://doi.org/10.3390/atmos9100371).
- Dupont, S. and E. G. Patton (2012). “Influence of stability and seasonal canopy changes on micrometeorology within and above an orchard canopy: The CHATS experiment”. *Agricultural and Forest Meteorology* 157, 11–29. DOI: [10.1016/J.AGRFORMET.2012.01.011](https://doi.org/10.1016/J.AGRFORMET.2012.01.011).
- Eicker, M. O. de, R. Zah, R. Triviño, and H. Hurni (2008). “Spatial accuracy of a simplified disaggregation method for traffic emissions applied in seven mid-sized Chilean cities”. *Atmospheric Environment* 42.7, 1491–1502. DOI: <https://doi.org/10.1016/j.atmosenv.2007.10.079>.
- Fan, Y., Y. Li, A. Bejan, Y. Wang, and X. Yang (2017). “Horizontal extent of the urban heat dome flow”. *Scientific Reports* 7.1, 11681. DOI: [10.1038/s41598-017-09917-4](https://doi.org/10.1038/s41598-017-09917-4).
- Fast, J. D., W. I. Gustafson Jr., R. C. Easter, R. A. Zaveri, J. C. Barnard, E. G. Chapman, G. A. Grell, and S. E. Peckham (2006). “Evolution of ozone, particulates, and aerosol direct radiative forcing in the vicinity of Houston using a fully coupled meteorology-chemistry-aerosol model”. *Journal of Geophysical Research: Atmospheres* 111.D21. DOI: [10.1029/2005JD006721](https://doi.org/10.1029/2005JD006721).
- Fay, B. and L. Neunhäuserer (2006). “Evaluation of high-resolution forecasts with the non-hydrostatic numerical weather prediction model Lokalmmodell for urban air pollution episodes in Helsinki, Oslo and Valencia”. *Atmospheric Chemistry and Physics* 6.8, 2107–2128.
- Fitzjarrald, D. R., K. E. Moore, O. M. R. Cabral, J. Scliar, A. O. Manzi, and L. D. de Abreu Sá (1990). “Daytime turbulent exchange between the Amazon forest and the atmosphere”. *Journal of Geophysical Research* 95.D10, 16825. DOI: [10.1029/JD095iD10p16825](https://doi.org/10.1029/JD095iD10p16825).

- Francis, L. F. M. and M. B. Jensen (2017). “Benefits of green roofs: A systematic review of the evidence for three ecosystem services”. *Urban Forestry & Urban Greening* 28, 167–176. DOI: [10.1016/J.UFUG.2017.10.015](https://doi.org/10.1016/J.UFUG.2017.10.015).
- Freire, L. S., T. Gerken, J. Ruiz-Plancarte, D. Wei, J. D. Fuentes, G. G. Katul, N. L. Dias, O. C. Acevedo, and M. Chamecki (2017). “Turbulent mixing and removal of ozone within an Amazon rainforest canopy”. *Journal of Geophysical Research: Atmospheres* 122.5, 2791–2811. DOI: [10.1002/2016JD026009](https://doi.org/10.1002/2016JD026009).
- Gago, E., J. Roldan, R. Pacheco-Torres, and J. Ordóñez (2013). “The city and urban heat islands: A review of strategies to mitigate adverse effects”. *Renewable and Sustainable Energy Reviews* 25, 749–758. DOI: [10.1016/J.RSER.2013.05.057](https://doi.org/10.1016/J.RSER.2013.05.057).
- Goulden, M. L., S. D. Miller, and H. R. da Rocha (2006). “Nocturnal cold air drainage and pooling in a tropical forest”. *Journal of Geophysical Research* 111.D8, D08S04. DOI: [10.1029/2005JD006037](https://doi.org/10.1029/2005JD006037).
- Grell, G. A., S. E. Peckham, R. Schmitz, S. A. McKeen, G. Frost, W. C. Skamarock, and B. Eder (2005). “Fully coupled “online” chemistry within the WRF model”. *Atmospheric Environment* 39.37, 6957–6975. DOI: <https://doi.org/10.1016/j.atmosenv.2005.04.027>.
- Hardwick, S. R., R. Toumi, M. Pfeifer, E. C. Turner, R. Nilus, and R. M. Ewers (2015). “The relationship between leaf area index and microclimate in tropical forest and oil palm plantation: Forest disturbance drives changes in microclimate”. *Agricultural and Forest Meteorology* 201, 187–195. DOI: [10.1016/J.AGRFORMET.2014.11.010](https://doi.org/10.1016/J.AGRFORMET.2014.11.010).
- Henao, J. J., J. F. Mejía, A. M. Rendón, and J. F. Salazar (2020a). “Sub-kilometer dispersion simulation of a CO tracer for an inter-Andean urban valley”. *Atmospheric Pollution Research*. DOI: [10.1016/j.apr.2020.02.005](https://doi.org/10.1016/j.apr.2020.02.005).
- Henao, J. J., A. M. Rendón, and J. F. Salazar (2020b). “Trade-off between urban heat island mitigation and air quality in urban valleys”. *Urban Climate* 31, 100542. DOI: [10.1016/j.uclim.2019.100542](https://doi.org/10.1016/j.uclim.2019.100542).
- Hess, G. D., K. J. Tory, M. E. Cope, S. Lee, K. Puri, P. C. Manins, and M. Young (2004). “The Australian Air Quality Forecasting System. Part II: Case Study of a Sydney 7-Day Photochemical Smog Event”. *Journal of Applied Meteorology* 43.5, 663–679. DOI: [10.1175/2094.1](https://doi.org/10.1175/2094.1).
- Kalnay, E. and M. Cai (2003). “Impact of urbanization and land-use change on climate”. *Nature* 423.6939, 528–531. DOI: [10.1038/nature01675](https://doi.org/10.1038/nature01675).

- Kuik, F., A. Lauer, G. Churkina, H. A. C. Denier van der Gon, D. Fenner, K. A. Mar, and T. M. Butler (2016). “Air quality modelling in the Berlin–Brandenburg region using WRF-Chem v3.7.1: sensitivity to resolution of model grid and input data”. *Geoscientific Model Development* 9.12, 4339–4363. DOI: [10.5194/gmd-9-4339-2016](https://doi.org/10.5194/gmd-9-4339-2016).
- Largerion, Y. and C. Staquet (2016). “Persistent inversion dynamics and wintertime PM10 air pollution in Alpine valleys”. *Atmospheric Environment* 135, 92–108. DOI: [10.1016/J.ATMOENV.2016.03.045](https://doi.org/10.1016/J.ATMOENV.2016.03.045).
- Leukauf, D., A. Gohm, and M. W. Rotach (2016). “Quantifying horizontal and vertical tracer mass fluxes in an idealized valley during daytime”. *Atmospheric Chemistry and Physics* 16.20, 13049–13066. DOI: [10.5194/acp-16-13049-2016](https://doi.org/10.5194/acp-16-13049-2016).
- Loibl, W., R. Orthofer, and W. Winiwarter (1993). “Spatially disaggregated emission inventory for anthropogenic NMVOC in Austria”. *Atmospheric Environment. Part A. General Topics* 27.16, 2575–2590. DOI: [https://doi.org/10.1016/0960-1686\(93\)90031-S](https://doi.org/10.1016/0960-1686(93)90031-S).
- Ma, S., M. Goldstein, A. J. Pitman, N. Haghdadi, and I. MacGill (2017). “Pricing the urban cooling benefits of solar panel deployment in Sydney, Australia”. *Scientific Reports* 7.1, 43938. DOI: [10.1038/srep43938](https://doi.org/10.1038/srep43938).
- Mahrt, L. (2014). “Stably Stratified Atmospheric Boundary Layers”. *Annual Review of Fluid Mechanics* 46.1, 23–45. DOI: [10.1146/annurev-fluid-010313-141354](https://doi.org/10.1146/annurev-fluid-010313-141354).
- Makar, P., S. Gravel, V. Chirkov, K. Strawbridge, F. Froude, J. Arnold, and J. Brook (2006). “Heat flux, urban properties, and regional weather”. *Atmospheric Environment* 40.15, 2750–2766. DOI: [10.1016/J.ATMOENV.2005.11.061](https://doi.org/10.1016/J.ATMOENV.2005.11.061).
- Malek, E., T. Davis, R. S. Martin, and P. J. Silva (2006). “Meteorological and environmental aspects of one of the worst national air pollution episodes (January, 2004) in Logan, Cache Valley, Utah, USA”. *Atmospheric Research* 79.2, 108–122. DOI: [10.1016/J.ATMOSRES.2005.05.003](https://doi.org/10.1016/J.ATMOSRES.2005.05.003).
- McKeen, S., S. H. Chung, J. Wilczak, G. Grell, I. Djalalova, S. Peckham, W. Gong, V. Bouchet, R. Moffet, Y. Tang, G. R. Carmichael, R. Mathur, and S. Yu (2007). “Evaluation of several PM2.5 forecast models using data collected during the ICARTT/NEAQS 2004 field study”. *Journal of Geophysical Research: Atmospheres* 112.D10. DOI: [10.1029/2006JD007608](https://doi.org/10.1029/2006JD007608).
- Mejia, J., J. Gillies, V. Etyemezian, and R. Glick (2019). “A very-high resolution (20m) measurement-based dust emissions and dispersion modeling approach for

- the Oceano Dunes, California”. *Atmospheric Environment* 218, 116977. DOI: [10.1016/j.atmosenv.2019.116977](https://doi.org/10.1016/j.atmosenv.2019.116977).
- Miller, S. D., M. L. Goulden, and H. R. da Rocha (2007). “The effect of canopy gaps on subcanopy ventilation and scalar fluxes in a tropical forest”. *Agricultural and Forest Meteorology* 142.1, 25–34. DOI: [10.1016/J.AGRFORMET.2006.10.008](https://doi.org/10.1016/J.AGRFORMET.2006.10.008).
- Morini, E., A. G. Touchaei, F. Rossi, F. Cotana, and H. Akbari (2018). “Evaluation of albedo enhancement to mitigate impacts of urban heat island in Rome (Italy) using WRF meteorological model”. *Urban Climate* 24, 551–566. DOI: [10.1016/J.UCLIM.2017.08.001](https://doi.org/10.1016/J.UCLIM.2017.08.001).
- Motzer, T. (2005). “Micrometeorological aspects of a tropical mountain forest”. *Agricultural and Forest Meteorology* 135.1-4, 230–240. DOI: [10.1016/J.AGRFORMET.2005.11.019](https://doi.org/10.1016/J.AGRFORMET.2005.11.019).
- Offerle, B., C. S. B. Grimmond, K. Fortuniak, and W. Pawlak (2006). “Intraurban Differences of Surface Energy Fluxes in a Central European City”. *Journal of Applied Meteorology and Climatology* 45.1, 125–136. DOI: [10.1175/JAM2319.1](https://doi.org/10.1175/JAM2319.1).
- Pypker, T., M. Unsworth, B. Lamb, E. Allwine, S. Edburg, E. Sulzman, A. Mix, and B. Bond (2007). “Cold air drainage in a forested valley: Investigating the feasibility of monitoring ecosystem metabolism”. *Agricultural and Forest Meteorology* 145.3-4, 149–166. DOI: [10.1016/J.AGRFORMET.2007.04.016](https://doi.org/10.1016/J.AGRFORMET.2007.04.016).
- Rendón, A. M., J. F. Salazar, C. A. Palacio, V. Wirth, and B. Brötz (2014). “Effects of Urbanization on the Temperature Inversion Breakup in a Mountain Valley with Implications for Air Quality”. *Journal of Applied Meteorology and Climatology* 53.4, 840–858. DOI: [10.1175/JAMC-D-13-0165.1](https://doi.org/10.1175/JAMC-D-13-0165.1).
- Rotach, M. W., A. Gohm, M. N. Lang, D. Leukauf, I. Stiperski, and J. S. Wagner (2015). “On the Vertical Exchange of Heat, Mass, and Momentum Over Complex, Mountainous Terrain”. *Frontiers in Earth Science* 3, 76. DOI: [10.3389/feart.2015.00076](https://doi.org/10.3389/feart.2015.00076).
- Saaroni, H., J. Amorim, J. Hiemstra, and D. Pearlmutter (2018). “Urban Green Infrastructure as a tool for urban heat mitigation: Survey of research methodologies and findings across different climatic regions”. *Urban Climate* 24, 94–110. DOI: [10.1016/J.UCLIM.2018.02.001](https://doi.org/10.1016/J.UCLIM.2018.02.001).
- Saide, P., R. Zah, M. Osses, and M. O. de Eicker (2009). “Spatial disaggregation of traffic emission inventories in large cities using simplified top-down methods”. *Atmospheric Environment* 43.32, 4914–4923. DOI: <https://doi.org/10.1016/j.atmosenv.2009.07.013>.

- Santamouris, M. (2014). “Cooling the cities? A review of reflective and green roof mitigation technologies to fight heat island and improve comfort in urban environments”. *Solar Energy* 103, 682–703. DOI: [10.1016/J.SOLENER.2012.07.003](https://doi.org/10.1016/J.SOLENER.2012.07.003).
- Santos, M., E. Santos, C. Wagner-Riddle, S. Brown, K. Stropes, R. Staebler, and J. Nippert (2019). “Evaluating a Lagrangian inverse model for inferring isotope CO₂ exchange in plant canopies”. *Agricultural and Forest Meteorology* 276-277, 107651. DOI: [10.1016/J.AGRFORMET.2019.107651](https://doi.org/10.1016/J.AGRFORMET.2019.107651).
- Serafin, S., B. Adler, J. Cuxart, S. De Wekker, A. Gohm, B. Grisogono, N. Kalthoff, D. Kirshbaum, M. Rotach, J. Schmidli, I. Stiperski, Ž. Večenaj, and D. Zardi (2018). “Exchange Processes in the Atmospheric Boundary Layer Over Mountainous Terrain”. *Atmosphere* 9.3, 102. DOI: [10.3390/atmos9030102](https://doi.org/10.3390/atmos9030102).
- Shrestha, K. L., A. Kondo, A. Kaga, and Y. Inoue (2009). “High-resolution modeling and evaluation of ozone air quality of Osaka using MM5-CMAQ system”. *Journal of Environmental Sciences* 21.6, 782–789. DOI: [https://doi.org/10.1016/S1001-0742\(08\)62341-4](https://doi.org/10.1016/S1001-0742(08)62341-4).
- Shuttleworth, W. J. (1985). “DAILY VARIATIONS OF TEMPERATURE AND HUMIDITY WITHIN AND ABOVE AMAZONIAN FOREST”. *Weather* 40.4, 102–108. DOI: [10.1002/j.1477-8696.1985.tb07489.x](https://doi.org/10.1002/j.1477-8696.1985.tb07489.x).
- Skamarock, C., B. Klemp, J. Dudhia, O. Gill, Z. Liu, J. Berner, W. Wang, G. Powers, G. Duda, D. Barker, and X.-y. Huang (2019). “A Description of the Advanced Research WRF Model Version 4”. DOI: [10.5065/1DFH-6P97](https://doi.org/10.5065/1DFH-6P97).
- Staebler, R. M. and D. R. Fitzjarrald (2005). “Measuring Canopy Structure and the Kinematics of Subcanopy Flows in Two Forests”. *Journal of Applied Meteorology* 44.8, 1161–1179. DOI: [10.1175/JAM2265.1](https://doi.org/10.1175/JAM2265.1).
- Tan, Z., K. K.-L. Lau, and E. Ng (2016). “Urban tree design approaches for mitigating daytime urban heat island effects in a high-density urban environment”. *Energy and Buildings* 114, 265–274. DOI: [10.1016/J.ENBUILD.2015.06.031](https://doi.org/10.1016/J.ENBUILD.2015.06.031).
- Theobald, M., B. Loubet, C. Ammann, L. Branislava, B. Chojnicki, L. Ganzeveld, B. Grosz, M. Kaasik, S. Noe, J. Olejnik, J. Rinne, M. Shapkalijevski, D. Simpson, O. Tchepel, J.-P. Tuovinen, T. Weidinger, and R. Wichink Kruit (2015). “In-Canopy Turbulence—State of the Art and Potential Improvements”. In: *Review and Integration of Biosphere-Atmosphere Modelling of Reactive Trace Gases and Volatile Aerosols*. Ed. by R.-S. Massad and B. Loubet. Dordrecht: Springer Netherlands, 215–223. DOI: [10.1007/978-94-017-7285-3_13](https://doi.org/10.1007/978-94-017-7285-3_13).

- Toro A, R., M. Kvakić, Z. B. Klaić, D. Koračin, R. G. Morales S, and M. A. Leiva G (2019). “Exploring atmospheric stagnation during a severe particulate matter air pollution episode over complex terrain in Santiago, Chile”. *Environmental Pollution* 244, 705–714. DOI: [10.1016/J.ENVPOL.2018.10.067](https://doi.org/10.1016/J.ENVPOL.2018.10.067).
- Tuia, D., M. O. de Eicker, R. Zah, M. Osses, E. Zarate, and A. Clappier (2007). “Evaluation of a simplified top-down model for the spatial assessment of hot traffic emissions in mid-sized cities”. *Atmospheric Environment* 41.17, 3658–3671. DOI: <https://doi.org/10.1016/j.atmosenv.2006.12.045>.
- Wang, F., S. D. Chambers, Z. Zhang, A. G. Williams, X. Deng, H. Zhang, G. Lonati, J. Crawford, A. D. Griffiths, A. Ianniello, and I. Allegrini (2016). “Quantifying stability influences on air pollution in Lanzhou, China, using a radon-based “stability monitor”: Seasonality and extreme events”. *Atmospheric Environment* 145, 376–391. DOI: [10.1016/J.ATMOENV.2016.09.014](https://doi.org/10.1016/J.ATMOENV.2016.09.014).
- Wang, W. (2009). “The Influence of Thermally-Induced Mesoscale Circulations on Turbulence Statistics Over an Idealized Urban Area Under a Zero Background Wind”. *Boundary-Layer Meteorology* 131.3, 403–423. DOI: [10.1007/s10546-009-9378-2](https://doi.org/10.1007/s10546-009-9378-2).
- Whiteman, C. D., S. W. Hoch, J. D. Horel, and A. Charland (2014). “Relationship between particulate air pollution and meteorological variables in Utah’s Salt Lake Valley”. *Atmospheric Environment* 94, 742–753. DOI: [10.1016/J.ATMOENV.2014.06.012](https://doi.org/10.1016/J.ATMOENV.2014.06.012).
- Zhang, N., X. Wang, and Z. Peng (2014). “Large-Eddy Simulation of Mesoscale Circulations Forced by Inhomogeneous Urban Heat Island”. *Boundary-Layer Meteorology* 151.1, 179–194. DOI: [10.1007/s10546-013-9879-x](https://doi.org/10.1007/s10546-013-9879-x).

Chapter 2

Trade-off between urban heat island mitigation and air quality in urban valleys

This chapter is a reproduction of Henao et al., [2020](#), published in Urban Climate.

2.1 Abstract

The number of studies on urban cooling strategies has been continuously growing. A common premise is that urban heat island (UHI) mitigation has a net beneficial effect on urban environmental quality and sustainability. Here we evaluate how UHI mitigation affects air quality in an idealized urban valley by means of large-eddy simulations. A passive tracer represents air pollution transport in three UHI mitigation scenarios and under two initial stability conditions. Contrary to the common premise, our results demonstrate that UHI mitigation can worsen air quality in urban valleys, via the alteration of the mechanisms of air pollution transport. Our results also show the theoretical possibility of finding moderate UHI mitigation strategies in which UHI is reduced while limiting the impacts on air quality. A fundamental implication is that these strategies should be explored through case-specific realistic simulations for guiding decision-making in real systems. Large and often expensive urban transformations should not be accomplished under the generalized assumption that UHI mitigation improves environmental quality. Building a more general understanding of the potential impacts of UHI mitigation, as well as of the mechanisms behind, is a continuing challenge with important implications for urban management and planning.

2.2 Introduction

A growing body of scientific literature indicates that urban heat island (UHI) mitigation, through urban cooling strategies, is being increasingly considered as a measure for improving the quality and sustainability of urban environments (Gago et al., [2013](#);

Santamouris, 2014; Aleksandrowicz et al., 2017; Francis and Jensen, 2017; Saaroni et al., 2018). Frequently studied strategies for urban cooling are oriented towards modifying the way in which cities are structured by introducing or modifying elements such as green spaces, trees, albedo, pavement surfaces, vegetation, or building types and materials (Gago et al., 2013; Li and Norford, 2016; Francis and Jensen, 2017; Pomerantz, 2018); or even more comprehensive urban design strategies such as the Water Sensitive Urban Design (Coutts et al., 2013). From this perspective, surface temperature reduction is often regarded as an indicator of environmental quality improvement related to the effectiveness of the UHI mitigation strategies (Santamouris, 2014; Tan et al., 2016; Ma et al., 2017; Morini et al., 2018).

With over 50% of the world's land surface considered as complex terrain (Rotach et al., 2014), many urban areas are located within complex terrains such as mountain valleys, i.e. urban valleys. The transport of air pollutants emitted from the surface of urban valleys is strongly dependent on interactions between local-scale processes related to both static and dynamic factors. Topography is the main static (time-invariant at scales relevant for air pollution studies and related decision-making) factor because of its role as an impermeable barrier for atmospheric flows (Zardi and Whiteman, 2013). The dynamics of the atmospheric boundary layer and thermally-driven flows are strongly affected by the topographical setting of complex terrains (De Wekker and Kossmann, 2015; Lang et al., 2015; Wagner et al., 2015b; Serafin et al., 2018).

The ventilation of urban valleys is sensitive to the occurrence and subsequent evolution of low-level atmospheric stability, related to temperature inversions (Rendón et al., 2014; De Wekker and Kossmann, 2015; Leukauf et al., 2016; Serafin et al., 2018). A stable layer constitutes a thermodynamical barrier, which in combination with static topographical barriers, can strongly restrict the transport mechanisms responsible for venting air pollutants out of urban valleys (Lehner and Gohm, 2010; Giovannini et al., 2014; Rendón et al., 2014; Rendón et al., 2015). Indeed, severe air pollution events have been related to the evolution of stability (inversion layers) in cities located in complex terrain such as Santiago in Chile (Toro A et al., 2019), Logan and Salt Lake in the United States of America (Malek et al., 2006; Whiteman et al., 2014), Grenoble in France (Largerion and Staquet, 2016), and the Lanzhou valley in China (Wang et al., 2016). Consistent with its relevance for air quality and associated public health, the evolution of stable (inversion) layers in valleys has remained among the key research topics in mountain meteorology (Serafin et al., 2018).

The dynamics of air pollution transport mechanisms in urban valleys is sensitive to local-scale phenomena (e.g. those related to the surface energy balance) which can be (inadvertently or not) altered by urban modifications (planned or not). For instance, the destabilization of low-level stable layers (breakup of inversion layers) can occur as a result of the combined effect of two locally-induced processes: the ascent of the stable layer bottom with the development of a convective boundary layer (CBL), and the descent of the stable layer top with the removal of air beneath the stable layer by upslope flows (Whiteman and McKee, 1982). These destabilization processes can be affected by UHI mitigation strategies, simply because they can alter the surface sensible heat flux through modifications of the urban properties (Makar et al., 2006). In turn, a weakening of atmospheric destabilization (inversion breakup) processes can result in large reductions of the total mass of pollutants (tracer) exported out of a valley (Leukauf et al., 2016).

A challenging situation for decision making arises when separate studies highlight contrasting (beneficial versus adverse) impacts of UHI mitigation for the same urban environment. For instance, the City of Chicago has implemented a variety of UHI mitigation measures that produced a noticeable impact on citywide albedo (Mackey et al., 2012). These measures include several hectares of green roofs which, as a beneficial impact on air quality, have a strong potential to remove air pollutants: model estimates indicate that around 20 ha of green roofs can remove about 1,700 kg of air pollutants during one year in Chicago (Yang et al., 2008). However, contrasting results have highlighted adverse air quality impacts of the same UHI mitigation measure. In particular, Sharma et al., 2016 showed that green and cool roofs can have detrimental impacts on air quality in Chicago through multiple alterations of the lower atmosphere dynamics, including reduced vertical mixing, a lower boundary layer depth, and weaker convective rolls. This example highlights the need of considering the interactions between UHI mitigation and air quality impacts and, more importantly, the continuing challenge of building a more general understanding of these impacts and the mechanisms behind (Taha, 2015; Yang et al., 2015). Advancing this general understanding is crucial for informing decision-makers about the environmental quality and sustainability of urban areas (Baklanov et al., 2018; De Wekker et al., 2018).

In the present study, we use Large-Eddy Simulations (LES) to investigate the impact of UHI mitigation on the daytime evolution of the atmospheric flow field, and the associated mechanisms of air pollution transport in idealized urban valleys,

under the influence of different levels of atmospheric stability. A number of previous studies have shown that this type of idealized modelling approaches are fundamental for advancing the quantitative understanding of atmospheric dynamics over complex and/or urban terrains (Serafin and Zardi, 2010; Schmidli et al., 2011; Rendón et al., 2014; Leukauf et al., 2016). Below, we first present evidence of a trade-off between UHI mitigation and air quality (Section 2.4.1), then we study the mechanisms behind this trade-off (Section 2.4.2), and finally we discuss the implications for real urban valleys (Section 2.5) and conclude (Section 2.6).

2.3 Model and experiment design

2.3.1 Numerical model

The numerical simulations were performed with the Weather Research and Forecasting model (WRF), version 4.0 (Skamarock et al., 2019). This model is supported by the National Center for Atmospheric Research (NCAR, United States of America), but it is a true community model and, arguably, the world's most widely used numerical weather prediction model (Powers et al., 2017). We implemented WRF in LES mode (WRF-LES), a common approach for studying atmospheric dynamics in idealized complex terrains (e.g. Catalano and Moeng, 2010; Lehner and Whiteman, 2012; Burns and Chemel, 2014; Wagner et al., 2014; Leukauf et al., 2015).

WRF is a nonhydrostatic, fully compressible numerical model, which uses an Arakawa-C staggered grid with a terrain-following hydrostatic-pressure vertical coordinate (Skamarock and Klemp, 2008). Time integration is done with a third-order Runge-Kutta scheme, and advection of scalars and momentum with a fifth-order horizontal, and a third-order vertical schemes. Sub-grid scale turbulence is parameterized using a turbulent kinetic energy (TKE) 1.5-order closure scheme (Deardorff, 1980) modified to account for the effect of anisotropic grids (grid aspect ratio) on the mixing length (Scotti et al., 1993), such as in some previous successful implementations of WRF-LES for complex terrains (e.g. Catalano and Moeng, 2010; Burns and Chemel, 2014). The diffusion coefficient C_k in the sub-grid scale scheme is set to 0.10 (Moeng et al., 2007), and surface heat and momentum fluxes are computed with the revised MM5 Monin-Obukhov scheme by Jiménez et al., 2012.

2.3.2 Topography and model domain

The 3-D model domain has 512x150x151 staggered grid points along the x , y , and z directions. The grid has a constant horizontal resolution $\Delta x = \Delta y = 50$ m, while the vertical grid is stretched using a hyperbolic tangent function (Burns and Chemel, 2014) that provides decreasing resolution with increasing height (in the z -direction): $\Delta z \approx 20$ m above the ground and $\Delta z \approx 100$ m at the top of the domain, which is fixed at 8,000 m.

The terrain geometry represents an idealized valley, uniform in the y -direction (along-valley) and symmetric about the valley center in the x -direction (across valley). The idealized topography (Fig. 2.1) includes two cosine-shaped slopes as described by (Rampanelli et al., 2004; Rendón et al., 2014)

$$z(x) = h \begin{cases} 1, & |x - x_0| > s_x + v_x \\ \frac{1}{2} \left[1 - \cos \left(\pi \frac{|x - x_0| - v_x}{s_x} \right) \right], & v_x < |x - x_0| < s_x + v_x \\ 0, & |x - x_0| < v_x \end{cases} \quad (2.1)$$

where $z(x)$ is the height of the terrain above the valley floor (m), h is the maximum depth of the valley ($h = 1,000$ m), x_0 is the x coordinate of the valley center, s_x is the width of the slopes ($s_x = 8,000$ m), and v_x is the half-width of the valley floor ($v_x = 2,300$ m). In addition, two plateaus (2,500-m-length) are included in the modelling domain in order to have the lateral boundaries far from the top of the slopes.

2.3.3 Initial and boundary conditions

All simulations are initialized with an atmosphere at rest and a constant potential temperature gradient $\partial\theta/\partial z$. Two stability levels are considered, given by $\partial\theta/\partial z = 1$ K km⁻¹ (low) and $\partial\theta/\partial z = 3$ K km⁻¹ (high). Initial surface potential temperature and pressure are set to 290 K and 1,000 hPa, respectively. We limit our study to a dry atmosphere and neglect the Coriolis effect.

Periodic lateral boundary conditions are applied on horizontal x and y directions. This is possible due to the characteristics of the idealized valley: uniform in the along-valley direction (y) and symmetric in the across-valley direction (x), with boundaries far from the top of the slopes. Further, the definition of periodic boundary conditions is consistent with our focus on local-scale phenomena because they are tightly

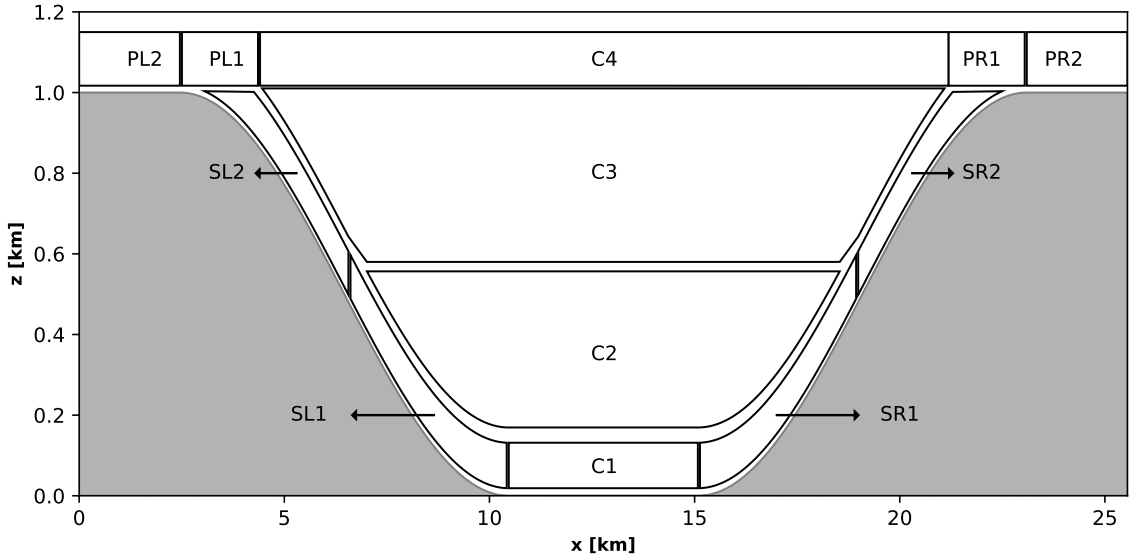


Figure 2.1: Cross-section of the idealized urban valley topography (i.e. the $x - z$ plane). Terrain is uniform in the y -direction (along-valley). An urban area covers the entire valley floor (surface area below C1). The named volumes are used for the analysis.

related to decision-making at the urban valley level (e.g. decisions related to urban modification and its impact on local atmospheric dynamics). The uppermost 2 km of the domain are covered with an implicit Rayleigh damping layer (Klemp et al., 2008) to avoid unrealistic reflection of upward-propagating gravity-waves, with a damping coefficient of 0.2 s^{-1} .

2.3.4 UHI mitigation scenarios

In all cases, the valley surface is divided into homogeneous areas of urban and rural land cover, which can differ only in their surface forcing (sensible heat flux). Representing UHI as differences in surface sensible heat flux has been implemented in previous studies (Wang, 2009; Zhang et al., 2014). An idealized diurnal cycle of sensible heat flux is defined through the function (Rendón et al., 2014)

$$Q_h(x, t) = \frac{1}{2} Q_S(x) \left[1 - \cos \left(\frac{2\pi}{T} t \right) \right], \quad (2.2)$$

where x is the cross-valley coordinate, $Q_h(x, t)$ is the space-time varying flux of sensible heat in W m^{-2} , $Q_S(x)$ is a maximum reference value depending on whether the

surface at x is urban ($Q_S(x) = Q_u \text{ W m}^{-2}$) or rural ($Q_S(x) = Q_r = 100 \text{ W m}^{-2}$), t is the elapsed time, and T is the total time of simulation ($T = 12 \text{ h}$). There is no dependence of $Q_h(x, t)$ on y because of the homogeneity of the valley in that direction. The prescribed sensible heat flux does not consider effects such as topographic shading, which can lead to spatial variability in sensible heat flux in valleys (Rotach et al., 2008). However, the relevance of topographic shading depends on the characteristics of specific valleys, such as its geographic location, axis orientation or valley width (e.g. Colette et al., 2003; Rendón et al., 2015), and it is not necessarily relevant for the mechanisms of air pollution transport in tropical valleys, specially near the equator (Rendón et al., 2015).

The urban area covers the entire valley floor (Fig. 2.1). Five UHI mitigation scenarios are defined through the Q_u value. The focus is given to three scenarios, with the default UHI (no-mitigation) based on the typical values for urban and rural areas reported in Fan et al., 2017. First, a no-mitigation scenario in which $Q_r \ll Q_u = 200 \text{ W m}^{-2}$. Second, a moderate-mitigation scenario in which $Q_r < Q_u = 150 \text{ W m}^{-2}$. And third, a full-mitigation scenario in which urban and rural areas exhibit the same sensible heat flux, i.e. $Q_r = Q_u = 100 \text{ W m}^{-2}$. The resulting maximum urban-rural contrasts of these scenarios (50 and 100 W m^{-2}) are comparable to observations (Christen and Vogt, 2004; Offerle et al., 2006).

Two additional, more extreme cases of UHI are also included in the analysis, having $Q_u = 250 \text{ W m}^{-2}$ and $Q_u = 400 \text{ W m}^{-2}$ (i.e., contrasts of 150 and 300 W m^{-2}). Similar contrasts have been applied in ideal numerical simulations (e.g. Wang, 2009; Zhang et al., 2014). With these scenarios, the focus is given to cases where urban areas are warmer than adjacent rural areas (“heat islands”), and do not consider cases where “urban cool islands” develop (e.g. Giovannini et al., 2011).

2.3.5 Air pollution: passive tracer

Air pollution transport is represented through a passive tracer, exclusively emitted from the urban area. The surface flux of passive tracer is set to an arbitrary fixed rate, which is continuously emitted (every time step) in the lowermost grid-cell. The same amount of pollutant (tracer) is released in all scenarios. Model output provides tracer mass mixing ratios (r), which are converted to normalized mixing ratios in order to have results independent of the emission rate. Normalized tracer mixing ratios are defined as r/r_{max} , with r_{max} being the maximum mixing ratio of all simulations.

2.3.6 Averaging procedure

An averaging method for calculation of turbulence statistics is performed over the y -axis, as it is the only axis with homogeneity in the flow (topography varies only in the x -axis). The results presented below represent averaged values $\bar{\phi}$ (Catalano and Moeng, 2010),

$$\bar{\phi}(x, z, t) = \frac{1}{L_y} \int_0^{L_y} \phi(x, y, z, t) dy, \quad (2.3)$$

where $L_y = 7.5$ km is the domain length in the along-valley direction, and ϕ the instantaneous value of a given variable.

2.3.7 Turbulent kinetic energy

Total TKE is computed as the sum of the resolved-scale and subgrid-scale TKE, with the sub-grid component directly obtained from the model and the resolved-scale (TKE_{Res}) component given by

$$TKE_{Res} = \frac{1}{2} (\overline{u'^2} + \overline{v'^2} + \overline{w'^2}) \quad (2.4)$$

where the instantaneous deviations from the mean, ϕ' , are

$$\phi'(x, y, z, t) = \phi(x, y, z, t) - \bar{\phi}(x, z, t). \quad (2.5)$$

2.4 Results

2.4.1 Trade-off: impacts of UHI mitigation on air quality

There is a trade-off between UHI mitigation and air quality, which is evident for both stability levels. Figures 2.2 and 2.3 show that increased UHI mitigation generally leads to worse air quality. The worsening is especially pronounced in the early morning due to the initial conditions of atmospheric stability. At 0800, for low stability, most of the emitted tracer remains trapped below the mountaintop level in the full-

mitigation scenario, whereas at the same time in the less-mitigation scenarios (i.e. no- and moderate-mitigation scenarios) tracer masses have started to leave the valley atmosphere. Differences are even larger in the more extreme UHI scenarios, with the tracer plume reaching a height of about 2 km for the maximum contrast (supplementary Fig. A1). Afterwards, the full-mitigation scenario presents overall higher tracer concentrations. These same relations between scenarios occur for high stability (Fig. 2.3), but with higher tracer concentrations in the lower valley atmosphere, especially in the full-mitigation scenario during the morning.

The worsening of air quality due to increased UHI mitigation is further clarified by Figure 2.4, which shows how the tracer accumulates (on average) within each of the volumes presented in Figure 2.1. Throughout the daytime, air quality in the lower valley atmosphere (i.e. volumes C1, C2, and SR1; Fig. 2.4a–e,g) is worse in the mitigation scenarios (full and moderate), for both stability cases. In the upper valley atmosphere (i.e. volumes C3 and SR2; Fig. 2.4f,h,i,k), the full-mitigation scenario exhibits higher concentrations most of the time, except in the morning due to transport processes and stability. These processes will be revised in the next section.

Worsening of air quality due to UHI mitigation is aggravated by increased stability. Comparisons between Figures 2.2 and 2.3, as well as between left and right columns of Figure 2.4, show that increased atmospheric stability (initial condition) exacerbates tracer accumulation, especially in the lower atmosphere. Of particular importance is that the air quality worsening, due to stability, is more pronounced in C1, i.e. over the urban area, which is relevant from the public health perspective. For this same volume, tracer concentrations in the full-mitigation scenario exhibit a decreasing trend in the morning, for the low initial stability (Fig. 2.4a). In contrast, concentrations remain high when initial stability is high (Fig. 2.4c). Within the C1 volume, tracer concentrations approach a constant minimum value during most of the afternoon in the less-mitigation scenarios. The moderate-mitigation scenario is generally better than the full-mitigation scenario, and always produce lower maximum concentrations that occur in the morning under low or high stability. However, an exception occurs in the afternoon under low stability (Fig. 2.4a). In the afternoon, while concentrations are about the same in the full- and no-mitigation scenarios, they are higher in the moderate-mitigation scenario. This difference between the moderate and other scenarios is related to two contrasting effects. First, as compared to the full-mitigation scenario, the UHI-induced convergence in the moderate scenario

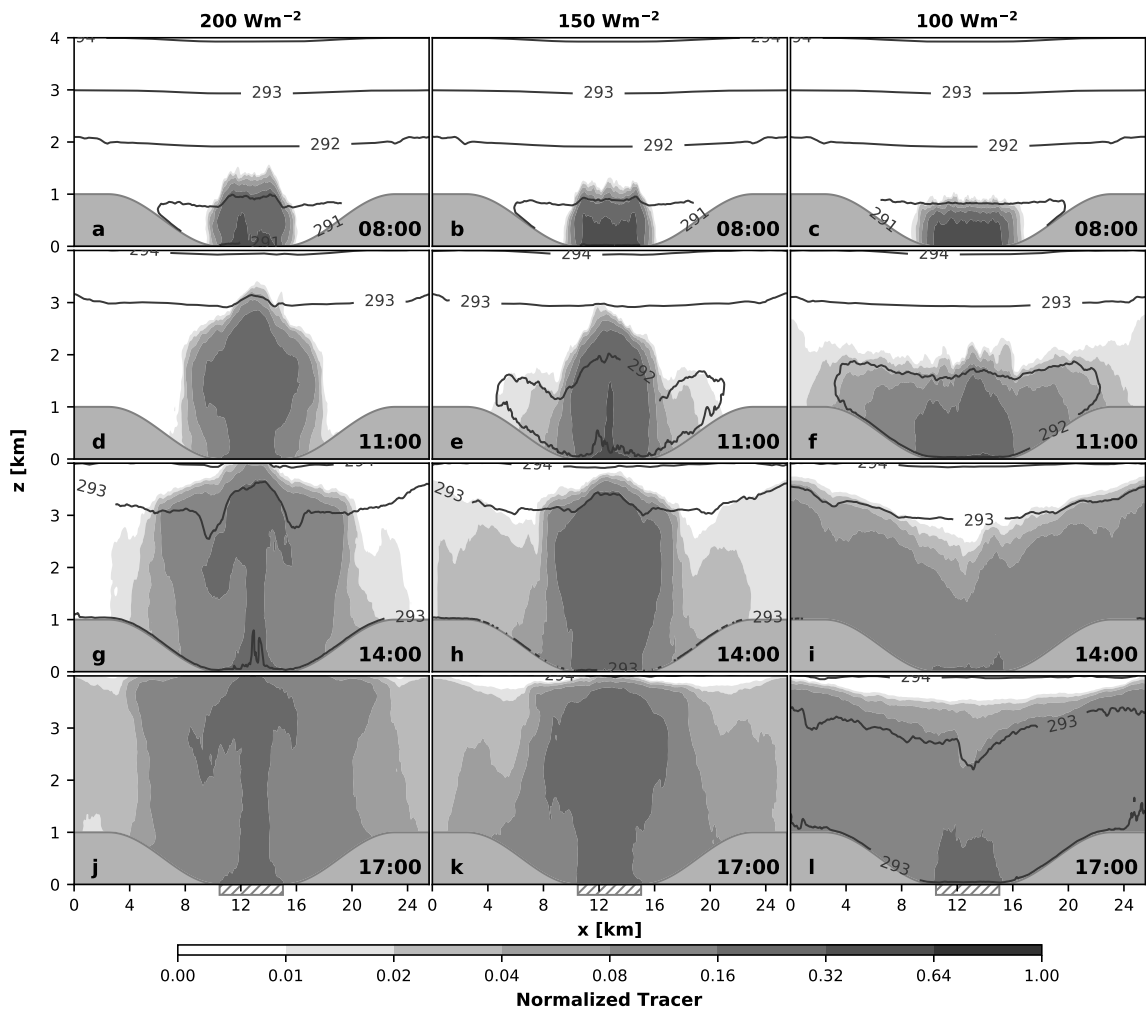


Figure 2.2: Daytime evolution of normalized tracer mixing ratio from morning (top) to afternoon (bottom), with low stability ($\partial\theta/\partial z = 1 \text{ K km}^{-1}$ at initial condition). UHI mitigation varies from no- (left) to moderate- (center) and full-mitigation (right) scenarios. Isentropes are shown every 1 K. The gray hatched box indicates the location of the urban area. See supplementary Fig. A1 for results of the other scenarios

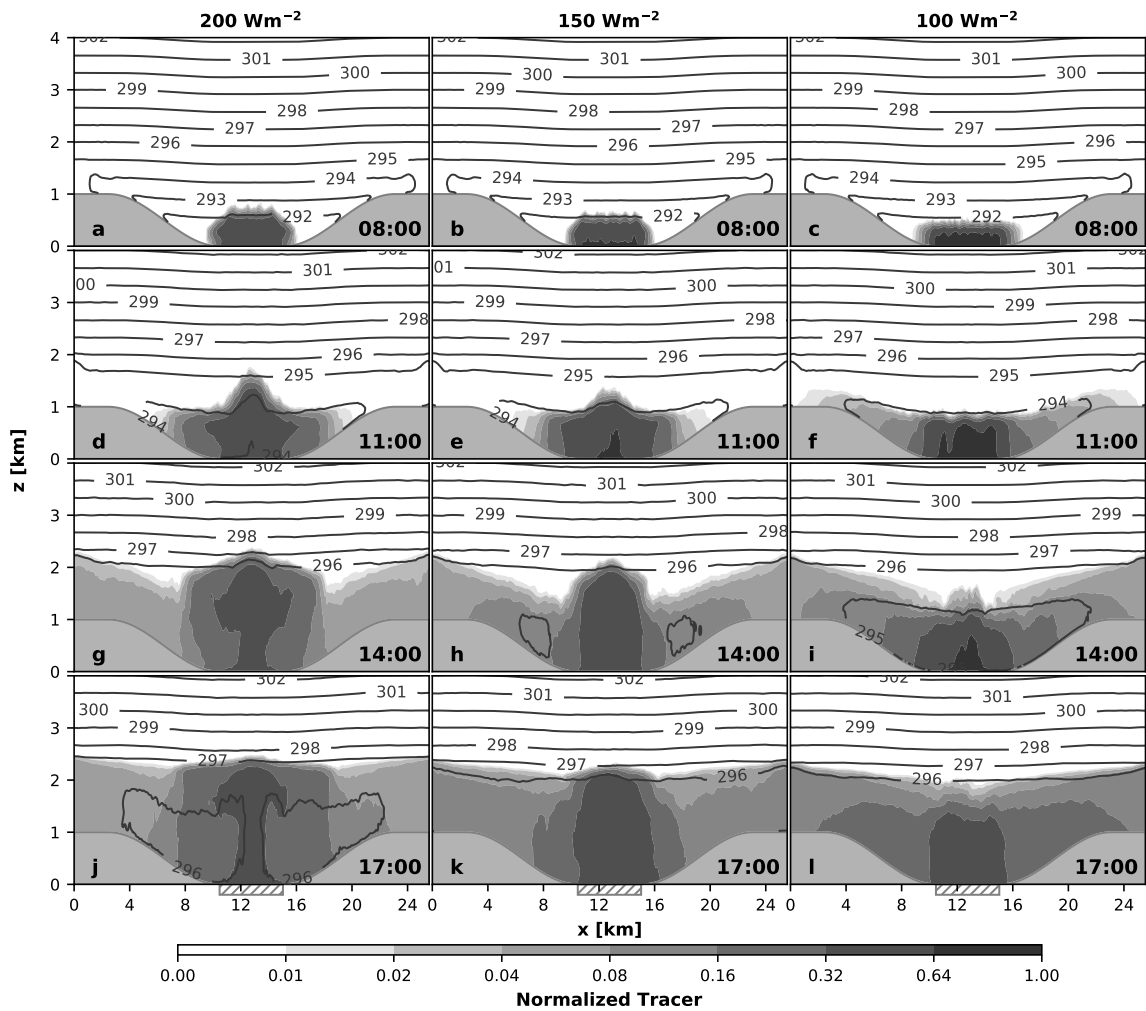


Figure 2.3: As in Fig. 2.2 but for high stability ($\partial\theta/\partial z = 3 \text{ K km}^{-1}$ at initial condition). See supplementary Fig. A2 for results of the other scenarios

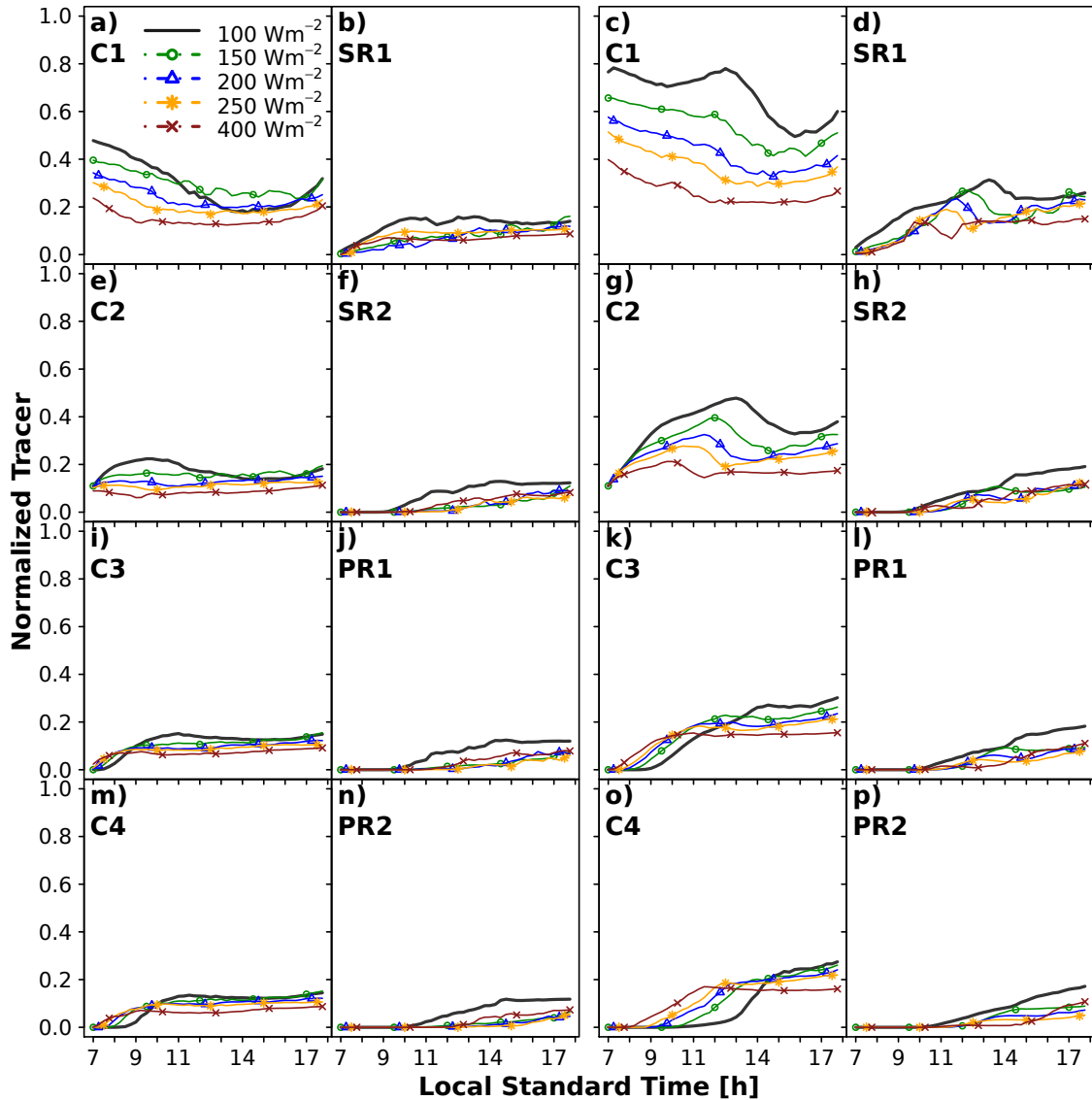


Figure 2.4: Daytime evolution of normalized tracer mixing ratio depending on the UHI mitigation scenario and initial stability: low (left and middle-left) or high (middle-right and right). Each panel shows average values for the volumes in Fig. 2.1. Each line represents a UHI mitigation scenario, as indicated by the corresponding Q_u value in panel a. The results of symmetric volumes (SL1, SL2, PL1, and PL2; not shown) are not presented.

reduces transport to the slopes (note that concentrations in SR1 are lower in the moderate scenario during the afternoon, Fig. 2.4b), i.e., tracer masses tend to concentrate over the center of the valley. Second, as compared the no-mitigation, the low-level convergence is weaker in the moderate scenario, and, therefore, less efficient to enhance the vertical transport of pollutants. These results further illustrate the inherent complexity of trade-offs between urban mitigation and air quality, even in our idealized simulations.

Notably, there is a non-linear relation between the magnitude of an UHI mitigation measure (in terms of surface sensible heat flux reductions) and its impact on air quality. For instance, a reduction from 250 W m^{-2} to 200 W m^{-2} (the Q_S value in Eq. 2.2) results in an air quality worsening which is less severe than the one caused by an equivalent reduction from 200 W m^{-2} to 150 W m^{-2} (Fig. 2.4a,c).

2.4.2 Air pollution transport mechanisms

UHI mitigation impacts on air quality occur through alterations in the mechanisms of air pollution transport, which depend on the evolution of the wind (Figs. 2.5 and 2.6) and turbulence (Figs. 2.7 and 2.8) fields. These alterations are mainly related to slope flows (Section 2.4.2.1), the development of the CBL and transport over the valley center (Section 2.4.2.2), and atmospheric stability and destabilization (Section 2.4.2.3).

2.4.2.1 Transport through the slopes

UHI mitigation alters the slope flows dynamics in several ways. At 0800, upslope flows develop in all scenarios for both low (Fig. 2.5a–c) and high (Fig. 2.6a–c) stability. Afterwards, in the less-mitigation scenarios, these upslope flows are either partially (e.g. Fig. 2.6h) or fully (supplementary Figs. A3 and A4) reversed. The extent and intensity of this flow pattern increases with increasing urban-rural thermal contrast, with downslope flows dominating about the lower half of the slopes in the no-mitigation scenario, the lower part of the slope in the moderate-mitigation scenario, and none (only upslope flows) in the full-mitigation scenario (Figs. 2.5 and 2.6, and supplementary Fig. A5).

As a result, slope flows exhibit opposite patterns (upslope versus downslope) between the full- and the less-mitigation scenarios. The prevalence of upslope flows (during the day) in the full-mitigation scenario coincides with the expected dynamics

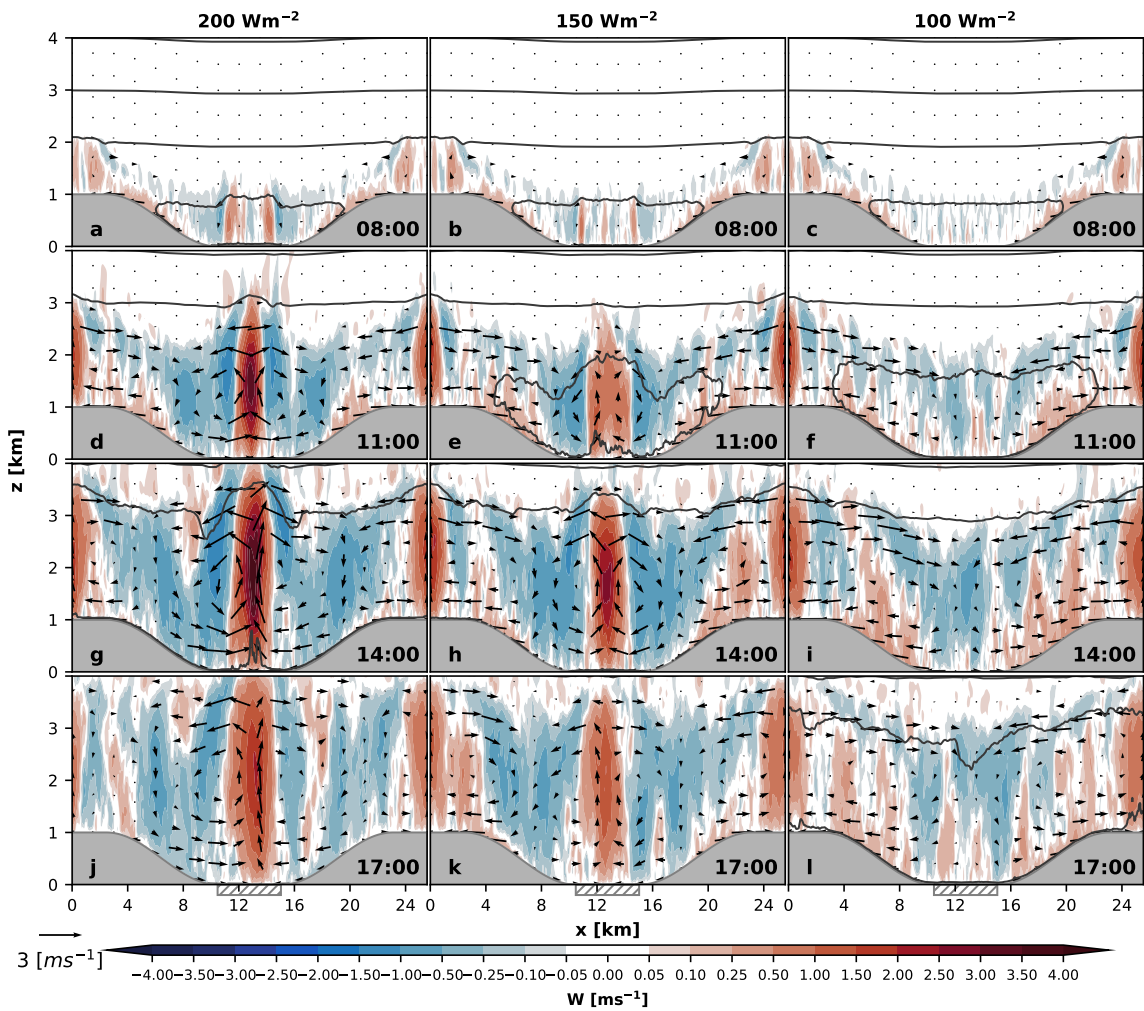


Figure 2.5: Daytime evolution of the wind field (vectors) starting with low stability. Colors show the w wind component. See supplementary Fig. A3 for results of the other scenarios

in rural valleys (Zardi and Whiteman, 2013). The reversal of upslope to downslope flows is a key effect of the interactions of urban heating with slope winds (Ganbat et al., 2015a; Ganbat et al., 2015b), which could have strong implications for air quality (Rendón et al., 2014). Numerical simulations around the metropolitan areas of Seoul, Korea (Ryu and Baik, 2013) and Ulaanbaatar, Mongolia (Ganbat and Baik, 2015) have also reported conversion of upslope to downslope winds, due to thermal contrast between the urban areas and mountains in the vicinity.

Low tracer accumulations during the morning in volumes SR2, PR1, and PR2 indicate a relative weaker ventilation along the slopes (Fig. 2.4f,h,j,l,n,p). This occurs in all scenarios, but not for the same reasons. Reduced upslope transport in the

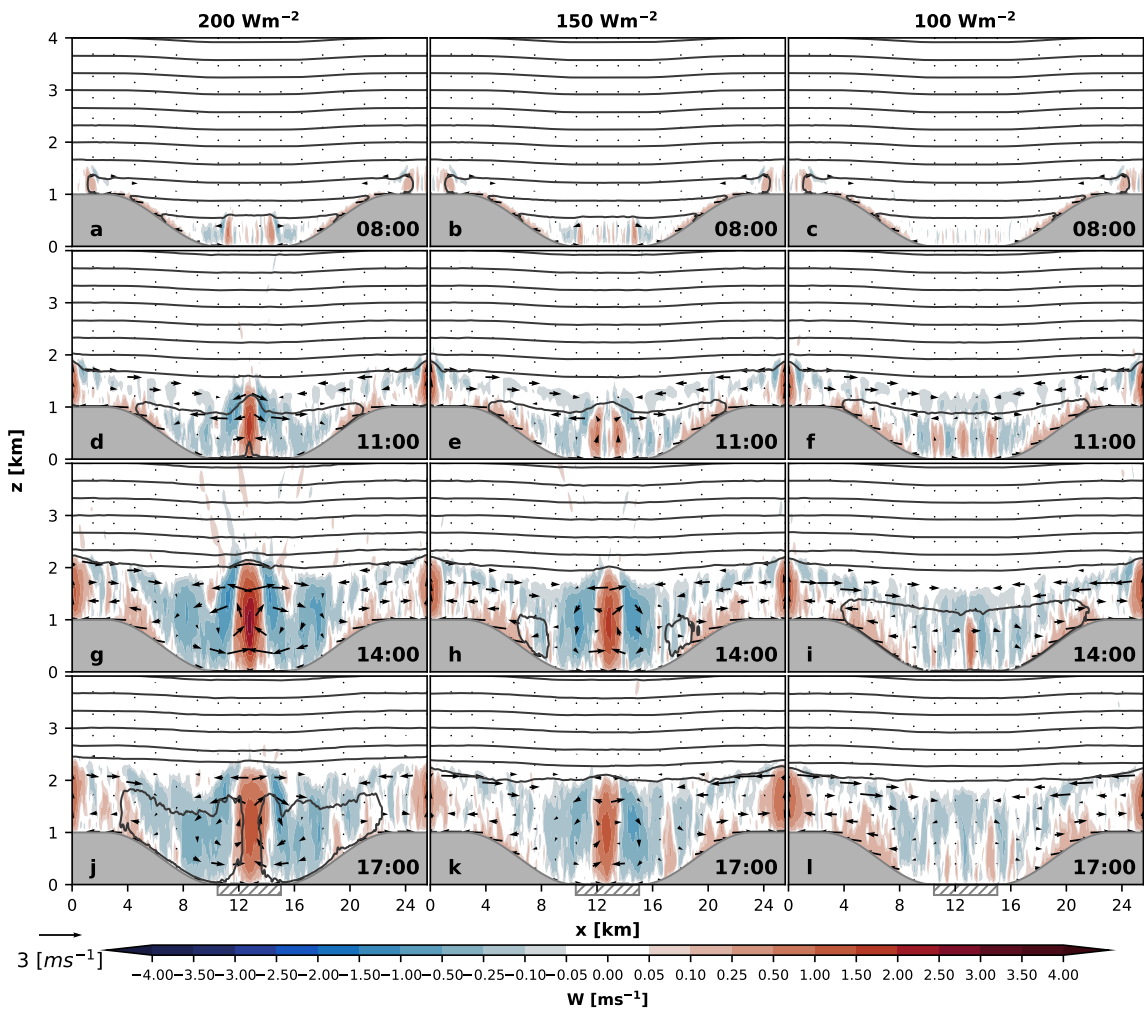


Figure 2.6: As in Fig. 2.5 but starting with high stability. See supplementary Fig. A4 for results of the other scenarios

less-mitigation scenarios is explained by the formation of a UHI-induced circulation, with wind directions towards the valley center near the lower slopes and the urban-rural border (supplementary Fig. A5). In the full-mitigation scenario, upslope flows are not fully developed in the morning, resulting in weak upslope transport. The weak upslope transport is further reduced by increased stability (e.g. compare Figs. 2.5f and 2.6f), which coincides with higher concentrations over the valley floor (e.g. compare panels a and c of Fig. 2.4). Relative to the less-mitigation scenarios, the upper slope volumes (SR2, PR1, and PR2) in the full-mitigation scenario present higher concentrations after the late morning, due to the persistence of upslope flows (solid line above other lines in volumes SR2, PR1, and PR2 during the afternoon; Fig. 2.4f,h,j,l,n,p). This is explained by a larger transport over the slopes in the

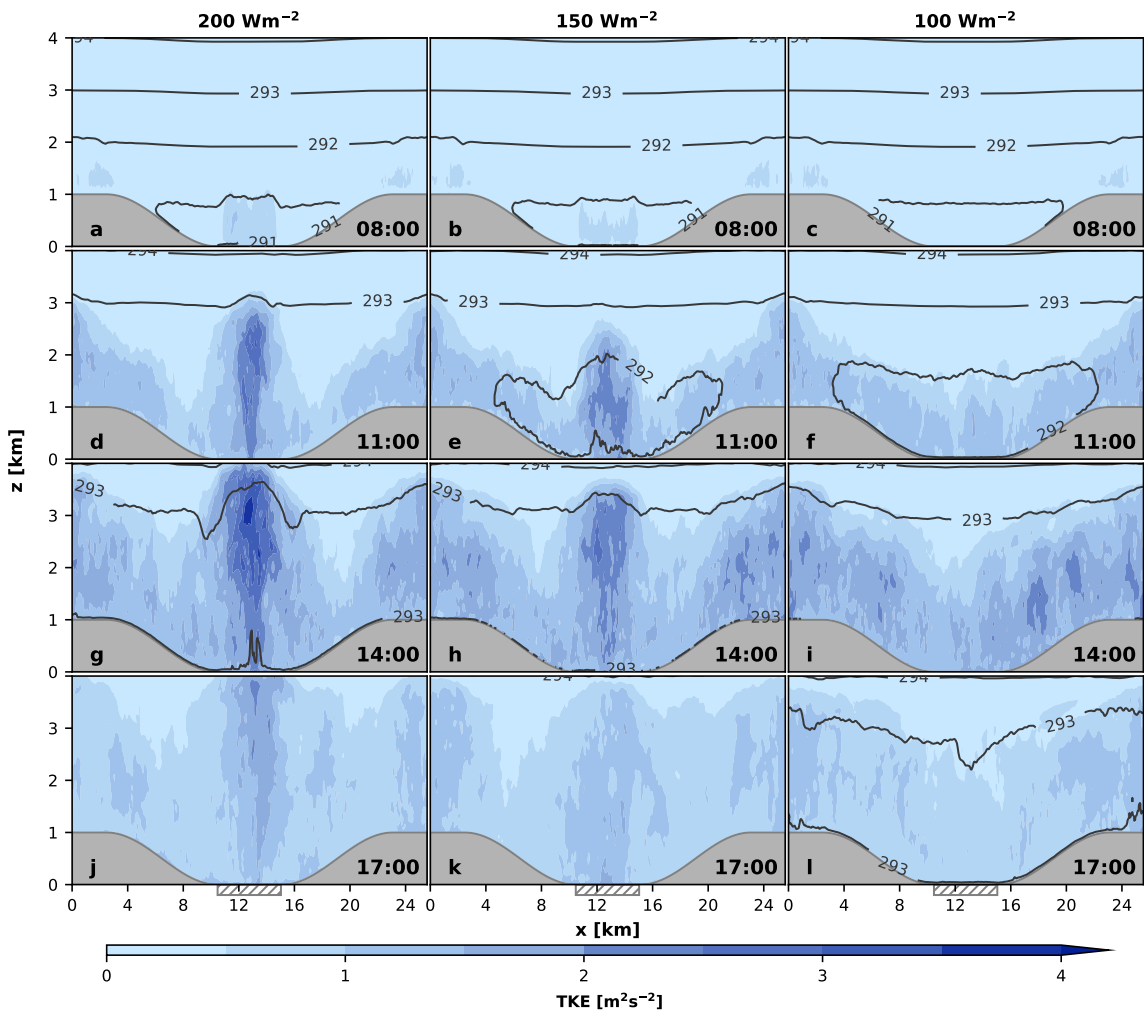


Figure 2.7: Daytime evolution of total TKE starting with low stability. Contours show isentropes every 1 K. See supplementary Fig. A6 for results of the other scenarios.

full-mitigation scenario and more through the center in the less-mitigation scenarios.

Upslope flows are an important mechanism for venting air pollutants out of a valley floor (e.g. Panday and Prinn, 2009). Therefore, the concurrence of upslope (downslope) flows and worse (better) air quality in the full-mitigation scenario (less-mitigation scenarios) might be a counter-intuitive result. However, the impact of slope (upslope or downslope) flows on pollutant accumulation in a valley floor depends on how these flows are linked to the upward transport through valley center. Indeed, downslope flows can be linked to intense low-level convergence and upward transport through a valley center, which may be an efficient mechanism for valley ventilation. This linkage is explored in next section.

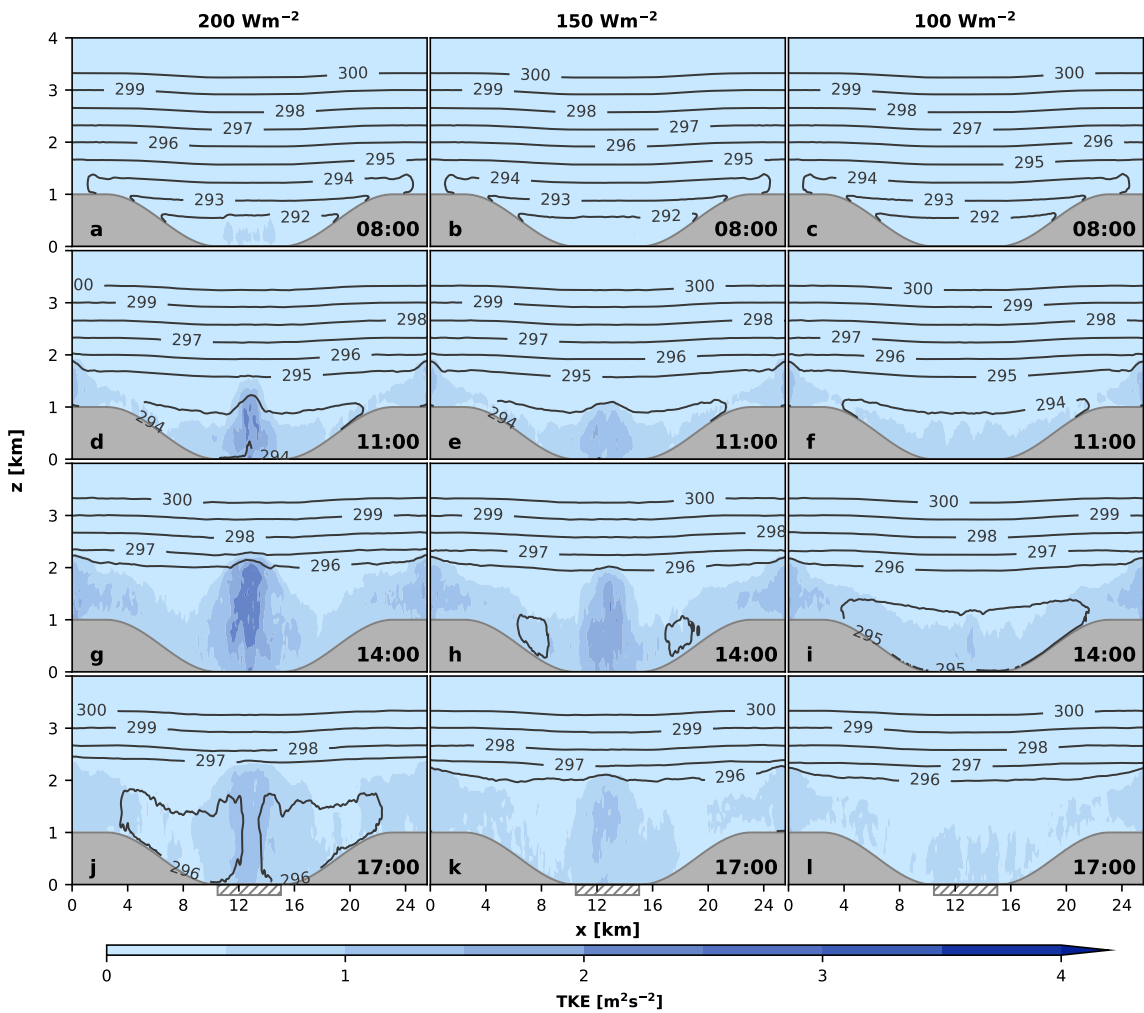


Figure 2.8: As in Fig. 2.7 but starting with high stability. See supplementary Fig. A7 for results of the other scenarios.

2.4.2.2 Transport through the valley center and cross-valley circulation

The upward transport of tracer masses through the valley center is sensitive to UHI mitigation. In general, increased UHI mitigation translates into weakened vertical (upward) motions (Figs. 2.5 and Fig. 2.6) and turbulence (Figs. 2.7 and 2.8) over the urban valley floor. The resulting tracer transport depends not only on the vertical transport, but also on its coupling with the slope flows and interactions with stability. Variations in this interplay result in different cross-valley circulation patterns. Two clear patterns develop depending on the intensity of UHI mitigation. In the less-mitigation scenarios, a cross-valley circulation pattern predominates for most of the day (left and middle columns of Figs. 2.5 and 2.6 after 1100), including downslope

flows, low-level convergence over the valley floor, and ascending motions through the valley center. This ascending motion is driven by intense production of turbulence over the heated urban area (left and middle columns of Figs. 2.7 and 2.8). Previous studies have also reported strong updrafts over urban areas associated to UHI-induced circulations and daytime downslope flows, with comparable vertical velocities (Ryu and Baik, 2013; Ryu et al., 2013; Ganbat et al., 2015a). Hence, a fundamental impact of UHI mitigation is to weaken this circulation and the associated vertical transport of pollutants over the urban area.

A different cross-valley circulation pattern dominates the flow field in the full-mitigation scenario (right column of Figs. 2.5 and 2.6), including upslope flows, and a number of updrafts and downdrafts randomly distributed over the urban valley floor. This CBL structure suggests that turbulence generated by buoyancy due to the upward heat flux from the surface dominates relative to turbulence generated by mean shear (Schmidt and Schumann, 1989). During morning, the updrafts and downdrafts barely reach the mountaintop level and, therefore, they do not constitute a mechanism for venting pollutants out of the valley but, instead, for vertical mixing within the valley atmosphere. This implies that pollutants emitted from the surface can recirculate within the valley atmosphere.

UHI mitigation can have strong impacts on the spatial and temporal distribution of pollutants through effects on these circulation patterns. UHI mitigation reduces vertical transport from the urban surface to the free atmosphere, i.e. from C1 to C4 passing through C2 and C3. As a result, the concentration of pollutants in C3 and C4 (the more elevated volumes above the valley center) is lower in the full-mitigation scenario during the early morning: solid line is below other lines in Figure 2.4i,k,m,o. This, along with a weaker upslope transport (previous section), explains the larger tracer concentrations within C1 and C2 in the full-mitigation scenario: the solid line is mostly above the others in Figure 2.4a,c,e,g.

Of particular importance from the public health perspective is that UHI mitigation reduces ventilation in C1, i.e. the region immediately above the urban area. Tracer masses can be vented out of C1 through both upslope flows and ascending motions. In the morning, ventilation in C1 leads to a decreasing trend in concentrations for all scenarios, but not due to the same mechanisms. In the full-mitigation scenario, the decreasing trend results from the combined effect of upslope flows, which increase tracer concentrations along the valley sidewalls (Fig. 2.4b,d), and turbulent vertical mixing which increase concentrations above C1 (Fig. 2.4e,g,i,k). This in-

crease of concentrations above C1 differs greatly depending on stability. During the early morning, tracer masses transported vertically reach the C3 volume when initial stability is low (Fig. 2.4i), but not when it is high (Fig. 2.4k). Under high stability, higher concentrations remain within C1 (Fig. 2.4c) and C2 (Fig. 2.4g). The presence of updrafts and downdrafts implies that tracer masses can be continuously exchanged between these two volumes. In contrast, in the less-mitigation scenarios, the prevalence of downslope flows implies that ventilation in C1 occurs mainly through ascending motions. These mechanisms are further clarified, for instance, by Figures 2.2 and 2.3 at 1100, in which tracer masses are less distributed along the slopes and more concentrated over the valley center for the less-mitigation scenarios than for the full-mitigation scenario.

2.4.2.3 Atmospheric stability

Increased stability generally exacerbates the negative impacts of UHI mitigation on air quality by adding restrictions to the ventilation mechanisms, as it reduces both ascending winds (Fig. 2.5 versus Fig. 2.6) and turbulence (Fig. 2.7 versus Fig. 2.8). For instance, tracer concentrations over the urban area (in C1) and above the mountaintop level (in C4), respectively, reach much higher values (panel a versus panel c of Fig. 2.4) and remain lower for a longer time (panel m versus panel o of Fig. 2.4) under high stability.

Figure 2.9 shows the time-height tracer distribution horizontally averaged over the urban area. As a simple proof of concept, we include an approximate value of the CBL height, estimated as the height at which the mean potential temperature gradient $\partial\theta/\partial z$ exceeds a threshold of 0.001 K m^{-1} , starting at the lowest level (Catalano and Moeng, 2010 and Leukauf et al., 2016 used a similar procedure). This illustrates two important points. First, that tracer masses remain substantially concentrated below the stable layer; and second, that UHI mitigation delays the destabilization process. For instance, the difference in the duration of the destabilization process between the no- (Fig. 2.9d) and full-mitigation (Fig. 2.9f) scenarios is greater than 3 hours (from ~ 1000 to ~ 1300). Maximum CBL height for high (low) stability are 1.8 (3.4) km for the full-mitigation scenario, 2.0 (3.6) km for the moderate-mitigation scenario, and 2.1 (3.8) km for the no-mitigation scenario. For the larger UHI contrasts of 150 and 300 W m^{-2} , values increase to 2.2 (4.1) km and 2.4 (4.6) km, respectively. CBL height increases with increasing thermal contrast and decreasing stability.

In the full-mitigation scenario, for the high initial stability, an abrupt change in

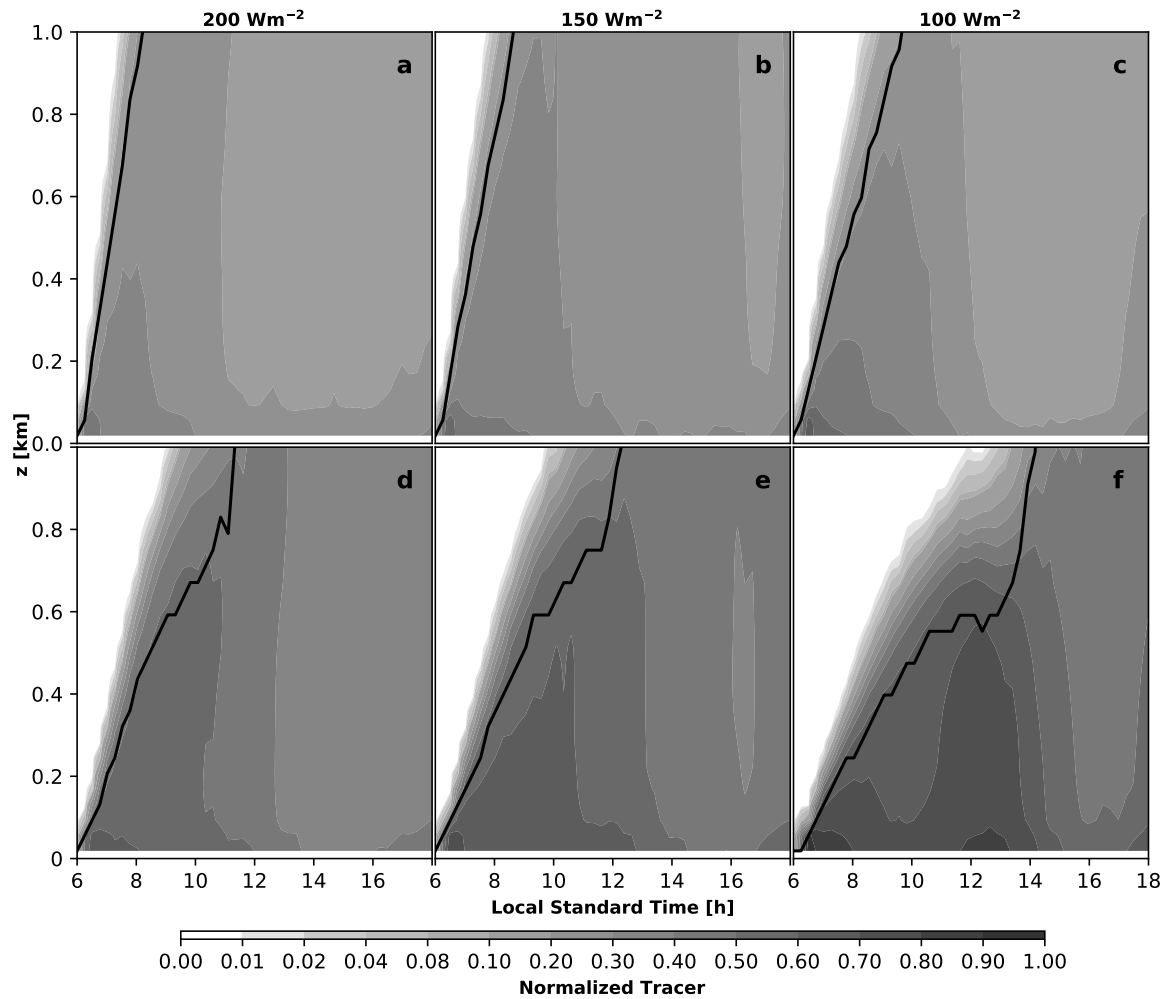


Figure 2.9: Time-height distribution of normalized tracer mixing ratio for the UHI mitigation scenarios, and for the low (top) and high (bottom) stability levels. Values represent spatial averages over the valley floor. The bold line shows the approximate height of the CBL. See supplementary Fig. A8 for results of the other scenarios.

tracer concentrations occurs around 1300 for volumes C1 (Fig. 2.4c), C2 (Fig. 2.4g), and C4 (Fig. 2.4o). While concentration decreases in the lower level volumes (C1 and C2), it increases above the mountaintop level (in C4). This transition describes the moment in which tracer masses escape the valley (i.e. reach the C4 volume), and is concurrent with the destabilization of the valley atmosphere (Fig. 2.9f), which in turn is related to the CBL growth from below the mountaintop level at 1100 (Fig. 2.8f) to above this level at 1400 (Fig. 2.8i). CBL growth is a fundamental process of atmospheric destabilization in valleys (Whiteman and McKee, 1982). By weakening this process, UHI mitigation can worsen air quality during temperature inversion events.

2.5 Discussion

This discussion is focused on the potential implications of our idealized results for management and planning of real urban systems. Although a number of previous studies have identified both beneficial and adverse environmental impacts of UHI mitigation (e.g. Fallmann et al., 2016; Ma et al., 2017; Morini et al., 2018; Falasca and Curci, 2018; Li et al., 2018; Epstein et al., 2017), the challenge of building a more general understanding of the mechanisms behind these contrasting impacts remains (Taha, 2015; Yang et al., 2015). Although idealized, our simulations reproduce key meteorological aspects of urban valleys and, more importantly, shed light on the physical mechanisms through which UHI mitigation interacts with the transport of air pollutants in such valleys. The goal of characterizing these mechanisms could be used to guide the design of observational studies in real systems (e.g. detection of slope winds reversal related to urban heating). Although several studies have reported observations of UHI-induced circulations resulting in strong low level convergence over urban areas (e.g. Hidalgo et al., 2008; Bornstein and Lin, 2000), distinguishing effects of urban areas on observed winds is a challenging task due to interactions among multi-scale flows (e.g. Lemonsu et al., 2006; Park, 2018).

Having used a passive tracer implies that our results do not consider potential effects of UHI mitigation on air quality through chemical reactions. For instance, UHI mitigation has been found to either decrease or increase ozone concentrations, depending on competing mechanisms such as reductions in temperature, higher concentration of primary pollutants, and variations in the amount of reflected solar radiation (Fallmann et al., 2016; Epstein et al., 2017; Falasca and Curci, 2018). However, the

transport of a passive tracer is representative of nonreactive (at the considered spatial and temporal scales) pollutants (e.g. particulate matter and carbon monoxide) which may be highly relevant for estimating health effects of e.g. vehicle emissions (Marshall et al., 2005). The significance of these considerations depends on the particularities of each city and the relevant pollutants.

The topographical settings of individual cities are relevant for pollutant transport, as the evolution of stable layers and valley circulations are sensitive to e.g. geometrical characteristics of valleys and urban areas. The present study is limited as different valley geometries were not analyzed. For instance, deeper valleys may exhibit stronger upslope winds (Wagner et al., 2015b) and longer lifetimes of temperature inversions (Colette et al., 2003); valley width seems to have little impact on slope flows (Wagner et al., 2015b), although differences between a narrow and a wide valley may arise (Serafin and Zardi, 2010); higher slope angles are associated to larger horizontal and vertical wind speeds (Atkinson, 1995). Urban area fraction is another feature of urban valleys that is relevant for the mechanisms of air pollution transport (Rendón et al., 2014). Low percentages of urban land may be associated with reversed cross-valley circulations producing downslope winds, but when the urban percentage is large (i.e., if the sidewalls are largely urbanized) the cross-valley circulation may be that of typical valleys with upslope winds (Rendón et al., 2014). However, even for the cases with large urban fractions and typical valley circulations, a reduction of the surface forcing (UHI mitigation) would delay the breakup of the temperature inversion and reduce the slope flows (Rendón et al., 2014; Leukauf et al., 2015), thus limiting ventilation.

Another important simplification of our model configuration is the lack of along-valley winds or mountain-plain circulations due to the quasi-two-dimensional topography (uniform in the along-valley direction). Although the presence of along-valley flows has little impact on the cross-valley circulation (e.g. Rampanelli et al., 2004; Schmidli, 2013), along-valley circulations can play an important role in ventilation as mass is transported from the boundary layer of an adjacent plain into the valley, while a return flow (valley to plain) occurs aloft (Wagner et al., 2015b). Hence, assuming that the air transported from the plain to the valley is non-polluted, the along-valley flow can be beneficial for air quality in the valley, due to the replacement of polluted air with clean air through this type of along-valley circulation. Although our experiments do not allow to explore the effect of UHI mitigation on this mechanism, it is interesting to note that its formation is associated with higher temperatures

over the valley than over the plain (Schmidli, 2013), and the up-valley flow intensifies with increasing temperature contrast (Wagner et al., 2015a). Therefore, weakening of this plain-to-valley thermal contrast through UHI mitigation could weaken the along-valley ventilation. Overall, the potential impacts of UHI mitigation on along-valley circulation adds complexity to the discussed trade-offs, which should be considered in future studies.

The number of studies on urban cooling strategies has been continuously growing (Yang et al., 2015; Aleksandrowicz et al., 2017; Francis and Jensen, 2017). Consequently, it is still a common (sometimes implicit) premise that UHI mitigation has a net beneficial effect on urban quality and sustainability (e.g. Taha, 2015; Ma et al., 2017; Morini et al., 2018). Contrary to this premise, our results demonstrate how UHI mitigation can cause a significant worsening of air quality in urban valleys, via the alteration of the physical mechanisms of air pollution transport. A fundamental implication for urban management and planning in real systems is that large and often cost-intensive (Pomerantz, 2018) urban transformations (e.g. replacement of materials) should not be accomplished under the assumption that UHI mitigation (cooling a city) will necessarily lead to improved environmental quality. Unexpected adverse impacts on air quality may emerge.

Our results also demonstrate the theoretical possibility of finding intermediate strategies for UHI mitigation in which urban heating can be reduced while limiting the adverse impacts on air quality. Such strategies can lead to important benefits of UHI mitigation (e.g. improving urban comfort) while not strongly deteriorating air quality. Finding such intermediate strategies is of practical importance for urban management and planning, and requires case-specific simulations.

The complex interactions between UHI mitigation and air quality, as well as the potential trade-offs, imply that real cases should be modelled with realistic models for informing decisions. Consequently, the common assumption that surface temperature reduction is, *per se*, an indicator of urban environmental quality improvement (e.g. Lee et al., 2015; Li and Norford, 2016; Ma et al., 2017; Yuan et al., 2017) may be misleading, especially in urban valleys. Finally, we want to emphasize that our intention is not to generally discourage the implementation of UHI mitigation strategies, but rather to highlight the urgent need to apply more comprehensive and integrated analysis for decision making. This is in the spirit of conceiving urban systems as highly complex and dynamic in nature (Masson et al., 2018).

2.6 Conclusions

Our large eddy simulations show that for an idealized urban valley with fixed emissions: (i) tracer concentrations generally increase with increasing UHI mitigation and stability, mainly as a consequence of reduced vertical transport through the center of the valley; (ii) UHI mitigation causes a transition from a daytime flow field with prevalent downslope flows, low-level convergence, and ascending motions over the urban valley center, to a flow field with prevalent upslope flows and turbulent mixing within the valley atmosphere (below the mountaintop level); (iii) UHI mitigation delays the destabilization of the valley atmosphere and, therefore, enhances the trapping effect of stable layers; and (iv) there is a non-linear relationship between the intensity of UHI mitigation (relative reduction in surface heating) and the increase of tracer concentrations, especially over the urban area, which opens the possibility of finding moderate mitigation scenarios in which the benefits of UHI mitigation outweigh its negative impacts on air quality.

Although idealized, our results provide evidence that UHI mitigation can cause significant air quality worsening in real urban valleys, and shed light on the physical mechanisms behind this impact. Typical events of increased atmospheric stability, or temperature inversion, can substantially exacerbate this adverse impact in real urban valleys. Those mechanisms are fundamentally related to the effect of urban cooling on reducing turbulence and ascending motions that may be fundamental for the ventilation of urban valleys. Collectively, our results and their implications demonstrate a relevant trade-off between UHI mitigation and air quality in real urban valleys. This trade-off, as well as its underlying mechanisms, should be thoroughly considered before deciding about the implementation of UHI mitigation strategies in real systems.

2.7 References

- Aleksandrowicz, O., M. Vuckovic, K. Kiesel, and A. Mahdavi (2017). “Current trends in urban heat island mitigation research: Observations based on a comprehensive research repository”. *Urban Climate* 21, 1–26. DOI: [10.1016/J.UCLIM.2017.04.002](https://doi.org/10.1016/J.UCLIM.2017.04.002).
- Atkinson, B. W. (1995). “Orographic and stability effects on valley-side drainage flows”. *Boundary-Layer Meteorology* 75.4, 403–428. DOI: [10.1007/BF00712271](https://doi.org/10.1007/BF00712271).

- Baklanov, A., C. Grimmond, D. Carlson, D. Terblanche, X. Tang, V. Bouchet, B. Lee, G. Langendijk, R. Kolli, and A. Hovsepyan (2018). “From urban meteorology, climate and environment research to integrated city services”. *Urban Climate* 23, 330–341. DOI: [10.1016/J.UCLIM.2017.05.004](https://doi.org/10.1016/J.UCLIM.2017.05.004).
- Bornstein, R. and Q. Lin (2000). “Urban heat islands and summertime convective thunderstorms in Atlanta: three case studies”. *Atmospheric Environment* 34.3, 507–516. DOI: [10.1016/S1352-2310\(99\)00374-X](https://doi.org/10.1016/S1352-2310(99)00374-X).
- Burns, P. and C. Chemel (2014). “Evolution of Cold-Air-Pooling Processes in Complex Terrain”. *Boundary-Layer Meteorology* 150.3, 423–447. DOI: [10.1007/s10546-013-9885-z](https://doi.org/10.1007/s10546-013-9885-z).
- Catalano, F. and C.-H. Moeng (2010). “Large-Eddy Simulation of the Daytime Boundary Layer in an Idealized Valley Using the Weather Research and Forecasting Numerical Model”. *Boundary-Layer Meteorology* 137.1, 49–75. DOI: [10.1007/s10546-010-9518-8](https://doi.org/10.1007/s10546-010-9518-8).
- Christen, A. and R. Vogt (2004). “Energy and radiation balance of a central European city”. *International Journal of Climatology* 24.11, 1395–1421. DOI: [10.1002/joc.1074](https://doi.org/10.1002/joc.1074).
- Colette, A., F. K. Chow, and R. L. Street (2003). “A Numerical Study of Inversion-Layer Breakup and the Effects of Topographic Shading in Idealized Valleys”. *Journal of Applied Meteorology* 42.9, 1255–1272. DOI: [10.1175/1520-0450\(2003\)042<1255:ANSOIB>2.0.CO;2](https://doi.org/10.1175/1520-0450(2003)042<1255:ANSOIB>2.0.CO;2).
- Coutts, A. M., N. J. Tapper, J. Beringer, M. Loughnan, and M. Demuzere (2013). “Watering our cities: The capacity for Water Sensitive Urban Design to support urban cooling and improve human thermal comfort in the Australian context”. *Progress in Physical Geography: Earth and Environment* 37.1, 2–28. DOI: [10.1177/0309133312461032](https://doi.org/10.1177/0309133312461032).
- De Wekker, S. F. J. and M. Kossmann (2015). “Convective Boundary Layer Heights Over Mountainous Terrain? A Review of Concepts”. *Frontiers in Earth Science* 3, 77. DOI: [10.3389/feart.2015.00077](https://doi.org/10.3389/feart.2015.00077).
- De Wekker, S. F. J., M. Kossmann, J. Knievel, L. Giovannini, E. Gutmann, and D. Zardi (2018). “Meteorological Applications Benefiting from an Improved Understanding of Atmospheric Exchange Processes over Mountains”. *Atmosphere* 9.10, 371. DOI: [10.3390/atmos9100371](https://doi.org/10.3390/atmos9100371).

- Deardorff, J. W. (1980). “Stratocumulus-capped mixed layers derived from a three-dimensional model”. *Boundary-Layer Meteorology* 18.4, 495–527. DOI: [10.1007/BF00119502](https://doi.org/10.1007/BF00119502).
- Epstein, S. A., S.-M. Lee, A. S. Katzenstein, M. Carreras-Sospedra, X. Zhang, S. C. Farina, P. Vahmani, P. M. Fine, and G. Ban-Weiss (2017). “Air-quality implications of widespread adoption of cool roofs on ozone and particulate matter in southern California.” *Proceedings of the National Academy of Sciences of the United States of America* 114.34, 8991–8996. DOI: [10.1073/pnas.1703560114](https://doi.org/10.1073/pnas.1703560114).
- Falasca, S. and G. Curci (2018). “Impact of Highly Reflective Materials on Meteorology, PM10 and Ozone in Urban Areas: A Modeling Study with WRF-CHIMERE at High Resolution over Milan (Italy)”. *Urban Science* 2.1, 18. DOI: [10.3390/urbansci2010018](https://doi.org/10.3390/urbansci2010018).
- Fallmann, J., R. Forkel, and S. Emeis (2016). “Secondary effects of urban heat island mitigation measures on air quality”. *Atmospheric Environment* 125, 199–211. DOI: [10.1016/J.ATMOENV.2015.10.094](https://doi.org/10.1016/J.ATMOENV.2015.10.094).
- Fan, Y., Y. Li, A. Bejan, Y. Wang, and X. Yang (2017). “Horizontal extent of the urban heat dome flow”. *Scientific Reports* 7.1, 11681. DOI: [10.1038/s41598-017-09917-4](https://doi.org/10.1038/s41598-017-09917-4).
- Francis, L. F. M. and M. B. Jensen (2017). “Benefits of green roofs: A systematic review of the evidence for three ecosystem services”. *Urban Forestry & Urban Greening* 28, 167–176. DOI: [10.1016/J.UFUG.2017.10.015](https://doi.org/10.1016/J.UFUG.2017.10.015).
- Gago, E., J. Roldan, R. Pacheco-Torres, and J. Ordóñez (2013). “The city and urban heat islands: A review of strategies to mitigate adverse effects”. *Renewable and Sustainable Energy Reviews* 25, 749–758. DOI: [10.1016/J.RSER.2013.05.057](https://doi.org/10.1016/J.RSER.2013.05.057).
- Ganbat, G. and J.-J. Baik (2015). “Local circulations in and around the Ulaanbaatar, Mongolia, metropolitan area”. *Meteorology and Atmospheric Physics* 127.4, 393–406. DOI: [10.1007/s00703-015-0374-4](https://doi.org/10.1007/s00703-015-0374-4).
- Ganbat, G., J.-J. Baik, and Y.-H. Ryu (2015a). “A numerical study of the interactions of urban breeze circulation with mountain slope winds”. *Theoretical and Applied Climatology* 120.1-2, 123–135. DOI: [10.1007/s00704-014-1162-7](https://doi.org/10.1007/s00704-014-1162-7).
- Ganbat, G., J. M. Seo, J.-Y. Han, and J.-J. Baik (2015b). “A theoretical study of the interactions of urban breeze circulation with mountain slope winds”. *Theoretical and Applied Climatology* 121.3-4, 545–555. DOI: [10.1007/s00704-014-1252-6](https://doi.org/10.1007/s00704-014-1252-6).

- Giovannini, L., D. Zardi, and M. de Franceschi (2011). “Analysis of the Urban Thermal Fingerprint of the City of Trento in the Alps”. *Journal of Applied Meteorology and Climatology* 50.5, 1145–1162. DOI: [10.1175/2010JAMC2613.1](https://doi.org/10.1175/2010JAMC2613.1).
- Giovannini, L., D. Zardi, M. de Franceschi, and F. Chen (2014). “Numerical simulations of boundary-layer processes and urban-induced alterations in an Alpine valley”. *International Journal of Climatology* 34.4, 1111–1131. DOI: [10.1002/joc.3750](https://doi.org/10.1002/joc.3750).
- Henao, J. J., A. M. Rendón, and J. F. Salazar (2020). “Trade-off between urban heat island mitigation and air quality in urban valleys”. *Urban Climate* 31, 100542. DOI: [10.1016/j.uclim.2019.100542](https://doi.org/10.1016/j.uclim.2019.100542).
- Hidalgo, J., G. Pigeon, and V. Masson (2008). “Urban-breeze circulation during the CAPITOU experiment: observational data analysis approach”. *Meteorology and Atmospheric Physics* 102.3-4, 223–241. DOI: [10.1007/s00703-008-0329-0](https://doi.org/10.1007/s00703-008-0329-0).
- Jiménez, P. A., J. Dudhia, J. F. González-Rouco, J. Navarro, J. P. Montávez, and E. García-Bustamante (2012). “A Revised Scheme for the WRF Surface Layer Formulation”. *Monthly Weather Review* 140.3, 898–918. DOI: [10.1175/MWR-D-11-00056.1](https://doi.org/10.1175/MWR-D-11-00056.1).
- Klemp, J. B., J. Dudhia, and A. D. Hassiotis (2008). “An Upper Gravity-Wave Absorbing Layer for NWP Applications”. *Monthly Weather Review* 136.10, 3987–4004. DOI: [10.1175/2008MWR2596.1](https://doi.org/10.1175/2008MWR2596.1).
- Lang, M. N., A. Gohm, and J. S. Wagner (2015). “The impact of embedded valleys on daytime pollution transport over a mountain range”. *Atmospheric Chemistry and Physics* 15.20, 11981–11998. DOI: [10.5194/acp-15-11981-2015](https://doi.org/10.5194/acp-15-11981-2015).
- Largeron, Y. and C. Staquet (2016). “Persistent inversion dynamics and wintertime PM10 air pollution in Alpine valleys”. *Atmospheric Environment* 135, 92–108. DOI: [10.1016/J.ATMOENV.2016.03.045](https://doi.org/10.1016/J.ATMOENV.2016.03.045).
- Lee, S., Y. Ryu, and C. Jiang (2015). “Urban heat mitigation by roof surface materials during the East Asian summer monsoon”. *Environmental Research Letters* 10.12, 124012. DOI: [10.1088/1748-9326/10/12/124012](https://doi.org/10.1088/1748-9326/10/12/124012).
- Lehner, M. and A. Gohm (2010). “Idealised Simulations of Daytime Pollution Transport in a Steep Valley and its Sensitivity to Thermal Stratification and Surface Albedo”. *Boundary-Layer Meteorology* 134.2, 327–351. DOI: [10.1007/s10546-009-9442-y](https://doi.org/10.1007/s10546-009-9442-y).

- Lehner, M. and C. D. Whiteman (2012). “The Thermally Driven Cross-Basin Circulation in Idealized Basins under Varying Wind Conditions”. *Journal of Applied Meteorology and Climatology* 51.6, 1026–1045. DOI: [10.1175/JAMC-D-11-0181.1](https://doi.org/10.1175/JAMC-D-11-0181.1).
- Lemonsu, A., S. Bastin, V. Masson, and P. Drobinski (2006). “Vertical Structure of the Urban Boundary Layer over Marseille Under Sea-Breeze Conditions”. *Boundary-Layer Meteorology* 118.3, 477–501. DOI: [10.1007/s10546-005-7772-y](https://doi.org/10.1007/s10546-005-7772-y).
- Leukauf, D., A. Gohm, and M. W. Rotach (2016). “Quantifying horizontal and vertical tracer mass fluxes in an idealized valley during daytime”. *Atmospheric Chemistry and Physics* 16.20, 13049–13066. DOI: [10.5194/acp-16-13049-2016](https://doi.org/10.5194/acp-16-13049-2016).
- Leukauf, D., A. Gohm, M. W. Rotach, and J. S. Wagner (2015). “The Impact of the Temperature Inversion Breakup on the Exchange of Heat and Mass in an Idealized Valley: Sensitivity to the Radiative Forcing”. *Journal of Applied Meteorology and Climatology* 54.11, 2199–2216. DOI: [10.1175/JAMC-D-15-0091.1](https://doi.org/10.1175/JAMC-D-15-0091.1).
- Li, H., F. Meier, X. Lee, T. Chakraborty, J. Liu, M. Schaap, and S. Sodoudi (2018). “Interaction between urban heat island and urban pollution island during summer in Berlin”. *Science of The Total Environment* 636, 818–828. DOI: [10.1016/J.SCITOTENV.2018.04.254](https://doi.org/10.1016/J.SCITOTENV.2018.04.254).
- Li, X.-X. and L. K. Norford (2016). “Evaluation of cool roof and vegetations in mitigating urban heat island in a tropical city, Singapore”. *Urban Climate* 16, 59–74. DOI: [10.1016/J.UCLIM.2015.12.002](https://doi.org/10.1016/J.UCLIM.2015.12.002).
- Ma, S., M. Goldstein, A. J. Pitman, N. Haghdad, and I. MacGill (2017). “Pricing the urban cooling benefits of solar panel deployment in Sydney, Australia”. *Scientific Reports* 7.1, 43938. DOI: [10.1038/srep43938](https://doi.org/10.1038/srep43938).
- Mackey, C. W., X. Lee, and R. B. Smith (2012). “Remotely sensing the cooling effects of city scale efforts to reduce urban heat island”. *Building and Environment* 49, 348–358. DOI: [10.1016/J.BUILDENV.2011.08.004](https://doi.org/10.1016/J.BUILDENV.2011.08.004).
- Makar, P., S. Gravel, V. Chirkov, K. Strawbridge, F. Froude, J. Arnold, and J. Brook (2006). “Heat flux, urban properties, and regional weather”. *Atmospheric Environment* 40.15, 2750–2766. DOI: [10.1016/J.ATMOENV.2005.11.061](https://doi.org/10.1016/J.ATMOENV.2005.11.061).
- Malek, E., T. Davis, R. S. Martin, and P. J. Silva (2006). “Meteorological and environmental aspects of one of the worst national air pollution episodes (January, 2004) in Logan, Cache Valley, Utah, USA”. *Atmospheric Research* 79.2, 108–122. DOI: [10.1016/J.ATMOSRES.2005.05.003](https://doi.org/10.1016/J.ATMOSRES.2005.05.003).

- Marshall, J. D., S.-K. Teoh, and W. W. Nazaroff (2005). “Intake fraction of nonreactive vehicle emissions in US urban areas”. *Atmospheric Environment* 39.7, 1363–1371. DOI: [10.1016/J.ATMOENV.2004.11.008](https://doi.org/10.1016/J.ATMOENV.2004.11.008).
- Masson, V., A. Lemonsu, and J. Voogt (2018). “The 9th International Conference on Urban Climate”. *Urban Climate* 23, 1–7. DOI: [10.1016/J.UCLIM.2017.07.007](https://doi.org/10.1016/J.UCLIM.2017.07.007).
- Moeng, C.-H., J. Dudhia, J. Klemp, and P. Sullivan (2007). “Examining Two-Way Grid Nesting for Large Eddy Simulation of the PBL Using the WRF Model”. *Monthly Weather Review* 135.6, 2295–2311. DOI: [10.1175/MWR3406.1](https://doi.org/10.1175/MWR3406.1).
- Morini, E., A. G. Touchaei, F. Rossi, F. Cotana, and H. Akbari (2018). “Evaluation of albedo enhancement to mitigate impacts of urban heat island in Rome (Italy) using WRF meteorological model”. *Urban Climate* 24, 551–566. DOI: [10.1016/J.UCLIM.2017.08.001](https://doi.org/10.1016/J.UCLIM.2017.08.001).
- Offerle, B., C. S. B. Grimmond, K. Fortuniak, and W. Pawlak (2006). “Intraurban Differences of Surface Energy Fluxes in a Central European City”. *Journal of Applied Meteorology and Climatology* 45.1, 125–136. DOI: [10.1175/JAM2319.1](https://doi.org/10.1175/JAM2319.1).
- Panday, A. K. and R. G. Prinn (2009). “Diurnal cycle of air pollution in the Kathmandu Valley, Nepal: Observations”. *Journal of Geophysical Research* 114.D9, D09305. DOI: [10.1029/2008JD009777](https://doi.org/10.1029/2008JD009777).
- Park, M.-S. (2018). “Overview of Meteorological Surface Variables and Boundary-layer Structures in the Seoul Metropolitan Area during the MAPS-Seoul Campaign”. *Aerosol and Air Quality Research* 18.9, 2157–2172. DOI: [10.4209/aaqr.2017.10.0428](https://doi.org/10.4209/aaqr.2017.10.0428).
- Pomerantz, M. (2018). “Are cooler surfaces a cost-effect mitigation of urban heat islands?” *Urban Climate* 24, 393–397. DOI: [10.1016/J.UCLIM.2017.04.009](https://doi.org/10.1016/J.UCLIM.2017.04.009).
- Powers, J. G., J. B. Klemp, W. C. Skamarock, C. A. Davis, J. Dudhia, D. O. Gill, J. L. Coen, D. J. Gochis, R. Ahmadov, S. E. Peckham, G. A. Grell, J. Michalakes, S. Trahan, S. G. Benjamin, C. R. Alexander, G. J. Dimego, W. Wang, C. S. Schwartz, G. S. Romine, Z. Liu, C. Snyder, F. Chen, M. J. Barlage, W. Yu, and M. G. Duda (2017). “The Weather Research and Forecasting Model: Overview, System Efforts, and Future Directions”. *Bulletin of the American Meteorological Society* 98.8, 1717–1737. DOI: [10.1175/BAMS-D-15-00308.1](https://doi.org/10.1175/BAMS-D-15-00308.1).
- Rampanelli, G., D. Zardi, and R. Rotunno (2004). “Mechanisms of Up-Valley Winds”. *Journal of the Atmospheric Sciences* 61.24, 3097–3111. DOI: [10.1175/JAS-3354.1](https://doi.org/10.1175/JAS-3354.1).

- Rendón, A. M., J. F. Salazar, C. A. Palacio, and V. Wirth (2015). “Temperature Inversion Breakup with Impacts on Air Quality in Urban Valleys Influenced by Topographic Shading”. *Journal of Applied Meteorology and Climatology* 54.2, 302–321. DOI: [10.1175/JAMC-D-14-0111.1](https://doi.org/10.1175/JAMC-D-14-0111.1).
- Rendón, A. M., J. F. Salazar, C. A. Palacio, V. Wirth, and B. Brötz (2014). “Effects of Urbanization on the Temperature Inversion Breakup in a Mountain Valley with Implications for Air Quality”. *Journal of Applied Meteorology and Climatology* 53.4, 840–858. DOI: [10.1175/JAMC-D-13-0165.1](https://doi.org/10.1175/JAMC-D-13-0165.1).
- Rotach, M. W., M. Andretta, P. Calanca, A. P. Weigel, and A. Weiss (2008). “Boundary layer characteristics and turbulent exchange mechanisms in highly complex terrain”. *Acta Geophysica* 56.1, 194–219. DOI: [10.2478/s11600-007-0043-1](https://doi.org/10.2478/s11600-007-0043-1).
- Rotach, M. W., G. Wohlfahrt, A. Hansel, M. Reif, J. Wagner, and A. Gohm (2014). “The World is Not Flat: Implications for the Global Carbon Balance”. *Bulletin of the American Meteorological Society* 95.7, 1021–1028. DOI: [10.1175/BAMS-D-13-00109.1](https://doi.org/10.1175/BAMS-D-13-00109.1).
- Ryu, Y.-H. and J.-J. Baik (2013). “Daytime Local Circulations and Their Interactions in the Seoul Metropolitan Area”. *Journal of Applied Meteorology and Climatology* 52.4, 784–801. DOI: [10.1175/JAMC-D-12-0157.1](https://doi.org/10.1175/JAMC-D-12-0157.1).
- Ryu, Y.-H., J.-J. Baik, and J.-Y. Han (2013). “Daytime urban breeze circulation and its interaction with convective cells”. *Quarterly Journal of the Royal Meteorological Society* 139.671, 401–413. DOI: [10.1002/qj.1973](https://doi.org/10.1002/qj.1973).
- Saaroni, H., J. Amorim, J. Hiemstra, and D. Pearlmutter (2018). “Urban Green Infrastructure as a tool for urban heat mitigation: Survey of research methodologies and findings across different climatic regions”. *Urban Climate* 24, 94–110. DOI: [10.1016/J.UCLIM.2018.02.001](https://doi.org/10.1016/J.UCLIM.2018.02.001).
- Santamouris, M. (2014). “Cooling the cities? A review of reflective and green roof mitigation technologies to fight heat island and improve comfort in urban environments”. *Solar Energy* 103, 682–703. DOI: [10.1016/J.SOLENER.2012.07.003](https://doi.org/10.1016/J.SOLENER.2012.07.003).
- Schmidli, J. (2013). “Daytime Heat Transfer Processes over Mountainous Terrain”. *Journal of the Atmospheric Sciences* 70.12, 4041–4066. DOI: [10.1175/JAS-D-13-083.1](https://doi.org/10.1175/JAS-D-13-083.1).
- Schmidli, J., B. Billings, F. K. Chow, S. F. J. de Wekker, J. Doyle, V. Grubišić, T. Holt, Q. Jiang, K. A. Lundquist, P. Sheridan, S. Vosper, C. D. Whiteman, A. A. Wyszogrodzki, and G. Zänagl (2011). “Intercomparison of Mesoscale Model

- Simulations of the Daytime Valley Wind System”. *Monthly Weather Review* 139.5, 1389–1409. DOI: [10.1175/2010MWR3523.1](https://doi.org/10.1175/2010MWR3523.1).
- Schmidt, H. and U. Schumann (1989). “Coherent structure of the convective boundary layer derived from large-eddy simulations”. *Journal of Fluid Mechanics* 200, 511–562. DOI: [10.1017/S0022112089000753](https://doi.org/10.1017/S0022112089000753).
- Scotti, A., C. Meneveau, and D. K. Lilly (1993). “Generalized Smagorinsky model for anisotropic grids”. *Physics of Fluids A: Fluid Dynamics* 5.9, 2306–2308. DOI: [10.1063/1.858537](https://doi.org/10.1063/1.858537).
- Serafin, S., B. Adler, J. Cuxart, S. De Wekker, A. Gohm, B. Grisogono, N. Kalthoff, D. Kirshbaum, M. Rotach, J. Schmidli, I. Stiperski, Ž. Večenaj, and D. Zardi (2018). “Exchange Processes in the Atmospheric Boundary Layer Over Mountainous Terrain”. *Atmosphere* 9.3, 102. DOI: [10.3390/atmos9030102](https://doi.org/10.3390/atmos9030102).
- Serafin, S. and D. Zardi (2010). “Daytime Heat Transfer Processes Related to Slope Flows and Turbulent Convection in an Idealized Mountain Valley”. *Journal of the Atmospheric Sciences* 67.11, 3739–3756. DOI: [10.1175/2010JAS3428.1](https://doi.org/10.1175/2010JAS3428.1).
- Sharma, A., P. Conry, H. J. S. Fernando, A. F. Hamlet, J. J. Hellmann, and F. Chen (2016). “Green and cool roofs to mitigate urban heat island effects in the Chicago metropolitan area: evaluation with a regional climate model”. *Environmental Research Letters* 11.6, 064004. DOI: [10.1088/1748-9326/11/6/064004](https://doi.org/10.1088/1748-9326/11/6/064004).
- Skamarock, C., B. Klemp, J. Dudhia, O. Gill, Z. Liu, J. Berner, W. Wang, G. Powers, G. Duda, D. Barker, and X.-y. Huang (2019). “A Description of the Advanced Research WRF Model Version 4”. DOI: [10.5065/1DFH-6P97](https://doi.org/10.5065/1DFH-6P97).
- Skamarock, W. C. and J. B. Klemp (2008). “A time-split nonhydrostatic atmospheric model for weather research and forecasting applications”. *Journal of Computational Physics* 227.7, 3465–3485. DOI: [10.1016/J.JCP.2007.01.037](https://doi.org/10.1016/J.JCP.2007.01.037).
- Taha, H. (2015). “Meteorological, emissions and air-quality modeling of heat-island mitigation: recent findings for California, USA”. *International Journal of Low-Carbon Technologies* 10.1, 3–14. DOI: [10.1093/ijlct/ctt010](https://doi.org/10.1093/ijlct/ctt010).
- Tan, Z., K. K.-L. Lau, and E. Ng (2016). “Urban tree design approaches for mitigating daytime urban heat island effects in a high-density urban environment”. *Energy and Buildings* 114, 265–274. DOI: [10.1016/J.ENBUILD.2015.06.031](https://doi.org/10.1016/J.ENBUILD.2015.06.031).
- Toro A, R., M. Kvakić, Z. B. Klaić, D. Koraćin, R. G. Morales S, and M. A. Leiva G (2019). “Exploring atmospheric stagnation during a severe particulate matter air pollution episode over complex terrain in Santiago, Chile”. *Environmental Pollution* 244, 705–714. DOI: [10.1016/J.ENVPOL.2018.10.067](https://doi.org/10.1016/J.ENVPOL.2018.10.067).

- Wagner, J. S., A. Gohm, and M. W. Rotach (2015a). “Influence of along-valley terrain heterogeneity on exchange processes over idealized valleys”. *Atmospheric Chemistry and Physics* 15.12, 6589–6603. DOI: [10.5194/acp-15-6589-2015](https://doi.org/10.5194/acp-15-6589-2015).
- (2015b). “The impact of valley geometry on daytime thermally driven flows and vertical transport processes”. *Quarterly Journal of the Royal Meteorological Society* 141.690, 1780–1794. DOI: [10.1002/qj.2481](https://doi.org/10.1002/qj.2481).
- Wagner, J. S., A. Gohm, and M. W. Rotach (2014). “The Impact of Horizontal Model Grid Resolution on the Boundary Layer Structure over an Idealized Valley”. *Monthly Weather Review* 142.9, 3446–3465. DOI: [10.1175/MWR-D-14-00002.1](https://doi.org/10.1175/MWR-D-14-00002.1).
- Wang, F., S. D. Chambers, Z. Zhang, A. G. Williams, X. Deng, H. Zhang, G. Lonati, J. Crawford, A. D. Griffiths, A. Ianniello, and I. Allegrini (2016). “Quantifying stability influences on air pollution in Lanzhou, China, using a radon-based “stability monitor”: Seasonality and extreme events”. *Atmospheric Environment* 145, 376–391. DOI: [10.1016/J.ATMOENV.2016.09.014](https://doi.org/10.1016/J.ATMOENV.2016.09.014).
- Wang, W. (2009). “The Influence of Thermally-Induced Mesoscale Circulations on Turbulence Statistics Over an Idealized Urban Area Under a Zero Background Wind”. *Boundary-Layer Meteorology* 131.3, 403–423. DOI: [10.1007/s10546-009-9378-2](https://doi.org/10.1007/s10546-009-9378-2).
- Whiteman, C. D., S. W. Hoch, J. D. Horel, and A. Charland (2014). “Relationship between particulate air pollution and meteorological variables in Utah’s Salt Lake Valley”. *Atmospheric Environment* 94, 742–753. DOI: [10.1016/J.ATMOENV.2014.06.012](https://doi.org/10.1016/J.ATMOENV.2014.06.012).
- Whiteman, C. D. and T. B. McKee (1982). “Breakup of Temperature Inversions in Deep Mountain Valleys: Part II. Thermodynamic Model”. *Journal of Applied Meteorology* 21.3, 290–302. DOI: [10.1175/1520-0450\(1982\)021<0290:BOTIID>2.0.CO;2](https://doi.org/10.1175/1520-0450(1982)021<0290:BOTIID>2.0.CO;2).
- Yang, J., Z.-H. Wang, and K. E. Kaloush (2015). “Environmental impacts of reflective materials: Is high albedo a ‘silver bullet’ for mitigating urban heat island?” *Renewable and Sustainable Energy Reviews* 47, 830–843. DOI: [10.1016/J.RSER.2015.03.092](https://doi.org/10.1016/J.RSER.2015.03.092).
- Yang, J., Q. Yu, and P. Gong (2008). “Quantifying air pollution removal by green roofs in Chicago”. *Atmospheric Environment* 42.31, 7266–7273. DOI: [10.1016/J.ATMOENV.2008.07.003](https://doi.org/10.1016/J.ATMOENV.2008.07.003).

- Yuan, J., K. Emura, and C. Farnham (2017). “Is urban albedo or urban green covering more effective for urban microclimate improvement?: A simulation for Osaka”. *Sustainable Cities and Society* 32, 78–86. DOI: [10.1016/J.SCS.2017.03.021](https://doi.org/10.1016/J.SCS.2017.03.021).
- Zardi, D. and C. D. Whiteman (2013). “Diurnal Mountain Wind Systems”. In: *Mountain Weather Research and Forecasting*. Springer, Dordrecht, 35–119. DOI: [10.1007/978-94-007-4098-3_2](https://doi.org/10.1007/978-94-007-4098-3_2).
- Zhang, N., X. Wang, and Z. Peng (2014). “Large-Eddy Simulation of Mesoscale Circulations Forced by Inhomogeneous Urban Heat Island”. *Boundary-Layer Meteorology* 151.1, 179–194. DOI: [10.1007/s10546-013-9879-x](https://doi.org/10.1007/s10546-013-9879-x).

Chapter 3

Sub-kilometer dispersion simulation of a CO tracer for an inter-Andean urban valley

This chapter is a reproduction of Henao et al., [2020b](#), published in Atmospheric Pollution Research.

3.1 Abstract

Air quality planning and management can benefit from the ability of numerical models to produce skillful forecasts. However, obtaining these forecasts is a continuing challenge, particularly in complex terrain. Here we examine the dispersion of traffic emissions in the Aburrá valley (located in the Colombian Andes) during an episode of severe air pollution, using the WRF-Chem and a Lagrangian model at sub-kilometer resolution. We focus on the identification of areas with higher CO concentrations (the pollutant analyzed), and examine the role of local and regional airflows in the distribution of CO inside the valley. The meteorological model performance, considering different planetary boundary layer parameterizations and grid sizes, is evaluated using available observations. Overall, the meteorological model performance is within recommended benchmarks for complex terrain. Model performance improves with increasing grid resolution for surface temperature and wind direction, but not for wind speed. Both dispersion models reproduce important features of the spatial and diurnal variability of CO in the valley, but underestimate CO concentrations throughout the simulation period. The south and southeast areas of the valley present the largest CO concentrations, associated with a prevalent northerly transport along the valley axis and reduced transport on the eastern slope. The representation of CO improves when the model adequately reproduces observed rainfall, due to effects of rainfall on boundary layer height and stability, which condition dispersion. Better simulation of transport processes is crucial for informing decisions on air quality management in critical areas such as urban valleys.

3.2 Introduction

Many urban areas located in complex terrain have experienced episodes of severe air pollution (e.g. Mexico City: De Foy et al., 2006; Kathmandu: Bhardwaj et al., 2018; Santiago de Chile: Cuchiara et al., 2017). High pollutant concentrations are usually associated with reduced mixing in the lower atmosphere, due to strong atmospheric stability, weak winds, or both (De Wekker et al., 2018). Strong atmospheric stability can be frequent in mountainous terrain (Whiteman et al., 2004; Mahrt, 2014), which constitutes a thermodynamical barrier that in combination with topographical barriers, can restrict the transport mechanisms responsible for venting pollutants out of urban areas (Lehner and Gohm, 2010; Giovannini et al., 2014; Rendón et al., 2014; Rendón et al., 2015). Such conditions highlight the need of developing air quality management plans in urban areas located in complex terrain.

Chemical transport models are valuable tools for the understanding and management of air quality for a variety of applications, including air quality forecasting (Baklanov et al., 2014) and the evaluation of mitigation scenarios (e.g. Colette et al., 2013). However, the use of numerical models for the assessment of different alternatives relies on the ability of such models to produce skillful forecasts and numerical simulations. Several factors have been identified as causes of inaccuracy in air quality modeling, including aspects related to meteorological processes and variables, emissions, physical and chemical processes, chemical boundary conditions, and model configuration (Zhang et al., 2012a; Zhang et al., 2012b, and references therein). Two of these critical factors are: 1) a good representation of PBL processes, which determine turbulent exchange, the extent of the vertical mixing and entrainment of pollutants into the free atmosphere (Hess et al., 2004; McKeen et al., 2007; Cuchiara et al., 2014); and 2) a fine grid resolution, especially for urbanized complex terrain (Fay and Neunhäuserer, 2006; Shrestha et al., 2009). However, a fine grid resolution does not necessarily imply better model results (e.g. Kuik et al., 2016), and most PBL parameterization are designed for spatial resolutions in the range of 10–100 km and are not scale-aware (e.g. Shin and Dudhia, 2016).

Emission inventories (EI) are also a critical component of air quality modeling, which should consider total emissions, as well as their spatial and temporal distribution (Saide et al., 2009; Kuik et al., 2016). Increasing model grid resolution should be accompanied by increasing EI spatial and temporal resolutions (Schaap et al., 2015), which have been reported to improve the ability of models to accurately estimate

pollutants distribution (Taghavi et al., 2005; González et al., 2018). Two methods have commonly been used for the construction of EI, namely “bottom-up” and “top-down” approaches (Loibl et al., 1993; Tuia et al., 2007; Eicker et al., 2008). In the bottom-up approach, emissions are determined for small individual subunits within a larger unit (Loibl et al., 1993): in the case of traffic emissions, emissions for every road segment are obtained based on traffic information from each segment, which is usually obtained using a traffic model (Tuia et al., 2007). The top-down approach consists of calculating total emissions for the larger unit as a whole, which are then distributed in space for individual subunits using statistical data related to the geographical units (Loibl et al., 1993): for traffic emissions, this involves the calculation of total emissions using aggregated traffic data, which are then distributed in space using, for example, population density or the road network (Gómez et al., 2018). In urban areas with deficiencies in available information, the simpler “top-down” method has been successfully implemented (Saide et al., 2009; Gómez et al., 2018). Although this approach is limited as compared to the more accurate (but time-consuming and information-intensive) bottom-up approach (Eicker et al., 2008), it can produce simple albeit realistic representations of emissions, especially when traffic-related data (e.g. traffic counts) is included (Saide et al., 2009).

In this study we conduct air quality simulations to examine the spatial and temporal distribution of mobile emissions in the Metropolitan Area of the Aburrá Valley (AMVA, Spanish acronym) during a severe air pollution episode in March 2016. This urban area (AMVA), located in a narrow and steep valley in the tropical Andes (Fig. 3.1), has experienced severe air pollution events with important implications for public health (Rodríguez-Villamizar et al., 2018). The most critical episodes are exceedances of fine particulate matter ($PM_{2.5}$), predominantly produced by vehicle emissions ($\sim 80\%$; AMVA, 2017a), which are related to a combination of factors, including topography, meteorological dynamics, and a high population density (~ 4 million inhabitants in $1,157 \text{ km}^2$). These episodes have usually occurred during the transition from dry (December to February and June to August) to rainy (March to May and September to November) seasons, but have been especially severe in March (Herrera-Mejía and Hoyos, 2019).

According to Herrera-Mejía and Hoyos, 2019, pollutant concentrations in AMVA are determined by planetary boundary layer (PBL) height, with adverse conditions (e.g. those of March) occurring when PBL heights do not exceed the average depth of the valley ($\sim 1,000 \text{ m}$), and nocturnal rainfall is reduced. In AMVA, the net ef-

fect of rainfall on the concentration of particulate matter depends on the time of occurrence, with nocturnal rainfall resulting in concentration reductions due to wet deposition, while diurnal rainfall leads to increases in concentration (Roldán-Henao et al., 2020). This negative effect of diurnal rainfall on concentrations occurs due to a stabilization of the atmosphere occurring earlier than under dry conditions, caused by the combination of a negative cloud radiative forcing and a convective cold pool, leading to an accumulation of pollutants near the surface that offsets the removal by wet deposition (Roldán-Henao et al., 2020). The intra-annual variability in pollutant concentrations is related to the latitudinal migration of the intertropical convergence zone (ITCZ), that with its associated cloudiness and precipitation affects surface radiation and hence PBL height (Herrera-Mejía and Hoyos, 2019). Mejía-Echeverry et al., 2018 explored the spatial distribution of pollutants in AMVA using magnetic biomonitoring techniques as a proxy of particulate matter pollution levels. Their findings indicate higher pollutant concentrations in the valley bottom, especially to the south and southeast, while lower concentrations were found to the north and in areas located at higher altitudes. This spatial distribution is related to (but not completely explained by) the closeness to emission sources.

Growing public and government concern about air quality in AMVA resulted in new plans to address critical air pollution episodes and to improve air quality in the future (AMVA, 2017b). However, the design and effectiveness of measures to reduce air pollution (either in AMVA or other urban valleys) can significantly benefit from an improved understanding of pollution dynamics, including the dynamical nature of emissions and mechanisms of air pollution transport, which is still limited in the region.

Here we evaluate the role of the local and regional airflows in the dispersion of pollutants, and then identify areas that result in higher CO concentrations due to transport processes, relative to the local emissions. Due to the complexity of the terrain, we further use the simulations to examine the effect of increasing spatial resolution and three different PBL parameterizations on the resulting meteorology.

The remainder of the paper is organized as follows: section 3.3 provides the description of the modeling framework, the available observations, and the strategy for the model performance evaluation; section 3.4 presents the meteorological and dispersion model simulations and comparisons with the observations; section 3.5 discuss the results, and section 3.6 concludes.

3.3 Data and Methods

3.3.1 Modeling framework

Two different models are used to analyze the dispersion of mobile emissions in the AMVA region. One is the fully-coupled WRF-Chem (Grell et al., 2005), a version of the Weather Research and Forecasting model (WRF; Skamarock et al., 2008) that resolves simultaneously meteorology with particulates and trace gases (Fast et al., 2006). The other model is a Lagrangian dispersion model developed at the Desert Research Institute (Mejia et al., 2019), that is run offline with meteorology from the WRF model.

In this study, mobile emissions are represented by a passive tracer emulating carbon monoxide (CO). Although particulate matter (PM) is a more critical pollutant in AMVA, CO is selected in this study for several reasons: The main objective focuses on the transport of pollutants associated with mobile sources, rather than on a specific (or critical) pollutant; CO emissions have a higher contribution from mobile sources than PM_{2.5} in the study site (98% vs 80%; AMVA, 2015); the limitations of the local EI do not allow to implement full chemistry simulations at the desired resolutions; the tracer simulations do not include chemical reactions, which is important for PM but not so much for CO, especially at the spatial and temporal scales of the study (the atmospheric lifetime of CO in the tropics is about a month; Staudt et al. 2001); and the absence of important CO sources from outside the boundaries (upwind) of the simulation domain. Additionally, CO is less affected than PM by wet deposition (Zhang and Batterman, 2010; Yoo et al., 2014), and has a very low deposition velocity (Castellanos et al., 2011). Dry and wet deposition are not considered in the simulations. The assumption that CO represents traffic emissions is common to several studies (e.g. Tuia et al., 2007; Saide et al., 2011).

The dispersion simulations cover a period of 18 days, between March 06 and 24, 2016 (starting and ending at 00 GMT). A severe air pollution episode occurred during this period: Between March 01 and 18, all stations reported air quality indexes for PM_{2.5} that were either unhealthy or unhealthy for sensitive groups and, therefore, local authorities declared an environmental emergency and imposed traffic restrictions, among other measures.

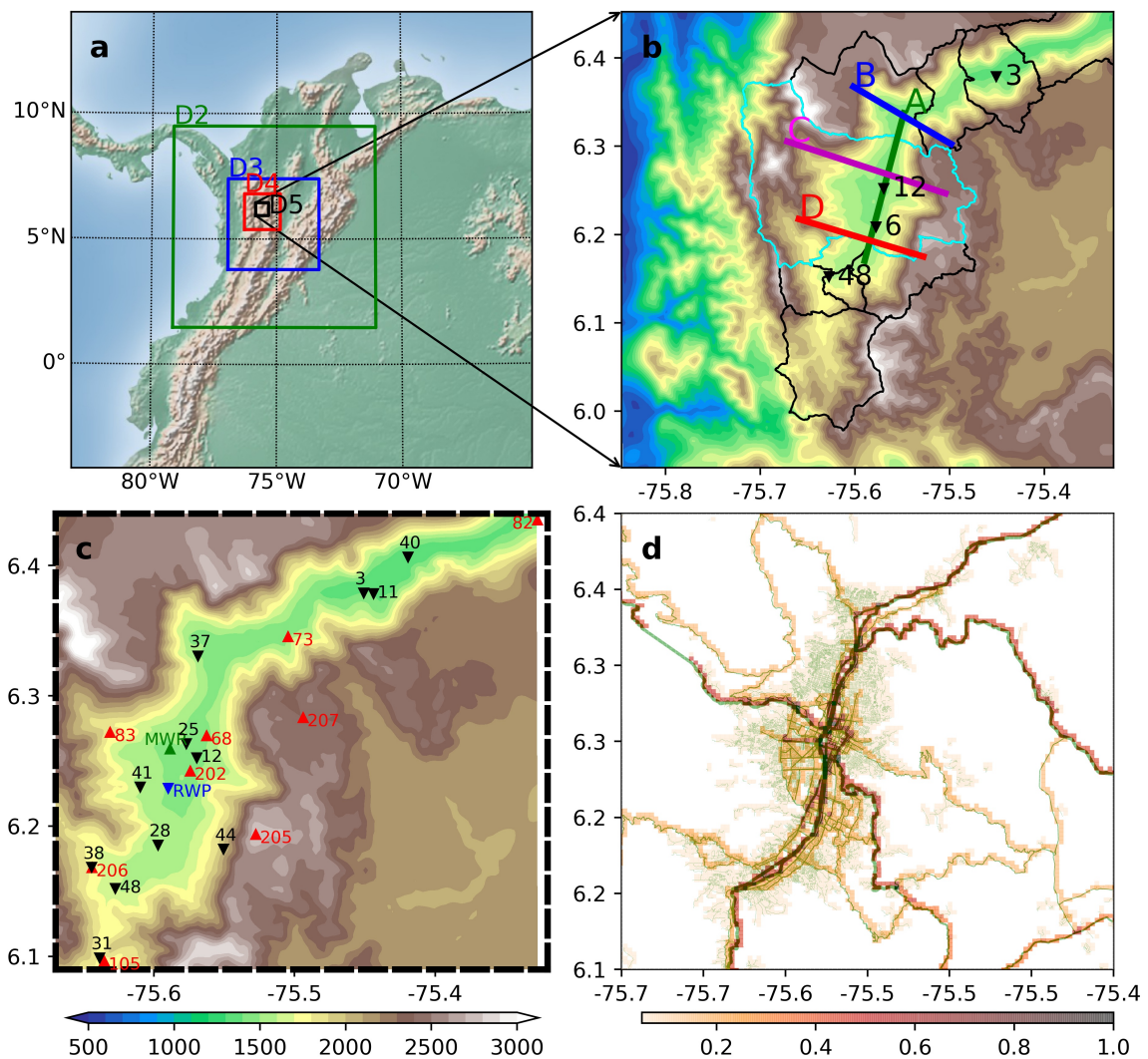


Figure 3.1: Top panels: (a) Domain configuration for the WRF simulations. (b) Enlarged version of D5 with the model topography shaded, the location/code of CO stations (black triangles), the studied transects and AMVA limits in black, with the main municipality (Medellin) in cyan. Panel (c) shows location/code of surface meteorological stations (red and black triangles), a microwave radiometer (green triangle, MWR) and a radar wind profiler (blue triangle, RWP). Colorbar in (c) represents terrain height in m for (b) and (c). Panel (d) shows a zoom of the road network (green lines with line-width representing road category), and the spatial distribution of adimensional CO emissions for each grid cell (colorbar): the emission at each grid cell is divided by the maximum emission.

3.3.1.1 WRF-Chem model setup

We implement the WRF-Chem version 3.9.1.1 using five one-way nested domains (in a telescoping grid arrangement) with a 3:1 grid ratio (Fig. 3.1a). Horizontal grid spacings range from 24.3 km in the outer domain (D1) to 300 m in the innermost domain (D5). The model top is 50 hPa with 71 full sigma vertical levels. Initial and boundary conditions are updated every 6 hours using the NCEP Climate Forecast System Version 2 (CFSv2) 6-hourly products (initialized four times per day; Saha et al., 2014). Four-dimensional data assimilation is implemented with weak spectral nudging (with zonal and meridional wavenumbers set to 3) but only applied on the outer domain and above the boundary layer for constraining temperature, winds, and specific humidity, which help preserve the CFSv2 synoptic scale behavior at the interior of the model (Castro et al., 2005). The construction of the topography for domains D1 through D4 is carried using the WRF readily available USGS (U.S. Geological Survey) global 30 arc-second dataset; for domain D5 (300 m grid size) we implement the hole-filled and 250 m resampled Shuttle Radar Topography Mission (SRTM) database (Jarvis et al., 2008). The original void-filled version of the SRTM (90 m grid size) presented no-data voids in the study area, whereas the 30 arc-second USGS database is too coarse to represent the complex topography of AMVA at the resolution of this domain. For land cover/use we implement the MODIS (Moderate Resolution Imaging Spectroradiometer) 20 category land dataset rather than the USGS database, due to a large underestimation of the urban area in the latter (Supplementary Fig. B1).

The model is configured to include a passive tracer representing CO in domain D5, covering the entire AMVA region (Fig. 3.1b). Emissions (section 3.3.1.3) are updated every hour in the lowest grid mass points, with a 300 m horizontal resolution. Further details of the WRF settings are provided in Table 3.1.

Three meteorological experiments (no Chem) with different PBL parameterization schemes were performed for verification of the model performance against surface temperature and wind observations. The selected schemes are the Mellor—Yamada—Janjic (MYJ; Janjic, 1994), the Mellor—Yamada—Nakanishi—Niino 2.5 (MYNN; Nakanishi and Niino, 2006) and the Shin—Hong (ShinHong; Shin and Hong, 2015). MYJ is a 1.5-order local closure PBL scheme, with improvements on the Mellor—Yamada (MY) scheme at relatively low computational expense (Cohen et al., 2015); the MYNN is a 1.5-order, local closure PBL scheme, with improvements to

Table 3.1: Additional details and physical parameterizations employed in the experiments.

<i>Domain and integration settings</i>					
Domain	D1	D2	D3	D4	D5
Horizontal grid size	24.3 km	8.1 km	2.7 km	900 m	300 m
Horizontal grid points	85x85	112x112	151x151	178x178	193x193
Time step	90 s	30 s	10 s	3.33 s	1.11 s
Vertical levels	71				
<i>Physical parameterizations</i>					
Surface layer	Revised MM5 M-O (Jiménez et al., 2012), except for MYJ PBL that requires the scheme by Janjic 1994.				
Land surface	Noah-MP model (Niu et al., 2011)				
Microphysics	Thompson (Thompson et al., 2008)				
PBL	MYNN (Nakanishi and Niino, 2006); MYJ (Janjic, 1994); ShinHong (Shin and Hong, 2015)				
Radiation	Shortwave: Dudhia (Dudhia, 1989); Longwave: RRTM (Mlawer et al., 1997)				
Cumulus	KF (Kain, 2004)		Turned off		

the MY scheme based on large-eddy simulations -LES- (Nakanishi and Niino, 2006). The ShinHong scheme is a non-local, grid-size dependent (scale-aware) scheme based on the Yonsei University scheme, with promising results at high resolutions (Shin and Hong, 2015, hereafter refer as ShinHong). The inclusion of the ShinHong scheme obeys to its ability to work at sub-kilometer resolutions falling in the so-called *gray-zone* or *terra incognita*, in which neither traditional PBL nor LES are expected to perform appropriately (Wyngaard, 2004). In spite of the difficulties of modeling at these resolutions, this refined modeling should not be dismissed as increasing grid resolution has many potential benefits, including a better representation of terrain and land cover (Zhou et al., 2014).

3.3.1.2 Lagrangian model

A Lagrangian Stochastic Particle Dispersion Model, developed at the Desert Research Institute (Mejia et al., 2019), was adapted to the WRF model configuration (D5 only). The movement of the particles (forward trajectories) is based on the Thomson 1987

assumption for the separation of the flow into a mean wind field and a turbulent velocity fluctuation (advection plus turbulent diffusion). A trajectory velocity for each particle is obtained by the sum of the grid point mean Eulerian velocity and a velocity perturbation at the sub-grid scale. The mean wind fields at every time step are derived from WRF, using a linear interpolation between the 15-min time increments of the model output (described in section 3.3.1.1). The sub-grid scale turbulent fluctuations are determined using the subgrid-scale WRF-TKE (from the PBL parameterization) and a random number generator with zero mean and variance equal to the time step dt (Thomson, 1987).

Particles are released using the same time-space variable emissions implemented in WRF-Chem (described below in subsection 3.3.1.3). The emission fields are linearly interpolated every dt (30 s) from the hourly emissions. Particles are released in the center of each emitting grid cell, at different emission rates. An injection function was developed using a histogram of 12 equally spaced classes, following Mejia et al., 2019. For instance, at every dt , the injection function releases n particles for an emitting grid point falling in the first class of the histogram; $2 \times n$ particles for an emitting grid point falling in the second class, and so on, until releasing $12 \times n$ particles for those grid points in the 12th class. n was fixed as 10 through the integration period. This upper bound of the emissions particle injection function is somehow arbitrary, but constitutes a tradeoff between the computational burden of large number of particles and the statistical robustness of downwind concentration estimates. In order to obtain concentrations in the same units of the WRF-Chem output, the number of particles at any domain grid cell is related to the defined classes of the injection function (a method analog to that used for determining the injection rate).

3.3.1.3 Emission disaggregation

The local EI in the AMVA region (AMVA, 2017a) provides total annual emissions for criteria pollutants in the entire region. In order to distribute the available emissions in space and time (for the domain and simulation period), we implemented a simple, albeit realistic, method based on top-down approaches that use available traffic information (road network, road category and traffic counts). In this study we did not use population density maps, a typical component of top-down approaches (e.g. Tuia et al., 2007; Saide et al., 2009), as its fundamental assumption of a linear relationship between population density and vehicles/emissions can be misleading, as areas with high population density do not necessarily present high vehicle possessions (e.g. Tuia

et al., 2007).

The road network and road category information was derived from the OpenStreetMap (OSM; Haklay and Weber 2008) database. The official database was not used because it does not include road categories. A comparison between the two databases resulted in similar spatial coverages and road distribution (not shown). Four types of roads from the OSM database are considered for the analysis: trunk, primary, secondary and residential. These categories include the main roads and residential areas. Previous studies (in Chile) found that adding additional information (i.e. to the principal road network) did not improve significantly the spatial distribution of emissions (Tuia et al., 2007; Saide et al., 2009). The available traffic count information provides the number of vehicles per hour for every weekday (Supplementary Fig. B2). This information represents mean values in the urban area for a typical week, derived from closed-circuit television cameras operated by the local mobility authority.

For the temporal and spatial distribution of emissions, the total annual CO emissions from mobile sources ($166,939 \text{ ton yr}^{-1}$; AMVA, 2017a) are converted into ton per week. Then, they are distributed in time as hourly emissions (kg per hour) for every weekday (Monday through Sunday) based on the normalized number of vehicles per hour for every day of the week, as follows:

$$E_{ij} = TE \frac{TC_{ij}}{\sum_{i=1}^7 \sum_{j=1}^{24} TC_{ij}} \quad (3.1)$$

where E_{ij} is the emission for the weekday i and hour j . TE is the total weekly emission and TC_{ij} is the number of vehicles for weekday i and hour j .

The spatial distribution is based on the road types contained in each domain grid cell (Fig. 3.1d). We assumed different emission factors for each road type (f_c): $f_c = 8$ for trunk roads, $f_c = 6$ for primary roads, $f_c = 3$ for secondary roads, and $f_c = 1$ for residential roads. A more appropriate way for the definition of these factors is using traffic information for each road type (e.g. Saide et al., 2009; Gómez et al., 2018), but this information was unavailable at the moment of the study. The emission for each grid is then determined as follows:

$$E_{kij} = E_{ij} \sum_{c=1}^4 \frac{w_c}{NP_c} H_c \quad (3.2)$$

$$w_c = \frac{f_c NP_c}{\sum_{c=1}^4 f_c NP_c} \quad (3.3)$$

where E_{kij} represents the emission for grid cell k , weekday i , and hour j . w_c is the weight for category c , f_c is the emission factor for category c , NP_c is the number of grid points for category c , and H_c is the Heaviside step function, with $H_c = 1$ if the grid cell k contains a road of category c , and $H_c = 0$ otherwise. The resulting emission contribution for each road category is 33% for trunk, 17% for primary, 32% for secondary and 18% for residential. The emissions are converted to moles per square kilometer and hour, which is the units on the emissions files for gaseous species in WRF-Chem.

Despite its simplicity, this approach provides a parsimonious description of pollutants emissions in the AMVA region that is adequate for our goal of studying pollutants dynamics and transport processes, rather than air quality forecasting. The implemented modeling framework can be used for other emission inventories. There is a need in the study area for a more accurate EI, based on the more complete bottom-up approach. This will be explored in future studies.

Additionally, in order to assess whether some areas have a relatively higher concentration due to either higher emissions or as a result of transport processes, we use a concentrations to emissions ratio, determined at every grid cell for a given time as follows:

$$C/E = \frac{C_k}{\varepsilon_k} \quad (3.4)$$

where C_k is the concentration in grid cell k and ε_k the emission for the same grid cell, converted to ppmv, as follows:

$$\varepsilon_k = 10^6 \frac{E_k M_{dry\ air}}{\rho_{air} \Delta z} \quad (3.5)$$

where E_k are emissions in $\text{mol m}^{-2} \text{hr}^{-1}$, $M_{dry\ air}$ is the molar mass of dry air ($0.02897 \text{ kg mol}^{-1}$), ρ_{air} is air density in kg m^{-3} and Δz is the grid cell height in m.

This ratio is intended as an indicator of average dynamics, with the aim of highlighting areas in which exchanges tend to increase or decrease concentrations. Large ratio values indicate that local emissions do not completely explain local concentrations, implying that there is a transport of polluted air to the specific grid cell, whereas smaller values indicate that concentrations could be larger owing to the local

emissions, but are reduced due to transport of less polluted air.

3.3.2 Observations

For the evaluation of the model against observations we used the meteorological and air quality networks in the AMVA region, managed by SIATA (<https://siata.gov.co>). For the analysis of surface meteorological variables, in addition to the meteorological stations (MET network; red triangles in Fig. 3.1c), we include the air quality stations (AQ network; black triangles in Fig. 3.1c) that provide observed surface temperature, wind speed and wind direction. Although the AQ stations are not intended for the measurement of surface winds, these stations offer a unique opportunity in areas where no other observations are available. However, we removed five AQ stations (with codes 12, 25, 28, 31 and 41) from the wind analysis, based on an in-situ revision of their location and nearby obstacles.

Location of MET stations in urban areas pose great challenges for satisfying World Meteorological Organization (WMO) requirements (e.g. Oke, 2007). For instance, the location of stations on top of buildings may not be representative of the general flow (WMO, 2014). No special adjustments were implemented to consider the effect of urban roughness on the wind field near the sites. All stations included in the analysis satisfy the restriction of maximum 15% of no-data voids in the variables of interest. The analysis of wind direction includes all valid measurements, as the application of the usual procedure of filtering out observations with wind speeds lower than 0.5 m/s did not greatly change the results, while it reduces the available information significantly. The variables analyzed from the MET network are resampled to the coarser 1-hour frequency of the WRF output and the AQ network.

A radar wind profiler (RWP; blue triangle in Fig. 3.1c) and a microwave radiometer (MWR; green triangle in Fig. 3.1c) allow the analysis of upper-air wind and temperature, respectively. The available RWP (RAPTOR VAD-BL - DeTect, Inc.) data have a 1-hour temporal resolution and a ~ 60 m vertical resolution in the high-resolution mode, that can provide measurements from 77 m to about 3,500 m above terrain (57 vertical levels). The MWR (MP-3000A - Radiometrics Corporation) has a temporal resolution of 2 minutes and variable vertical resolution that increases with height: 50 m from the surface to 500 m, 100 m from 500 to 2000 m, and 250 m from 2 to 10 km, having 58 vertical levels. The MWR has been reported to have a good agreement with radiosonde data for potential temperature, especially below

1km (Roldán-Henao et al., 2020). The MWR temporal resolution is resampled to the hourly frequency of the other observations.

Estimations of boundary layer height, with a temporal resolution of 5 minutes, were obtained from Herrera-Mejía and Hoyos, 2019. Their estimates are based on the bulk Richardson number (Rib), which is determined using temperature and wind profiles from a multi-sensor approach, combining the MWR and the RWP sensors. Their analysis indicate that the estimations with the Rib are more robust than other methods they applied. According to Collaud Coen et al., 2014, which also used the Rib method and a MWR to determine PBL height, surface temperature has a large impact in PBL estimations. Collaud Coen et al. calculated the uncertainty in PBL height estimations by varying surface temperature by $\pm 0.5^\circ$, and were found to be around ± 50 -100 m for maximum PBL heights, but larger values (500 m) resulted before sunset. An exploratory analysis using the same variation in surface temperature (the accuracy of the MWR is 0.5 K) suggests that similar values are valid for AMVA. We refer the reader to Herrera-Mejía and Hoyos, 2019 for further information on the used PBL height data.

3.3.3 Model performance evaluation

We implemented standard statistics for error metrics to evaluate the meteorological model performance by comparing model estimates to observed hourly values, including the mean bias error (MBE), mean absolute error (MAE), and the root-mean-square error (RMSE), calculated as follows:

$$MBE = \frac{1}{N} \sum_{i=1}^N (F_i - O_i) \quad (3.6)$$

$$MAE = \frac{1}{N} \sum_{i=1}^N |F_i - O_i| \quad (3.7)$$

$$RMSE = \sqrt{\frac{1}{N} \sum_{i=1}^N (F_i - O_i)^2} \quad (3.8)$$

with N number of prediction-observation ($F - O$) pairs.

Given the circular nature of wind direction, we used the modified wind direction proposed by Lee and Fernando (2004) for the computation of wind direction statistical measures. The “modified wind direction” is determined either adding or subtracting

360° from the prediction (F), in order to minimize the absolute difference between the predicted (F) and observed (O) wind direction.

Model performance benchmarks that are frequently used in air quality modeling (e.g. Emery et al., 2001; Tesche et al., 2002; Kemball-Cook et al., 2005) are included as a reference for the model performance. These benchmarks are developed to assess the model results relative to the range of other model applications, rather than using them as an accepting or rejecting criteria (Tesche et al., 2002). One important consideration is that these benchmarks are based on applications in the United States (U.S.), and it is known that model performance of wind speed and direction is highly variable among regions with different terrain conditions. Although these benchmarks are based on applications with the MM5 model, they have been applied to WRF simulations in different regions (e.g. Zhang et al. 2014 in the U.S.; Borge et al. 2008 in Spain; Wang et al. 2010 in China; Franco et al. 2019 in Brazil).

The proposed benchmarks in Tesche et al. (2002) and Emery et al. (2001) are: for temperature MBE within ± 0.5 K and MAE ≤ 2 K; for wind speed MBE within ± 0.5 m/s and RMSE ≤ 2 m/s; for wind direction MBE within ± 10 and MAE $\leq 30^\circ$. Additionally, as these benchmarks are derived from applications on locations with mainly flat terrain, that hardly represent the topographic conditions of the study area, we include and focus on benchmarks that were specifically developed for complex terrain (Kemball-Cook et al., 2005): for temperature MBE within ± 2 K and MAE ≤ 3.5 K; for wind speed RMSE ± 2.5 m/s; for wind direction MAE $\leq 55^\circ$.

3.4 Results

3.4.1 Model Evaluation

3.4.1.1 Surface wind and temperature

In this section we present the summary of the model performance metrics for all available stations, including a comparison between the three PBL schemes implemented and three spatial resolutions (i.e., using results for domains D3, D4, and D5). The model performance of 2-m temperature (T2), 10-m wind speed (WS) and 10-m wind direction (WD) for individual stations is presented in Figure 3.2, the network-averaged values are given in Table 3.2, and the diurnal cycle and day-to-day variability of T2 and WS are shown in Figure 3.3.

Table 3.2: Model performance of 2-m temperature (T2), 10-m wind speed (WS) and 10-m wind direction (WD). Values for each domain are averaged over all available stations and the three PBLs, and values for each PBL are averaged over all available stations and the three domains.

	T2 MBE (°C)	WS RMSE (m/s)	WD MAE (°)
ShinHong	-0.93	2.32	47
MYNN	-1.10	2.27	47
MYJ	-1.58	2.51	49
D5	-0.86	2.61	46
D4	-1.14	2.44	48
D3	-1.60	2.06	49

The model performance for the different configurations studied (domains and PBL schemes) is within recommendations for T2 (MBE ≤ 2 °C) and WD (MAE ≤ 55 °), with network-averaged T2 MBE values from -1.60 °C to -0.86 °C, and WD MAE values from 46° to 49° (Table 2). For WS, RMSE values range from within to slightly outside the recommended benchmark (RMSE ≤ 2.5 m/s), with RMSE values from 2.06 to 2.61 m/s (Table 3.2).

Overall, the ShinHong and MYNN PBL schemes resulted in similar performances for surface temperature and wind, but with ShinHong being slightly better for T2, while MYNN for WS. The MYJ PBL scheme presented larger error metrics for the three variables (Table 3.2).

Increasing grid resolution resulted in decreasing error metrics for T2 and WD (MBE and MAE, respectively), but it produced increasing RMSE values for WS (Table 3.2), with mean RMSE values increasing from 2.1 m/s at 2.7 km resolution to 2.6 m/s at 300 m (Table 3.2). The largest differences in WS performance between the three grid sizes are found in stations with worse performances (e.g. see stations 37, 68, 202 in Fig. 3.2 and Supplementary Fig. B3).

Modeled T2 is adequately captured in most of the study area (Fig. 3.2a), with at least one model configuration resulting in MBE values within recommendations for all stations. Surface wind performance is better for stations located at higher altitudes to the east and for stations to the northeast, after the valley axis shifts from S-N to SW-NE (Fig. 3.1), while it is worse towards the center and south. For example,

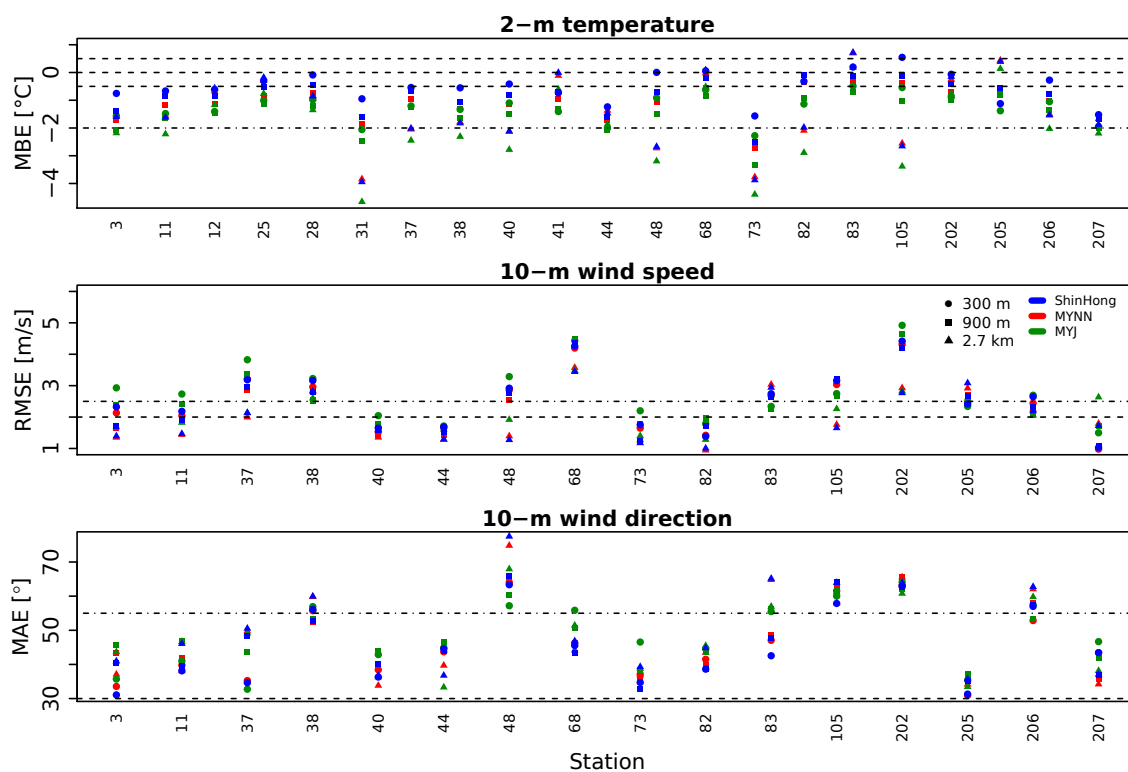


Figure 3.2: Model performance of 2-m temperature or T2 (top), 10-m wind speed or WS (middle), and 10-m wind direction or WD (bottom) for the three PBL schemes implemented and domains D5, D4 and D3. Recommended benchmarks are represented as dashed (dot-dash) lines for flat (complex) terrain.

results at stations 40, 44, 73 and 207 (east and northeast) performed well for WS and WD (Fig. 3.2b,c), while results at stations 48, 105 and 202 (center and south) exhibit larger errors (Fig. 3.2b,c). At the highest spatial resolution (D5), all PBL schemes led to network-averaged MBE values for T2 within the benchmark of $\pm 2^\circ\text{C}$, however results from the MYJ scheme exceeded this benchmark in some individual stations (Fig. 3.2a). Likewise, for WS (Fig. 3.2b) and WD (Fig. 3.2c), error metrics fall outside benchmarks at some individual stations. However, in all cases, there are more stations in which errors are lower than recommended benchmarks.

In general, the model underestimates T2 (there are cold biases), with larger biases in periods with higher temperatures (e.g. between March 16 and 17, Fig. 3.3c), but a relatively constant cold bias throughout the day (Fig. 3.3a). An exception occurs from 15 to 18 LST, when the model results approach observations. This reduced bias seems to be related to the representation of observed rainfall in the model (Supplementary

Fig. B4), which may affect the timing of the maximum temperature. Importantly, the model adequately captures the diurnal (Fig. 3.3a) and day-to-day (Fig. 3.3c) variability of T2, although differences in performance from one station to other can be relatively large (Supplementary Fig. B5).

The model produces a realistic representation of the diurnal variability of WS, with maximum values in the afternoon and reduced values throughout the night and early morning (Fig. 3.3b). However, the model overestimates WS, especially in the afternoon, and delays the occurrence of a maximum WS (around 18 LST compared to 15-16 LST in the observations; Fig. 3.3b,d). Model results reproduce periods of smaller (March 11–13) and larger (March 16–19) day-to-day variability, with a local minimum around March 16–18 (Fig. 3.3d). Nevertheless, as compared to observations, this day-to-day variability is wider in the model, especially between March 7 and 11. For WS, the difference in performance between the best and worst performing stations is considerably large (Supplementary Fig. B5). The worse performance of MYJ relative to the other PBL schemes is more pronounced during the afternoon, from 12 to 17 LST (Fig. 3.3b). The improved performance of WS for domains with coarser grid sizes (D4 and D3) is not prevalent throughout the entire simulation period, and mainly occurs between March 10 and 14 regarding biases (Fig. 3.3d).

The comparison between ground-based observations and model results (Figs. 3.2 and 3.3) indicates that the model has the ability to reproduce important features of the atmospheric dynamics in the complex terrain of AMVA. Model limitations are consistent with the state of the art (this will be further discussed in Section 3.5).

3.4.1.2 PBL height

Figure 3.4 shows the mean diurnal cycle of observed and modeled boundary layer height for the three implemented PBL schemes. In general, the three schemes overestimate maximum PBL height from 12–18 LST. For that specific period, MYJ presents the lowest PBL heights and is closer to observations, while MYNN results in the highest PBL. In contrast, during the night and in the early morning (18–06 LST), MYNN is closer to observations, but with higher values, while MYJ and ShinHong exhibit similar and shallower PBL heights. Observed PBL height peaks around 12–13 LST, while the three schemes show the highest values around 2 hours later. The large overestimation of maximum PBL height seems to be related to the representation of rainfall in the model, with maximum PBL height in the model closer to that observed during dry days (orange dots in Fig. 3.4). These patterns resulting from each PBL

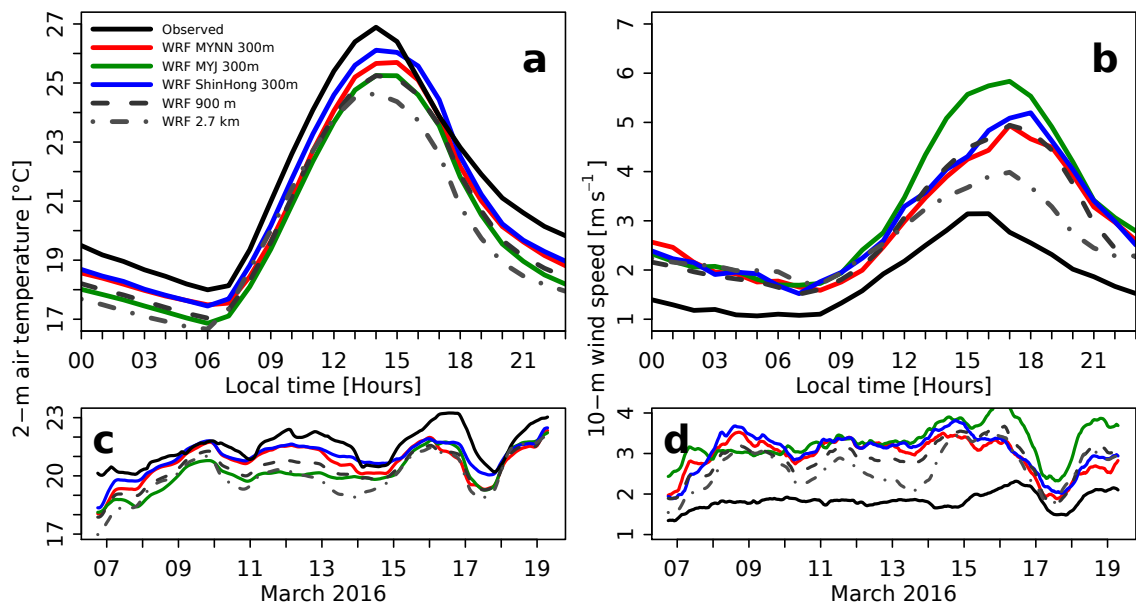


Figure 3.3: Diurnal cycles of (a) T2, and (b) WS. Time series of 24-hour moving-averages for (c) T2, and (d) WS. All values are network-averaged, see supplementary Fig. B5 for results of the best and worst performing stations. Wind speed analysis (panels b and d) do not consider stations that exceeded recommendations for all model configurations (i.e., stations 202, 68, 38 are not included; Fig. 3.2b). Results from D4 and D3 are averaged for the 3 PBLs to facilitate visualization (dashed and dot-dash lines, respectively).

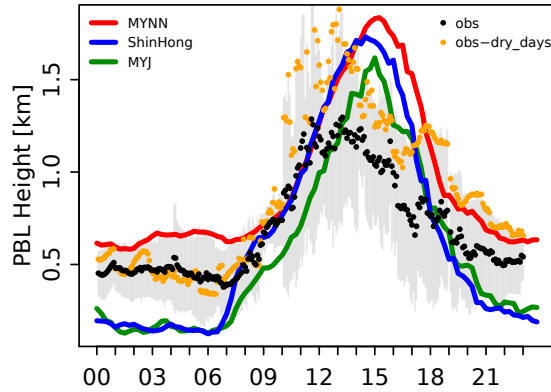


Figure 3.4: Diurnal cycles of observed and modeled PBL height. Shaded area indicates ± 0.5 standard deviation of the observations. Analysis for the entire simulation period, except for the observations during dry days, orange dots, averaged over March 11, 16, 18 and 19 when no rainfall occurred: see Fig. 3.9d.

scheme occur for the entire simulation period (supplementary Fig. B6), and the three schemes resulted in similar performance in terms of errors, with MAEs of 377 m for ShinHong, 383 m for MYNN and 350 m for MYJ, calculated with hourly values for the entire period of analysis.

3.4.1.3 Upper-air wind and temperature

The analysis of upper-air wind is focused at 1.3 km above terrain, where the flow is dominated by the large-scale forcing of the easterly trade winds, and at 0.2 km above terrain, which is within the boundary layer and away from the built environment. Potential temperature (θ) is analyzed at heights of 50 m and 800 m above terrain (50-m and 800-m θ). These two levels provide an estimate of vertical gradient $\partial\theta/\partial z$ within the valley atmosphere, which is determinant for the stability conditions and is an important modulator of the boundary layer structure (Herrera-Mejía and Hoyos, 2019). Model results at the desired vertical levels are obtained by applying linear interpolation between model levels closest to the desired vertical level, using the closest grid point to the MWR and RWP. Table B1 presents the performance of the three PBL schemes.

For potential temperature, the MAE and correlation coefficient (r) for each PBL are similar at both heights, and there is a general cold bias (Table B1, Fig. 3.5). The ShingHong PBL scheme showed the best performance, while MYJ exhibited the worst; however, small error differences indicate relatively low sensitivity to the PBL

Table 3.3: Upper-air mean absolute error (MAE) and correlation coefficient (r) for potential temperature (θ) and the zonal and meridional (U,V) wind components using observations from a radar wind profiler (RWP) and a microwave radiometer (MWR). The analysis is performed on 24-h moving averages of results from domain D5 (0.3 km resolution) using the closest grid point to the instruments. See supplementary table B1 for results with hourly data.

	0.2 km				1.3 km				50 m		800 m	
	U		V		U		V		θ		θ	
	MAE	r	MAE	r	MAE	r	MAE	r	MAE	r	MAE	r
	(m/s)		(m/s)		(m/s)		(m/s)		(K)		(K)	
ShinHong	0.7	0.6	2.3	0.2	0.9	0.5	0.8	0.7	1.0	0.8	1.0	0.9
MYNN	0.8	0.6	2.4	0.4	0.8	0.6	0.7	0.7	1.2	0.7	1.2	0.8
MYJ	0.6	0.6	1.6	0.5	1.1	0.6	0.6	0.8	1.7	0.8	1.6	0.8

schemes. There is also a low sensitivity to PBL scheme for the zonal wind component at 200 m above terrain, with the three PBL schemes resulting in comparable MAE and r values. However, for the V component, the performance is worse than that of U, with the MYJ resulting in the smallest MAE and largest r. At 1.3 km above terrain, MYJ performed best for V and worst for U, while MYNN performed best for U, and similar to MYJ for V. ShinHong performed worse for both components, although differences in performance are relatively small.

Based on the previous analysis (especially on the results for surface wind, section 3.4.1.1), the MYNN PBL scheme was selected for the dispersion experiment using both WRF-Chem (configuration described in Table 3.1) and Lagrangian models. Using the MYNN implies that there are some overestimations of the maximum PBL heights, but a better representation during the night and early morning.

Figures 3.5 and 3.6 depict the time series of upper-air potential temperature and wind components. We include data from the ERA5 reanalysis (Copernicus Climate Change Service (CS3), 2017) in order to have an additional reference for the evaluation of the model. The model presents a cold bias in 50-m θ , especially during the day when maximum temperatures are underestimated (Fig. 3.5a). In contrast, the 800-m θ cold bias is mainly associated with a more pronounced nocturnal cooling in the model (Fig. 3.5b). Importantly, the model is able to capture the diurnal and day-to-day variability of potential temperature at 50 m and 800 m above terrain. Near the surface, ERA5 has a day-to-day performance similar to that of the model (Fig. 3.5a),

but presents a lower diurnal variability with evident limitations in capturing both maximum and minimum temperatures (ERA5 data varies within a narrower range). At 800 m above terrain, ERA5 shows an even smaller variability and a generally larger magnitude. These ERA5 limitations are likely related to its relatively coarse spatial resolution; however, it is interesting that Fig. 3.5 does not show excessively large differences between ERA5, high-resolution WRF, and radiometer measurements.

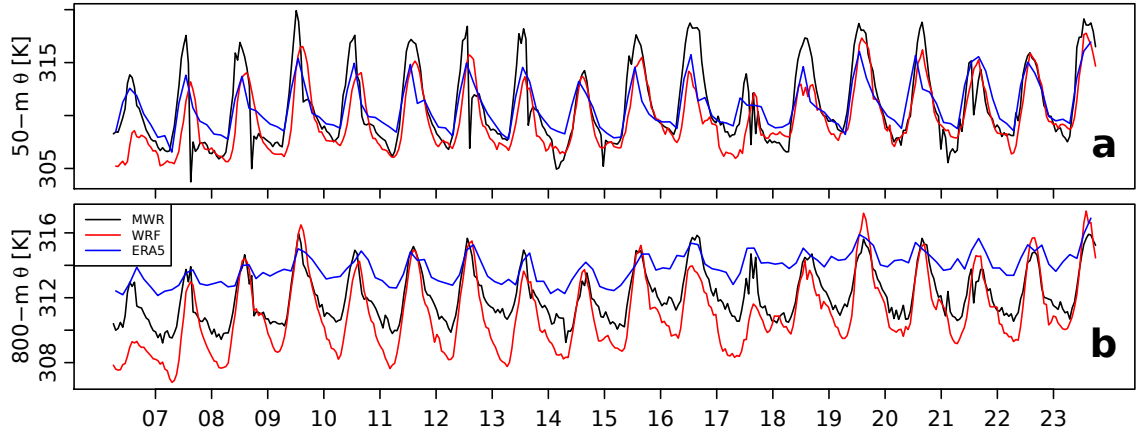


Figure 3.5: Time series of potential temperature at 50 m (a) and 800 m (b) above terrain, from the microwave radiometer –MWR– (black) and the corresponding (closest) pixel in the WRF-Chem model configuration (red) and ERA5 (blue).

For upper-air wind, the model presents a good representation of U at 200 m, with a MAE of 0.8 m/s, and slightly underestimates U at 1.3 km (Table B1). The model is able to capture the day-to-day variability for U at both heights, resulting in the same error metrics (MYNN, Table B1). However, for the V component the performance is better at 1.3 km above terrain. At 200 m above terrain, the model presents overestimation in the maximum U (Fig. 3.6c), and generally overestimates the V component, especially from March 08-17, resulting in a larger variability as compared to observations and ERA5 (Fig. 3.6d). After March 17, the representation of V improves, exhibiting reduced biases. Despite exhibiting large overestimations in the V component at 200 m, modeled wind direction at this height agrees well with observations (supplementary figure B7). Model results for day-to-day variability of U and V compare well with both RWP and ERA5 at 1.3km (Fig. 3.6a,b). At 200 m, ERA5 presents a reduced diurnal variability as compared to the model and the RWP, and almost no day-to-day variability for the V component (Fig. 3.6c,d).

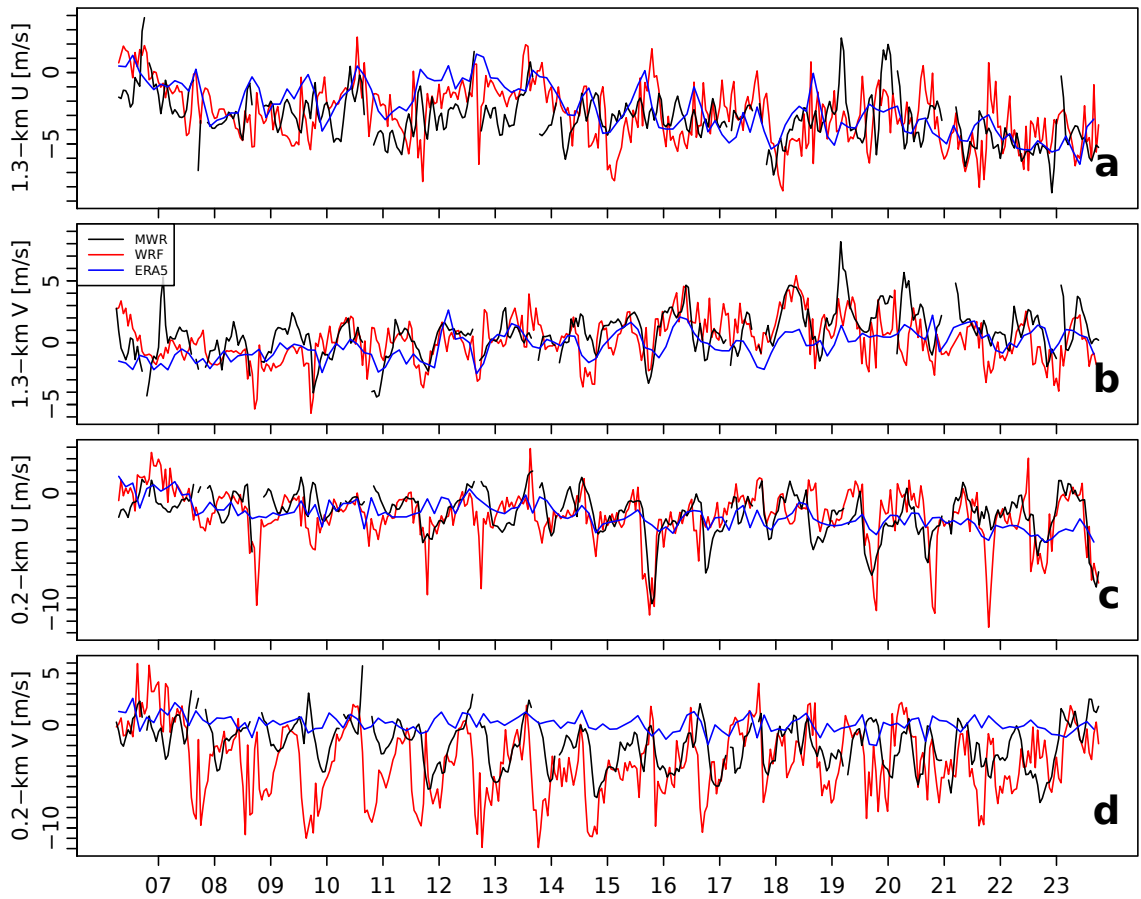


Figure 3.6: As Fig. 3.5 but for zonal (a) and meridional (b) wind components at 1.3 km (a, b) and 200 m (c, d) above terrain. Black lines represent the Radar Wind Profiler (RWP).

In general, our results show that, relative to remote-sensing observations and the ERA5 reanalysis, the model is able to capture adequately the diurnal and day-to-day variability of upper-air potential temperature and wind components.

3.4.2 Carbon monoxide tracer

Below we present a comparison of the CO passive tracer resulting from the two dispersion models against surface observations. The diurnal and day-to-day variability of modeled and observed CO are presented in Figures 3.7 and 3.8, respectively.

There is a relatively large underestimation of CO in both dispersion models as compared to observations, which present larger temporal and spatial variability (Figure

3.7, left panels). The differences in magnitude of modeled CO tracer and observations are expected due to idealizations present in both the official EI, and the top-down method used for the spatial and temporal distribution of emissions. However, despite a larger spatial variability in observations, both models are able to capture higher CO concentrations in stations around the center (stations 6 and 12) than in those located to the south (station 48) and north (station 3). The spatial differences are more pronounced throughout the day in the observations, and mostly at night and in the morning in the models.

We introduced standardized concentrations, subtracting the mean and dividing by the standard deviation, in order to focus the performance evaluation of the dispersion models on temporal variability (Fig. 3.7, right panels). Both models are able to capture important patterns of the diurnal variability: maximum concentrations around 7–8 LST, a continuous decrease afterwards, and increases of CO concentrations again around 18 LST. In the early morning, around 01–05 LST, the models present an earlier increase in concentrations compared to observations (Fig. 3.7, right panels). The diurnal cycle in both models is very similar, with the exception of results at station 48, where the Lagrangian model presents a maximum at night (Fig. 3.7h). Overall, the Lagrangian model produces higher concentrations than WRF-Chem, especially at night (Fig. 3.7, left panels).

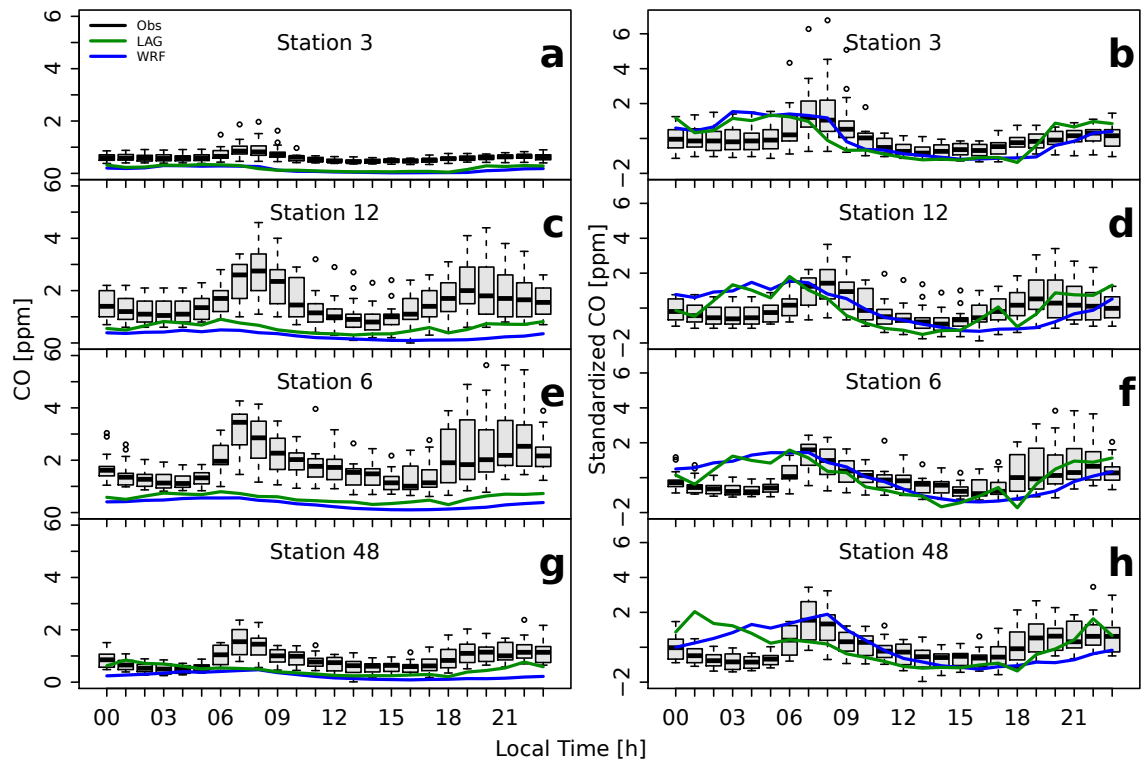


Figure 3.7: Diurnal cycles of simulated CO concentration at the first full model level and observed CO concentration at the available air quality stations. Left (right) panels show actual (standardized, i.e. centered and scaled) concentrations.

Modeled CO has a smaller day-to-day variability relative to observations for most of the simulation period, especially between March 8 and 16 where there is barely any variability (Fig. 3.8). For the final period of the simulation, the models perform better, especially from March 17 to 19 (Fig. 3.8 and Supplementary Fig. B8). Both models present a similar day-to-day variability for the simulation period, especially in the center of the valley (Fig. 3.8b,c), with differences for short periods in the north and south (Fig. 3.8a,d).

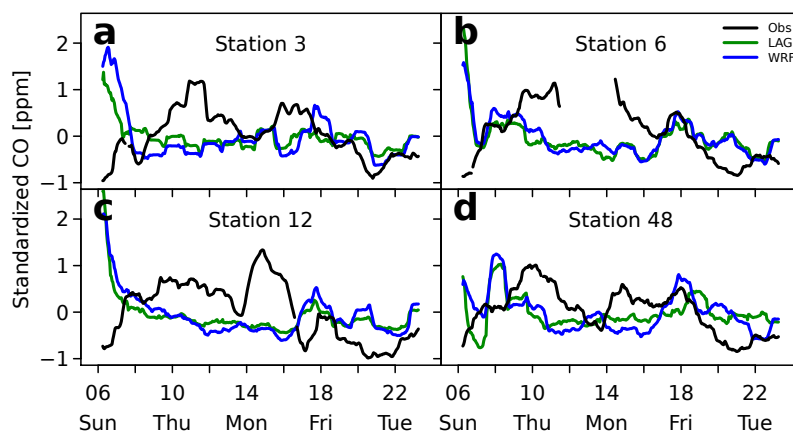


Figure 3.8: Standardized 24-hour moving averages of CO for the simulation period. A similar figure with hourly time series is presented in supplementary figure B8.

In order to understand the model (WRF-Chem) limitations in representing CO dispersion, we include some variables relevant for dispersion in the analysis (Fig. 3.9d). The differences in the day-to-day variability of the observations and the model seem to be related to a poor representation of rainfall in the model (Fig. 3.9d), and thus, on the net effect of diurnal rainfall on PBL height and stability in AMVA, which leads to increases in pollutant concentrations (Roldán-Henao et al., 2020). For most of the simulation the model was not able to represent rainfall adequately, with almost no modeled rainfall from March 8 to 16, when significant amounts of rainfall were observed, especially during the afternoon. Rainfall in the mountainous region of Colombia is negatively correlated with PBL height in AMVA, especially when rainfall predominantly occurs during the daytime (Herrera-Mejía and Hoyos, 2019). Days with rainfall occurring in the early afternoon present negative anomalies in daytime PBL height between 600 and 800 m in comparison to dry weather (Roldán-Henao et al., 2020).

On the contrary, for March 17, when both dispersion models had a relatively good representations of CO (Fig. 3.8), modeled rainfall was in agreement with observations (Fig. 3.9d), as well as PBL heights being closer to observations (Fig. 3.9b). The increase of CO concentrations from March 17 to 19 is consistent with a reduction in PBL height (Fig. 3.9b), and an increase in the potential temperature gradient between the surface and the top of the valley (Fig. 3.9c), resulting in increased stability and reduced vertical mixing. During this period, PBL heights were below average, staying below the mean height of the valley mountains ($\sim 1,000$ m) for relatively long periods of time, which is consistent with states of restricted dispersion (Leukauf et al., 2015;

Herrera-Mejía and Hoyos, 2019).

The other periods with observed increases in concentrations (March 9, 10 and 15), are associated with observed rainfall in the afternoon (Fig. 3.9d). Rain events in the afternoon can be associated with decreased PBL height and increased stability, but as these rainfall events were not captured in the model, there are no increases in modeled concentration for those two periods. One exemption is the event in the afternoon of March 13, when CO concentrations remained low.

The rain event in the early morning of March 14 was properly captured (Fig. 3.9d), but not that of the previous afternoon. This event only affected modeled PBL height in the morning, but not in the afternoon. The effect of rainfall on pollutant concentrations in the city depends on the timing of occurrence (Roldán-Henao et al., 2020), due to competing direct (wet deposition) and indirect effects (reductions in PBL height and increases in stability).

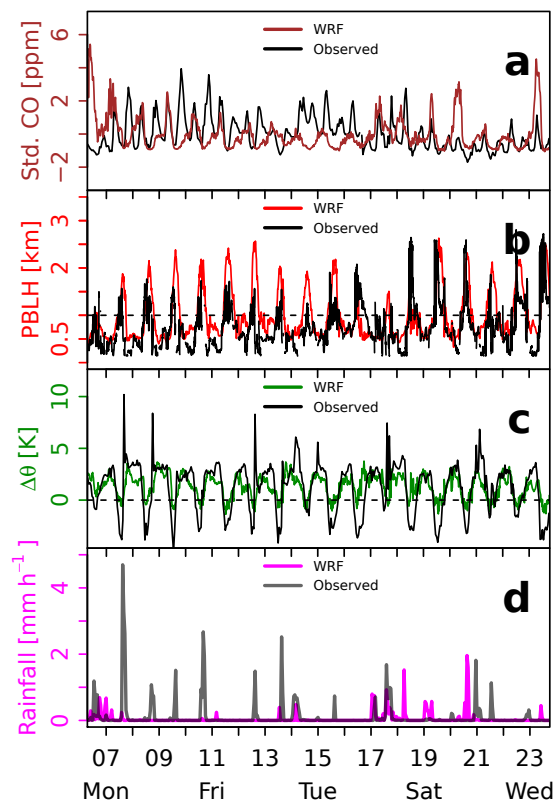


Figure 3.9: Time series of standardized CO (a), PBL height (b), potential temperature difference between 50 and 800 m above terrain (c), and hourly rainfall (d). Dashed line in panel b represents the mean valley depth.

3.4.3 Spatial Distribution of the Tracer

To analyze the spatial and temporal distribution of CO in AMVA, we present horizontal and vertical cross-sections of tracer concentration and wind vectors. Figure 3.10 shows a comparison of the simulation-averaged CO and C/E ratio resulting from both dispersion models, and Figures 3.11 and 3.12 present the diurnal evolution of the horizontal and vertical distribution of CO.

Although there are differences in concentration (already described in sect. 3.4.2), the horizontal distribution in both models is in agreement, with high concentrations along the valley axis (parallel to the river) and especially towards the south of the main municipality and east of the river (6.15-6.20N, 75.55-75.60W, Fig. 3.10a,b). We will refer to this specific area as south and southeast from here on, taking as a reference the main municipality and referring to areas inside the valley. High concentration of pollutants along the river is consistent with the location of high category roads in this area.

The largest ratio values are found to the south (especially southeast) in both models (Fig. 3.10c,d), indicating that the relatively higher concentrations in these areas occur not only due to the emissions, but also due to transport processes that lead to higher concentrations. Although both models agree on the spatial distribution, the Lagrangian model presents more areas with larger ratio values, indicating that exchange processes are less efficient in that model (Fig. 3.10d).

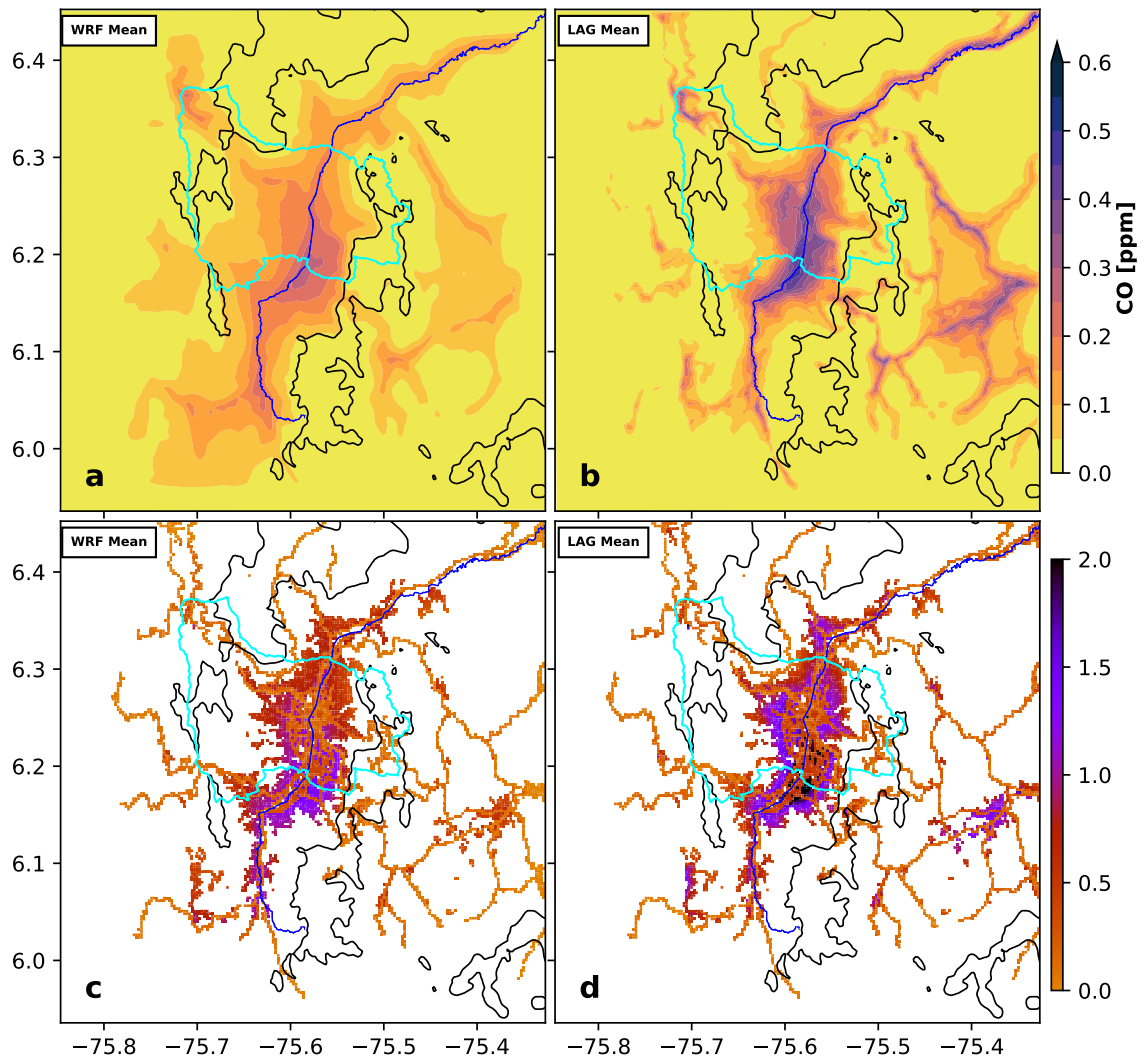


Figure 3.10: Horizontal distribution of CO tracer concentrations (a, b) and simulated concentrations to emissions (C/E) ratio (c, d), both averaged over the entire simulation period. Blue line: Aburrá River. Black lines: 2,500 m terrain height contour. Cyan lines: main municipality limits.

Larger CO concentrations during the morning (Fig. 3.11, 06 LST) are consistent with increased atmospheric stability and the decoupling of the atmosphere inside the valley from the large-scale flow above. The main transport of pollutants is associated with the along-valley wind from the north (Fig. 3.11, 06 LST). This along-valley flow remains from the north throughout the day (it does not reverse as in a typical valley circulation), which contributes to explain the relatively larger concentrations to the south of the valley (Fig. 3.11, Supplementary Fig. B7). The reason why the along-

valley flow does not reverse at night is still unknown, but it may be related to the anthropogenic heat of the urban area, which can affect valley flows (e.g. Giovannini et al., 2014; Henao et al., 2020a). At noon, CO is distributed by means of the northerly flow and with the development of upslope flows (Fig. 3.11, 12 LST). Later in the afternoon, with the growth of the convective boundary layer (CBL), the valley atmosphere couples with the large-scale easterly flow, with downslope easterly winds east of the river and a stronger northerly flow to the west (Fig. 3.11, 18 LST). Lower CO concentrations in the afternoon are associated to PBL heights exceeding the mean mountaintop ($\sim 2,500$ m.a.s.l.) and the stronger along-valley flow (this will be discussed below). At night, with the collapse of the CBL, concentrations increase again as the winds weaken (Fig. 3.11, 00 LST).

For the vertical distribution of the CO tracer we focus on four different transects (Fig. 3.1b): one along-valley transect (Fig. 3.12a,b) and three across-valley transects (Fig. 3.12c-h). Figure 3.12a,b highlights the persistent northerly flow, which intensifies and deepens in the afternoon, and the associated larger concentrations to the south that occur both at the surface and at higher levels (Fig. 3.12a). In the morning, PBL heights in the center of the valley are below mean mountaintop, limiting the advection of pollutants to the free atmosphere (Fig. 3.12, left panels). The atmosphere in the morning is decoupled from the large-scale easterly flow, with weak slope flows inside the valley (Fig. 3.12c,e,g); the relatively strong winds within the PBL in the eastern slope in transect B (Fig. 3.12c) are a consequence of the curvature of the valley axis at this location (Fig. 3.1b). In the afternoon, the height of the CBL surpasses the mountain ridges, pollutants are detrained from the valley and are transported by the easterly flow aloft, and the relatively stronger surface winds inside the valley (Fig. 3.12, right panels).

Figure 3.13 presents the probability of source regions for particles that contributed to tracer concentrations in three different areas of AMVA: one south (panel a), one in the center (panel b), and one to the north (panel c). The area to the south is selected as it presents the largest C/E ratios and CO concentrations, and the other two are representative of different areas of AMVA and both are along the river, which presents relatively large CO concentrations. Indeed, the local contribution dominates in all selected areas. However, the largest contribution from outside is mostly from the north, with some contribution from the east but almost no contribution from the south and west. This result confirms and highlights the role of the northerly along-valley flow in the transport of pollutants to the south, even from areas relatively

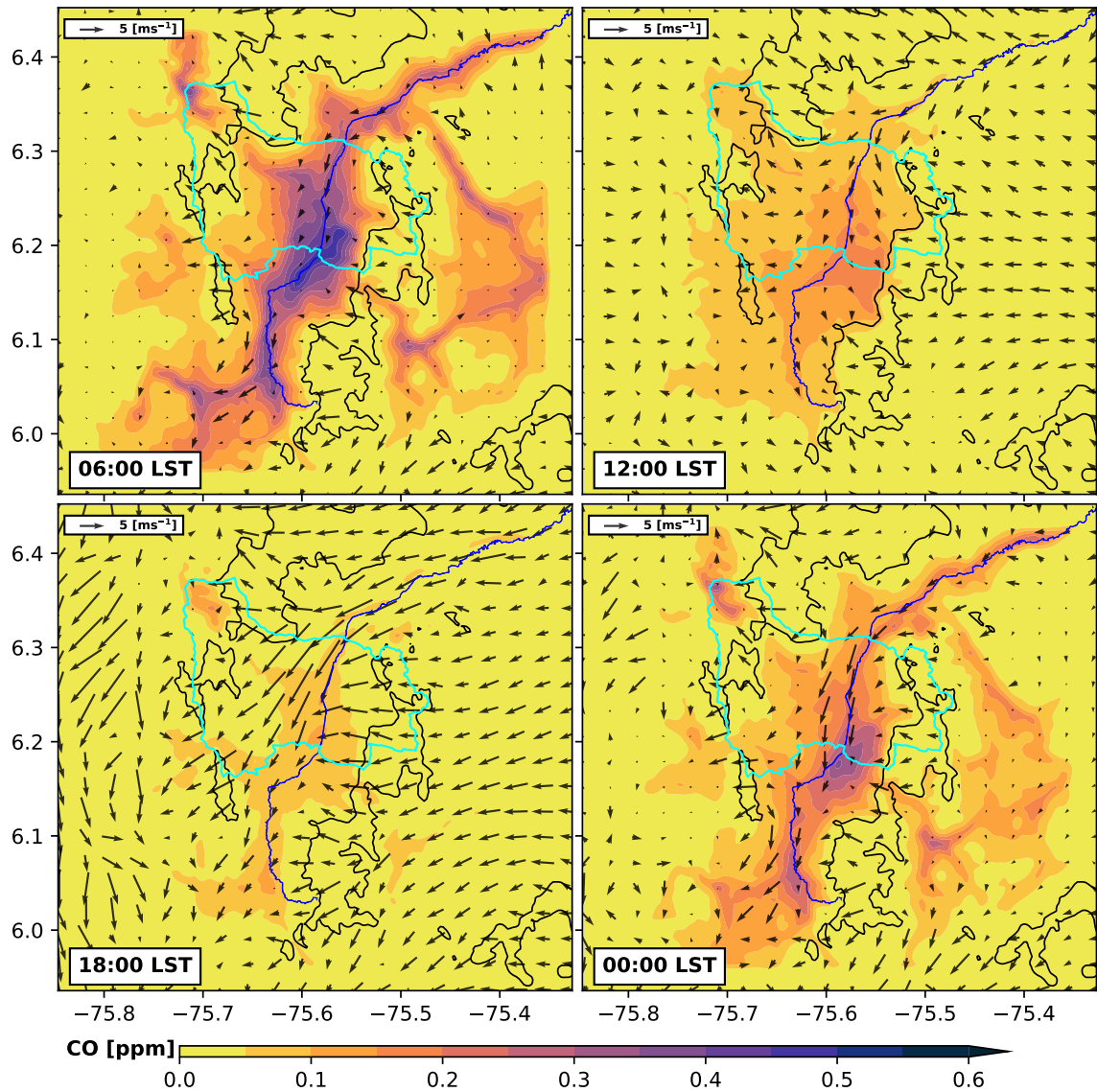


Figure 3.11: Horizontal distribution of the simulated CO tracer shaded, averaged for the first three full model levels, and the horizontal 10-m wind vectors U,V at 06, 12, 18 and 00 LST, from the simulation-averaged diurnal cycle; wind vectors are shown at every tenth grid point in the horizontal directions. Blue line: Aburrá River. Black lines: 2,500 m terrain height contour. Cyan lines: main municipality limits.

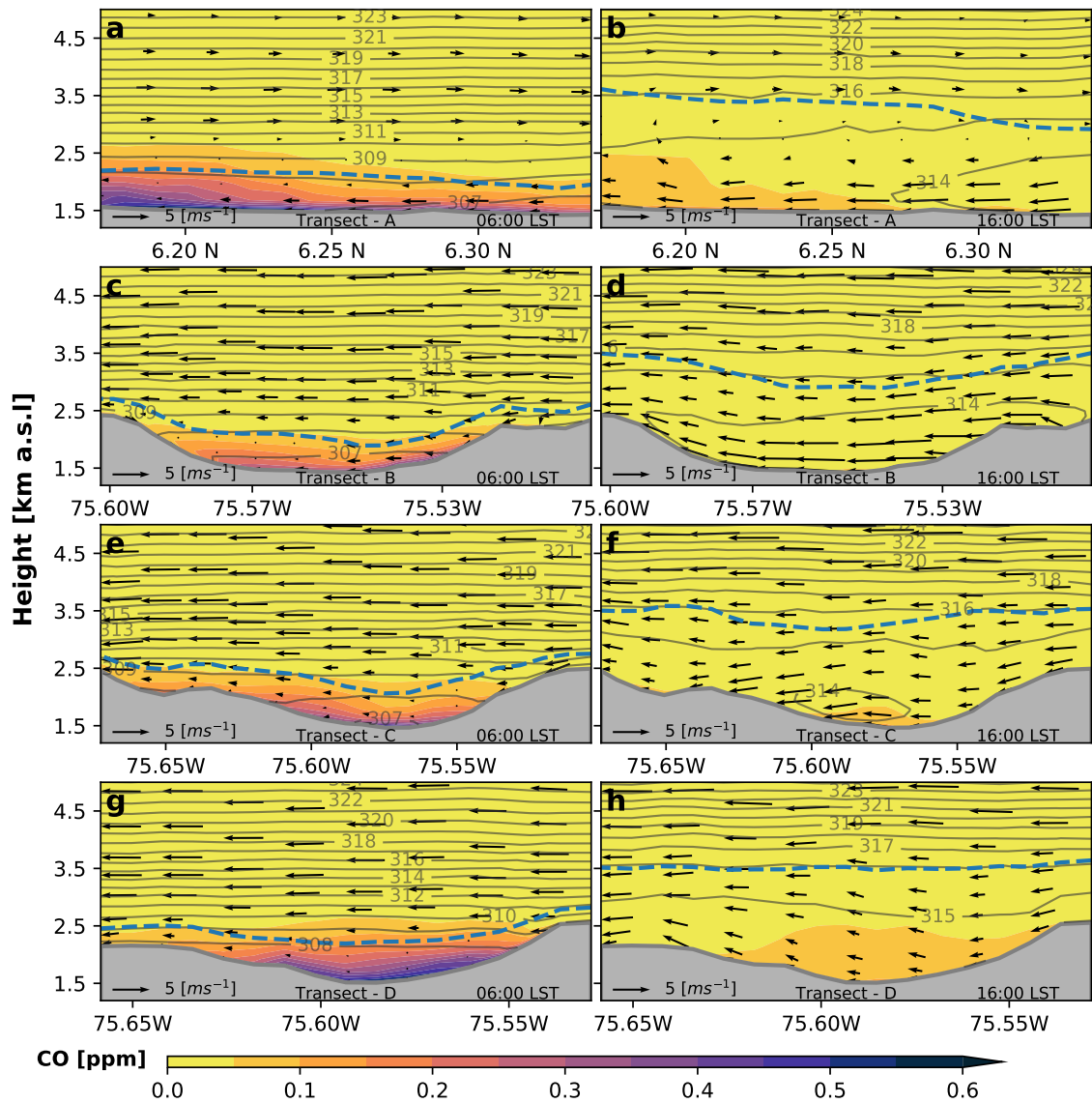


Figure 3.12: Vertical cross sections for the transects shown in Fig. 1b with the CO tracer shaded. Left (right) panels present morning (afternoon) situations. Along-valley oriented transect A include wind vectors with V, W (a, b); across-valley transects B, C, D include wind vectors with U, W (c-h). Wind vectors are shown at every second grid point in x direction. Isentropes are presented as grey contours every 1 K. PBL height is indicated with a blue dashed line.

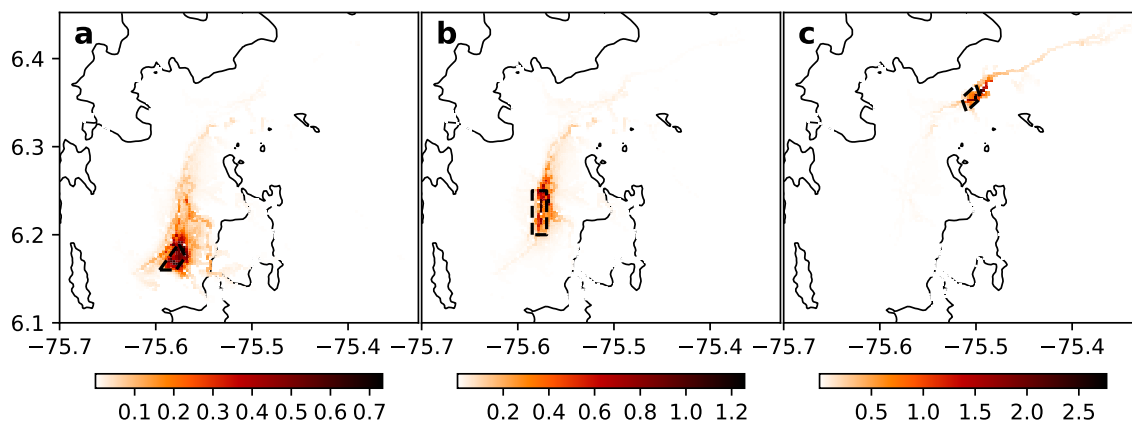


Figure 3.13: Percent probability of source grid cells for particles reaching the polygons shown in black dashed lines, within the first 3 vertical levels. Values considering the entire simulation period with the Lagrangian model. Solid black lines: 2,500 m terrain height contour.

far.

The described flow patterns within the valley allow us to describe the main mechanisms behind the relatively larger CO concentrations in the south and southeast of the main municipality (6.15-6.20N, 75.55-75.60W). First, there is a persistent northerly transport due to the up-valley wind (from the north) that does not seem to reverse at night. In the early morning, the main transport mechanism is related to the northerly along-valley flow (Fig. 3.11, 06 LST), as the slope flows are relatively weak (Fig. 3.12g). Later in the morning and early afternoon, upslope flows start developing at both eastern and western slopes (Fig. 3.11, 12 LST), conforming normal slope flow diurnal patterns (Zardi and Whiteman, 2013). However, the CBL grows and the valley atmosphere starts mixing with the large-scale easterly flow around 14-15 LST. Over the eastern slope, the upslope flow is compensated by the easterly flow that has been mixed down the valley, while the flows superimpose at the western slope. This results in weaker transport and dispersion over the eastern slope (Fig. 3.12h), consistent with larger CO concentrations. During the night, the across-valley flow weakens and the along-valley flow from the north dominates transport again, with weaker winds towards the eastern valley slope (6.2N, 75.58W) due to the interaction between the downslope flow and the along-valley flow (Fig. 3.11, 00 LST).

The outlined mean flow characteristics are valid for the ShinHong and MYNN PBLs. MYJ resulted in a weaker along-valley flow during the night and early morning,

and weaker downslope flows in the eastern slope during the afternoon, especially to the south. A similar pattern occurs for the different grid sizes, with D4 (900 m) presenting a flow consistent to that of D5, but D3 (2,700 m) resulted in a more uniform along-valley flow in the morning, and weaker downslope flows in the eastern slope, during the afternoon. This is probably a consequence of the representation of topography, that produces a more homogeneous valley for D3 (Supplementary Fig. B9).

3.5 Discussion

Our results show that the WRF model performance for surface temperature and wind is within recommended benchmarks for complex terrain. Surface temperature and wind direction performed adequately (within recommendations) for all model configurations, but the performance of wind speed resulted in relatively large overestimations, especially at the highest spatial resolution (using a grid size of 300 m), in which only the MYNN PBL produced error metrics within recommendations. Overestimations of wind speeds in valleys is a tendency of the WRF model (Jiménez and Dudhia, 2012). Relative to other high-resolution WRF applications in complex terrain in Colombia, our simulations present better performances for wind direction, but have slightly larger errors for wind speed (Reboredo et al., 2015; Nedbor-Gross et al., 2017; González et al., 2018). However, wind speed error metrics similar or even larger than those reported here are common in high-resolution simulations in complex terrain (e.g. Carvalho et al., 2012; Horvath et al., 2012; Zhang et al., 2013; Gómez-Navarro et al., 2015; Wagenbrenner et al., 2016; Falasca and Curci, 2018).

The scale-aware ShinHong PBL scheme was included in the simulations because the spatial resolution used to represent the complex topography of the region falls into the so-called “terra incognita” (Wyngaard, 2004). However, the sensitivity of surface temperature and wind to the PBL schemes was relatively low. This result is in agreement with previous studies using the ShinHong PBL scheme (e.g. Fovell and Gallagher, 2018; Huang et al., 2018), and surface wind error metrics of comparable magnitudes have been reported for this PBL scheme (Gevorgyan, 2018; Huang et al., 2018). Wind sensitivity to selection of PBL schemes has been found to be low relative to other model physics schemes, such as land surface (Cao and Fovell, 2018) or urban canopy (Huang et al., 2018). One of the potential advantages of using the ShinHong scheme is in the representation of PBL height (Gao et al., 2018) and potential tem-

perature profiles (Huang et al., 2018; Xu et al., 2018). This is consistent with our result that simulations using the ShinHong scheme produce a more realistic vertical profile of potential temperature during the daytime (Supplementary Fig. B10), but not necessarily for PBL height, where the ShinHong scheme results in lower PBL heights as compared to the observations at night, and overestimations during the daytime (Fig. 3.4).

The highest spatial resolution led to a better performance for surface temperature and wind direction, but worse for wind speed. The improvements in the representation of surface temperature can be explained by a better representation of topography, which translates into a reduced difference between model and real terrain elevations (Supplementary Fig. B11). This well-known relation between the representation of local (at a point) temperature and topographic elevation has also been found in previous studies (e.g. Chow et al., 2006; Soares et al., 2012). Although a better representation of surface wind would also be expected with a better representation of topographic features (e.g. Jiménez and Dudhia, 2012; Jiménez and Dudhia, 2013), this is not always the case (e.g. Horvath et al., 2012; Nedbor-Gross et al., 2017; Falasca and Curci, 2018). It is important to note that the used surface stations are located in highly urbanized areas, with specific locations that may be far from ideal. In spite of the performance for wind speed, the employed high resolution is justified due to the complex topography of the region, with losses in topographic features for the coarser domains (Supplementary Fig. B9), which may be related to the better performance in wind direction at the highest resolution.

The study period falls at the beginning of the first rainy season. Indeed, we selected this period because of the influence of increased cloudiness and precipitation (associated with the ITCZ) on PBL height and, therefore, on air quality. Increased cloudiness can restrict diurnal surface heating, which in turn weakens the development of thermal winds and the PBL, that are key components of transport processes in valleys (Rendón et al., 2014; Leukauf et al., 2016; Herrera-Mejía and Hoyos, 2019). However, simulating moist and mixing processes are challenging and pose large uncertainties. It was noted that the models resulted in a better representation of CO when observed rainfall was adequately captured by the model. Even though rainfall did not affect directly CO (wet deposition is not considered in the models), the interactions of rainfall with PBL height, atmospheric stability and vertical mixing influence CO dynamics. This suggests that a good representation of rainfall is a critical challenge to more accurately represent the dynamics of pollutants (even those not largely affected

by wet deposition), as well as to disentangle the drivers of dispersion processes and uncertainties related to emissions and pollutant pathways.

Regarding CO dispersion, both models (WRF-Chem and Lagrangian model) show higher CO concentrations south and southeast of the main municipality (near 6.2N, 75.58W), which is in agreement with previous studies that analyzed the spatial distribution of pollutants in the region using biomarkers (Schrimppff, 1984; Mejía-Echeverry et al., 2018). These areas to the southeast of the Valley show the largest CO concentrations in both models, as well as the largest C/E ratios, meaning that their relatively high concentration is not only due to local emissions, but also due to transport processes, mainly an along-valley flow from the north and reduced winds at the eastern slope.

The Lagrangian model produces higher CO concentrations (although both models underestimated concentrations) and leads to more areas presenting larger C/E ratios. Uncertainties that are inherent to the emission inventory do not allow to assess which dispersion model performs better. It is also worth noting that no boundary conditions were applied for CO, which can also be relevant for a better representation of CO concentrations. The online simulation of the Eulerian framework (WRF-Chem) has the advantage that it produces a coherent representation of transport processes at the integration time step. Further developments with a full chemistry configuration will allow coupling with atmospheric processes (e.g. radiation, wet deposition, etc), which is not that critical for CO but can be relevant for other species, including particulate matter and ozone, among others. The Lagrangian model has advantages such as being grid free, computationally efficient, and its tagging functionality, which enable different analysis based on information about emission sources and atmospheric fields for individual particles. This practical advantages of the Lagrangian model may be highly relevant in operational analyses.

3.6 Conclusions

We performed sub-kilometer grid size numerical simulations with the WRF-Chem model (run online) and a Lagrangian model (run offline) to study the spatial and temporal distribution of mobile emissions (represented by CO) in an urban valley (the AMVA region), for a critical period of air quality exceedances. We evaluated the meteorological model performance against observations, for three PBL schemes and three different grid sizes, based on standard model performance evaluation techniques.

Overall, the MYNN and ShinHong PBL schemes resulted in a similar performance, and both superior to MYJ. The ShinHong PBL (scale-aware) resulted in better performance metrics for surface and upper-air temperature, but MYNN was slightly better for surface and upper-air wind. However, model performance sensitivity to PBL was relatively low.

Decreasing grid size improved the model performance for surface temperature and wind direction, but worsened the performance for wind speed, with larger overestimations at the highest spatial resolution.

There are relatively higher concentrations of CO towards the south and southeast of the main municipality. Analysis with the C/E ratio, relating concentrations to emissions, indicated that these areas, especially to the southeast, present larger pollutant concentrations due to transport processes. This same C/E ratio could be used to characterize areas that experience increased concentrations due to exchange processes in other regions of the world.

The spatial distribution of pollutants is associated with the prevalent along-valley wind from the north, which transports pollutants to the south throughout the day, and weaker winds in the eastern slope during the afternoon, due to compensations between the upslope flow and the easterlies.

CO concentrations are larger in the morning, when the atmosphere is decoupled from the large-scale easterly flow aloft and PBL height is lower than the mountain ridges. During the afternoon, when PBL heights exceed the mean mountain top, pollutants are transported out of the valley by the easterly winds aloft and a stronger along-valley wind from the north.

3.7 References

- AMVA - Área Metropolitana del Valle de Aburrá (2015). *Inventario de Emisiones Atmosféricas del Valle de Aburrá, año base 2013. In Spanish. Prepared by Universidad Pontificia Bolivariana - Grupo de Investigaciones Ambientales*. Convenio de Asociación No. CA 315 de 2014. Medellín: Área Metropolitana del Valle de Aburrá.
- (2017a). *Documento del Plan Integral de Gestión de la Calidad del Aire - PIGECA. In Spanish. Prepared by AMVA, Clean Air Institute and Universidad Pontificia Bolivariana*. Convenio de Asociación No. CA 529 de 2011. Medellín: Área Metropolitana del Valle de Aburrá.

- AMVA - Área Metropolitana del Valle de Aburrá (2017b). *Inventario de Emisiones Atmosféricas del Valle de Aburrá - Actualización 2015*. In Spanish. Prepared by Universidad Pontificia Bolivariana - Grupo de Investigaciones Ambientales. Convenio de Asociación No. CA 335 de 2016. Medellín: Área Metropolitana del Valle de Aburrá.
- Baklanov, A., K. Schlünzen, P. Suppan, J. Baldasano, D. Brunner, S. Aksoyoglu, G. Carmichael, J. Douros, J. Flemming, R. Forkel, S. Galmarini, M. Gauss, G. Grell, M. Hirtl, S. Joffre, O. Jorba, E. Kaas, M. Kaasik, G. Kallos, X. Kong, U. Korsholm, A. Kurganskiy, J. Kushta, U. Lohmann, A. Mahura, A. Manders-Groot, A. Maurizi, N. Moussiopoulos, S. T. Rao, N. Savage, C. Seigneur, R. S. Sokhi, E. Solazzo, S. Solomos, B. Sørensen, G. Tsegas, E. Vignati, B. Vogel, and Y. Zhang (2014). “Online coupled regional meteorology chemistry models in Europe: current status and prospects”. *Atmospheric Chemistry and Physics* 14.1, 317–398. DOI: [10.5194/acp-14-317-2014](https://doi.org/10.5194/acp-14-317-2014).
- Bhardwaj, P., M. Naja, M. Rupakheti, A. Lupascu, A. Mues, A. Kumar Panday, R. Kumar, K. Singh Mahata, S. Lal, H. C. Chandola, and M. G. Lawrence (2018). “Variations in surface ozone and carbon monoxide in the Kathmandu Valley and surrounding broader regions during SusKat-ABC field campaign: Role of local and regional sources”. *Atmospheric Chemistry and Physics* 18.16, 11949–11971. DOI: [10.5194/acp-18-11949-2018](https://doi.org/10.5194/acp-18-11949-2018).
- Borge, R., V. Alexandrov, J. J. del Vas, J. Lumbreras, and E. Rodríguez (2008). “A comprehensive sensitivity analysis of the WRF model for air quality applications over the Iberian Peninsula”. *Atmospheric Environment* 42.37, 8560–8574. DOI: <https://doi.org/10.1016/j.atmosenv.2008.08.032>.
- Cao, Y. and R. G. Fovell (2018). “Downslope Windstorms of San Diego County. Part II: Physics Ensemble Analyses and Gust Forecasting”. *Weather and Forecasting* 33.2, 539–559. DOI: [10.1175/WAF-D-17-0177.1](https://doi.org/10.1175/WAF-D-17-0177.1).
- Carvalho, D., A. Rocha, M. Gómez-Gesteira, and C. Santos (2012). “A sensitivity study of the WRF model in wind simulation for an area of high wind energy”. *Environmental Modelling & Software* 33, 23–34. DOI: [10.1016/J.ENVSOFT.2012.01.019](https://doi.org/10.1016/J.ENVSOFT.2012.01.019).
- Castellanos, P., L. T. Marufu, B. G. Doddridge, B. F. Taubman, J. J. Schwab, J. C. Hains, S. H. Ehrman, and R. R. Dickerson (2011). “Ozone, oxides of nitrogen, and carbon monoxide during pollution events over the eastern United States: An

- evaluation of emissions and vertical mixing”. *Journal of Geophysical Research* 116.D16, D16307. DOI: [10.1029/2010JD014540](https://doi.org/10.1029/2010JD014540).
- Castro, C. L., R. A. Pielke Sr., and G. Leoncini (2005). “Dynamical downscaling: Assessment of value retained and added using the Regional Atmospheric Modeling System (RAMS)”. *Journal of Geophysical Research: Atmospheres* 110.D5. DOI: [10.1029/2004JD004721](https://doi.org/10.1029/2004JD004721).
- Chow, F. K., A. P. Weigel, R. L. Street, M. W. Rotach, and M. Xue (2006). “High-Resolution Large-Eddy Simulations of Flow in a Steep Alpine Valley. Part I: Methodology, Verification, and Sensitivity Experiments”. *Journal of Applied Meteorology and Climatology* 45.1, 63–86. DOI: [10.1175/JAM2322.1](https://doi.org/10.1175/JAM2322.1).
- Cohen, A. E., S. M. Cavallo, M. C. Coniglio, and H. E. Brooks (2015). “A Review of Planetary Boundary Layer Parameterization Schemes and Their Sensitivity in Simulating Southeastern U.S. Cold Season Severe Weather Environments”. *Weather and Forecasting* 30.3, 591–612. DOI: [10.1175/WAF-D-14-00105.1](https://doi.org/10.1175/WAF-D-14-00105.1).
- Colette, A., B. Bessagnet, R. Vautard, S. Szopa, S. Rao, S. Schucht, Z. Klimont, L. Menut, G. Clain, F. Meleux, G. Curci, and L. Rouïl (2013). “European atmosphere in 2050, a regional air quality and climate perspective under CMIP5 scenarios”. *Atmospheric Chemistry and Physics* 13.15, 7451–7471. DOI: [10.5194/acp-13-7451-2013](https://doi.org/10.5194/acp-13-7451-2013).
- Collaud Coen, M., C. Praz, A. Haeefe, D. Ruffieux, P. Kaufmann, and B. Calpini (2014). “Determination and climatology of the planetary boundary layer height above the Swiss plateau by in situ and remote sensing measurements as well as by the COSMO-2 model”. *Atmospheric Chemistry and Physics* 14.23, 13205–13221. DOI: [10.5194/acp-14-13205-2014](https://doi.org/10.5194/acp-14-13205-2014).
- Copernicus Climate Change Service (CS3) (2017). *ERA5: Fifth generation of ECMWF atmospheric reanalyses of the global climate*. Copernicus Climate Change Service Climate Data Store (CDS). <https://cds.climate.copernicus.eu/>.
- Cuchiara, G. C., X. Li, J. Carvalho, and B. Rappenglück (2014). “Intercomparison of planetary boundary layer parameterization and its impacts on surface ozone concentration in the WRF/Chem model for a case study in houston/texas”. *Atmospheric Environment* 96, 175–185. DOI: [10.1016/j.atmosenv.2014.07.013](https://doi.org/10.1016/j.atmosenv.2014.07.013).
- Cuchiara, G. C., B. Rappenglück, M. A. Rubio, E. Lissi, E. Gramsch, and R. D. Garreaud (2017). “Modeling study of biomass burning plumes and their impact on urban air quality; a case study of Santiago de Chile”. *Atmospheric Environment* 166, 79–91. DOI: [10.1016/j.atmosenv.2017.07.002](https://doi.org/10.1016/j.atmosenv.2017.07.002).

- De Foy, B., J. R. Varela, L. T. Molina, and M. J. Molina (2006). “Rapid ventilation of the Mexico City basin and regional fate of the urban plume”. *Atmospheric Chemistry and Physics* 6.8, 2321–2335. DOI: [10.5194/acp-6-2321-2006](https://doi.org/10.5194/acp-6-2321-2006).
- De Wekker, S. F. J., M. Kossmann, J. Knievel, L. Giovannini, E. Gutmann, and D. Zardi (2018). “Meteorological Applications Benefiting from an Improved Understanding of Atmospheric Exchange Processes over Mountains”. *Atmosphere* 9.10, 371. DOI: [10.3390/atmos9100371](https://doi.org/10.3390/atmos9100371).
- Dudhia, J. (1989). “Numerical Study of Convection Observed during the Winter Monsoon Experiment Using a Mesoscale Two-Dimensional Model”. *Journal of the Atmospheric Sciences* 46.20, 3077–3107. DOI: [10.1175/1520-0469\(1989\)046<3077:NSOCOD>2.0.CO;2](https://doi.org/10.1175/1520-0469(1989)046<3077:NSOCOD>2.0.CO;2).
- Eicker, M. O. de, R. Zah, R. Triviño, and H. Hurni (2008). “Spatial accuracy of a simplified disaggregation method for traffic emissions applied in seven mid-sized Chilean cities”. *Atmospheric Environment* 42.7, 1491–1502. DOI: <https://doi.org/10.1016/j.atmosenv.2007.10.079>.
- Emery, C., E. Tai, and G. Yarwood (2001). *Enhanced meteorological modeling and performance evaluation for two Texas ozone episodes*. Prepared for the Texas natural resource conservation commission, by ENVIRON International Corporation.
- Falasca, S. and G. Curci (2018). “High-resolution air quality modeling: Sensitivity tests to horizontal resolution and urban canopy with WRF-CHIMERE”. *Atmospheric Environment* 187, 241–254. DOI: <https://doi.org/10.1016/j.atmosenv.2018.05.048>.
- Fast, J. D., W. I. Gustafson Jr., R. C. Easter, R. A. Zaveri, J. C. Barnard, E. G. Chapman, G. A. Grell, and S. E. Peckham (2006). “Evolution of ozone, particulates, and aerosol direct radiative forcing in the vicinity of Houston using a fully coupled meteorology-chemistry-aerosol model”. *Journal of Geophysical Research: Atmospheres* 111.D21. DOI: [10.1029/2005JD006721](https://doi.org/10.1029/2005JD006721).
- Fay, B. and L. Neunhäuserer (2006). “Evaluation of high-resolution forecasts with the non-hydrostatic numerical weather prediction model Lokalmmodell for urban air pollution episodes in Helsinki, Oslo and Valencia”. *Atmospheric Chemistry and Physics* 6.8, 2107–2128.
- Fovell, R. and A. Gallagher (2018). “Winds and Gusts during the Thomas Fire”. *Fire* 1.3, 47. DOI: [10.3390/fire1030047](https://doi.org/10.3390/fire1030047).
- Franco, D. M. P., M. de Fatima Andrade, R. Y. Ynoue, and J. Ching (2019). “Effect of Local Climate Zone (LCZ) classification on ozone chemical transport model

- simulations in Sao Paulo, Brazil”. *Urban Climate* 27, 293–313. DOI: <https://doi.org/10.1016/j.uclim.2018.12.007>.
- Gao, C., X. Zhang, W. Wang, A. Xiu, D. Tong, and W. Chen (2018). “Spatiotemporal Distribution of Satellite-Retrieved Ground-Level PM_{2.5} and Near Real-Time Daily Retrieval Algorithm Development in Sichuan Basin, China”. *Atmosphere* 9.2, 78. DOI: [10.3390/atmos9020078](https://doi.org/10.3390/atmos9020078).
- Gevorgyan, A. (2018). “A Case Study of Low-Level Jets in Yerevan Simulated by the WRF Model”. *Journal of Geophysical Research: Atmospheres* 123.1, 300–314. DOI: [10.1002/2017JD027629](https://doi.org/10.1002/2017JD027629).
- Giovannini, L., D. Zardi, M. de Franceschi, and F. Chen (2014). “Numerical simulations of boundary-layer processes and urban-induced alterations in an Alpine valley”. *International Journal of Climatology* 34.4, 1111–1131. DOI: [10.1002/joc.3750](https://doi.org/10.1002/joc.3750).
- Gómez-Navarro, J. J., C. C. Raible, and S. Dierer (2015). “Sensitivity of the WRF model to PBL parametrisations and nesting techniques: evaluation of wind storms over complex terrain”. *Geoscientific Model Development* 8.10, 3349–3363. DOI: [10.5194/gmd-8-3349-2015](https://doi.org/10.5194/gmd-8-3349-2015).
- Gómez, C., C. González, M. Osses, and B. Aristizábal (2018). “Spatial and temporal disaggregation of the on-road vehicle emission inventory in a medium-sized Andean city. Comparison of GIS-based top-down methodologies”. *Atmospheric Environment* 179, 142–155. DOI: <https://doi.org/10.1016/j.atmosenv.2018.01.049>.
- González, C., R. Ynoue, A. Vara-Vela, N. Rojas, and B. Aristizábal (2018). “High-resolution air quality modeling in a medium-sized city in the tropical Andes: Assessment of local and global emissions in understanding ozone and PM₁₀ dynamics”. *Atmospheric Pollution Research* 9.5, 934–948. DOI: <https://doi.org/10.1016/j.apr.2018.03.003>.
- Grell, G. A., S. E. Peckham, R. Schmitz, S. A. McKeen, G. Frost, W. C. Skamarock, and B. Eder (2005). “Fully coupled “online” chemistry within the WRF model”. *Atmospheric Environment* 39.37, 6957–6975. DOI: <https://doi.org/10.1016/j.atmosenv.2005.04.027>.
- Haklay, M. and P. Weber (2008). “OpenStreetMap: User-Generated Street Maps”. *IEEE Pervasive Computing* 7.4, 12–18. DOI: [10.1109/MPRV.2008.80](https://doi.org/10.1109/MPRV.2008.80).
- Henao, J., A. Rendón, and J. Salazar (2020a). “Trade-off between urban heat island mitigation and air quality in urban valleys”. *Urban Climate* 31. DOI: [10.1016/j.uclim.2019.100542](https://doi.org/10.1016/j.uclim.2019.100542).

- Henao, J. J., J. F. Mejía, A. M. Rendón, and J. F. Salazar (2020b). “Sub-kilometer dispersion simulation of a CO tracer for an inter-Andean urban valley”. *Atmospheric Pollution Research*. DOI: [10.1016/j.apr.2020.02.005](https://doi.org/10.1016/j.apr.2020.02.005).
- Herrera-Mejía, L. and C. D. Hoyos (2019). “Characterization of the atmospheric boundary layer in a narrow tropical valley using remote-sensing and radiosonde observations and the WRF model: the Aburrá Valley case-study”. *Quarterly Journal of the Royal Meteorological Society*, qj.3583. DOI: [10.1002/qj.3583](https://doi.org/10.1002/qj.3583).
- Hess, G. D., K. J. Tory, M. E. Cope, S. Lee, K. Puri, P. C. Manins, and M. Young (2004). “The Australian Air Quality Forecasting System. Part II: Case Study of a Sydney 7-Day Photochemical Smog Event”. *Journal of Applied Meteorology* 43.5, 663–679. DOI: [10.1175/2094.1](https://doi.org/10.1175/2094.1).
- Horvath, K., D. Koracin, R. Vellore, J. Jiang, and R. Belu (2012). “Sub-kilometer dynamical downscaling of near-surface winds in complex terrain using WRF and MM5 mesoscale models”. *Journal of Geophysical Research: Atmospheres* 117.D11. DOI: [10.1029/2012JD017432](https://doi.org/10.1029/2012JD017432).
- Huang, M., Z. Gao, S. Miao, and F. Chen (2018). “Sensitivity of urban boundary layer simulation to urban canopy models and PBL schemes in Beijing”. *Meteorology and Atmospheric Physics*, 1–14. DOI: [10.1007/s00703-018-0634-1](https://doi.org/10.1007/s00703-018-0634-1).
- Janjic, Z. I. (1994). “The Step-Mountain Eta Coordinate Model: Further Developments of the Convection, Viscous Sublayer, and Turbulence Closure Schemes”. *Monthly Weather Review* 122.5, 927–945. DOI: [10.1175/1520-0493\(1994\)122<0927:TSMECM>2.0.CO;2](https://doi.org/10.1175/1520-0493(1994)122<0927:TSMECM>2.0.CO;2).
- Jarvis, A., H. I. Reuter, A. Nelson, and E. Guevara (2008). “Hole-filled SRTM for the globe Version 4”. *available from the CGIAR-CSI SRTM 90m Database*.
- Jiménez, P. A. and J. Dudhia (2012). “Improving the Representation of Resolved and Unresolved Topographic Effects on Surface Wind in the WRF Model”. *Journal of Applied Meteorology and Climatology* 51.2, 300–316. DOI: [10.1175/JAMC-D-11-084.1](https://doi.org/10.1175/JAMC-D-11-084.1).
- (2013). “On the Ability of the WRF Model to Reproduce the Surface Wind Direction over Complex Terrain”. *Journal of Applied Meteorology and Climatology* 52.7, 1610–1617. DOI: [10.1175/JAMC-D-12-0266.1](https://doi.org/10.1175/JAMC-D-12-0266.1).
- Jiménez, P. A., J. Dudhia, J. F. González-Rouco, J. Navarro, J. P. Montávez, and E. García-Bustamante (2012). “A Revised Scheme for the WRF Surface Layer Formulation”. *Monthly Weather Review* 140.3, 898–918. DOI: [10.1175/MWR-D-11-00056.1](https://doi.org/10.1175/MWR-D-11-00056.1).

- Kain, J. S. (2004). “The Kain–Fritsch Convective Parameterization: An Update”. *Journal of Applied Meteorology* 43.1, 170–181. DOI: [10.1175/1520-0450\(2004\)043<0170:TKCPAU>2.0.CO;2](https://doi.org/10.1175/1520-0450(2004)043<0170:TKCPAU>2.0.CO;2).
- Kemball-Cook, S., Y. Jia, C. Emery, R. Morris, Z. Wang, and G. Tonnesen (2005). *Alaska MM5 Modeling for the 2002 Annual Period to Support Visibility Modeling*. Prepared for the Western Regional Partnership, Denver, Colorado. Prepared by ENVIRON International Corporation, Novato, California, and the University of California at Riverside, Center for Environmental Research and Technology.
- Kuik, F., A. Lauer, G. Churkina, H. A. C. Denier van der Gon, D. Fenner, K. A. Mar, and T. M. Butler (2016). “Air quality modelling in the Berlin–Brandenburg region using WRF-Chem v3.7.1: sensitivity to resolution of model grid and input data”. *Geoscientific Model Development* 9.12, 4339–4363. DOI: [10.5194/gmd-9-4339-2016](https://doi.org/10.5194/gmd-9-4339-2016).
- Lee, S.-M. and H. J. S. Fernando (2004). “Evaluation of Meteorological Models MM5 and HOTMAC Using PAFEX-I Data”. *Journal of Applied Meteorology* 43.8, 1133–1148. DOI: [10.1175/1520-0450\(2004\)043<1133:EOMMMA>2.0.CO;2](https://doi.org/10.1175/1520-0450(2004)043<1133:EOMMMA>2.0.CO;2).
- Lehner, M. and A. Gohm (2010). “Idealised Simulations of Daytime Pollution Transport in a Steep Valley and its Sensitivity to Thermal Stratification and Surface Albedo”. *Boundary-Layer Meteorology* 134.2, 327–351. DOI: [10.1007/s10546-009-9442-y](https://doi.org/10.1007/s10546-009-9442-y).
- Leukauf, D., A. Gohm, and M. W. Rotach (2016). “Quantifying horizontal and vertical tracer mass fluxes in an idealized valley during daytime”. *Atmospheric Chemistry and Physics* 16.20, 13049–13066. DOI: [10.5194/acp-16-13049-2016](https://doi.org/10.5194/acp-16-13049-2016).
- Leukauf, D., A. Gohm, M. W. Rotach, and J. S. Wagner (2015). “The Impact of the Temperature Inversion Breakup on the Exchange of Heat and Mass in an Idealized Valley: Sensitivity to the Radiative Forcing”. *Journal of Applied Meteorology and Climatology* 54.11, 2199–2216. DOI: [10.1175/JAMC-D-15-0091.1](https://doi.org/10.1175/JAMC-D-15-0091.1).
- Loibl, W., R. Orthofer, and W. Winiwarter (1993). “Spatially disaggregated emission inventory for anthropogenic NMVOC in Austria”. *Atmospheric Environment. Part A. General Topics* 27.16, 2575–2590. DOI: [https://doi.org/10.1016/0960-1686\(93\)90031-S](https://doi.org/10.1016/0960-1686(93)90031-S).
- Mahrt, L. (2014). “Stably Stratified Atmospheric Boundary Layers”. *Annual Review of Fluid Mechanics* 46.1, 23–45. DOI: [10.1146/annurev-fluid-010313-141354](https://doi.org/10.1146/annurev-fluid-010313-141354).
- McKeen, S., S. H. Chung, J. Wilczak, G. Grell, I. Djalalova, S. Peckham, W. Gong, V. Bouchet, R. Moffet, Y. Tang, G. R. Carmichael, R. Mathur, and S. Yu (2007).

- “Evaluation of several PM_{2.5} forecast models using data collected during the ICARTT/NEAQS 2004 field study”. *Journal of Geophysical Research: Atmospheres* 112.D10. DOI: [10.1029/2006JD007608](https://doi.org/10.1029/2006JD007608).
- Mejía-Echeverry, D., M. A. E. Chaparro, J. F. Duque-Trujillo, M. A. E. Chaparro, and A. G. Castañeda Miranda (2018). “Magnetic Biomonitoring as a Tool for Assessment of Air Pollution Patterns in a Tropical Valley Using *Tillandsia* sp.” *Atmosphere* 9.7, 283. DOI: [10.3390/atmos9070283](https://doi.org/10.3390/atmos9070283).
- Mejia, J., J. Gillies, V. Etyemezian, and R. Glick (2019). “A very-high resolution (20m) measurement-based dust emissions and dispersion modeling approach for the Oceano Dunes, California”. *Atmospheric Environment* 218, 116977. DOI: [10.1016/j.atmosenv.2019.116977](https://doi.org/10.1016/j.atmosenv.2019.116977).
- Mlawer, E. J., S. J. Taubman, P. D. Brown, M. J. Iacono, and S. A. Clough (1997). “Radiative transfer for inhomogeneous atmospheres: RRTM, a validated correlated-k model for the longwave”. *Journal of Geophysical Research: Atmospheres* 102.D14, 16663–16682. DOI: [10.1029/97JD00237](https://doi.org/10.1029/97JD00237).
- Nakanishi, M. and H. Niino (2006). “An Improved Mellor–Yamada Level-3 Model: Its Numerical Stability and Application to a Regional Prediction of Advection Fog”. *Boundary-Layer Meteorology* 119.2, 397–407. DOI: [10.1007/s10546-005-9030-8](https://doi.org/10.1007/s10546-005-9030-8).
- Nedbor-Gross, R., B. H. Henderson, J. R. Davis, J. E. Pachón, A. Rincón, O. J. Guerrero, and F. Grajales (2017). “Comparing Standard to Feature-Based Meteorological Model Evaluation Techniques in Bogotá, Colombia”. *Journal of Applied Meteorology and Climatology* 56.2, 391–413. DOI: [10.1175/JAMC-D-16-0058.1](https://doi.org/10.1175/JAMC-D-16-0058.1).
- Niu, G.-Y., Z.-L. Yang, K. E. Mitchell, F. Chen, M. B. Ek, M. Barlage, A. Kumar, K. Manning, D. Niyogi, E. Rosero, M. Tewari, and Y. Xia (2011). “The community Noah land surface model with multiparameterization options (Noah-MP): 1. Model description and evaluation with local-scale measurements”. *Journal of Geophysical Research: Atmospheres* 116.D12. DOI: [10.1029/2010JD015139](https://doi.org/10.1029/2010JD015139).
- Oke, T. R. (2007). “Siting and Exposure of Meteorological Instruments at Urban Sites”. In: *Air Pollution Modeling and Its Application XVII*. Ed. by C. Borrego and A.-L. Norman. Boston, MA: Springer US, 615–631. DOI: https://doi.org/10.1007/978-0-387-68854-1_66.
- Reboredo, B., R. Arasa, and B. Codina (2015). “Evaluating sensitivity to different options and parameterizations of a coupled air quality modelling system over Bogotá, Colombia. Part I: WRF Model configuration”. *Open Journal of Air Pollution* 4.02, 47.

- Rendón, A. M., J. F. Salazar, C. A. Palacio, and V. Wirth (2015). “Temperature Inversion Breakup with Impacts on Air Quality in Urban Valleys Influenced by Topographic Shading”. *Journal of Applied Meteorology and Climatology* 54.2, 302–321. DOI: [10.1175/JAMC-D-14-0111.1](https://doi.org/10.1175/JAMC-D-14-0111.1).
- Rendón, A. M., J. F. Salazar, C. A. Palacio, V. Wirth, and B. Brötz (2014). “Effects of Urbanization on the Temperature Inversion Breakup in a Mountain Valley with Implications for Air Quality”. *Journal of Applied Meteorology and Climatology* 53.4, 840–858. DOI: [10.1175/JAMC-D-13-0165.1](https://doi.org/10.1175/JAMC-D-13-0165.1).
- Rodríguez-Villamizar, L., N. Rojas-Roa, L. Blanco-Becerra, V. Herrera-Galindo, and J. Fernández-Niño (2018). “Short-Term Effects of Air Pollution on Respiratory and Circulatory Morbidity in Colombia 2011–2014: A Multi-City, Time-Series Analysis”. *International journal of environmental research and public health* 15.8, 1610.
- Roldán-Henao, N., C. D. Hoyos, L. Herrera-Mejía, and A. Isaza (2020). “An Investigation of the Precipitation Net Effect on the Particulate Matter Concentration in a Narrow Valley: Role of Lower Troposphere Stability”. *Journal of Applied Meteorology and Climatology*, JAMC–D–18–0313.1. DOI: [10.1175/JAMC-D-18-0313.1](https://doi.org/10.1175/JAMC-D-18-0313.1).
- Saha, S., S. Moorthi, X. Wu, J. Wang, S. Nadiga, P. Tripp, D. Behringer, Y.-T. Hou, H.-y. Chuang, M. Iredell, M. Ek, J. Meng, R. Yang, M. P. Mendez, H. van den Dool, Q. Zhang, W. Wang, M. Chen, and E. Becker (2014). “The NCEP Climate Forecast System Version 2”. *Journal of Climate* 27.6, 2185–2208. DOI: [10.1175/JCLI-D-12-00823.1](https://doi.org/10.1175/JCLI-D-12-00823.1).
- Saide, P., R. Zah, M. Osses, and M. O. de Eicker (2009). “Spatial disaggregation of traffic emission inventories in large cities using simplified top-down methods”. *Atmospheric Environment* 43.32, 4914–4923. DOI: <https://doi.org/10.1016/j.atmosenv.2009.07.013>.
- Saide, P. E., G. R. Carmichael, S. N. Spak, L. Gallardo, A. E. Osses, M. A. Mena-Carrasco, and M. Pagowski (2011). “Forecasting urban PM10 and PM2.5 pollution episodes in very stable nocturnal conditions and complex terrain using WRF–Chem CO tracer model”. *Atmospheric Environment* 45.16, 2769–2780. DOI: <https://doi.org/10.1016/j.atmosenv.2011.02.001>.
- Schaap, M., C. Cuvelier, C. Hendriks, B. Bessagnet, J. Baldasano, A. Colette, P. Thunis, D. Karam, H. Fagerli, A. Graff, R. Kranenburg, A. Nyiri, M. Pay, L. Rouil, M. Schulz, D. Simpson, R. Stern, E. Terrenoire, and P. Wind (2015). “Performance of European chemistry transport models as function of horizontal resolution”. *Atmospheric Environment* 112, 90–105. DOI: [10.1016/j.atmosenv.2015.04.003](https://doi.org/10.1016/j.atmosenv.2015.04.003).

- Schrimppf, E. (1984). “Air pollution patterns in two cities of Colombia, S. A. According to trace substances content of an epiphyte (*Tillandsia recurvata* L.)” *Water, Air, and Soil Pollution* 21.1-4, 279–315. DOI: [10.1007/BF00163631](https://doi.org/10.1007/BF00163631).
- Shin, H. H. and J. Dudhia (2016). “Evaluation of PBL Parameterizations in WRF at Subkilometer Grid Spacings: Turbulence Statistics in the Dry Convective Boundary Layer”. *Monthly Weather Review* 144.3, 1161–1177. DOI: [10.1175/MWR-D-15-0208.1](https://doi.org/10.1175/MWR-D-15-0208.1).
- Shin, H. H. and S.-Y. Hong (2015). “Representation of the Subgrid-Scale Turbulent Transport in Convective Boundary Layers at Gray-Zone Resolutions”. *Monthly Weather Review* 143.1, 250–271. DOI: [10.1175/MWR-D-14-00116.1](https://doi.org/10.1175/MWR-D-14-00116.1).
- Shrestha, K. L., A. Kondo, A. Kaga, and Y. Inoue (2009). “High-resolution modeling and evaluation of ozone air quality of Osaka using MM5-CMAQ system”. *Journal of Environmental Sciences* 21.6, 782–789. DOI: [https://doi.org/10.1016/S1001-0742\(08\)62341-4](https://doi.org/10.1016/S1001-0742(08)62341-4).
- Skamarock, W. C., J. B. Klemp, J. Dudhia, D. O. Gill, D. M. Barker, M. G. Duda, X.-Y. Huang, W. Wang, and J. G. Powers (2008). “A description of the advanced research WRF version 3, NCAR Technical Note”. *National Center for Atmospheric Research, Boulder, Colorado, USA*. DOI: [10.5065/D68S4MVH](https://doi.org/10.5065/D68S4MVH).
- Soares, P. M. M., R. M. Cardoso, P. M. A. Miranda, J. de Medeiros, M. Belo-Pereira, and F. Espirito-Santo (2012). “WRF high resolution dynamical downscaling of ERA-Interim for Portugal”. *Climate Dynamics* 39.9-10, 2497–2522. DOI: [10.1007/s00382-012-1315-2](https://doi.org/10.1007/s00382-012-1315-2).
- Staudt, A. C., D. J. Jacob, J. A. Logan, D. Bachiochi, T. N. Krishnamurti, and G. W. Sachse (2001). “Continental sources, transoceanic transport, and interhemispheric exchange of carbon monoxide over the Pacific”. *Journal of Geophysical Research: Atmospheres* 106.D23, 32571–32589. DOI: [10.1029/2001JD900078](https://doi.org/10.1029/2001JD900078).
- Taghavi, M., S. Cautenet, and J. Arteta (2005). “Impact of a highly detailed emission inventory on modeling accuracy”. *Atmospheric Research* 74.1, 65–88. DOI: <https://doi.org/10.1016/j.atmosres.2004.06.007>.
- Tesche, T., D. McNally, and C. Tremback (2002). *Operational evaluation of the MM5 meteorological model over the continental United States: Protocol for annual and episodic evaluation*. Prepared for the US Environmental Protection Agency, Office of Air Quality Planning and Standards, prepared by Alpine Geophysics, LLC, Ft. Wright, KY.

- Thompson, G., P. R. Field, R. M. Rasmussen, and W. D. Hall (2008). “Explicit Forecasts of Winter Precipitation Using an Improved Bulk Microphysics Scheme. Part II: Implementation of a New Snow Parameterization”. *Monthly Weather Review* 136.12, 5095–5115. DOI: [10.1175/2008MWR2387.1](https://doi.org/10.1175/2008MWR2387.1).
- Thomson, D. J. (1987). “Criteria for the selection of stochastic models of particle trajectories in turbulent flows”. *Journal of Fluid Mechanics* 180, 529–556. DOI: [10.1017/S0022112087001940](https://doi.org/10.1017/S0022112087001940).
- Tuia, D., M. O. de Eicker, R. Zah, M. Osses, E. Zarate, and A. Clappier (2007). “Evaluation of a simplified top-down model for the spatial assessment of hot traffic emissions in mid-sized cities”. *Atmospheric Environment* 41.17, 3658–3671. DOI: <https://doi.org/10.1016/j.atmosenv.2006.12.045>.
- Wagenbrenner, N. S., J. M. Forthofer, B. K. Lamb, K. S. Shannon, and B. W. Butler (2016). “Downscaling surface wind predictions from numerical weather prediction models in complex terrain with WindNinja”. *Atmospheric Chemistry and Physics* 16.8, 5229–5241. DOI: [10.5194/acp-16-5229-2016](https://doi.org/10.5194/acp-16-5229-2016).
- Wang, L., C. Jang, Y. Zhang, K. Wang, Q. Zhang, D. Streets, J. Fu, Y. Lei, J. Schreifels, K. He, J. Hao, Y.-F. Lam, J. Lin, N. Meskhidze, S. Voorhees, D. Evarts, and S. Phillips (2010). “Assessment of air quality benefits from national air pollution control policies in China. Part I: Background, emission scenarios and evaluation of meteorological predictions”. *Atmospheric Environment* 44.28, 3442–3448. DOI: <https://doi.org/10.1016/j.atmosenv.2010.05.051>.
- Whiteman, C. D., B. Pospichal, S. Eisenbach, P. Weihs, C. B. Clements, R. Steinacker, E. Mursch-Radlgruber, M. Dorninger, C. D. Whiteman, B. Pospichal, S. Eisenbach, P. Weihs, C. B. Clements, R. Steinacker, E. Mursch-Radlgruber, and M. Dorninger (2004). “Inversion Breakup in Small Rocky Mountain and Alpine Basins”. *Journal of Applied Meteorology* 43.8, 1069–1082. DOI: [10.1175/1520-0450\(2004\)043<1069:IBISRM>2.0.CO;2](https://doi.org/10.1175/1520-0450(2004)043<1069:IBISRM>2.0.CO;2).
- World Meteorological Organization (2014). *Guide to Meteorological Instruments and Methods of Observation*. Geneva: World Meteorological Organization.
- Wyngaard, J. C. (2004). “Toward Numerical Modeling in the “Terra Incognita””. *Journal of the Atmospheric Sciences* 61.14, 1816–1826. DOI: [10.1175/1520-0469\(2004\)061<1816:TNMITT>2.0.CO;2](https://doi.org/10.1175/1520-0469(2004)061<1816:TNMITT>2.0.CO;2).
- Xu, H., Y. Wang, and M. Wang (2018). “The Performance of a Scale-Aware Nonlocal PBL Scheme for the Subkilometer Simulation of a Deep CBL over the Taklimakan Desert”. *Advances in Meteorology* 2018, 1–12. DOI: [10.1155/2018/8759594](https://doi.org/10.1155/2018/8759594).

- Yoo, J.-M., Y.-R. Lee, D. Kim, M.-J. Jeong, W. R. Stockwell, P. K. Kundu, S.-M. Oh, D.-B. Shin, and S.-J. Lee (2014). “New indices for wet scavenging of air pollutants (O₃, CO, NO₂, SO₂, and PM₁₀) by summertime rain”. *Atmospheric Environment* 82, 226–237. DOI: <https://doi.org/10.1016/j.atmosenv.2013.10.022>.
- Zardi, D. and C. D. Whiteman (2013). “Diurnal Mountain Wind Systems”. In: *Mountain Weather Research and Forecasting - Recent Progress and Current Challenges*. Ed. by F. K. Chow, S. F. J. De Wekker, and S. B. J. Springer, Dordrecht, 35–119. DOI: [10.1007/978-94-007-4098-3_2](https://doi.org/10.1007/978-94-007-4098-3_2).
- Zhang, H., Z. Pu, and X. Zhang (2013). “Examination of Errors in Near-Surface Temperature and Wind from WRF Numerical Simulations in Regions of Complex Terrain”. *Weather and Forecasting* 28.3, 893–914. DOI: [10.1175/WAF-D-12-00109.1](https://doi.org/10.1175/WAF-D-12-00109.1).
- Zhang, H., G. Chen, J. Hu, S.-H. Chen, C. Wiedinmyer, M. Kleeman, and Q. Ying (2014). “Evaluation of a seven-year air quality simulation using the Weather Research and Forecasting (WRF)/Community Multiscale Air Quality (CMAQ) models in the eastern United States”. *Science of The Total Environment* 473-474, 275–285. DOI: <https://doi.org/10.1016/j.scitotenv.2013.11.121>.
- Zhang, K. and S. Batterman (2010). “Near-road air pollutant concentrations of CO and PM_{2.5}: A comparison of MOBILE6.2/CALINE4 and generalized additive models”. *Atmospheric Environment* 44.14, 1740–1748. DOI: <https://doi.org/10.1016/j.atmosenv.2010.02.008>.
- Zhang, Y., M. Bocquet, V. Mallet, C. Seigneur, and A. Baklanov (2012a). “Real-time air quality forecasting, part I: History, techniques, and current status”. *Atmospheric Environment* 60, 632–655. DOI: <https://doi.org/10.1016/j.atmosenv.2012.06.031>.
- (2012b). “Real-time air quality forecasting, part II: State of the science, current research needs, and future prospects”. *Atmospheric Environment* 60, 656–676. DOI: <https://doi.org/10.1016/j.atmosenv.2012.02.041>.
- Zhou, B., J. S. Simon, and F. K. Chow (2014). “The Convective Boundary Layer in the Terra Incognita”. *Journal of the Atmospheric Sciences* 71.7, 2545–2563. DOI: [10.1175/JAS-D-13-0356.1](https://doi.org/10.1175/JAS-D-13-0356.1).

Chapter 4

Diurnal and seasonal dynamics of near-ground thermal stratification across neighboring Amazon forest and cropland sites

4.1 Abstract

Thermal stratification within and above forest canopies is relevant for the exchange of mass, heat and momentum between forests and the atmosphere. Here we study the diurnal and seasonal dynamics of vertical temperature profiles in a dense Amazon forest, as well as a comparison of these dynamics between forested and non-forested landscapes. We achieve this through a comparative analysis using two meteorological towers, one located in a primary forest and the other in a neighboring agricultural site. Our results show that thermal stratification within the forest canopy can be divided in three profile types. During the daytime, the forest is characterized by a below-canopy temperature inversion (stably stratified) and neutral or unstable conditions above-canopy. At night, the situation is reversed with near neutral conditions in the lower layers and a stable atmosphere starting either within canopy or above the canopy top. This diurnal oscillation occurs almost simultaneously and with opposite behaviors below- and above-canopy, with temperature gradients switching signs around 06 and 18 local time. The dry season results in stronger and more persistent daytime below-canopy inversions, and a nighttime inversion with larger gradients and starting within canopy (instead of above). The thermal stratification near the forest surface is mostly unaffected from the turbulence above the canopy top. In contrast to forest, the cropland site is characterized by mostly unstable conditions during the day and a temperature inversion during the night. Our results provide new insights on the dynamics of thermal stratification within forest canopies and could be useful for model-based studies on land-atmosphere interactions and forest loss impacts.

4.2 Introduction

Some of the main impacts of global change originate from land use/land cover changes (Foley et al., 2005). One of the most extensive land cover transformations occurring in the world is the loss of tropical forests in the Amazon (Supplementary Fig. C1; Hansen et al., 2013; Potapov et al., 2017), which may be further exacerbated in the future due to a variety of factors including fires, droughts and social issues (Lambin et al., 2003; Le Page et al., 2017; Salazar et al., 2018). Forest conversion to pastureland or cropland due to agricultural expansion has been a major driver of this loss (Morton et al., 2006; Gibbs et al., 2010). Threats to the Amazon forests have raised concerns about the potential impacts that the loss of these forests might have on the climate at local to global scales (Costa et al., 2007; Swann et al., 2015). Essential for the understanding and prediction of these impacts is the study of differences between vegetated landscapes (e.g. forests and pastureland or cropland) and how these differences affect land-atmosphere interactions (Bonan, 2008; Ellison et al., 2017).

It has long been known that a characteristic feature of the near-ground atmosphere in forests, and particularly in the Amazon, is the formation of below-canopy temperature inversion layers (i.e. stable layers) during daytime (e.g. Shuttleworth, 1985; Fitzjarrald et al., 1990; Culf et al., 1997). Within these layers, air temperature increases in the upward direction, i.e. it is higher in the canopy than at the ground surface. Here, the ‘canopy layer’ refers to the continuous crown layer, which differs from the more general meaning of ‘canopy layer’ that ranges from the surface to the mean tree/plant/building height (see, e.g., Rotach and Calanca, 2015). The formation of these temperature gradients occurs due to the effect of the vertical canopy structure on incident solar radiation, which is mostly absorbed in the upper canopy layers (Motzer, 2005; Goulden et al., 2006; Hardwick et al., 2015) and only a small fraction reaches the forest floor (Shuttleworth, 1984). These *undercanopy inversions* (we will use this term for any inversion occurring below the canopy top) are not unique of forests and can occur, instead, in any closed-canopy ecosystem in which solar radiation is predominantly absorbed in the canopy, causing a higher heating there than in the ground surface beneath (e.g. Jacobs et al., 1992). However, as compared to pastureland or cropland landscapes, Amazon forests can form much deeper inversion layers due to their tall trees and dense canopies (Fitzjarrald et al., 1990; Makarieva et al., 2006; Hardwick et al., 2015). A distinctive characteristic of Amazon forests, with dense and heterogeneous canopies, is that the upper and lower canopy layers

remain significantly decoupled during the day, due to the absorption of momentum in the upper canopy (e.g. Santana et al., 2018), with little turbulence able to penetrate and destroy the temperature inversion near the surface (Kruijt et al., 2000). This result contrasts with those from studies in forests with more homogeneous canopies (Dupont and Patton, 2012), open canopies (Gorsel et al., 2011) or in crops (Jacobs et al., 1992).

Undercanopy inversions are inherently dynamic. The diurnal cycle of incident solar radiation leads to a marked diurnal cycle of temperature gradients. Typical daytime conditions are a canopy warmer than the soil beneath it, i.e. a temperature inversion, whereas the soil remains warmer at nighttime, due to a rapid radiative cooling of the upper canopy (Makarieva et al., 2006; Szarzynski and Anhof, 2001). This diurnal variability has been generally described through average temperature profiles for daytime (inversion) and nighttime (no inversion) (e.g. Miller et al., 2007; Tóta et al., 2008; Fuentes et al., 2016). However, since solar radiation is highly variable at sub-daily time scales, typical daytime/nighttime temperature profiles provide only a simplified characterization of the diurnal cycle of undercanopy thermal stratification. A more detailed description of this diurnal evolution has not received wide attention.

Alternation between dry and wet seasons is a fundamental feature of climate in Equatorial Amazon, with manifold implications for natural and social phenomena (Restrepo-Coupe et al., 2013). For instance, around our study sites, there is a marked seasonality in precipitation, but there is little indication of water limitation in forests during the dry season (Hutyra et al., 2007; Restrepo-Coupe et al., 2013). The seasonal variability of the diurnal cycle of undercanopy thermal stratification has also received little attention in previous studies. For instance, Tóta et al., 2008 highlighted that undercanopy temperature profiles in an Amazon forest site (Reserva Biológica do Cuieiras) exhibit some common patterns between dry and wet seasons, while differ in that the dry season is relatively warmer. However, a more detailed description of the seasonal dynamics of thermal stratification in the Amazon forests is lacking.

Here we conduct an analysis of observational data aimed at advancing the understanding and quantitative characterization of the diurnal and seasonal dynamics of undercanopy thermal stratification in the Amazon forests, as well as of how these dynamics differ between forested and non-forested landscapes. We achieve this through a comparative analysis of two meteorological towers, one located in the Tapajós National Forest and the other in a neighboring site with cropland cover (more details are provided in Section 4.3).

We want to highlight three motivations for the present study. First, the current understanding of these dynamics is far from complete. Second, although there is no definitive evidence at present for specific impacts of such dynamics on climate (Theobald et al., 2015), a number of studies do indicate the possibility of relevant impacts through, for instance, their influence on land-atmosphere exchanges of scalars (Albertson et al., 2001; Staebler and Fitzjarrald, 2005; Miller et al., 2007; Pypker et al., 2007; Dupont and Patton, 2012; Freire et al., 2017; Santos et al., 2019). And third, current meteorological and chemical transport models rarely incorporate a detailed enough representation of in-canopy stability and turbulence (Theobald et al., 2015), missing these dynamics and how they can be altered by forest loss. The relevance of our findings regarding these motivations will be discussed in Section 4.5.

The remainder of the paper is organized as follows: section 4.3 describes the data and methods, section 4.4 presents results from the comparison between the forest and cropland sites (section 4.4.1), as well as new insights into the dynamics of forest inversions (section 4.4.2), which are discussed in section 4.5. Finally, conclusions are drawn in section 4.6.

4.3 Data and Methods

Data comes from two eddy covariance towers located in the state of Pará, Brazil (Fig. 4.1), which were established by the project Large Scale Biosphere-Atmosphere Experiment in Amazonia (LBA-ECO). The towers are approximately 20 km apart (straight line) in contrasting landscapes: one is located in a national forest reserve, identified as *Km67 Primary Forest Site* (54.95 W, 2.85 S), and the other in a cropland field, identified as *km77 Cropland Site* (54.89 W, 3.02 S). We will refer to both sites as K67 (forest) and K77 (cropland) from here on.

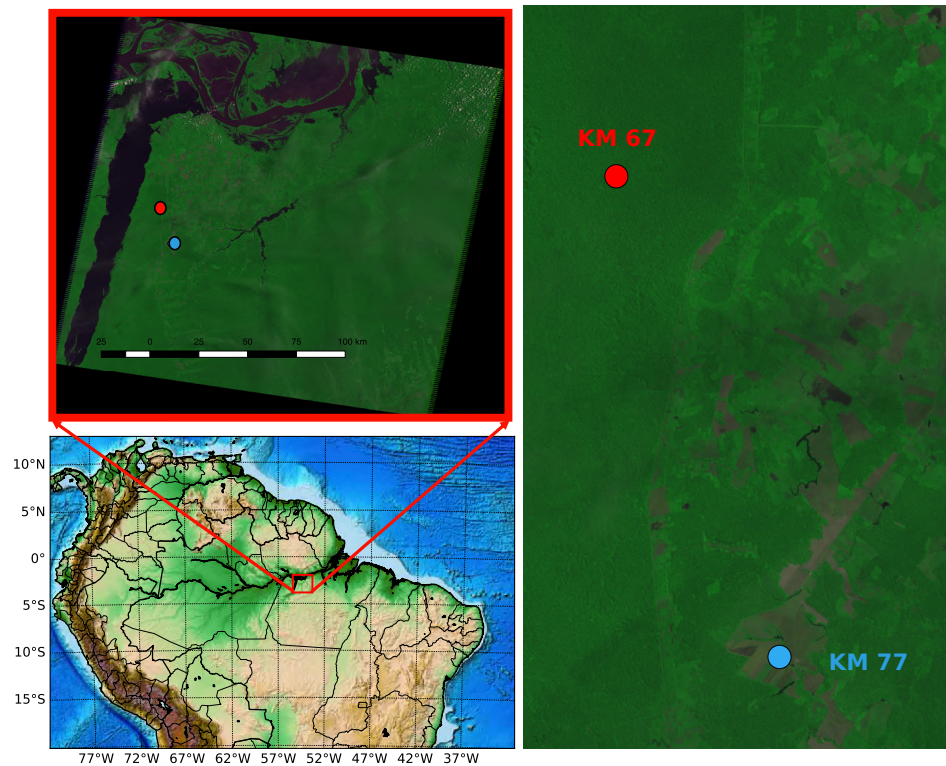


Figure 4.1: Location of K67 and K77 flux tower sites with topography (bottom panel) and LANDSAT-5 satellite image for 2004-08-31 (top and right panels).

The forest site (the K67 tower) is located on a flat terrain at the Tapajós National Forest (Belterra, State of Pará, Brazilian Amazon). The forest in the vicinity of the tower can be classified as primary (with few indications of anthropogenic disturbance, Hutrya et al., 2007). It is characterized by a continuous canopy from 18 to 40 m, with emergent trees up to 55 m (Nepstad et al., 2002), a relatively constant light absorption and a leaf area density gradually decreasing with height (Stark et al., 2012; Stark et al., 2015). The site receives 1920 mm of mean annual rainfall with a dry season (months with <100 mm of rainfall) that extends from July to December (Hutrya et al., 2007).

The second site (K77 tower) is located on a 500 ha field covered by cropland and surrounded by primary and secondary forest. The site is located east of the BR-163 highway 77 km marker (~25 km east of the Tapajós River), an area with extensive agricultural development. This site was converted from forest to pasture in the early nineties (Sakai et al., 2004). During the period of measurements (2001–2005), land use practice at the field changed from pasture to cultivation of upland rice and soybean, after the field was burned and plowed in November 2001 (Acevedo

et al., 2004; Fitzjarrald and Sakai, 2010).

Data used in this study are vertical profiles of temperature and water vapor concentration, as well as friction velocity (u_*) and wind speed (WS) at the top of each tower (i.e. above the canopy in the forest site; Table 4.1), covering a common 4-year observation period (2002–2005). For further details about the data and instrumentation, we refer the reader to (Hutyra et al., 2007; Sakai et al., 2004) and the LBA-ECO CD-03 (Fitzjarrald and Sakai, 2010) and CD-10 (Hutyra et al., 2008a; Hutyra et al., 2008b; Hutyra et al., 2008c).

Table 4.1: Site and data descriptions. Further information can be found in Fitzjarrald and Sakai, 2010; Hutyra et al., 2008a; Hutyra et al., 2008b.

Site	Biome type	Canopy height (m)	Measurement period (M/Y) 1 h resolution	Measurement levels* (m) WS, u_* : 64.1, 57.8
K67	Tropical rainforest	~40	01/02 - 01/06 1 h resolution	n=9: 0.6-61.9 WS, u_* : 64.1, 57.8
K77	Pasture-Agriculture	~0-0.6	01/01 - 12/05 0.5 h resolution	n=3: 2.2-11.3

*Number of T & H_2O measurement heights and its range (first line) and the measurement height of eddy fluxes (second line).

Raw data was processed to keep only measurements with complete data for a given date/time (i.e., measurements with missing data in any of the variables of interest are discarded). All analyses are performed using data from the common period (2002–2005). After data processing, the analyses are carried using 18,165 (49% in the dry season) and 63,278 (47% in the dry season) complete measurements for the forest (K67) and cropland (K77) sites, respectively. The large difference in the number of profiles for each site is mainly owing to the finer temporal resolution of measurements in the cropland site and data gaps in the forest site, but it is considered large enough to guarantee robust statistics for the diurnal and seasonal analysis.

Original data of atmospheric water vapor content is given as water vapor concentration at K67 and as specific humidity at K77. Here, we present them as mixing ratio in order to gain comparability across sites. Additionally, we calculated vapor pressure deficit (VPD) profiles (i.e., at each measurement level) as an indication of evaporative potential. Values of saturation vapor pressure, needed for VPD, were calculated from measured air temperature following Bolton, 1980.

Seasonal analysis of the data is carried considering the period from January 1 to

June 30 as the wet season, and from July 1 to December 31 as the dry season, typical for the eastern Amazon and previously used for analysis at both sites (Hutyra et al., 2007; Sakai et al., 2004).

We performed an exploratory analysis of the mean daily evolution of temperature to identify the main types of profiles occurring at each site. The resulting profile types are used to characterize the vertical profiles of temperature into different categories, which are used for further analysis.

4.4 Results

4.4.1 Comparison between forest and cropland sites

Figure 4.2 shows the diurnal evolution of the mean (hourly averages) temperature profiles at the forest (Fig. 4.2a) and cropland (Fig. 4.2b) sites, for the wet (solid lines) and dry (dashed lines) seasons. As compared to cropland, the near-ground atmosphere in the forest is characterized by the presence of temperature inversions during the daytime, larger seasonal variations in inversion gradients (these gradients are more pronounced during the dry season), and smaller seasonal variations in surface temperature (lower than 1 °C at the forest site while up to 4 °C at the cropland site).

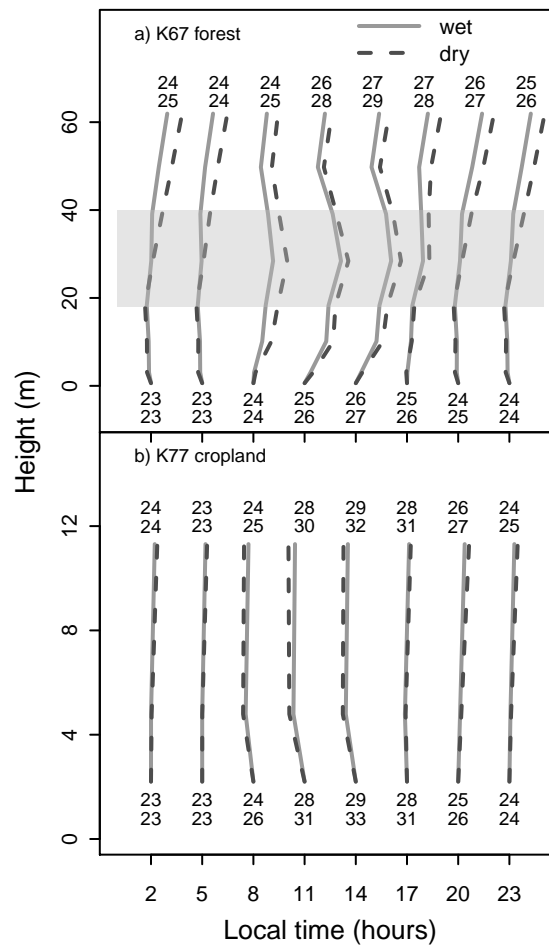


Figure 4.2: Daily evolution of the mean vertical temperature profile at a) K67 forest and b) K77 cropland sites. Mean profiles are standardized by subtracting at all levels the value of the lowest level. Values plotted represent temperature at the top/bottom of the profile for the wet/dry season in °C. The gray background in a) represents the continuous canopy between 18-40 m.

In the forest, all of the observed temperature profiles can be classified in three categories, relative to the location of inversions with respect to canopy boundaries (Fig. 4.3a-c). First, a temperature inversion occurs below the canopy bottom (below-canopy inversion, Fig. 4.3a); second, a temperature inversion starts within the canopy (in-canopy inversion, Fig. 4.3c); and third, a temperature inversion is absent below the canopy top (absent, Fig. 4.3b). Below- and in-canopy inversions are undercanopy inversions, but differ in their location relative to the continuous canopy. Box-plots in the figure describe the statistical distribution of all the studied profiles. For the sake of comparison, we use similar criteria to classify temperature profiles in the cropland

site: “inversion 1” when the temperature inversion starts at the lowest measurement level (Fig. 4.3d), “inversion 2” when it occurs between the second and third levels (Fig. 4.3f), and “absent” when there is no inversion (Fig. 4.3e). Although there is no data within the cropland canopy, the observed profiles in the cropland site are located at heights that would be below-canopy if a forest were there. Consequently, our comparison provides insights about the impacts of forest-to-cropland conversion on the near ground atmosphere. A direct consequence of forest absence would be the disappearance of relatively strong below- (Fig. 4.3a) and in-canopy (Fig. 4.3c) inversions.

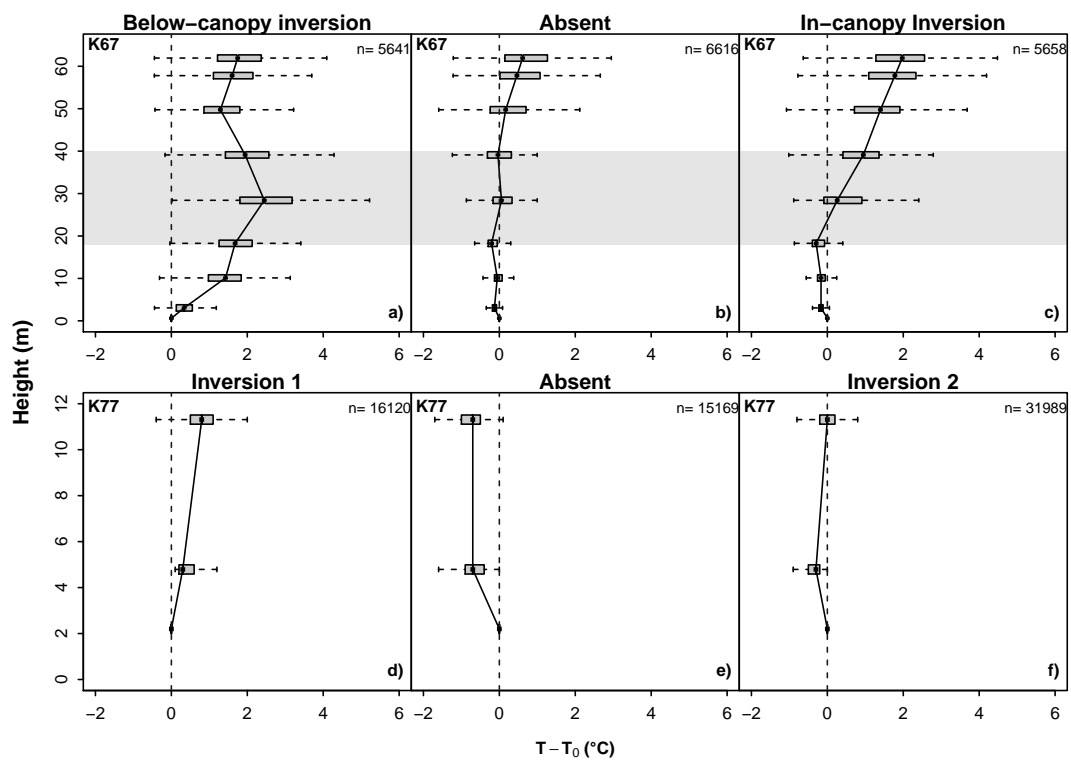


Figure 4.3: Categorized temperature profiles for the K67 forest site (top panels) and K77 cropland site (bottom panels). To facilitate visualization and comparison, all profiles have its origin point at zero, achieved by subtracting the value of the first level (T_0) to the values of all levels.

The occurrence of each type of temperature profile exhibits a marked diurnal cycle with pronounced differences between forest and cropland sites (Fig. 4.4) and a contrasting pattern of daytime/nighttime inversions. At the forest site, below-canopy inversion is the most common profile during daytime (particularly between 07 and 16 local time), while it is almost entirely absent during nighttime (from 18 to

05). The occurrence of below-canopy inversion peaks around noon, and the absence of undercanopy inversions (lighter bars in Fig. 4.4a,b) is rare during daytime. In contrast, at the cropland site, the absence of inversions is frequent during daytime, especially around noon (lighter bars in Fig. 4.4c,d). Also, during nighttime, while absence of inversion (below-canopy) is a common state at the forest (specially during the wet season, Fig. 4.4b), it is a rare state at the cropland site, where nighttime inversions (either 1 or 2) predominate.

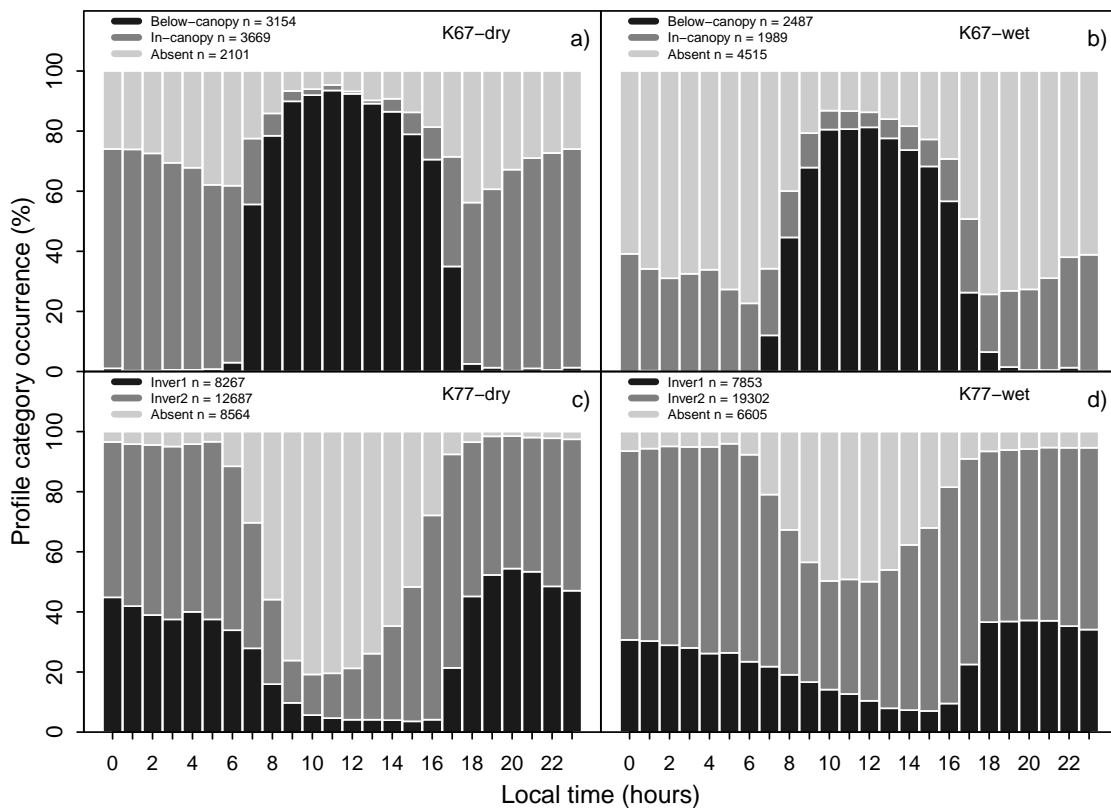


Figure 4.4: Diurnal cycle of occurrence of each temperature profile category in the forest (top, K67) and cropland (bottom, K77) sites during the dry (left) and wet (right) seasons. Values in legends are total number profiles for each category and season.

In the forest, undercanopy inversions predominate throughout the day during the dry season, with a transition between below-canopy inversion during daytime to in-canopy inversion at night (Fig. 4.4a). This points out a diurnal pattern in which an undercanopy inversion layer is moved up and down but it is not broken (except in the less frequent cases of absence inversion) during the dry season. This diurnal transition between daytime ground-based (below-canopy) and nighttime elevated (in-

canopy) inversions occurs, but it is less frequent, in the wet season (Fig. 4.4b). The most frequent transition in the wet season is between below-canopy inversion at daytime and absence of inversion at nighttime.

There is a marked seasonal difference in the nighttime structure of the under-canopy atmosphere in the forest. Nighttime in-canopy inversion predominates in the dry season, whereas absence of inversion is the most common nighttime state during the wet season (lighter bars are smaller in Fig. 4.4a than in Fig. 4.4b). In contrast, this seasonal difference is not evident in cropland: the absence of nighttime inversion (either 1 or 2) is a rare state in both seasons (Fig. 4.4c,d).

These dynamics of temperature inversions are fundamentally related with the dynamics of atmospheric moisture (hereby represented by mixing ratio r) and vapor pressure deficit (VPD) (Fig. 4.5). Considering the typical daytime state in both sites, there is a common pattern of seasonal variation between forest and cropland: temperature and VPD are higher in the dry season, while moisture is lower (this occurs at all levels of mean profiles). However, as compared to cropland, temperature, moisture, and VPD profiles exhibit a much lower seasonal variation at the forest site. For instance, the difference between temperature profiles for dry and wet seasons is lower than 1 C at every height in forest (Fig. 4.5a), while it is on the order of 2 C in cropland. As for moisture and VPD, this amplitude (i.e. difference between profiles) of seasonal variations is also reduced in the forest compared to the cropland site, especially near the surface.

At the forest site, the daytime stable conditions near the surface are associated to accumulation of scalars near the surface, indicated by higher mixing ratios of water vapor and carbon dioxide in the lower layers (Supplementary Fig. C2). This condition with higher water vapor concentrations and lower temperatures near the surface results in low VPD values, and consequently, in a low potential for surface evaporation. This result is in agreement with Miller et al., 2007; Tóta et al., 2008.

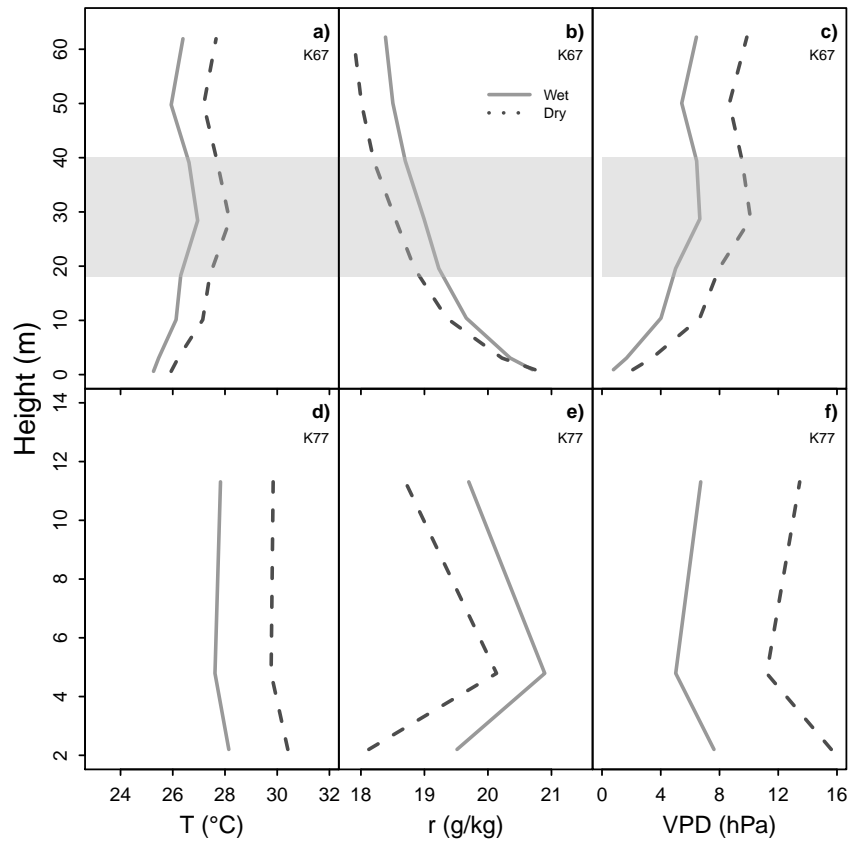


Figure 4.5: Mean daytime (07–17 local time) vertical profiles of temperature (a, d), mixing ratio (b, e) and vapor pressure deficit (c, f).

4.4.2 Forest

Below-canopy inversion layers in forest tend to last longer during the dry season (Fig. 4.6). Although the longest below-canopy inversion was observed during the wet season (13 hours), longer events (duration ranging from 9 to 11 hours) are much more common during the dry season. The duration of most below-canopy inversions is longer (shorter) or equal than 5 hours (6 hours) during the dry (wet) season.

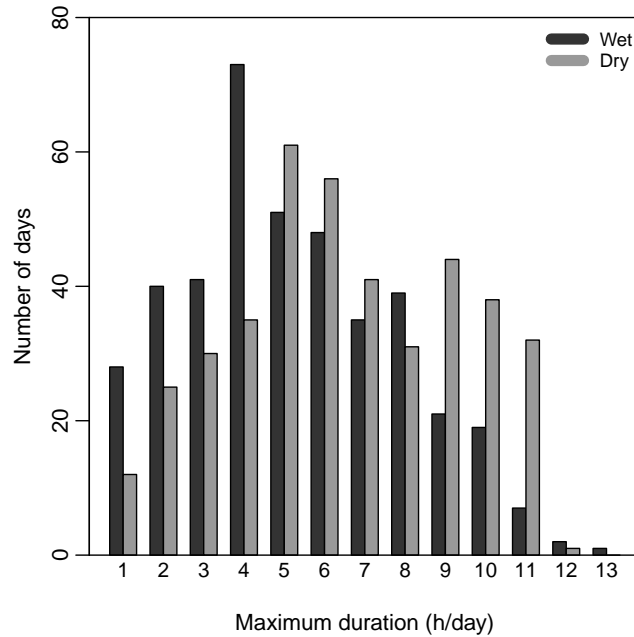


Figure 4.6: Maximum duration of below-canopy temperature inversion at forest for each season. Maximum duration refers to consecutive hourly profiles in a day categorized as surface-based inversion.

Temperature gradients exhibit an opposite pattern below and above the forest canopy, with some seasonal differences (Fig. 4.7). Below-canopy inversions ($\Delta T > 0$) at daytime are largely concurrent with unstable conditions ($\Delta T < 0$) above the canopy. This pattern is reversed at nighttime, wherein below-canopy instability ($\Delta T < 0$) coincides with above-canopy inversion ($\Delta T > 0$). Additionally, above-canopy inversions are generally weaker than below-canopy inversions. Maximum positive gradients above canopy are around $0.6 \times 10^{-1} \text{ }^\circ\text{C m}^{-1}$, whereas below canopy they range between around 0.8 and $1.1 \times 10^{-1} \text{ }^\circ\text{C m}^{-1}$.

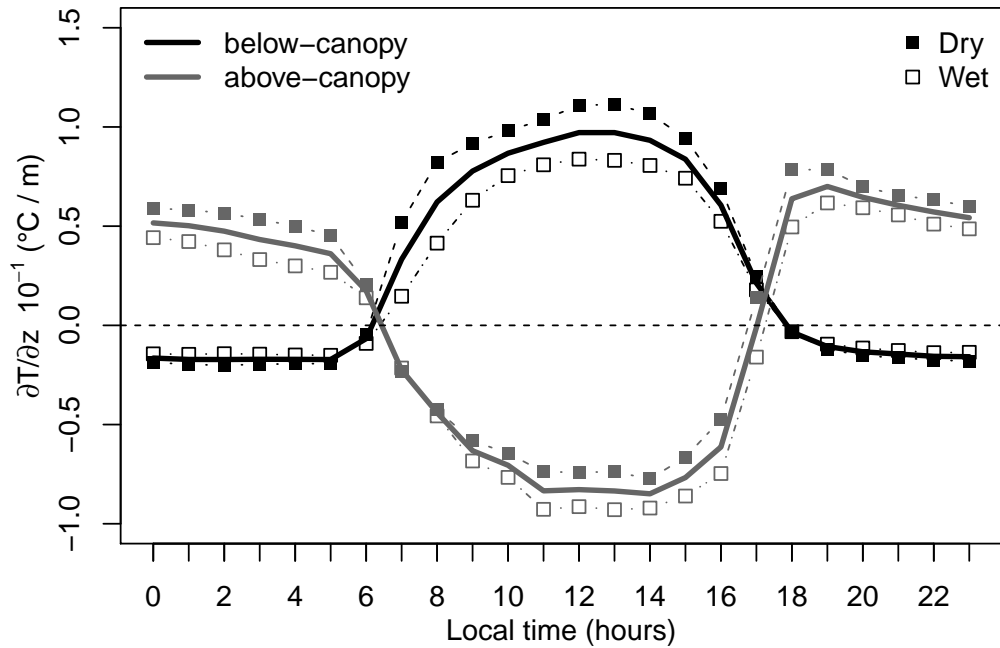


Figure 4.7: Diurnal cycles of temperature gradients above- and below-canopy, at the K67 forest site. Below-canopy: from 0.6m to 18m; Above-canopy: from 40m to 50m

An interesting feature of these patterns is that temperature gradients below and above the canopy switch signs in the early morning (≈ 06 local time) and late afternoon ($\approx 17-18$) (Fig. 4.7). This switching occurs almost simultaneously below and above the canopy, especially in the morning.

Figure 4.7 does not show large seasonal differences except for the magnitude of below-canopy gradients during the daytime, which are larger in the dry season. During the dry season below-canopy inversions are stronger from early morning to about noon, when the seasonal difference decreases and approaches zero in the late afternoon. At night, negative temperature gradients below the canopy are approximately equal for both seasons.

Although there is still some debate about the most reliable scale for determining the degree of coupling between above- and below-canopy layers (Acevedo et al., 2009; Thomas et al., 2013; Freundorfer et al., 2019), friction velocity (u_*) and wind speed (WS) above the canopy have been used as indicative of the degree of coupling in forests (Goulden et al., 1996; Santana et al., 2018). A common premise is that larger u_* and WS are linked to stronger coupling and, therefore, weaker undercanopy (either below- or in-canopy according to our categories) stability (e.g. Kruijt et al.,

2000; Santana et al., 2018). Figures 4.8 and 4.9 explore these relations.

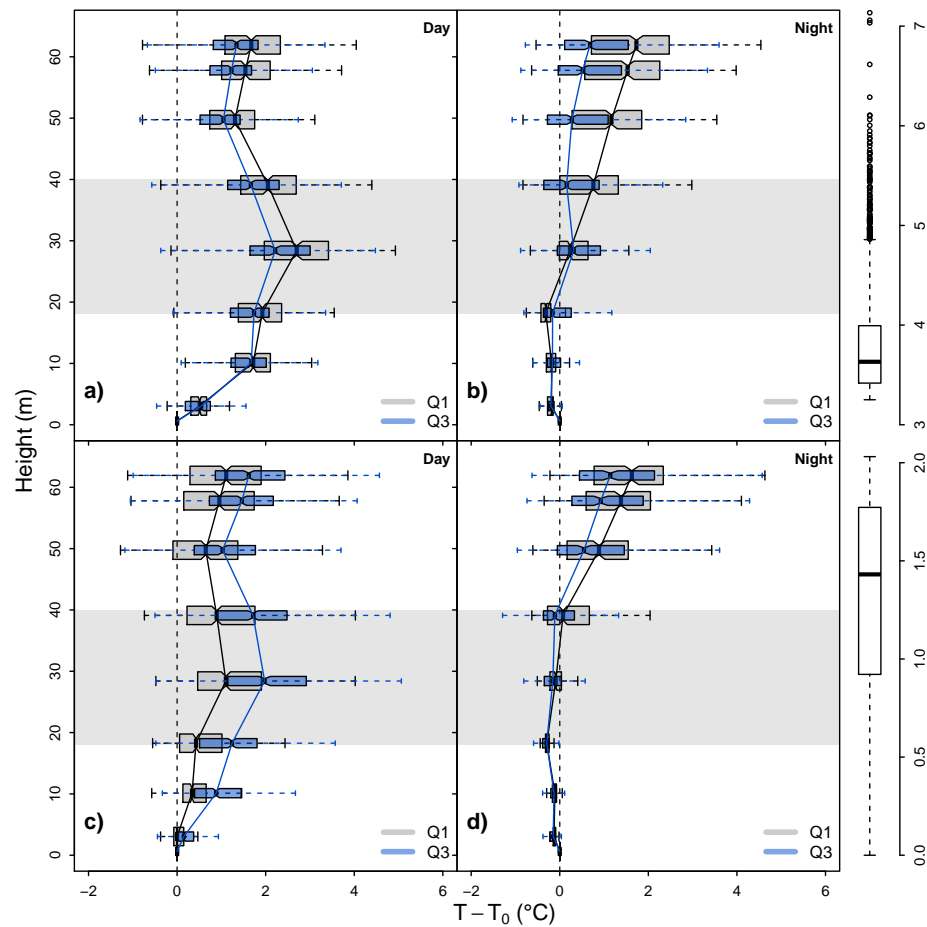


Figure 4.8: Temperature profiles during the day and night, for strong wind speeds (top, $WS > 3.3$ m/s) and weak wind speeds (bottom, $WS < 2$ m/s). Values in blue (gray) represent the upper (lower) quartile for either the strong (top) or weak (bottom) wind speed regimes. The boxplots in the right show the distribution of wind speed regimes in m/s.

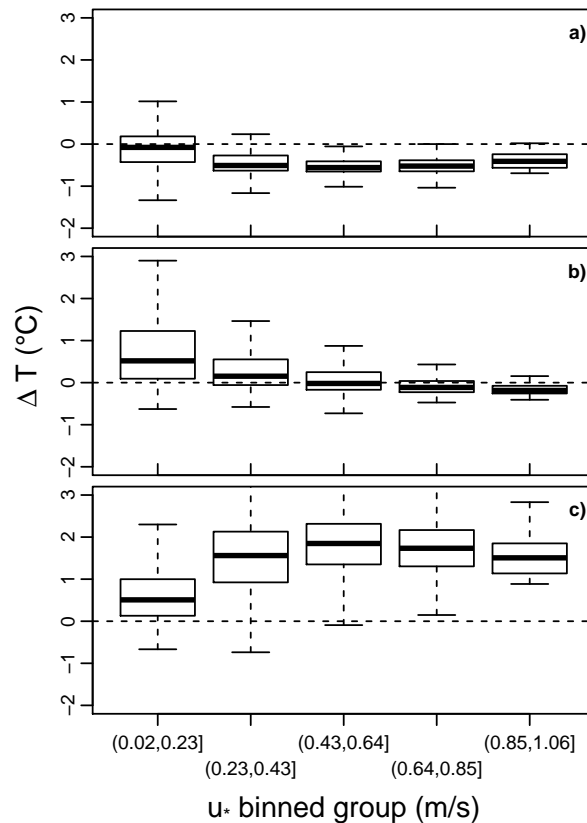


Figure 4.9: Temperature difference above the canopy (a; 40–50 m), in the canopy (b; 18–40 m) and below the canopy (c; 0.6–18 m) as a function of friction velocity. Values for daytime (07–17 local time).

Daytime inversions are not weaker for higher than for lower WS (Fig. 4.8a,c). Indeed, larger positive temperature gradients (i.e. stronger inversions) were found for higher WS values (Fig. 4.8c). This could be related to the fact that below-canopy turbulent transport depends much more on the below-canopy wind regime than on the turbulence strength above canopy (Freundorfer et al., 2019). Below-canopy inversion layers extend typically from ground-surface to the mid-canopy, with this depth not greatly varying between stronger and weaker winds (Fig. 4.8a,c). The strongest winds only seem to affect the temperature gradients in the upper-canopy layers (Fig. 4.8a). Collectively, these results suggest that increasing WS does not necessarily weaken below-canopy inversion layers. Although some coupling can occur even under stably stratified conditions (e.g. Jocher et al., 2018), this result suggests that the below-canopy layers are mostly unaffected from the turbulence strength above the canopy.

Figure 4.9 shows how the daytime temperature gradient varies with u_* at three different layers: above the canopy (Fig. 4.9a), within the canopy (Fig. 4.9b), and below the canopy (Fig. 4.9c). ΔT is not strictly the gradient but the difference in temperature between the top and bottom level in each layer, however, it is directly related with the sign and sensitivity of the gradient to u_* because the other factor in the gradient (i.e. Δz or the difference in elevation between the top and bottom level of each layer) is fixed for each layer.

The sensitivity of the sign and magnitude of the temperature gradients to variation in u_* differs between each layer. Above the canopy (Fig. 4.9a), this sensitivity is low and inversions (i.e. shallow inversions in the $\approx 20\text{m}$ depth layer above the canopy) are rare. In the canopy (Fig. 4.9b), there is a trend in which the temperature gradient decreases with increasing u_* . Increases in u_* lead to decreases in the positive temperature gradient found at lower values (< 0.43) to neutral or unstable conditions for the larger values (> 0.64). Nevertheless, below-canopy inversions (i.e. the typical daytime state, Figs. 4.4 and 4.8) seem to be less sensitive to variations in u_* and exhibit a counterintuitive trend (Fig. 4.9c). Below-canopy inversions are weaker, not stronger, for the lower u_* -values (first two boxes to the left). The sign and magnitude of the below-canopy inversion gradients do not vary greatly with greater u_* -values (last three boxes to the right). The fact that u_* seem to only have an effect in the canopy, but not below, can be an indication that most of the turbulence from above is absorbed there and does not reach the below-canopy layers.

4.5 Discussion

Due to its many environmental applications such as weather and climate forecasting and the exchange of scalars between vegetation and the atmosphere, many studies have focused on the understanding of micrometeorology within and above forest canopies (Dupont and Patton, 2012). In the Amazon forests, the LBA project has supported major advances in this regard (Gonçalves et al., 2013). One aspect of this understanding that has not received much attention is the quantitative characterization of the diurnal dynamics of undercanopy temperature inversions, as well as how this dynamics varies with seasons and between forested and non-forested landscapes. Our results provide new insights on the diurnal and seasonal dynamics. Of particular importance is the characterization of a diurnal cycle of undercanopy inversions in which an inversion layer oscillates up and down between the below-canopy layer

during daytime (Fig. 4.8a,c), and the in-canopy (Fig. 4.8b) or above-canopy (Fig. 4.8d) layers during nighttime. Figure 4.10 further clarifies this mechanism by showing how temperature gradients between consecutive levels vary throughout the day and between different layers: below-canopy and in-canopy. Despite some seasonal differences (e.g. in the intensity of nighttime elevated inversion), this oscillation occurs in both seasons (Fig. 4.10). We have no evidence of a similar mechanism under the cropland canopy, but it might be occurring as well. However, in either case, the potential effect of this mechanism on land-atmosphere interactions is likely related to the depth and strength of the undercanopy inversions, which is much larger in the forest.

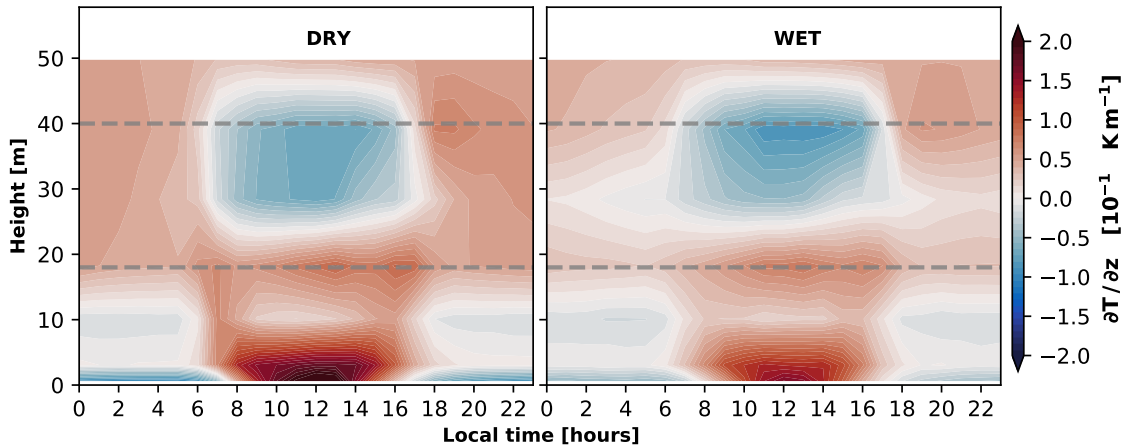


Figure 4.10: Diurnal oscillation of the undercanopy inversion layer occurring in both the dry (a) and wet (b) seasons. The inversion layer (red areas) oscillates between the below-canopy layer at daytime and the in-canopy or above canopy layers at nighttime. Gradients are computed between consecutive levels of measurement and represent average values for the whole study period.

Results presented in Figures 4.8 and 4.9 do not support the premise that higher above-canopy wind speed (WS) or friction velocity (u_*) are related directly to the occurrence of weaker undercanopy inversions, and hence suggest that other processes at play may alter this relation. Our present analysis demonstrates that an opposite relation (i.e. stronger stability under higher u_* or WS) is neither impossible nor rare in the Amazon forests. A more detailed classification of undercanopy inversions as in-canopy or below-canopy inversions seems to clarify this premise. While the strength of in-canopy inversions is inversely related with u_* (Fig. 4.9b), as expected, below-canopy inversions do not weaken, and can even strengthen, as u_* increases

(Fig. 4.9c). This suggests that the initial premise holds for the in-canopy but not for the below-canopy inversions, and that a generalization of undercanopy inversions (i.e. any inversion below the canopy top) may be misleading. This result could be related to the larger dependence of below-canopy turbulence on the wind conditions below- than above-canopy (Freundorfer et al., 2019).

One fundamental reason why these dynamics may be relevant is that they exert non-trivial effects on land-atmosphere exchanges of scalars (Albertson et al., 2001; Dupont and Patton, 2012). The extent to which these effects have impacts on climate at local or larger scales is uncertain. However, previous studies have highlighted the role of undercanopy inversions on the exchange of scalars. For instance, Miller et al., 2007 suggested that water vapor and carbon dioxide accumulated during the day in a nearby forest site due to the daytime stable stratification. Freire et al., 2017 found that the evolution of ozone concentrations in the Amazon forests is affected by the diurnal variability of below-canopy turbulent mixing, which should be considered for studying chemical and biophysical processes in forests. Additionally, some studies have associated errors in the calculation of carbon budgets with the decoupling of above- and below-canopy layers and thermal stratification within canopies (Wang et al., 2017; Jocher et al., 2018; Santos et al., 2019). Collectively, these studies imply that the described dynamics can have climate-relevant impacts, which could be large considering the extension of forests.

Climate models have been widely used to predict the potential consequences of the loss of Amazon forests on the climate at different spatial scales (Swann et al., 2015; Spracklen and Garcia-Carreras, 2015; Werth and Avissar, 2002). However, it is not clear that these models incorporate a detailed enough representation of undercanopy thermal stratification, as current parameterizations usually derive below-canopy turbulence from the above-canopy turbulence (Theobald et al., 2015). Some studies suggested that model predictions may be sensitive to the way in which these dynamics are represented within models (e.g. Siqueira and Katul, 2002; Santos et al., 2019). Consequently, there is a need for new approaches that include within-canopy processes for modeling surface-atmosphere interactions (Theobald et al., 2015; Saylor and Hicks, 2016). One challenge is that these dynamics take place at typical sub-grid scale of models: temperature variability within heights from ground-surface to 30–60 meters can be relatively large, whereas models usually have the lowest level located at heights of the order of tens of meters. Our results provide observation-based descriptions that may serve to test and improve parameterizations in order to represent, for

instance, the diurnal oscillation between below-canopy and in-canopy inversion layers that occurs in forests.

Overall, these considerations may be relevant for studies that are usually based on models, such as predictions of forest loss impacts, as well as how these impacts aggregate across scales. For instance, Russell et al., 2018 showed that forest thinning affects the degree of coupling between above- and below-canopy, which would be ignored if within canopy processes are not considered.

4.6 Conclusions

This study shows that thermal stratification within the forest canopy can be divided in three profile types: i) a temperature inversion from the surface to mid-canopy (below-canopy inversion); ii) a temperature inversion from within the canopy upwards (in-canopy inversion); and iii) a uniform temperature below the canopy top and an inversion above (absent).

In the forest site, the below-canopy layers are in general stably stratified during the day (below-canopy inversion (i)), while unstable at night (either in-canopy inversions (ii) or absent (iii)). In contrast, the cropland site typically presents unstable conditions during the day and stable conditions at night. Consequently, a direct impact of forest loss would be the disappearance of relatively strong temperature inversions near the surface during the day.

At the forest site, the daytime stable conditions near the surface are associated to a low potential for surface evaporation, due to low VPD values. In contrast, the cropland site presents larger VPD values and a larger seasonal variability.

At the forest site, temperature gradients above- and below-canopy present opposite patterns, but switch signs almost simultaneously in the early morning (06 local time) and late afternoon (18 local time). This pattern is present for both seasons, but the dry season is characterized by stronger and more persistent below-canopy inversions during the day, and an in-canopy inversion (dry season) or above-canopy inversion (wet season) at night.

Friction velocity and wind speed above the canopy seem to affect only the temperature gradient in the upper canopy layers, but the below-canopy thermal stratification is mostly unaffected from the turbulence above.

4.7 References

- Acevedo, O. C., O. L. L. Moraes, R. da Silva, D. R. Fitzjarrald, R. K. Sakai, R. M. Staebler, and M. J. Czikowsky (2004). “Inferring nocturnal surface fluxes from vertical profiles of scalars in an Amazon pasture”. *Global Change Biology* 10.5, 886–894. DOI: [10.1111/j.1529-8817.2003.00755.x](https://doi.org/10.1111/j.1529-8817.2003.00755.x).
- Acevedo, O. C., O. L. Moraes, G. A. Degrazia, D. R. Fitzjarrald, A. O. Manzi, and J. G. Campos (2009). “Is friction velocity the most appropriate scale for correcting nocturnal carbon dioxide fluxes?” *Agricultural and Forest Meteorology* 149.1, 1–10. DOI: [10.1016/J.AGRFORMET.2008.06.014](https://doi.org/10.1016/J.AGRFORMET.2008.06.014).
- Albertson, J. D., G. G. Katul, and P. Wiberg (2001). “Relative importance of local and regional controls on coupled water, carbon, and energy fluxes”. *Advances in Water Resources* 24.9-10, 1103–1118. DOI: [10.1016/S0309-1708\(01\)00042-2](https://doi.org/10.1016/S0309-1708(01)00042-2).
- Bolton, D. (1980). “The Computation of Equivalent Potential Temperature”. *Monthly Weather Review* 108.7, 1046–1053. DOI: [10.1175/1520-0493\(1980\)108<1046:TCOEPT>2.0.CO;2](https://doi.org/10.1175/1520-0493(1980)108<1046:TCOEPT>2.0.CO;2).
- Bonan, G. B. (2008). “Forests and Climate Change: Forcings, Feedbacks, and the Climate Benefits of Forests”. *Science* 320.5882, 1444–1449. DOI: [10.1126/science.1155121](https://doi.org/10.1126/science.1155121).
- Costa, M. H., S. N. M. Yanagi, P. J. O. P. Souza, A. Ribeiro, and E. J. P. Rocha (2007). “Climate change in Amazonia caused by soybean cropland expansion, as compared to caused by pastureland expansion”. *Geophysical Research Letters* 34.7, L07706. DOI: [10.1029/2007GL029271](https://doi.org/10.1029/2007GL029271).
- Culf, A., G. Fisch, Y. Malhi, and C. Nobre (1997). “The influence of the atmospheric boundary layer on carbon dioxide concentrations over a tropical forest”. *Agricultural and Forest Meteorology* 85.3-4, 149–158. DOI: [10.1016/S0168-1923\(96\)02412-4](https://doi.org/10.1016/S0168-1923(96)02412-4).
- Dupont, S. and E. G. Patton (2012). “Influence of stability and seasonal canopy changes on micrometeorology within and above an orchard canopy: The CHATS experiment”. *Agricultural and Forest Meteorology* 157, 11–29. DOI: [10.1016/J.AGRFORMET.2012.01.011](https://doi.org/10.1016/J.AGRFORMET.2012.01.011).
- Ellison, D., C. E. Morris, B. Locatelli, D. Sheil, J. Cohen, D. Murdiyarso, V. Gutierrez, M. van Noordwijk, I. F. Creed, J. Pokorny, D. Gaveau, D. V. Spracklen, A. B. Tobella, U. Ilstedt, A. J. Teuling, S. G. Gebrehiwot, D. C. Sands, B. Muys, B. Verbist, E. Springgay, Y. Sugandi, and C. A. Sullivan (2017). “Trees, forests and

- water: Cool insights for a hot world”. *Global Environmental Change* 43, 51–61. DOI: [10.1016/J.GLOENVCHA.2017.01.002](https://doi.org/10.1016/J.GLOENVCHA.2017.01.002).
- Fitzjarrald, D. and R. Sakai (2010). *LBA-ECO CD-03 Flux-Meteorological Data, km 77 Pasture Site, Para, Brazil: 2000-2005*. ORNL DAAC, Oak Ridge, Tennessee, USA. eng. DOI: [10.3334/ORNLDAAAC/962](https://doi.org/10.3334/ORNLDAAAC/962).
- Fitzjarrald, D. R., K. E. Moore, O. M. R. Cabral, J. Scola, A. O. Manzi, and L. D. de Abreu Sá (1990). “Daytime turbulent exchange between the Amazon forest and the atmosphere”. *Journal of Geophysical Research* 95.D10, 16825. DOI: [10.1029/JD095iD10p16825](https://doi.org/10.1029/JD095iD10p16825).
- Foley, J. A., R. DeFries, G. P. Asner, C. Barford, G. Bonan, S. R. Carpenter, F. S. Chapin, M. T. Coe, G. C. Daily, H. K. Gibbs, J. H. Helkowski, T. Holloway, E. A. Howard, C. J. Kucharik, C. Monfreda, J. A. Patz, I. C. Prentice, N. Ramankutty, and P. K. Snyder (2005). “Global Consequences of Land Use”. *Science* 309.5734, 570–574. DOI: [10.1126/science.1111772](https://doi.org/10.1126/science.1111772).
- Freire, L. S., T. Gerken, J. Ruiz-Plancarte, D. Wei, J. D. Fuentes, G. G. Katul, N. L. Dias, O. C. Acevedo, and M. Chamecki (2017). “Turbulent mixing and removal of ozone within an Amazon rainforest canopy”. *Journal of Geophysical Research: Atmospheres* 122.5, 2791–2811. DOI: [10.1002/2016JD026009](https://doi.org/10.1002/2016JD026009).
- Freundorfer, A., I. Rehberg, B. E. Law, and C. Thomas (2019). “Forest wind regimes and their implications on cross-canopy coupling”. *Agricultural and Forest Meteorology* 279, 107696. DOI: [10.1016/J.AGRFORMET.2019.107696](https://doi.org/10.1016/J.AGRFORMET.2019.107696).
- Fuentes, J. D., M. Chamecki, R. M. Nascimento dos Santos, C. Von Randow, P. C. Stoy, G. Katul, D. Fitzjarrald, A. Manzi, T. Gerken, A. Trowbridge, L. Souza Freire, J. Ruiz-Plancarte, J. M. Furtunato Maia, J. Tóta, N. Dias, G. Fisch, C. Schumacher, O. Acevedo, J. Rezende Mercer, and A. M. Yañez-Serrano (2016). “Linking Meteorology, Turbulence, and Air Chemistry in the Amazon Rain Forest”. *Bulletin of the American Meteorological Society* 97.12, 2329–2342. DOI: [10.1175/BAMS-D-15-00152.1](https://doi.org/10.1175/BAMS-D-15-00152.1).
- Gibbs, H. K., A. S. Ruesch, F. Achard, M. K. Clayton, P. Holmgren, N. Ramankutty, and J. A. Foley (2010). “Tropical forests were the primary sources of new agricultural land in the 1980s and 1990s.” *Proceedings of the National Academy of Sciences of the United States of America* 107.38, 16732–7. DOI: [10.1073/pnas.0910275107](https://doi.org/10.1073/pnas.0910275107).
- Gonçalves, L. G. G. de, J. S. Borak, M. H. Costa, S. R. Saleska, I. Baker, N. Restrepo-Coupe, M. N. Muza, B. Poulter, H. Verbeeck, J. B. Fisher, M. A. Arain, P. Arkin,

- B. P. Cestaro, B. Christoffersen, D. Galbraith, X. Guan, B. J. van den Hurk, K. Ichii, H. M. A. Imbuzeiro, A. K. Jain, N. Levine, C. Lu, G. Miguez-Macho, D. R. Roberti, A. Sahoo, K. Sakaguchi, K. Schaefer, M. Shi, W. J. Shuttleworth, H. Tian, Z.-L. Yang, and X. Zeng (2013). “Overview of the Large-Scale Biosphere–Atmosphere Experiment in Amazonia Data Model Intercomparison Project (LBA-DMIP)”. *Agricultural and Forest Meteorology* 182-183, 111–127. DOI: [10.1016/J.AGRFORMET.2013.04.030](https://doi.org/10.1016/J.AGRFORMET.2013.04.030).
- Gorsel, E. van, I. N. Harman, J. J. Finnigan, and R. Leuning (2011). “Decoupling of air flow above and in plant canopies and gravity waves affect micrometeorological estimates of net scalar exchange”. *Agricultural and Forest Meteorology* 151.7, 927–933. DOI: [10.1016/J.AGRFORMET.2011.02.012](https://doi.org/10.1016/J.AGRFORMET.2011.02.012).
- Goulden, M. L., S. D. Miller, and H. R. da Rocha (2006). “Nocturnal cold air drainage and pooling in a tropical forest”. *Journal of Geophysical Research* 111.D8, D08S04. DOI: [10.1029/2005JD006037](https://doi.org/10.1029/2005JD006037).
- Goulden, M. L., J. W. Munger, S.-M. Fan, B. C. Daube, and S. C. Wofsy (1996). “Measurements of carbon sequestration by long-term eddy covariance: methods and a critical evaluation of accuracy”. *Global Change Biology* 2.3, 169–182. DOI: [10.1111/j.1365-2486.1996.tb00070.x](https://doi.org/10.1111/j.1365-2486.1996.tb00070.x).
- Hansen, M. C., P. V. Potapov, R. Moore, M. Hancher, S. A. Turubanova, A. Tyukavina, D. Thau, S. V. Stehman, S. J. Goetz, T. R. Loveland, A. Kommareddy, A. Egorov, L. Chini, C. O. Justice, and J. R. G. Townshend (2013). “High-resolution global maps of 21st-century forest cover change.” *Science* 342.6160, 850–3. DOI: [10.1126/science.1244693](https://doi.org/10.1126/science.1244693).
- Hardwick, S. R., R. Toumi, M. Pfeifer, E. C. Turner, R. Nilus, and R. M. Ewers (2015). “The relationship between leaf area index and microclimate in tropical forest and oil palm plantation: Forest disturbance drives changes in microclimate”. *Agricultural and Forest Meteorology* 201, 187–195. DOI: [10.1016/J.AGRFORMET.2014.11.010](https://doi.org/10.1016/J.AGRFORMET.2014.11.010).
- Hutyra, L., J. Munger, E. Gottlieb, B. Daube, P. Camargo, and S. Wofsy (2008a). *LBA-ECO CD-10 H2O Profiles at km 67 Tower Site, Tapajos National Forest. ORNL DAAC, Oak Ridge, Tennessee, USA*. eng. DOI: [10.3334/ORNLDAAC/861](https://doi.org/10.3334/ORNLDAAC/861).
- (2008b). *LBA-ECO CD-10 Temperature Profiles at km 67 Tower Site, Tapajos National Forest. ORNL DAAC, Oak Ridge, Tennessee, USA*. eng. DOI: [10.3334/ORNLDAAC/863](https://doi.org/10.3334/ORNLDAAC/863).

- Hutyra, L., S. Wofsy, and S. Saleska (2008c). *LBA-ECO CD-10 CO₂ and H₂O Eddy Fluxes at km 67 Tower Site, Tapajos National Forest. ORNL DAAC, Oak Ridge, Tennessee, USA*. eng. DOI: [10.3334/ORNLDAAC/860](https://doi.org/10.3334/ORNLDAAC/860).
- Hutyra, L. R., J. W. Munger, S. R. Saleska, E. Gottlieb, B. C. Daube, A. L. Dunn, D. F. Amaral, P. B. de Camargo, and S. C. Wofsy (2007). “Seasonal controls on the exchange of carbon and water in an Amazonian rain forest”. *Journal of Geophysical Research: Biogeosciences* 112.G3. DOI: [10.1029/2006JG000365](https://doi.org/10.1029/2006JG000365).
- Jacobs, A., J. van Boxel, and R. Shaw (1992). “The dependence of canopy layer turbulence on within-canopy thermal stratification”. *Agricultural and Forest Meteorology* 58.3-4, 247–256. DOI: [10.1016/0168-1923\(92\)90064-B](https://doi.org/10.1016/0168-1923(92)90064-B).
- Jocher, G., J. Marshall, M. B. Nilsson, S. Linder, G. De Simon, T. Hörnlund, T. Lundmark, T. Näsholm, M. Ottosson Löfvenius, L. Tarvainen, G. Wallin, and M. Peichl (2018). “Impact of Canopy Decoupling and Subcanopy Advection on the Annual Carbon Balance of a Boreal Scots Pine Forest as Derived From Eddy Covariance”. *Journal of Geophysical Research: Biogeosciences* 123.2, 303–325. DOI: [10.1002/2017JG003988](https://doi.org/10.1002/2017JG003988).
- Kruijt, B., Y. Malhi, J. Lloyd, A. D. Nobre, A. C. Miranda, M. G. P. Pereira, A. Culf, and J. Grace (2000). “Turbulence Statistics Above And Within Two Amazon Rain Forest Canopies”. *Boundary-Layer Meteorology* 94.2, 297–331. DOI: [10.1023/A:1002401829007](https://doi.org/10.1023/A:1002401829007).
- Lambin, E. F., H. J. Geist, and E. Lepers (2003). “Dynamics of Land-Use and Land-Cover Change in Tropical Regions”. *Annual Review of Environment and Resources* 28.1, 205–241. DOI: [10.1146/annurev.energy.28.050302.105459](https://doi.org/10.1146/annurev.energy.28.050302.105459).
- Le Page, Y., D. Morton, C. Hartin, B. Bond-Lamberty, J. M. C. Pereira, G. Hurtt, and G. Asrar (2017). “Synergy between land use and climate change increases future fire risk in Amazon forests”. *Earth System Dynamics* 8.4, 1237–1246. DOI: [10.5194/esd-8-1237-2017](https://doi.org/10.5194/esd-8-1237-2017).
- Makarieva, A. M., V. G. Gorshkov, and B.-L. Li (2006). “Conservation of water cycle on land via restoration of natural closed-canopy forests: implications for regional landscape planning”. *Ecological Research* 21.6, 897–906. DOI: [10.1007/s11284-006-0036-6](https://doi.org/10.1007/s11284-006-0036-6).
- Miller, S. D., M. L. Goulden, and H. R. da Rocha (2007). “The effect of canopy gaps on subcanopy ventilation and scalar fluxes in a tropical forest”. *Agricultural and Forest Meteorology* 142.1, 25–34. DOI: [10.1016/J.AGRFORMET.2006.10.008](https://doi.org/10.1016/J.AGRFORMET.2006.10.008).

- Morton, D. C., R. S. DeFries, Y. E. Shimabukuro, L. O. Anderson, E. Arai, F. del Bon Espirito-Santo, R. Freitas, and J. Morissette (2006). “Cropland expansion changes deforestation dynamics in the southern Brazilian Amazon”. *Proceedings of the National Academy of Sciences* 103.39, 14637–14641. DOI: [10.1073/pnas.0606377103](https://doi.org/10.1073/pnas.0606377103).
- Motzer, T. (2005). “Micrometeorological aspects of a tropical mountain forest”. *Agricultural and Forest Meteorology* 135.1-4, 230–240. DOI: [10.1016/J.AGRFORMET.2005.11.019](https://doi.org/10.1016/J.AGRFORMET.2005.11.019).
- Nepstad, D. C., P. Moutinho, M. B. Dias-Filho, E. Davidson, G. Cardinot, D. Markewitz, R. Figueiredo, N. Vianna, J. Chambers, D. Ray, J. B. Guerreiros, P. Lefebvre, L. Sternberg, M. Moreira, L. Barros, F. Y. Ishida, I. Tohlver, E. Belk, K. Kalif, and K. Schwalbe (2002). “The effects of partial throughfall exclusion on canopy processes, aboveground production, and biogeochemistry of an Amazon forest”. *Journal of Geophysical Research* 107.D20, 8085. DOI: [10.1029/2001JD000360](https://doi.org/10.1029/2001JD000360).
- Potapov, P., M. C. Hansen, L. Laestadius, S. Turubanova, A. Yaroshenko, C. Thies, W. Smith, I. Zhuravleva, A. Komarova, S. Minnemeyer, and E. Esipova (2017). “The last frontiers of wilderness: Tracking loss of intact forest landscapes from 2000 to 2013”. *Science Advances* 3.1. DOI: [10.1126/sciadv.1600821](https://doi.org/10.1126/sciadv.1600821).
- Pypker, T., M. Unsworth, B. Lamb, E. Allwine, S. Edburg, E. Sulzman, A. Mix, and B. Bond (2007). “Cold air drainage in a forested valley: Investigating the feasibility of monitoring ecosystem metabolism”. *Agricultural and Forest Meteorology* 145.3-4, 149–166. DOI: [10.1016/J.AGRFORMET.2007.04.016](https://doi.org/10.1016/J.AGRFORMET.2007.04.016).
- Restrepo-Coupe, N., H. R. da Rocha, L. R. Hutyrá, A. C. da Araujo, L. S. Borma, B. Christoffersen, O. M. Cabral, P. B. de Camargo, F. L. Cardoso, A. C. L. da Costa, D. R. Fitzjarrald, M. L. Goulden, B. Kruijt, J. M. Maia, Y. S. Malhi, A. O. Manzi, S. D. Miller, A. D. Nobre, C. von Randow, L. D. A. Sá, R. K. Sakai, J. Tota, S. C. Wofsy, F. B. Zanchi, and S. R. Saleska (2013). “What drives the seasonality of photosynthesis across the Amazon basin? A cross-site analysis of eddy flux tower measurements from the Brasil flux network”. *Agricultural and Forest Meteorology* 182-183, 128–144. DOI: [10.1016/J.AGRFORMET.2013.04.031](https://doi.org/10.1016/J.AGRFORMET.2013.04.031).
- Rotach, M. and P. Calanca (2015). “Microclimate”. In: *Encyclopedia of Atmospheric Sciences (Second Edition)*. Ed. by G. R. North, J. Pyle, and F. Zhang. Second Edition. Oxford: Academic Press, 258–264. DOI: <https://doi.org/10.1016/B978-0-12-382225-3.00225-5>.

- Russell, E. S., H. Liu, H. Thistle, B. Strom, M. Greer, and B. Lamb (2018). “Effects of thinning a forest stand on sub-canopy turbulence”. *Agricultural and Forest Meteorology* 248, 295–305. DOI: [10.1016/J.AGRFORMET.2017.10.019](https://doi.org/10.1016/J.AGRFORMET.2017.10.019).
- Sakai, R. K., D. R. Fitzjarrald, O. L. Moraes, R. M. Staebler, O. C. Acevedo, M. J. Czikowsky, R. da Silva, E. Brait, and V. Miranda (2004). “Land-use change effects on local energy, water, and carbon balances in an Amazonian agricultural field”. *Global Change Biology* 10.5, 895–907. DOI: [10.1111/j.1529-8817.2003.00773.x](https://doi.org/10.1111/j.1529-8817.2003.00773.x).
- Salazar, A., A. Sanchez, J. C. Villegas, J. F. Salazar, D. Ruiz Carrascal, S. Sitch, J. D. Restrepo, G. Poveda, K. J. Feeley, L. M. Mercado, P. A. Arias, C. A. Sierra, M. d. R. Uribe, A. M. Rendón, J. C. Pérez, G. Murray Tortarolo, D. Mercado-Bettin, J. A. Posada, Q. Zhuang, and J. S. Dukes (2018). “The ecology of peace: preparing Colombia for new political and planetary climates”. *Frontiers in Ecology and the Environment* 16.9, 525–531. DOI: [10.1002/fee.1950](https://doi.org/10.1002/fee.1950).
- Santana, R. A., C. Q. Dias-Júnior, J. T. da Silva, J. D. Fuentes, R. S. do Vale, E. G. Alves, R. M. N. dos Santos, and A. O. Manzi (2018). “Air turbulence characteristics at multiple sites in and above the Amazon rainforest canopy”. *Agricultural and Forest Meteorology* 260-261, 41–54. DOI: [10.1016/J.AGRFORMET.2018.05.027](https://doi.org/10.1016/J.AGRFORMET.2018.05.027).
- Santos, M., E. Santos, C. Wagner-Riddle, S. Brown, K. Stropes, R. Staebler, and J. Nippert (2019). “Evaluating a Lagrangian inverse model for inferring isotope CO₂ exchange in plant canopies”. *Agricultural and Forest Meteorology* 276-277, 107651. DOI: [10.1016/J.AGRFORMET.2019.107651](https://doi.org/10.1016/J.AGRFORMET.2019.107651).
- Saylor, R. D. and B. B. Hicks (2016). “New directions: Time for a new approach to modeling surface-atmosphere exchanges in air quality models?” *Atmospheric Environment* 129, 229–233. DOI: [10.1016/J.ATMOENV.2016.01.032](https://doi.org/10.1016/J.ATMOENV.2016.01.032).
- Shuttleworth, W. J. (1985). “DAILY VARIATIONS OF TEMPERATURE AND HUMIDITY WITHIN AND ABOVE AMAZONIAN FOREST”. *Weather* 40.4, 102–108. DOI: [10.1002/j.1477-8696.1985.tb07489.x](https://doi.org/10.1002/j.1477-8696.1985.tb07489.x).
- Shuttleworth, W. J. (1984). “Observations of radiation exchange above and below Amazonian forest”. *Quarterly Journal of the Royal Meteorological Society* 110.466, 1163–1169. DOI: [10.1002/qj.49711046623](https://doi.org/10.1002/qj.49711046623).
- Siqueira, M. and G. Katul (2002). “Estimating Heat Sources And Fluxes In Thermally Stratified Canopy Flows Using Higher-Order Closure Models”. *Boundary-Layer Meteorology* 103.1, 125–142. DOI: [10.1023/A:1014526305879](https://doi.org/10.1023/A:1014526305879).

- Spracklen, D. V. and L. Garcia-Carreras (2015). “The impact of Amazonian deforestation on Amazon basin rainfall”. *Geophysical Research Letters* 42.21, 9546–9552. DOI: [10.1002/2015GL066063](https://doi.org/10.1002/2015GL066063).
- Staebler, R. M. and D. R. Fitzjarrald (2005). “Measuring Canopy Structure and the Kinematics of Subcanopy Flows in Two Forests”. *Journal of Applied Meteorology* 44.8, 1161–1179. DOI: [10.1175/JAM2265.1](https://doi.org/10.1175/JAM2265.1).
- Stark, S. C., B. J. Enquist, S. R. Saleska, V. Leitold, J. Schiette, M. Longo, L. F. Alves, P. B. Camargo, and R. C. Oliveira (2015). “Linking canopy leaf area and light environments with tree size distributions to explain Amazon forest demography”. *Ecology Letters* 18.7. Ed. by M. Uriarte, 636–645. DOI: [10.1111/ele.12440](https://doi.org/10.1111/ele.12440).
- Stark, S. C., V. Leitold, J. L. Wu, M. O. Hunter, C. V. de Castilho, F. R. C. Costa, S. M. McMahon, G. G. Parker, M. T. Shimabukuro, M. A. Lefsky, M. Keller, L. F. Alves, J. Schiette, Y. E. Shimabukuro, D. O. Brandão, T. K. Woodcock, N. Higuchi, P. B. de Camargo, R. C. de Oliveira, and S. R. Saleska (2012). “Amazon forest carbon dynamics predicted by profiles of canopy leaf area and light environment”. *Ecology Letters* 15.12. Ed. by J. Chave, 1406–1414. DOI: [10.1111/j.1461-0248.2012.01864.x](https://doi.org/10.1111/j.1461-0248.2012.01864.x).
- Swann, A. L., M. Longo, R. G. Knox, E. Lee, and P. R. Moorcroft (2015). “Future deforestation in the Amazon and consequences for South American climate”. *Agricultural and Forest Meteorology* 214–215, 12–24. DOI: [10.1016/J.AGRFORMET.2015.07.006](https://doi.org/10.1016/J.AGRFORMET.2015.07.006).
- Szarzynski, J. and D. Anhof (2001). “Micrometeorological conditions and canopy energy exchanges of a neotropical rain forest (Surumoni-Crane Project, Venezuela)”. *Plant Ecology* 153.1/2, 231–239. DOI: [10.1023/A:1017536512887](https://doi.org/10.1023/A:1017536512887).
- Theobald, M., B. Loubet, C. Ammann, L. Branislava, B. Chojnicki, L. Ganzeveld, B. Grosz, M. Kaasik, S. Noe, J. Olejnik, J. Rinne, M. Shapkalijevski, D. Simpson, O. Tchepel, J.-P. Tuovinen, T. Weidinger, and R. Wichink Kruit (2015). “In-Canopy Turbulence—State of the Art and Potential Improvements”. In: *Review and Integration of Biosphere-Atmosphere Modelling of Reactive Trace Gases and Volatile Aerosols*. Ed. by R.-S. Massad and B. Loubet. Dordrecht: Springer Netherlands, 215–223. DOI: [10.1007/978-94-017-7285-3_13](https://doi.org/10.1007/978-94-017-7285-3_13).
- Thomas, C. K., J. G. Martin, B. E. Law, and K. Davis (2013). “Toward biologically meaningful net carbon exchange estimates for tall, dense canopies: Multi-level eddy covariance observations and canopy coupling regimes in a mature Douglas-

- fir forest in Oregon”. *Agricultural and Forest Meteorology* 173, 14–27. DOI: [10.1016/J.AGRFORMET.2013.01.001](https://doi.org/10.1016/J.AGRFORMET.2013.01.001).
- Tóta, J., D. R. Fitzjarrald, R. M. Staebler, R. K. Sakai, O. M. M. Moraes, O. C. Acevedo, S. C. Wofsy, and A. O. Manzi (2008). “Amazon rain forest subcanopy flow and the carbon budget: Santarém LBA-ECO site”. *Journal of Geophysical Research: Biogeosciences* 113.G1, n/a–n/a. DOI: [10.1029/2007JG000597](https://doi.org/10.1029/2007JG000597).
- Wang, X., C. Wang, and B. Bond-Lamberty (2017). “Quantifying and reducing the differences in forest CO₂-fluxes estimated by eddy covariance, biometric and chamber methods: A global synthesis”. *Agricultural and Forest Meteorology* 247, 93–103. DOI: [10.1016/J.AGRFORMET.2017.07.023](https://doi.org/10.1016/J.AGRFORMET.2017.07.023).
- Werth, D. and R. Avissar (2002). “The local and global effects of Amazon deforestation”. *Journal of Geophysical Research* 107.D20, 8087. DOI: [10.1029/2001JD000717](https://doi.org/10.1029/2001JD000717).

Chapter 5

Conclusions and Outlook

The main goal of this dissertation was to examine the influence of atmospheric stability and land cover modifications on land-atmosphere interactions. This was achieved through the analysis of three case studies, concerning two different environments: two case studies in urban valleys, and one in a forest landscape. These case studies approach the general problem from different but interrelated perspectives. The studies in urban valleys focus on different aspects of the transport of pollutants with implications for air quality, while the forest case mainly deals with the dynamics of thermal stratification near the surface, with implications for scalar transport. This work was conducted using both numerical models and a variety of meteorological and air quality observations. Given that the preceding chapters include a conclusion section, only the most relevant findings and their contribution to the general problem are presented here.

First, this work challenged the common premise in urban planning that urban heat island (UHI) mitigation strategies (i.e., urban cooling) have a net beneficial effect for urban environmental quality and sustainability. Using large-eddy simulations for an idealized urban valley it was shown that urban cooling, through interactions with atmospheric stability and transport processes, might have adverse impacts on air quality. Results indicate that cooling the urban area increases the time that the valley atmosphere remains stably stratified, thereby limiting ventilation and increasing pollutant concentrations near the surface, especially for strong atmospheric stability. It was also shown that an UHI-induced circulation can enhance ventilation through ascending motions in the center of urban valleys, and that urban cooling weakens this transport mechanism, having an adverse impact for air quality. However, the aim is not to discourage UHI mitigation strategies in general, but to highlight the need to consider and assess both the positive and negative impacts of such measures through case-specific analysis, prior to their implementation.

Second, the transport of mobile emissions (represented by a passive tracer) in the

Aburrá Valley (Colombia) was studied for a period of severe air pollution through high-resolution numerical simulations. As compared to other areas in the valley, some areas to the south and southeast were identified as more prone to accumulation of pollutants (tracer). An analysis with an index relating concentrations to emissions reveals that transport processes from other areas play a considerable role in this accumulation. Such transport is mainly related to a prevalent along-valley flow from the north and relatively weaker winds on the eastern slope. PBL heights exceeding the mountain ridges were related to improved pollutant ventilation due to enhanced vertical mixing and the coupling of the valley atmosphere with the synoptic flow, which creates an east-west cross-valley circulation. Strong atmospheric stability and PBL heights lower than the mountain ridges were associated to higher pollutant concentrations near the surface, due to reduced mixing and weaker winds. Although wet deposition was not considered, modelled tracer concentrations improved when rainfall was adequately captured by the model. This, along with previous results, highlights the influence of rainfall on air quality through effects on PBL height and atmospheric stability.

Third, the thermal stratification near the surface of a dense Amazon forest and a nearby cropland site were analyzed using observations from meteorological towers located at each site. The focus was given to the diurnal and seasonal dynamics of temperature profiles at the forest site, especially the formation and evolution of below-canopy inversion layers. Although the occurrence of below-canopy inversion layers in forests is well-known, the quantitative description of these layers' dynamics at sub-daily time scales has been largely overlooked. Results from the observed data analysis provide new insights on this dynamics, as well as on its seasonal variability. The daytime at the forest is characterized by the presence of below-canopy temperature inversion layers and unstable conditions above the canopy. At night, neutral or unstable conditions occur below the canopy, while temperature inversion occurs above canopy. Temperature gradients above and below canopy switch signs almost simultaneously, resulting in the occurrence of a temperature inversion (either above- or below-canopy) throughout the day. At the cropland site, thermal stratification near the surface resembles that of the forest above the canopy, which suggest that a direct consequence of forest loss would be the disappearance of daytime stable layers near the surface (i.e. in the ~ 30 m-height layer below the pre-existing forest canopy). This below-canopy stable layers at the forest site are associated to large moisture contents near the surface, resulting in a lower potential for surface evaporation. The diurnal

oscillation at the forest site of a temperature inversion below canopy at daytime and above canopy at night occurs for both the wet and dry seasons, but with stronger and more persistent inversions during the dry season. Collectively, these findings suggest that atmospheric models in which below canopy turbulence is derived from the conditions above the canopy may be missing an important influence of forests on land-atmosphere exchanges, with implications for forest loss studies.

Overall, this dissertation provides new evidence about how land heterogeneity, including pronounced elevation gradients in valleys and contrast between urban and rural land or forest and cropland landscapes, affect land-atmosphere interactions through effects on near-ground atmospheric stability. This has important implications for the transport of air pollutants in urban valleys (Chapters 2 and 3) as well as for land-atmosphere exchanges in forest landscapes. Future studies can expand on these topics by addressing several aspects not considered in this dissertation. For instance, in relation to Chapter 2, the simulations were performed for an idealized urban valley. Future research may consider, for instance, realistic cases with real topography and a more detailed representation of the urban area (e.g. using urban parameterizations), the use of radiation parameterizations instead of prescribed fluxes, as well as the influence of synoptic flows, moisture processes, and chemical reactions. Chapter 3 highlights the urgent need of a realistic emission inventory with high spatial resolution for the Aburrá Valley. This would allow full-chemistry simulations to evaluate all criteria pollutants, which should also include processes such as wet deposition that is critically relevant in the study area. With respect to the meteorological model performance, it seems relevant to perform sensitivity analysis of land surface parameterizations and to consider urban parameterizations, given the large extent of the urban area inside the valley. With respect to Chapter 4, one important direction for future research is the study of the impacts of below-canopy dynamics through comparison of model simulations with more or less detailed representations of it.

Appendix

A Supplementary figures for chapter 2

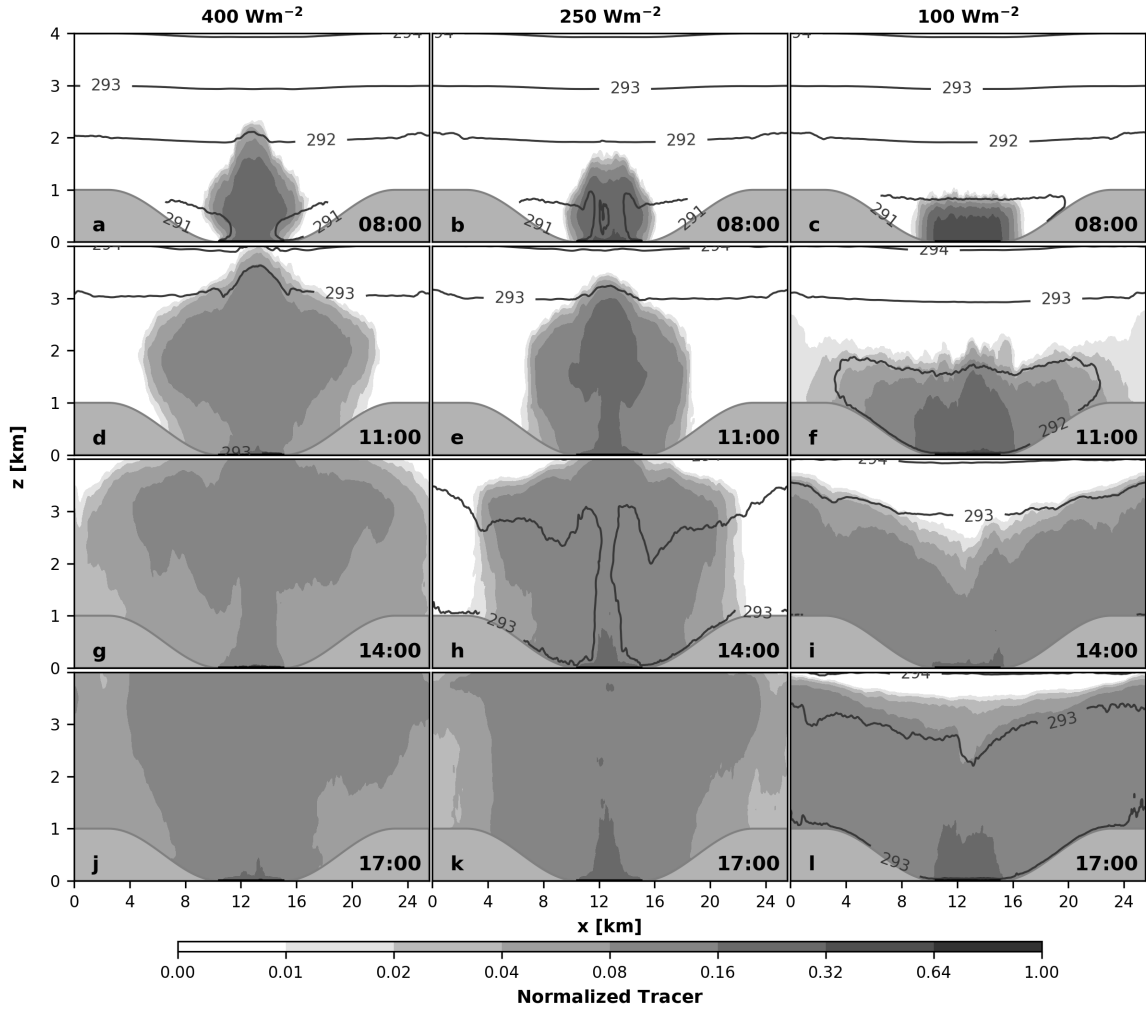


Figure A1: Daytime evolution of normalized tracer mixing ratio from morning (top) to afternoon (bottom), with low stability ($\partial\theta/\partial z = 1 \text{ K km}^{-1}$ at initial condition). UHI contrasts varies from 300 W m^{-2} (left) to 150 W m^{-2} (center) and no contrast, i.e., full-mitigation scenario (right). Isentropes are shown every 1 K.

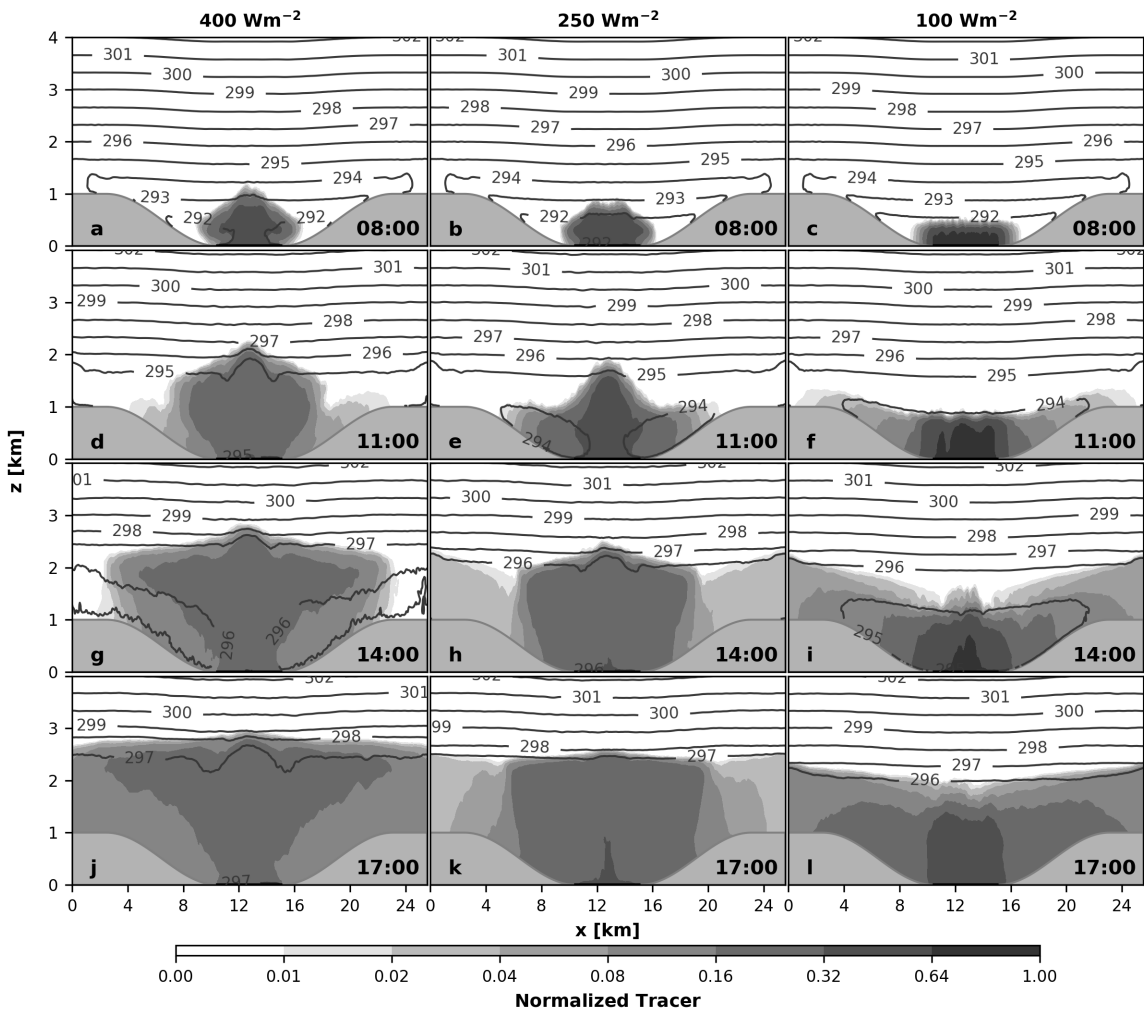


Figure A2: As in Fig. A1 but for high stability ($\partial\theta/\partial z = 3 \text{ K km}^{-1}$ at initial condition).

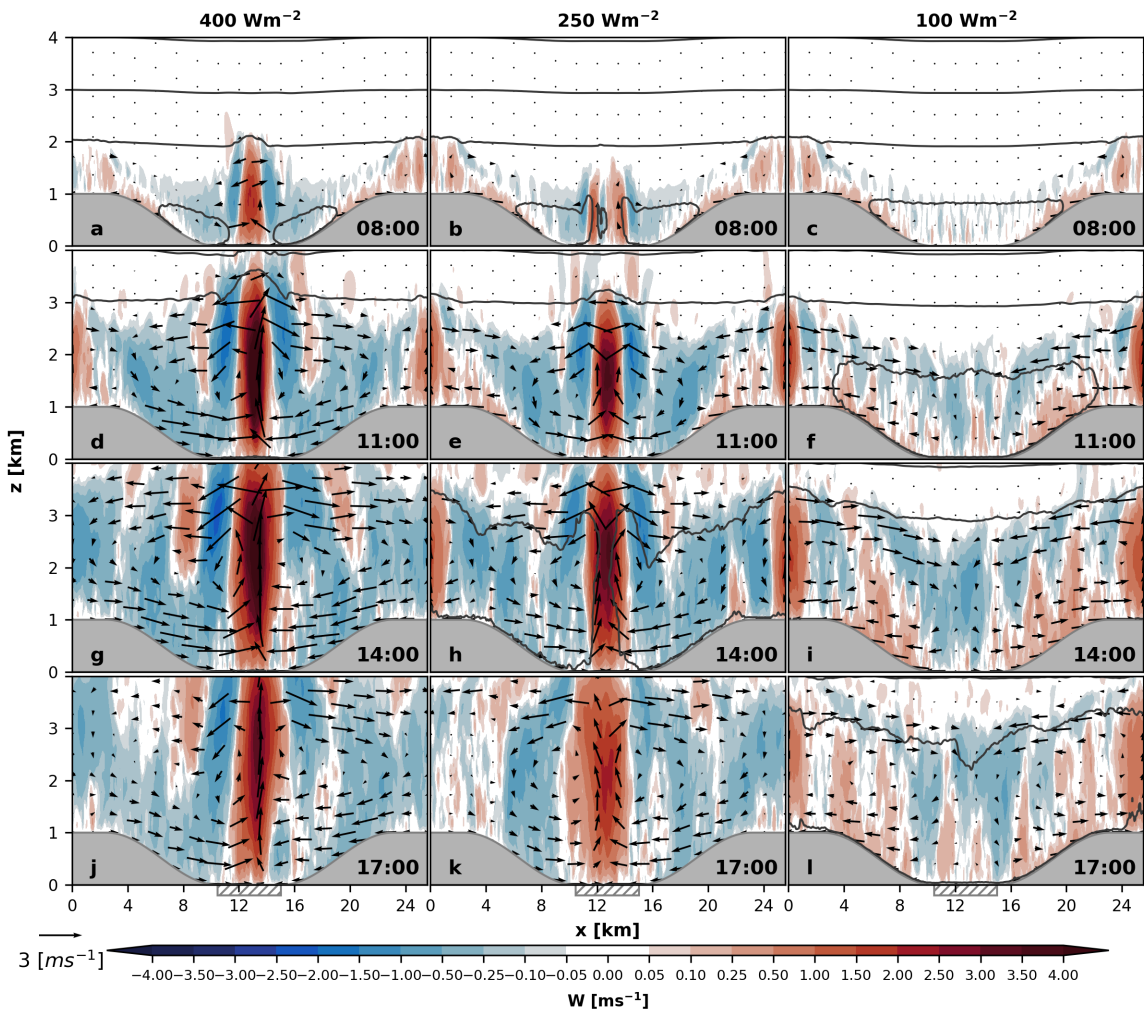


Figure A3: Daytime evolution of the wind field (vectors) starting with low stability. Colors show the w wind component.

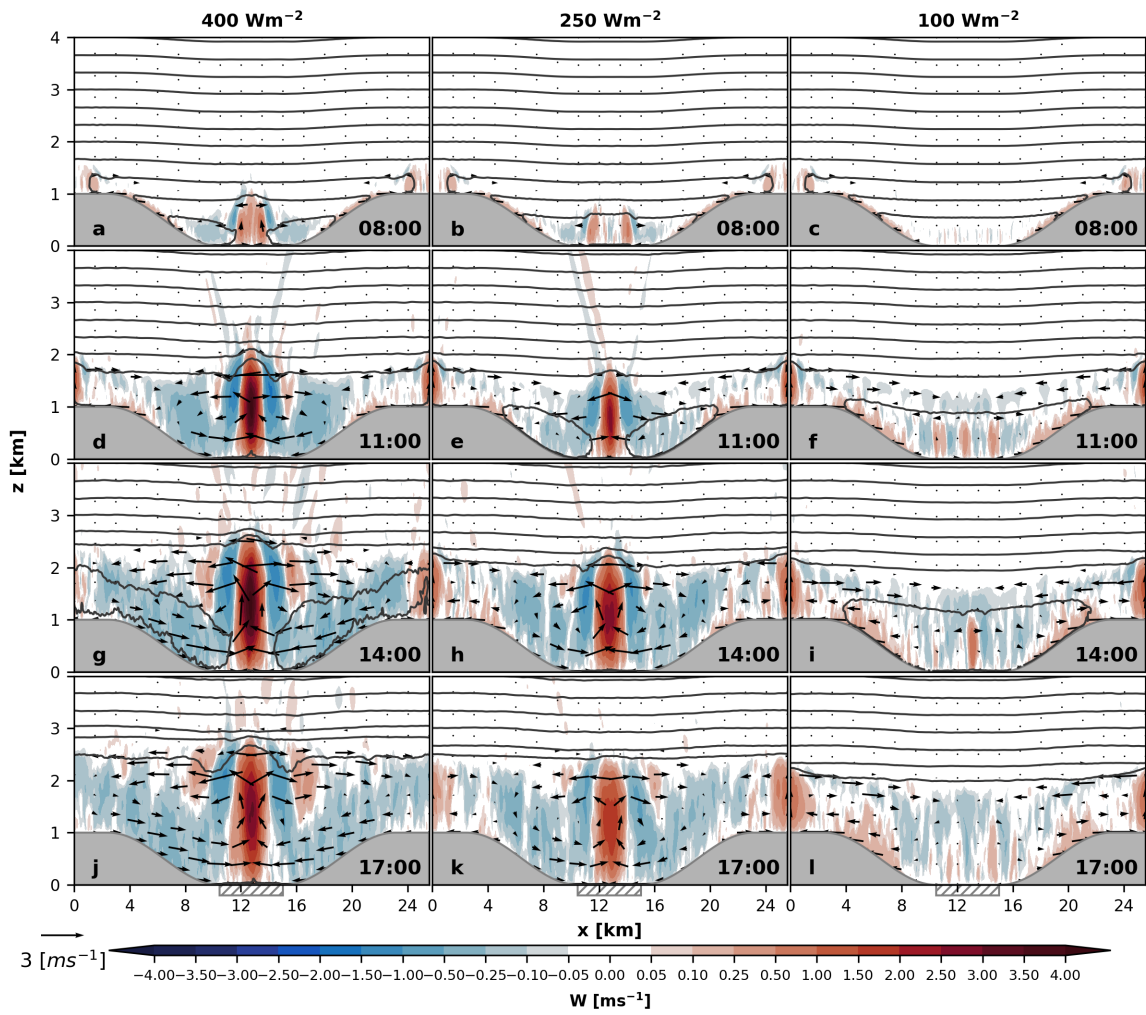


Figure A4: As in Fig. A3 but starting with high stability.

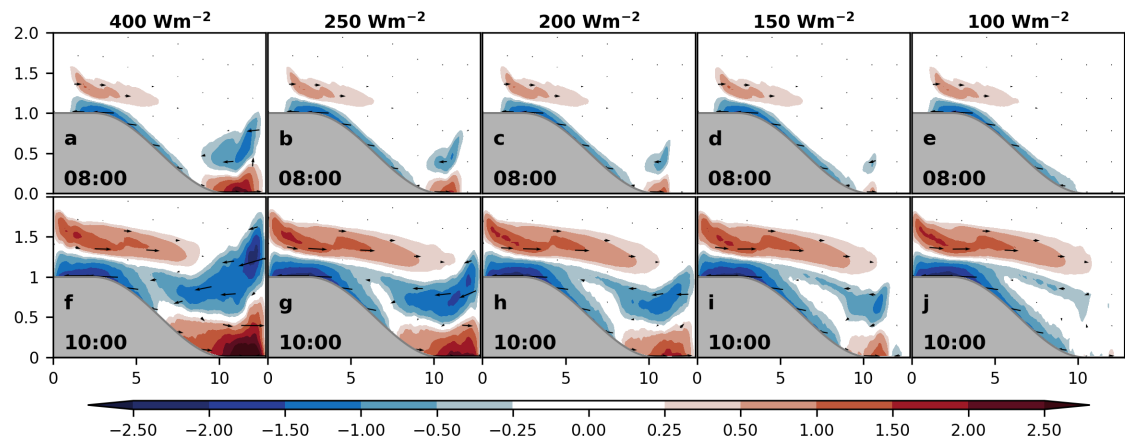


Figure A5: Cross-valley wind (U) in the morning for all UHI scenarios and high stability ($\partial\theta/\partial z = 3 \text{ K km}^{-1}$ at initial condition)

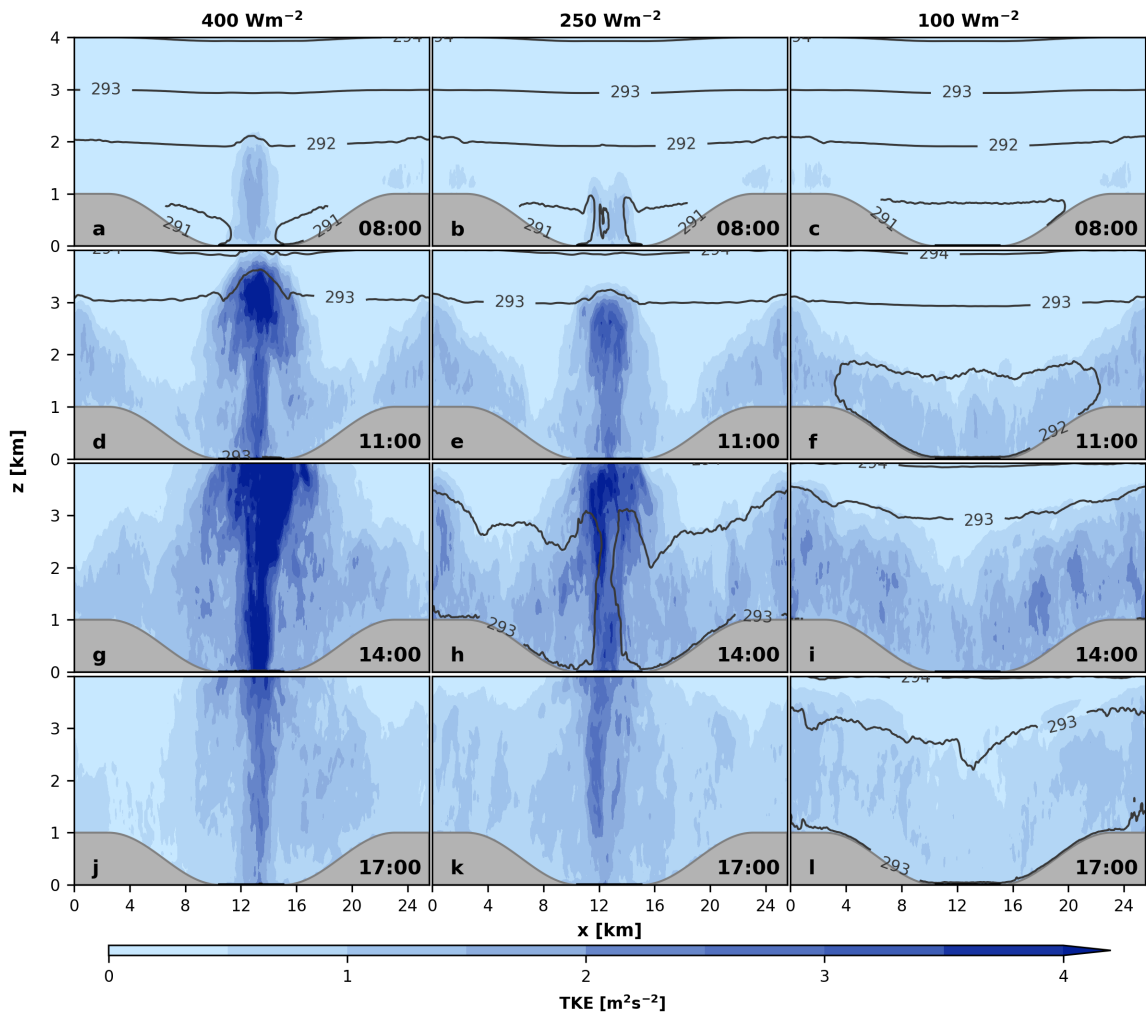


Figure A6: Daytime evolution of total TKE starting with low stability. Contours show isentropes every 1 K.

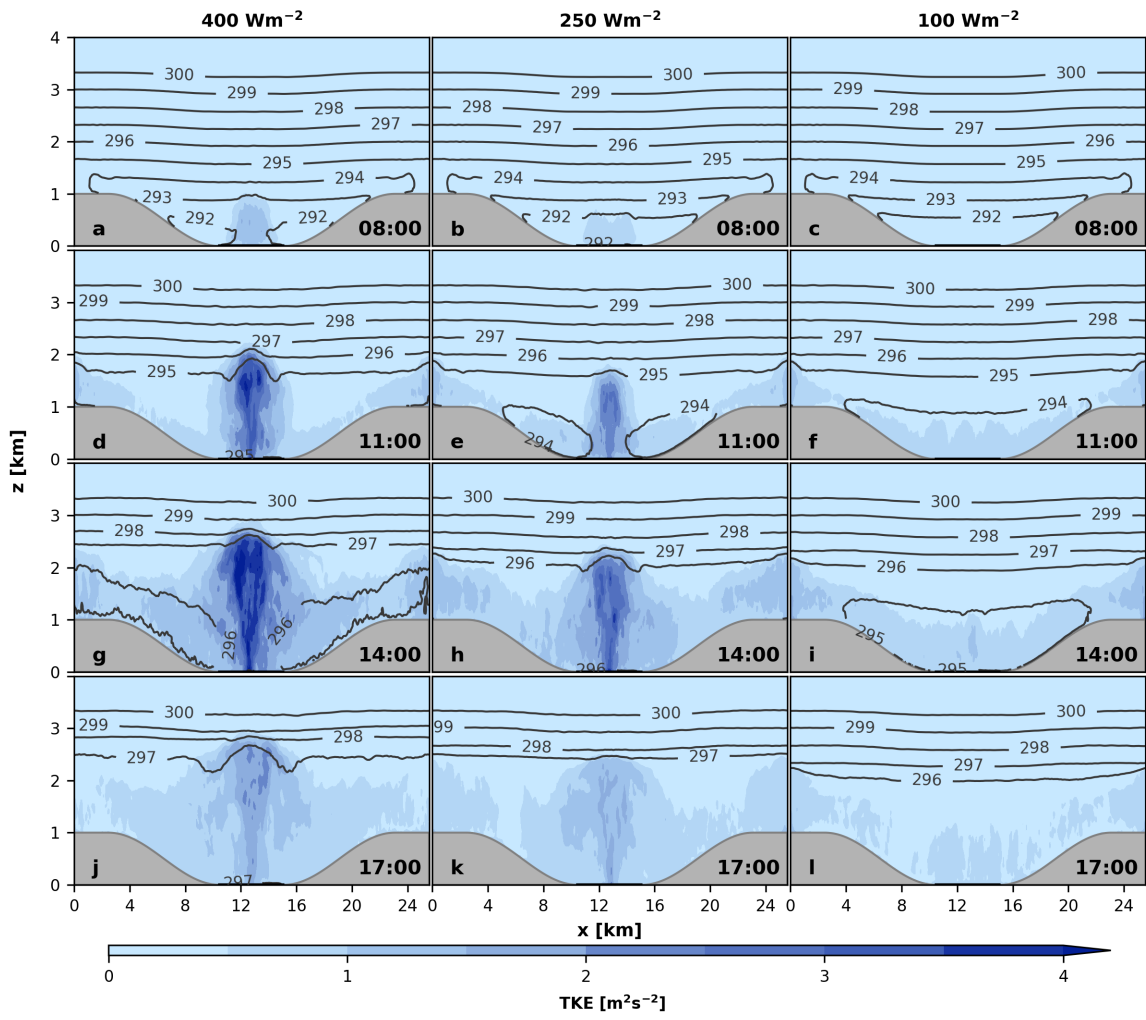


Figure A7: As in Fig. A6 but starting with high stability.

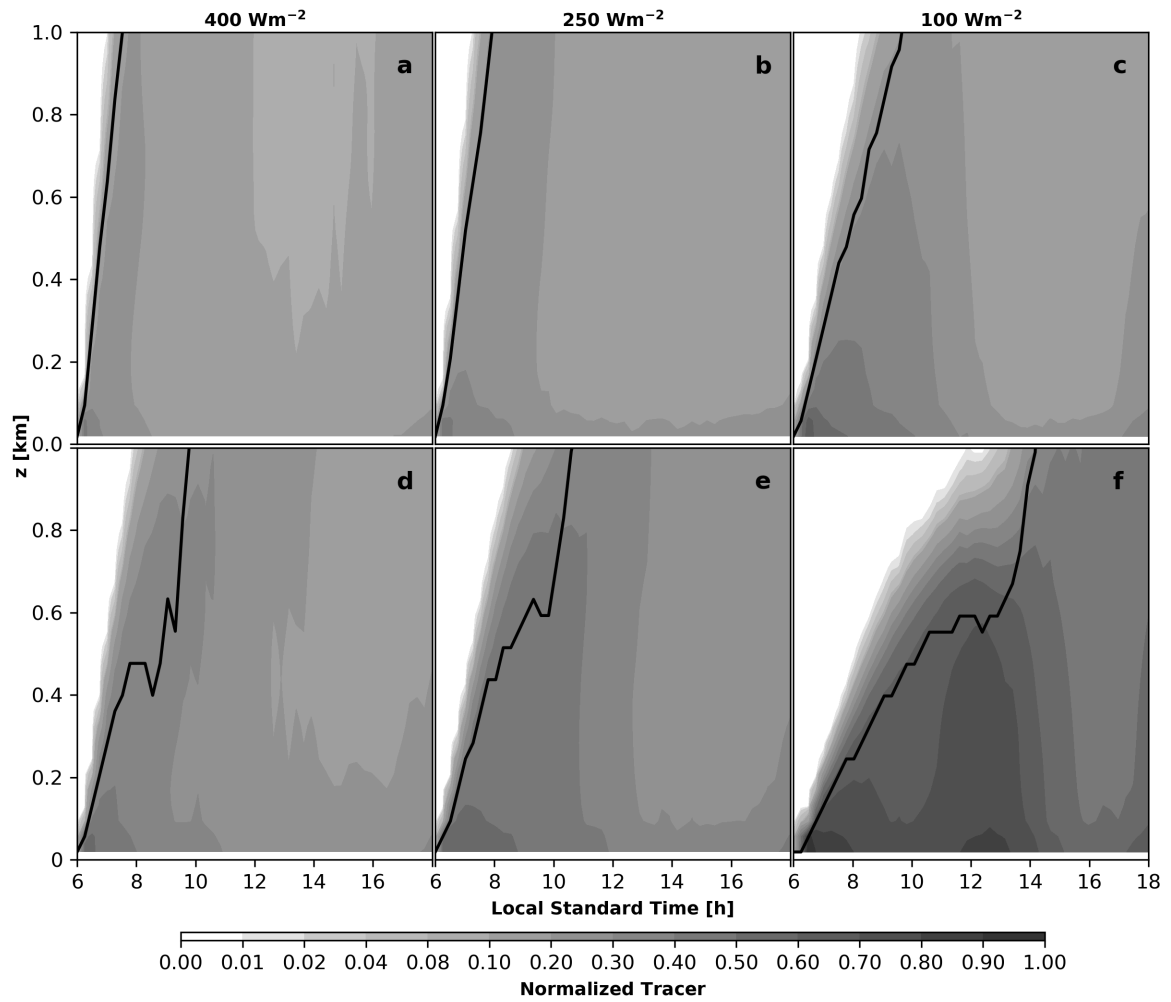


Figure A8: Time-height distribution of normalized tracer mixing ratio for the UHI mitigation scenarios, and for the low (top) and high (bottom) stability levels. Values represent spatial averages over the valley floor. The bold line shows the approximate height of the CBL.

B Supplementary figures for chapter 3

Table B1: Upper-air mean absolute error (MAE) and correlation coefficient (r) for potential temperature (θ) and the zonal and meridional (U,V) wind components using observations from a radar wind profiler (RWP) and a microwave radiometer (MWR). The analysis is performed with hourly results from domain D5 (0.3 km resolution) using the closest grid point to the instruments.

	0.2 km				1.3 km				50 m		800 m	
	U		V		U		V		θ		θ	
	MAE	r	MAE	r	MAE	r	MAE	r	MAE	r	MAE	r
	(m/s)		(m/s)	(m/s)		(m/s)		(m/s)	(K)		(K)	
ShinHong	1.4	0.4	2.8	0.2	1.7	0.3	1.6	0.3	1.0	0.8	1.2	0.9
MYNN	1.5	0.4	2.9	0.3	1.7	0.3	1.4	0.5	1.2	0.8	1.4	0.9
MYJ	1.6	0.4	2.8	0.4	1.7	0.3	1.5	0.4	1.7	0.8	1.7	0.9

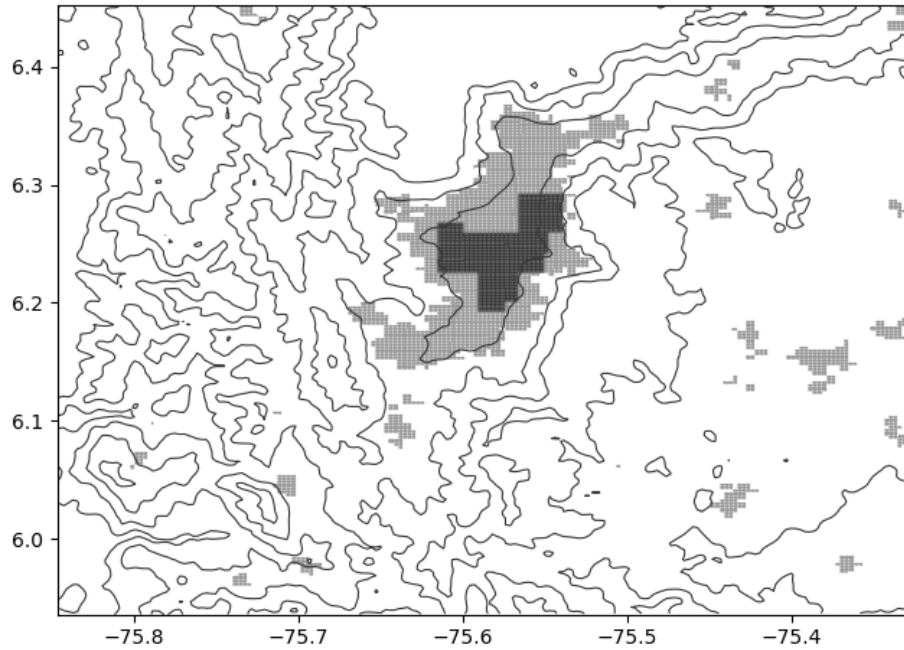


Figure B1: Urban category represented in land use databases: Modis 15 arc-second (light grey) and USGS 24-category database (dark grey).

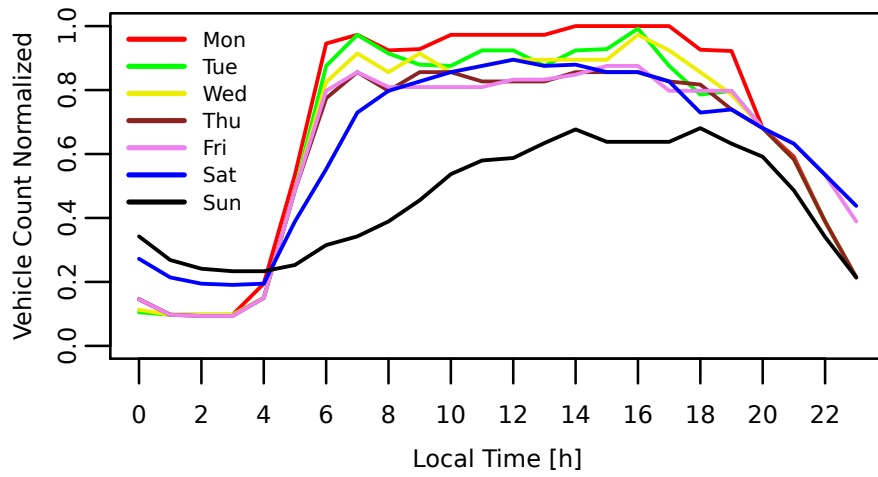


Figure B2: Normalized vehicle count for every weekday, derived from closed-circuit television cameras operated by the local mobility authority.

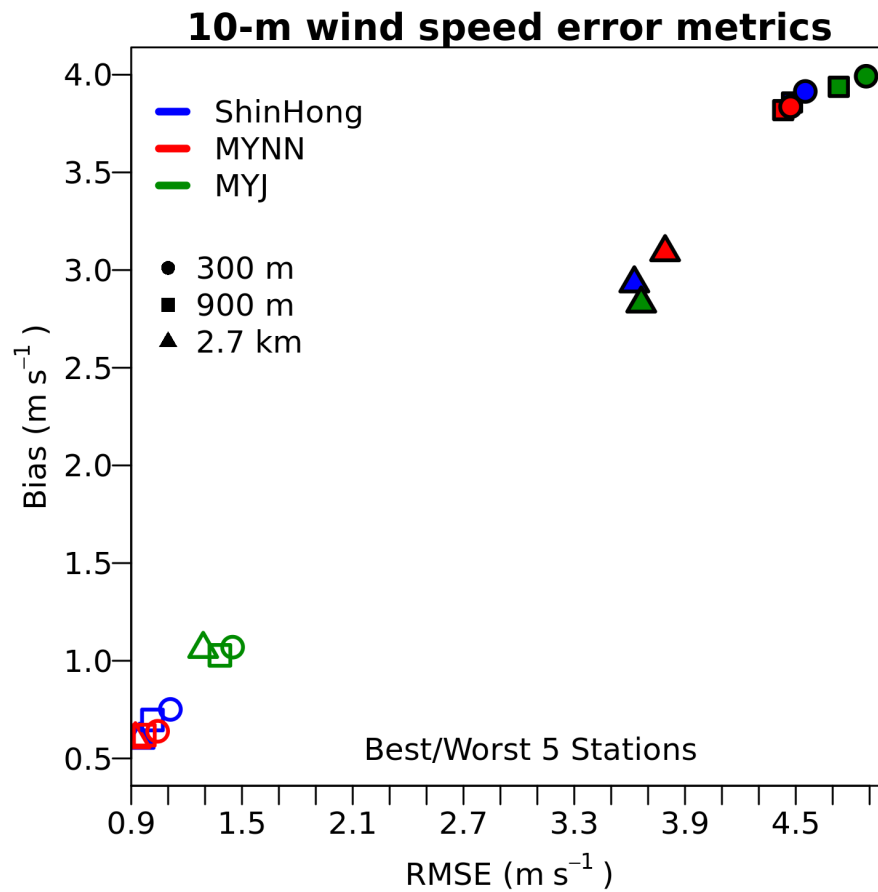


Figure B3: Wind speed mean bias error and root-mean-square error for the five best/worst stations. The largest differences across horizontal resolutions (between domains) occur for stations where the model performance is worse.

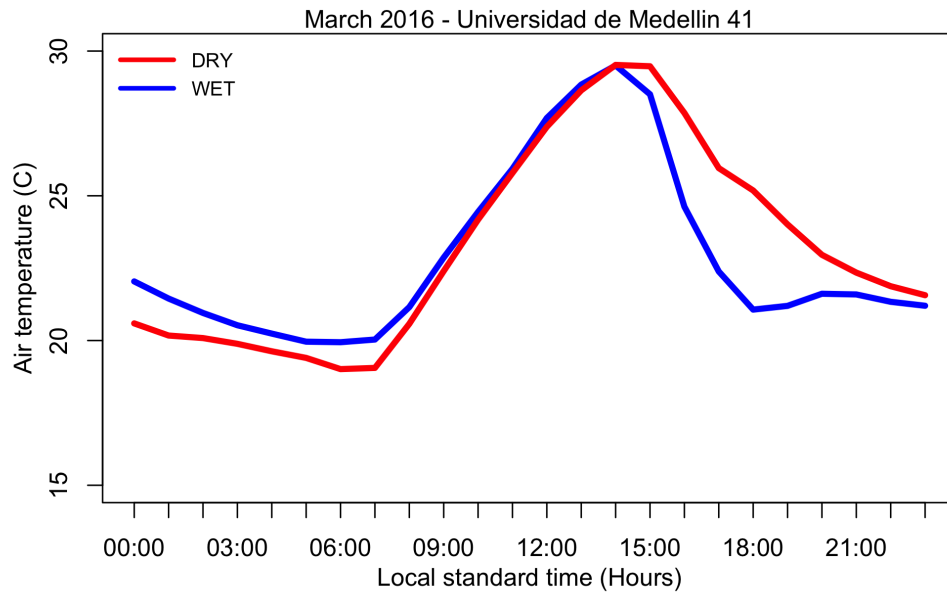


Figure B4: Diurnal cycle of T2 at station 41 for days with (blue) and without (red) rainfall.

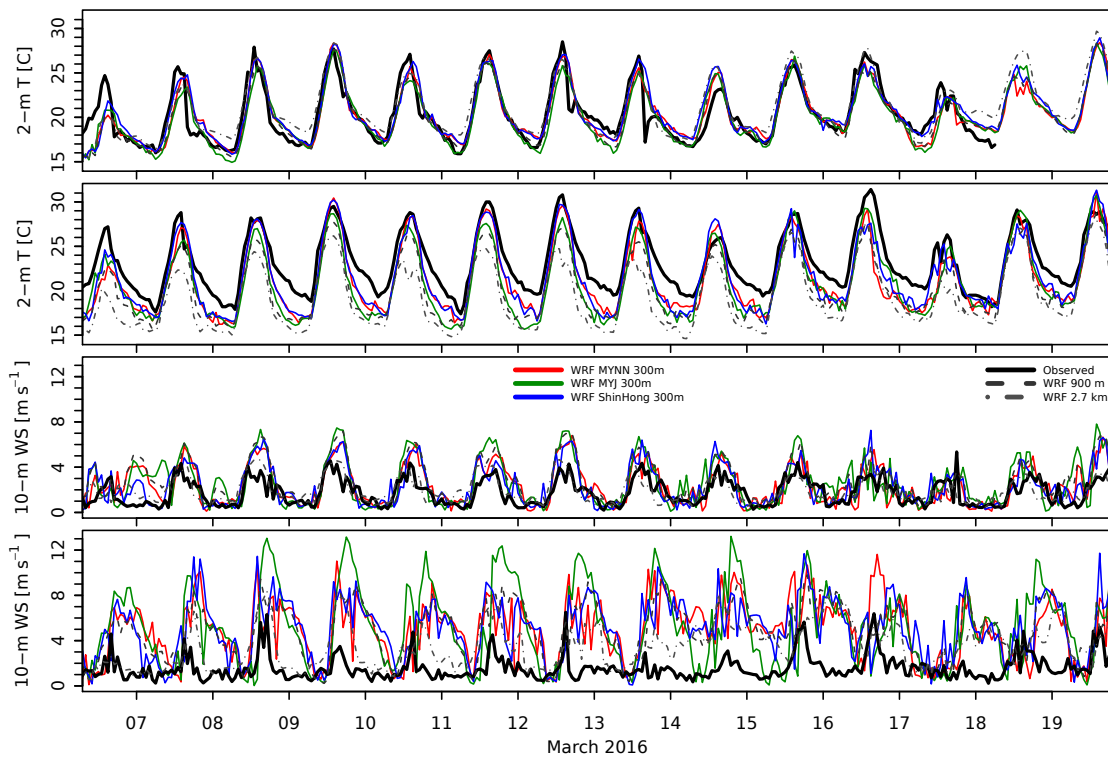


Figure B5: 2-m air temperature for the best (top, station 83) and worst (middle top, station 73) performing stations. 10-m wind speed for the best (middle bottom, station 82) and worst (bottom, station 202) performing stations. Time series constructed with hourly information.

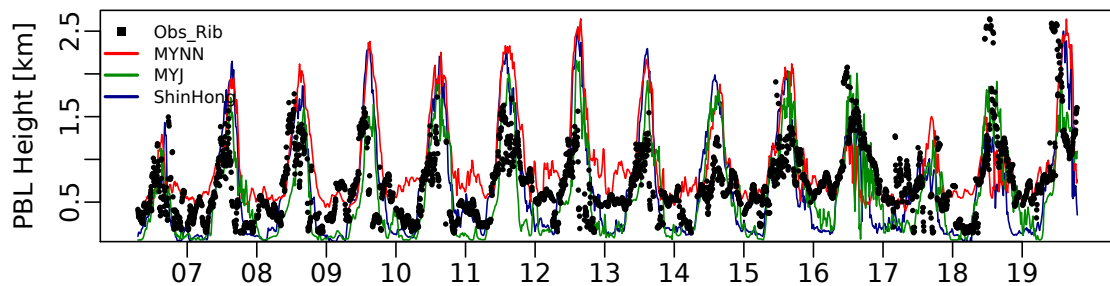


Figure B6: Time series of hourly PBL height. Observed PBL height is estimated with the bulk Richardson number, see methods for further details and data source.

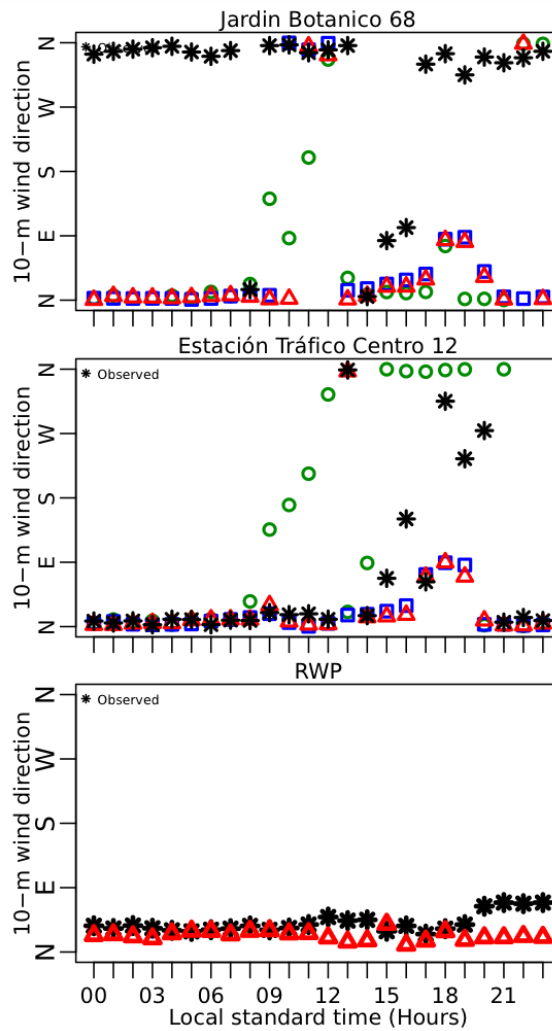


Figure B7: Diurnal cycles of wind direction at stations 68, 12, and at the radar wind profiler (RWP) at 200 m above terrain, exhibiting the predominant northerly flow. The 200 m height RWP observations are included for comparison with surface winds, as it is away from the built environment but within the PBL. Red triangles: MYNN PBL; blue squares: Shin-Hong PBL; green circles: MYJ PBL.

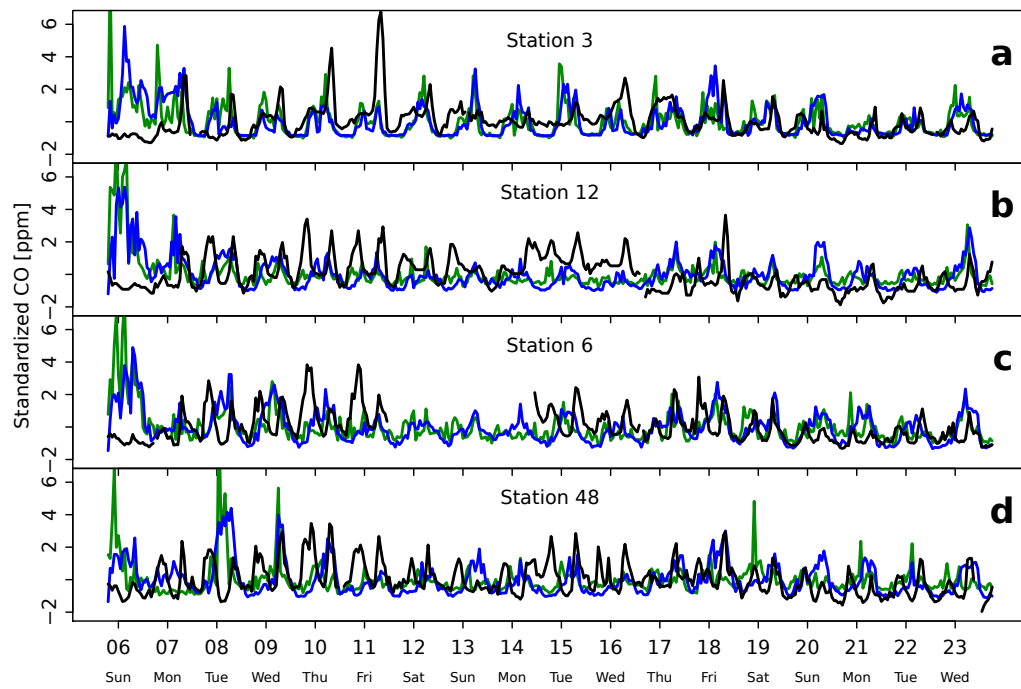


Figure B8: Hourly time series of standardized CO for the entire simulation period.

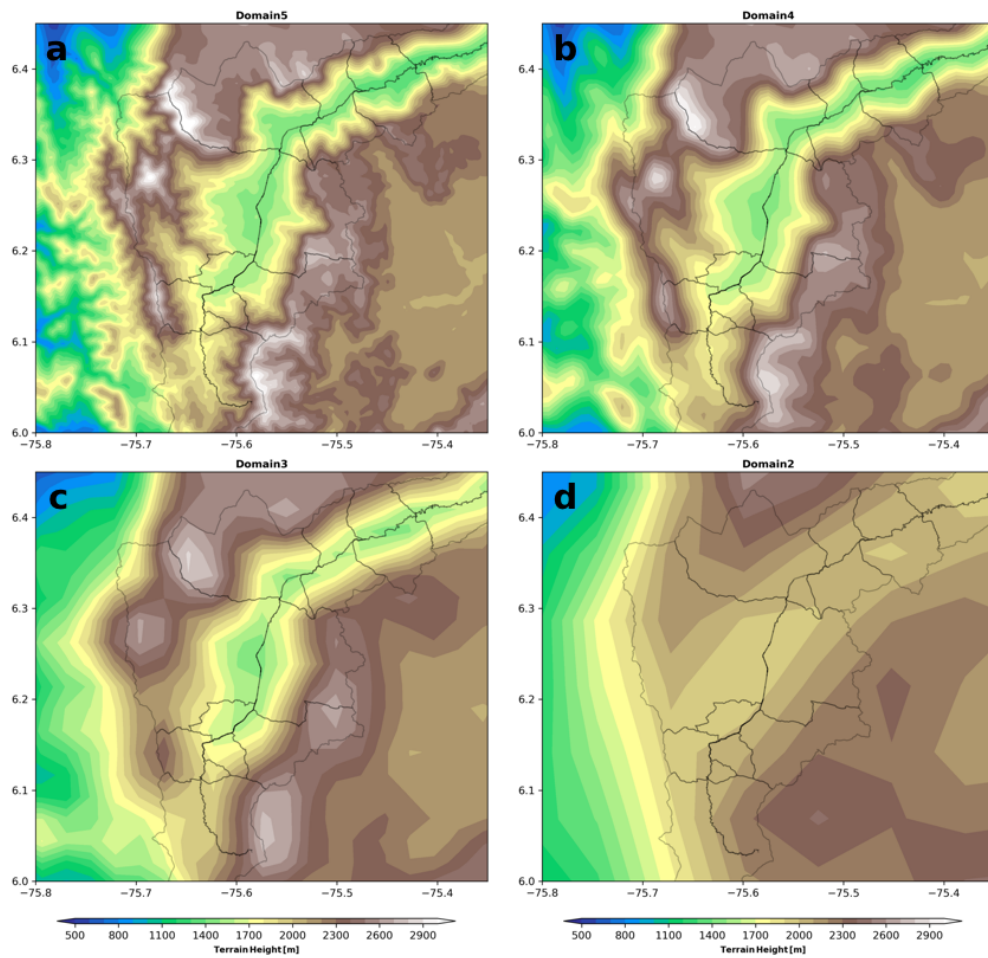


Figure B9: Model topography as represented in domains D2-D5, with grid sizes of: a) 300 m, b) 900 m, c) 2.7 km, and d) 8.4 km.

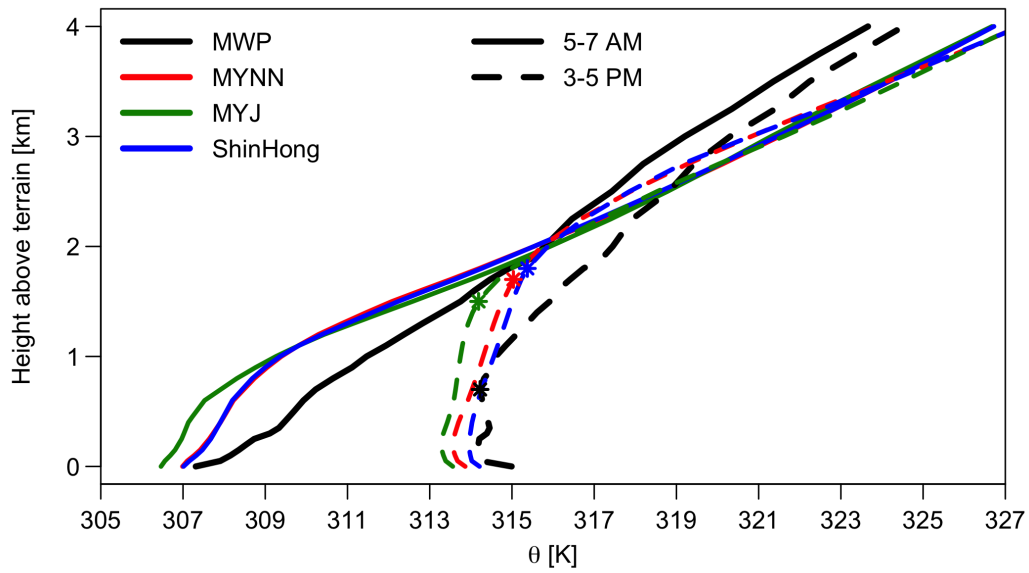


Figure B10: Vertical profiles of potential temperature during the morning (mean value for 7-5 AM) and afternoon (mean value for 3-5 PM), for the three PBL schemes used and observations with a microwave radiometer. Asterisks in the afternoon profiles show the estimated height of the convective boundary layer.

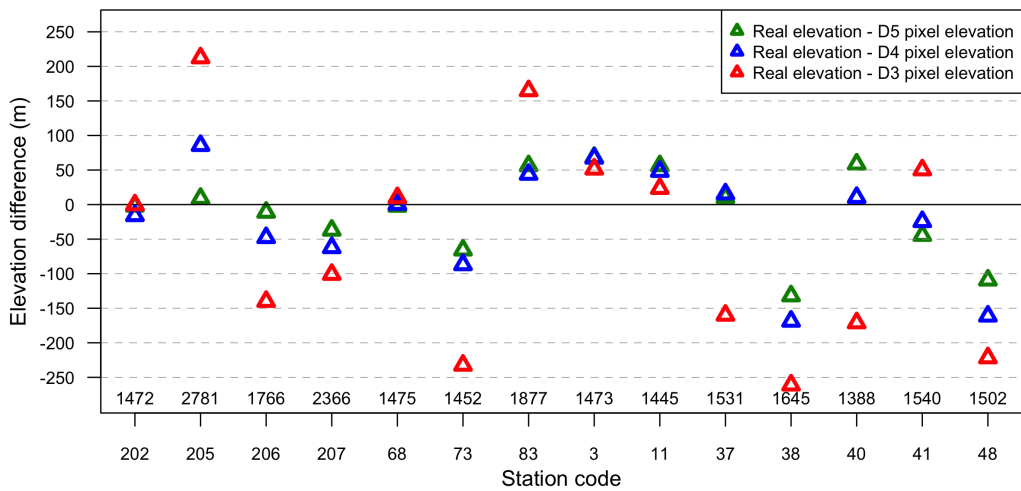


Figure B11: Difference in terrain elevation between the model (pixel) and real elevation. Some stations used in the study are not included because terrain elevation is not available. Model values correspond to closest model pixel.

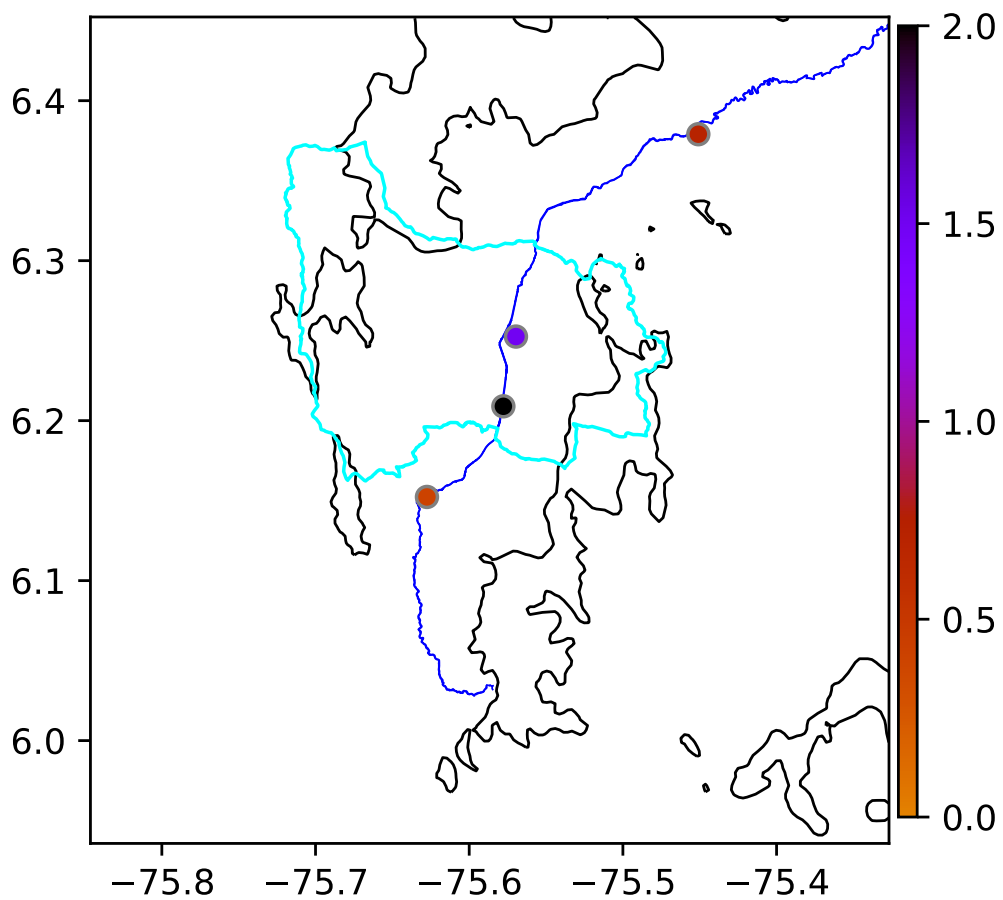


Figure B12: Observed index values. Calculated using the observed concentration but using the rest of the needed information from the model. *Note: this figure is not included in the published paper as it was created after for the thesis.*

C Supplementary figures for chapter 4

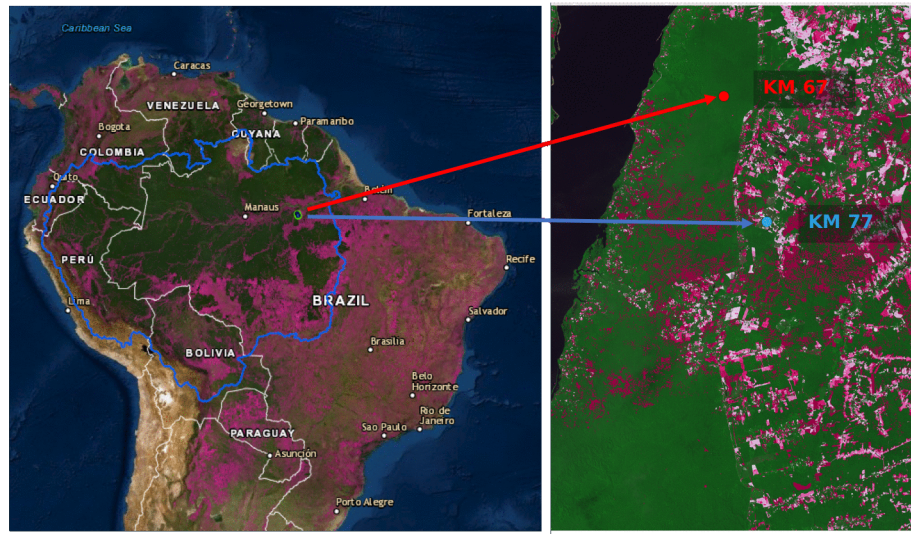


Figure C1: Forest cover loss from 2000 to 2012 in the Amazon basin (blue line in the left panel). Map produced with the Global Forest Watch map builder with data from Hansen et al. 2013 (full reference in section 4.7). Zoom into the study sites, overlaid with LANDSAT-5 satellite image (right panel).

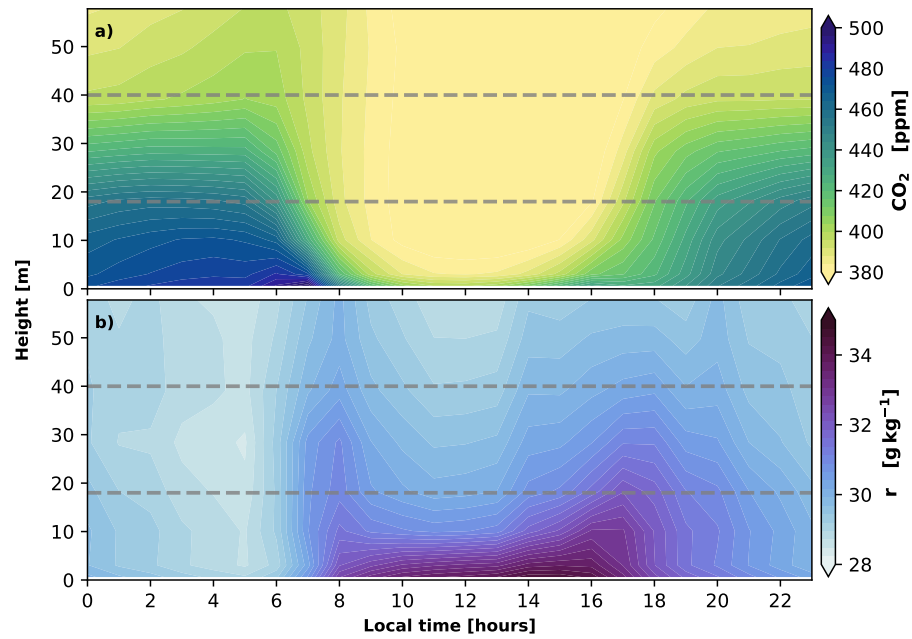


Figure C2: Mean diurnal cycles of carbon dioxide concentration (top) and water vapor mixing ratio (bottom). Mixing ratio (r), derived from water vapor concentration, and CO_2 concentrations were measured at 8 vertical levels from 0.91–62.24 m.